

**Structure and Binding Affinities of Geochemical Twin Fluorides:
From Bulk to Surface**

Inaugural-Dissertation

to obtain the academic degree

Doctor rerum naturalium (Dr. rer. nat.)

submitted to

the Department of Biology, Chemistry, Pharmacy
of Freie Universität Berlin

by

Jennifer Anders

from Bremerhaven, Germany

2023

This work was conducted under the supervision of
Prof. Dr. Beate Paulus (Freie Universität Berlin)
from August 2019 until July 2023

1st reviewer: Prof. Dr. Beate Paulus
2nd reviewer: Prof. Dr. Elena Voloshina

Date of defense: 11.10.2023

Selbstständigkeitserklärung

Hierdurch versichere ich, dass ich meine Dissertation selbstständig verfasst und keine anderen als die von mir angegebenen Quellen und Hilfsmittel verwendet habe.

Berlin, den

(Jennifer Anders)

Acknowledgements

First of all, I want to express my heartfelt gratitude towards Beate Paulus for providing me a doctoral study position in quantum chemistry, especially since I originally came from molecular mechanics. I want to thank you for your unwavering, generous support, for supervising the work within this thesis scientifically, for organizing funding for the whole past four years, for allowing a large autonomy within my scientific work (including special treats such as letting me be corresponding author on each paper or being open to publishing each of these open access), for all the cordial and open-hearted talks within the coffee room, as well as for always leaving your office door open for urgent questions to be answered. I want to express my utmost thanks for initiating the cooperation with AG Tonner-Zech by sending me to Leipzig and for funding last year's *European Summerschool in Quantum Chemistry*. From both, I have learned a tremendous amount about quantum chemical methods, while I also had a lot of fun. Finally, I want to express my sincerest gratitude for your perceptive and brave decision to advise a radical change of topic from solvation effects to the solid state after my first year. Leaving what felt like a dead end for a new, self-responsible challenge, was exactly right.

Secondly, I would like to thank Elena Voloshina. I am very grateful for your time, your passion for and your expertise on solid state calculations, as well as your eager willingness to share it when asked. Thank you for being the second reviewer of my thesis.

Thirdly, I want to thank my favorite geologist, Anselm Loges. Without your expertise, the whole topic of my thesis would have made no sense. Thank you bunches for sharing your enormous knowledge and beautiful slides on geochemistry enthusiastically with me, thank you for your thorough proofreading with witty comments, and sharing your mastery of LaTeX. I also want to explicitly thank you for lifting my initial, naive band gap measurement idea to a practical level and for realizing it. It was super interesting to actually participate in actual synchrotron measurements with you and Fabian.

To Fabian, I want to express my sincere gratitude, not only for spending an exhausting week with Anselm and I at BESSY II (without payment nor that it was part of your Master Thesis), but also for doing excellent work within your internship. I wish you the best for your recently started own doctoral study. The same wish goes out for two other internship students, Niklas and Henrik. Thank you for your eager willingness to learn and the effort you put into your work.

I also want to explicitly thank Ralf Tonner-Zech and his group, for their hearty welcome in Leipzig, which was really refreshing after the corona lock downs. Especially, I want to thank Jan-Niclas Luy, who very patiently, introduced me to the pEDA NOCV method.

Furthermore, I want to thank Dirk Andrae. Thank you for contributing to my academic growth through your engagement and dedication to teach independent from the lecture schedule, spreading your immense knowledge from wave function methods to your former

work on effective core potentials, leading to relativistic quantum chemistry, to arrive at finite nuclear volume effects, but also going all the way back to the mathematical foundations, and point groups. It was an honor teaching molecular symmetry with you. Apart from science, I also want to express my thanks for your environmental and sociopolitical considerations. Now, that I graduate, I hope to find the time to digest "*Bildung entscheidet über die Zukunft der Menschheit.*"

Moreover, I am indebted to the former TC group members Oliver, Jan (Olli), and (Jan) Felix, as well as Tim and Stefan, I am very grateful, that you always took the time to lend me a hand with my first shaky steps in coding, as well as for your vast scientific knowledge, which you eagerly shared with me.

My deepest appreciation goes to my caring mother and my lovely friends. Your encouragement, love, understanding, and your belief in my abilities has been so often a much needed refill of motivation, when the glass was less than half empty. Especially, I want to thank the five fellows, which have been with me all the way - up and down - from the freshman's year 11 years ago until now. Thank you a million times, (in alphabetical order:) Anna, Gene, Lawrence, Marlon, and Steffi. Steffi, it was a great pleasure to share the office with you for the past four years.

Not yet last, but definitely not least, I want to dearly thank the TC members (in alphabetical order:) Alina, Dilara, Fabi, Hana, Jiajun, Jian, Joana, Luca, Marius, Robert, Simon, and Tilen. Your camaraderie, humor, and open-hearted attitude have made the lunchtime and after-work chats, but also the overtimes enjoyable.

Finally, I wish to express my gratitude to all hitherto unnamed current and former members of the TC groups. Your support, no matter how small, has not gone unnoticed and is sincerely appreciated. The same applies for the teams of the ZEDAT and ZIP for their computational support, especially Boris Proppe, Robert Schüttler, and Christian Tuma.

Also, I would like to gratefully acknowledge the financial support, frequent and vivid scientific exchange (even despite corona times) provided by the CRC 1349, "*Fluorine-Specific Interactions,*" which in turn has been made possible by the German Research Foundation (DFG). Without the powerful computational resources provided by the ZEDAT, and even more so by the HLRN via generously granting my project bec00240 "*Quantum Description of Geological Twins*" for two years, no paper within this thesis, would have been possible. From which, three of these wouldn't be open access without the generous funding of the Freie Universität Berlin, which has been my dear "home-university" for the last eleven years.

"Geochemistry only really came of age as a science [...] when geologists, chemists, and physicists managed to bridge the chasms of mutual ignorance that had separated their various fields of inquiry."

– Francis Albarède
in *Geochemistry: An Introduction*^[1]

Table of Contents

List of Figures	ii
Lists of Abbreviations and Symbols	iii
Abstract and Kurzzusammenfassung	vi
List of Publications	ix
1 Introduction	1
2 Theory	7
2.1 Electronic Structure Calculations	7
2.1.1 Schrödinger Equation	7
2.1.2 Hartree Fock Method	9
2.1.3 Density Functional Theory	12
2.1.4 Dispersion Correction	15
2.1.5 Hubbard-Type Correction	16
2.1.6 Basis Sets and Core Potentials	18
2.2 Periodic Systems	22
2.2.1 Atomic and Electronic Structure of Ideal Crystals	22
2.2.2 Surface Energies and Abundances	26
2.2.3 Adsorption Energies via pEDA with NOCV Extension	29
2.3 Contributions from Special Relativity	32
2.4 Electronic Structure of Lanthanides	36
3 Publications	39
3.1 Paper A	39
3.2 Paper B.1	68
3.3 Paper B.2	93
3.4 Paper B.3	122
4 Summary and Discussion	153
5 Outlook	163
6 References	165

List of Figures

1.1	periodic table of elements and ionic radii of Sc, Y, Zr, Nb, Ln, Hf, and Ta . . .	2
1.2	scheme of a HFSE ore deposit formation of fluoride-rich hydrothermal veins . . .	3
2.1	2D lattice and basis of hcp Ho	22
2.2	Miller indices planes within waimirite-structured crystal	26
2.3	slab example of β -HoF ₃ (011)	27
2.4	Feynman-Stückelberg interpretation of the positive and negative energy solutions	33
2.5	4f and 5d-band energies along Ln(III)/Ln(II)-series and radial probability densities of Sm(III)	37
4.1	summary paper A: Zr:Hf affinities for fluoride vs. oxide or hydroxide as ideal crystals	154
4.2	summary part B: Y:Ho fluoride surface modeling and fluoride vs. chloride affinities at surfaces	156
4.3	summary paper B.1: YF ₃ vs. HoF ₃ surface stabilities and abundances	158
4.4	summary paper B.2: YF ₃ vs. HoF ₃ surface-adsorbate interactions with HF, HCl, or H ₂ O	160
4.5	summary paper B.3: YF ₃ surface-adsorbate interactions to HF, HCl, or H ₂ O applying pEDA	162

List of Abbreviations

AIMD	ab initio molecular dynamics	LCAO	linear combination of AOs
AMS	Amsterdam Modeling Suite	LDA	local density approximation
AO	atomic orbital	Ln	lanthanide; defined as La–Lu
aq.	aqueous	LR	long-range
bd	bulk-derived	M	metal atom
BJ	Becke-Johnson damping	MO	molecular orbital
BOA	Born-Oppenheimer approximation	NOCV	natural orbitals for chemical valence
CB	conduction band	PAW	projector augmented wave
cGTO	contracted GTO	PBE	Perdew-Becke-Ernzerhof
D	dimensional, as 2D, 3D, or 4D	pEDA	periodic EDA
D3	Grimme's dispersion correction nr. 3	REE	rare earth element; defined equal to Ln
DFA	density functional approximation	res.	residual
DFT	density functional theory	SCF	self-consistent field
DOS	density of states	sd	slab-derived
ECP	effective core potential	SD	Slater determinant
EDA	energy decomposition analysis	SE	Schrödinger equation
FBZ	first Brillouin zone	SI	supporting information
FCO	frozen core orbital	SOC	spin-orbit coupling
GGA	generalized gradient approximation	sr	scalar relativistic
GTO	Gaussian-type orbital	SR	short-range
H-bond	hydrogen bond	STO	Slater-type orbital
hcp	hexagonal closed-packed	s-ZORA	scaled ZORA
HF	Hartree-Fock	VASP	Vienna Ab Initio Simulation Package
HP	Hartree product	VB	valance band
HFSE	high field strength element; defined by $Q_{\text{ion}}/r_{\text{ion}} > 2 \text{ e \AA}^{-1}$	X	electronegative atom of O, F, or Cl
HSAB	hard and soft acids and bases	ZPE	zero point energy
HSE	Heyd-Scuseria-Ernzerhof	ZORA	zeroth-order regular approximation
Hub	Hubbard model		
IBZ	irreducible subset of FBZ		
KS	Kohn-Sham		

List of Symbols

α, β	spins	$\%_{\text{surf}}$	surface abundance within an ideal crystal according to its electronic energy
α, β, γ	lattice angles	A	surface area
$\bar{\alpha}$	averaged dipole polarizability in D3	A_{Hub}	amplitude of electron hopping
δ_{ij}	Kronecker delta	a_0	Bohr radius
ϵ	orbital energy	$\mathbf{a}_1, \mathbf{a}_2, \mathbf{a}_3$	real-space lattice vectors
ζ	exponent of STO	\mathbf{C}	coefficient matrix
η	screening parameter in HSE hybrid functionals	\hat{c}	electron annihilation operator
θ	polar angle	\hat{c}^\dagger	electron creation operator
Θ	energy-dependent scaling function used in ZORA	c_0	speed of light in vacuum
λ	reactant spin orbital	C_6^{AB}, C_8^{AB}	D3 dispersion coefficients
μ	chemical potential	CN	coordination number
ν	NOCV eigenvalue	E_A^{AB}	total electronic energy of compound A within local minimum atomic structure of compound AB
ρ	electron density	E_{gap}	band gap energy
$\rho_{\Delta\sigma}$	spin density	E_{surf}	surface energy
σ	spin function	ΔE_{attr}	attractive energy
$\underline{\sigma}$	Pauli spin matrices	ΔE_{disp}	dispersion energy
τ	exponent in GTO	ΔE_{elstat}	electrostatic energy
υ	azimuth angle	ΔE_{bond}	bonding energy
Υ_1, Υ_2	global D3(BJ) DFA-fitted parameters	$\Delta E_{\text{bond},\%}$	bonding energy multiplied by the respective $\%_{\text{surf}}$
ϕ	basis function	ΔE_{int}	interaction energy
$\phi_{\mathbf{k}}$	Bloch orbital	$\Delta E_{\text{int}}(\text{elec})$	electronic term of the interaction energy
Φ	time-dependent total wave function	ΔE_{orb}	orbital energy
Φ^{D}	Dirac spinor	$\Delta E_{\text{orb}}^{\text{direct}}$	direct σ -like coordination ($X-Y_{\text{surf}}$) contribution to the orbital energy
χ	spin orbital	$\Delta E_{\text{orb}}^{\text{H-bond}}$	H-bond ($X \cdots H-F_{\text{surf}}$) contribution to the orbital energy
ψ	spatial orbital	ΔE_{Pauli}	Pauli energy
Ψ	time-independent total wave function	ΔE_{prep}	preparation energy
$\tilde{\Psi}$	pseudo all-electron wave function used in PAW method		
Ψ^{NOCV}	NOCV wave function		
ω	imaginary frequency		
Ω	normalization constant of STO or GTO		

\hat{f}	one-electron Fock operator	\mathbf{p}	momentum vector
f_{BJ}	BJ damping constant used within D3(BJ)	\tilde{p}	projector function used in PAW method
f_{D}	damping function within D3	$P_{ij,\sigma}$	density matrix elements
f_{DFA}	DFA	P_{nl}	radial probability density
\mathbf{F}	Fock matrix	$\Delta\mathbf{P}^{\text{orb}}$	deformation density matrix
\mathbf{g}	metric of Minkowski space-time	Q_{ion}	ionic charge
\mathbf{G}	reciprocal lattice vector	r	radial distance of an electron to the nucleus
(hkl)	Miller indices	\mathbf{r}	spatial coordinate vector for an electron
\hbar	reduced Planck constant	r_{ion}	ionic radius
i	imaginary unit	R	interatomic distance
J	Coulomb integral	\mathbf{R}	spatial coordinate vector of an atom
\bar{J}	spherical averaged screened Coulomb interaction	R_{nl}	radial part of the AO
\mathbf{k}	wave vector	s_6, s_8	D3 scaling factors
K	exchange integral	$s_{\mathbf{k},1}, s_{\mathbf{k},2}, s_{\mathbf{k},3}$	shift of \mathbf{k} -grid points along $\mathbf{b}_1, \mathbf{b}_2, \mathbf{b}_3$
l	angular quantum number	t	time
m_e	rest mass of an electron	\mathbf{t}	UC translation vector
m_l	magnetic quantum number	T	kinetic energy
m_s	magnetic spin quantum number	U	effective on-site Coulomb interaction potential
n	principal quantum number	U_{eff}	effective U
\hat{n}	number operator for electrons	\bar{U}	spherical averaged U
N_{4f}	number of 4f-electrons according to the Aufbau principle	V	potential energy
N_ϕ	number of basis functions	\mathbf{x}	spatial coordinate vector and m_s for an electron
N_e	number of electrons	\mathbf{x}^{M}	Minkowski space-time vector
N_{F}	number of fluorine atoms	Y_{lm_l}	angular part of hydrogen(-like) orbital
$N_{\mathbf{k},1}, N_{\mathbf{k},2}, N_{\mathbf{k},3}$	number of \mathbf{k} -grid points along $\mathbf{b}_1, \mathbf{b}_2, \mathbf{b}_3$	Z	nuclear charge
N_{M}	number of metal atoms		
N_{N}	number of nuclei		
N_{uc}	number of unit cells		
N_{xF}	number of substoichiometric fluorine atoms		

Abstract

The geochemical transport of elements within Earth is mainly driven by ionic interactions. Element mobility is thus, determined by the charge and radius of the respective ions. From this follows, that two elements occurring as ions of equivalent charge and radius are also equally mobile. This leaves the concentration ratio between them unchanged. Such two elements are referred to as geochemical twins. Prominent examples are zirconium and hafnium, or yttrium and holmium. These twin elements only fractionate, if the geochemical transport mechanism is based on more than simple Coulomb interactions. It is known that fluoride-rich, hydrothermal veins must originate from such a mechanism, as these show strongly enriched concentrations of hafnium against zirconium, or yttrium against holmium. The nature of this mechanism is, however, still unsolved given the complex chemical compositions of the involved solids, melts, liquids, and gases, as well as the unfeasibility to measure the ongoing process. Rock samples only probe the final outcome, while lab and computational experiments only model tiny subsets of the actual system. So far, these experiments focused on the complexation of ions within aqueous solution. However, within the overall mechanism, frequent precipitation and re-solvation occur. These are processes, which demand an understanding of the respective solids and especially their surfaces. Such understanding may be provided by quantum chemical calculations. Yet, especially the solid geochemical twin fluorides have been a blind spot up to now.

The aim of this work is to shed some light on this area by investigating the subtle differences linked to their electronic structure. All calculations within this thesis are based on periodic density functional theory (DFT). Four papers contribute to this work, which are grouped according to the studied geochemical twin pair. Within paper **A**, the cohesive energies of the binary and ternary oxides and fluorides, as well as the mono-hydroxylation products are evaluated for the twin pair of zirconium and hafnium. The larger part of this thesis is devoted to the geochemical twin pair of yttrium and holmium as crystalline fluorides. The first of these papers, **B.1** analyzes the stabilities of the low-lying Miller indices surfaces to construct Wulff plots for both compounds, independently. For holmium, the degree of applied Hubbard-type correction is scanned. Building up on the results, possible surface interactions with compounds of hydrothermal fluids as water, hydrogen fluoride, and hydrogen chloride are studied in paper **B.2**. Onto the most abundant surfaces of both compounds, single and multiple adsorptions are considered. Finally, paper **B.3** investigates the chemical nature of these adsorbate-surface interactions. For yttrium fluoride, it illuminates the impact of the chosen surface, as well as of the adsorption site onto the covalent versus electrostatic interactions.

Kurzzusammenfassung

Der geochemische Transport von Elementen innerhalb der Erde wird hauptsächlich durch ionische Wechselwirkungen bestimmt. Die Mobilität der Elemente wird also durch die Ladung und den Radius der jeweiligen Ionen bestimmt. Daraus folgt, dass zwei Elemente, die als Ionen gleicher Ladung und gleichem Radius vorkommen, ebenfalls gleich mobil sind. Damit bleibt das Konzentrationsverhältnis zwischen beiden Elementen unverändert. Solche zwei Elemente werden als geochemische Zwillinge bezeichnet. Prominente Beispiele sind Zirkonium und Hafnium oder Yttrium und Holmium. Diese Zwillingselemente fraktionieren nur, wenn der geochemische Transportmechanismus auf mehr als einfachen Coulomb-Wechselwirkungen beruht. Es ist bekannt, dass fluoridreiche, hydrothermale Gänge aus einem solchen Mechanismus stammen müssen, da sie stark angereicherte Konzentrationen von Hafnium gegenüber Zirkonium oder Yttrium gegenüber Holmium aufweisen. Die Natur dieses Mechanismus ist jedoch noch nicht verstanden, was an der komplexen chemischen Zusammensetzungen der beteiligten Feststoffe, Schmelzen, Flüssigkeiten und Gasen beruht, sowie der Unmöglichkeit, den laufenden Prozess zu messen. Gesteinsproben zeigen nur das Endergebnis, während Labor- und Computereperimente nur winzige Teilprozesse des tatsächlichen Systems modellieren. Bislang konzentrierten sich diese Experimente auf die Ionenkomplexierung in wässriger Lösung. Innerhalb des Gesamtmechanismus kommt es jedoch häufig zu Ausfällungen und Resolvatisierungen. Dies sind Prozesse, die ein Verständnis der jeweiligen Feststoffe und insbesondere deren Oberflächen erfordern. Ein solches Verständnis kann durch quantenchemische Rechnungen gewonnen werden. Allerdings waren insbesondere die Fluoride der geochemischen Zwillinge als Feststoffe bisher ein blinder Fleck.

Ziel dieser Arbeit ist es, etwas Licht auf diesen Fleck zu streuen, indem die feinen Unterschiede beleuchtet werden, die sich aus ihrer elektronischen Struktur ableiten. Alle Berechnungen im Rahmen dieser Arbeit beruhen auf periodischer Dichtefunktionaltheorie (DFT). Vier Publikationen tragen zu dieser Arbeit bei. Diese sind gruppiert nach dem jeweiligen untersuchten geochemischen Zwillingpaar. In Publikation **A** werden die Kohäsionsenergien der binären und ternären Oxide und Fluoride sowie der Mono-Hydroxylierungsprodukte für das Zwillingpaar Zirkonium und Hafnium untersucht. Der größte Teil dieser Arbeit ist dem geochemischen Zwillingpaar Yttrium und Holmium als kristalline Fluoride gewidmet. In der ersten dieser Publikationen, **B.1**, werden die Stabilitäten der Oberflächen mit niedrig liegenden Miller'schen Indizes analysiert, um Wulff-Diagramme für beide Verbindungen unabhängig voneinander zu konstruieren. Für Holmium wird die Größe der angewandten Hubbard'schen Korrektur gescannt. Aufbauend auf diesen Ergebnissen werden mögliche Oberflächenwechselwirkungen mit Verbindungen aus hydrothermalen Flüssigkeiten wie Wasser, Fluorwasserstoff und Chlorwasserstoff in Publikation **B.2** behandelt. Auf den Oberflächen mit den größten Anteilen beider Verbindungen werden isolierte und multiple Adsorptionen untersucht. Schließlich erkundet Publikation **B.3** die chemische Natur dieser Adsorbat-Oberflächen-Wechselwirkungen.

Für Yttriumfluorid werden die Auswirkungen der gewählten Oberfläche, sowie der Adsorptionsstelle auf die kovalenten und elektrostatischen Wechselwirkungen beleuchtet.

List of Publications

- Paper A** "Stability of Hydroxo/Oxo/Fluoro Zirconates vs. Hafnates —A DFT Study",
J. Anders, F. Göritz, A. Loges, T. John, B. Paulus, *Inorganics*, **2022**, 10, 259.
<https://doi.org/10.3390/inorganics10120259>
- Paper B.1** "First Principle Surface Analysis of YF₃ and Isostructural HoF₃",
J. Anders, N. Limberg, B. Paulus, *Materials*, **2022**, 15, 6048.
<https://doi.org/10.3390/ma15176048>
- Paper B.2** "Chemical Adsorption of HF, HCl, and H₂O onto YF₃ and Isostructural HoF₃ Surfaces by First Principles",
J. Anders, H. Wiedenhaupt, B. Paulus, *Crystals*, **2023**, 13, 555.
<https://doi.org/10.3390/cryst13040555>
- Paper B.3** "Chemical Bonding of HF, HCl, and H₂O onto YF₃ Surfaces - Quantification by First Principles",
J. Anders, H. Wiedenhaupt, F. Kreuter, R. Tonner-Zech, B. Paulus, *J. Comput. Chem.*, **2023**, accepted and published online.
<https://doi.org/10.1002/jcc.27168>

1. Introduction

The field of natural science called geochemistry applies the principles of chemistry to gain insights into geological processes to, among others, understand and predict the transport pathways of elements within Earth.^[2] Most elements are transported as ions, from which most, conveniently, are found at a single stable oxidation state within natural conditions. The charge (Q_{ion}) and ionic radius (r_{ion}) of this ionic species determine the element's mobility within most geochemical processes. If two elements occur as ions of equivalent Q_{ion} and r_{ion} , they are subsequently transported equally along most geochemical pathways. To emphasize this similarity, such two elements are referred to as geochemical twins.^[3,4] Accordingly, most rock samples contain these twin elements at their chondritic ratio, which is their constant abundance ratio within the whole solar system. If deviations from this chondritic ratio occur, it suggests that quantities beyond Q_{ion} and r_{ion} are decisive along the transport pathways. Therefore, these ratios provide evidence for the geochemical history of a rock sample.

Within the periodic table of elements, such geochemical twin pairs are predominantly found among certain metals of the fifth and sixth period (see Fig. 1.1). The period number equals the highest principal quantum number within the set of occupied orbitals. By the principal quantum number, the radial expectation value of that orbital increases. Therefore, the overall atomic radii increase from one period to the next. The radial expectation values also slightly increase by the angular quantum number. However, this dependency is too small to counterbalance the stronger, attractive Coulomb forces towards the nucleus. Consequently, within the same period, the atomic radii shrink by each additional proton. The same applies to the series of lanthanides (Ln) of lanthanum to lutetium (La–Lu) within the sixth period leading to the famous lanthanide contraction. What is particular about these elements is the 4f-shell filled by each additional electron along the Ln-series. Because of its smaller principal quantum number, compared to the fully occupied $5s^2$, $5p^6$, and $6s^2$, or the singly occupied $5d^1$, its radial expectation value is also smaller. Hence, the 4f-shell is shielded by the electron density of these outer-lying orbitals. Consequently, the 4f-electrons are not directly accessible for chemical bond formations, which are mostly driven by 5d or 6s-electrons.^[5–11] For this reason, all Ln behave chemically similar, especially at their most stable, third oxidation state. The non-participation of the 4f-shell within chemical bonds, combined with the lanthanide contraction give rise to the geochemical twin-characters of yttrium (Y) and holmium (Ho), zirconium (Zr) and hafnium (Hf), as well as niobium (Nb) and tantalum (Ta). These are highlighted in Fig. 1.1, which also compares their r_{ion} with those elements grouped as, or associated to, rare earth elements (REE). Within the scientific community, the definition of REE varies whether alongside the group of Ln, it also includes Y or even Sc.^[12–20] This work refers to REE as the group of Ln. Also not uniformly defined is the group of high field strength elements (HFSE).^[3,20–22]

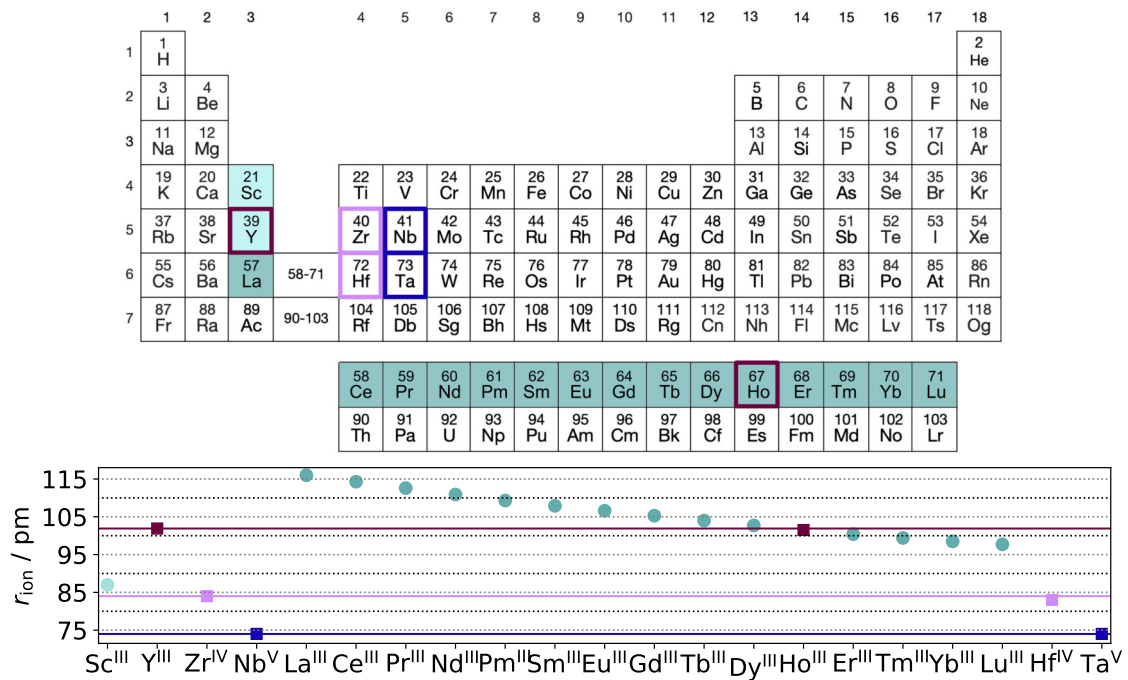


Figure 1.1 (top) periodic table of elements as adapted from [23] with highlighted lanthanides (La–Lu, dark cyan) and Sc and Y (light cyan), which are associated with them, as well as the geochemical twin pairs Y:Ho (dark purple), Zr:Hf (light purple), and Nb:Ta (blue) marked by squares; **(bottom)** ionic radii (r_{ion}) of the respective most stable cations as measured in eightfold coordination ordered according to atomic numbers.^[24]

Herein, the threshold of $Q_{ion}/r_{ion} > 2 \text{ e}\text{\AA}^{-1}$ is applied, of which follows that all elements mentioned so far belong to the group of HFSE. Within the simple concept of hard and soft Lewis acids and bases (HSAB),^[25] the HFSE are hard Lewis acids. Thus, among all available anions, the HFSE cations form the strongest complexes with fluoride, as F is the hardest of all naturally occurring Lewis bases. Within the upper continental crust, fluoride is even the second most abundant anion, after the omnipresent oxide.^[26] The mobility vs. precipitation of elements within or from aqueous (aq.) fluids form an interplay decisive for the formation of ore deposits. Such hydrothermal processes are regulated by temperature and pressure gradients, as well as the chemical composition of the fluid. Especially the availability of anions is critical for the mobility of those cations, which are only soluble as complexes. Due to their hard Lewis acidic character, this is particularly the case for the HFSE. As the Lewis acidity increases from the lighter to the heavier REE, REE deposits of economical interest with enriched concentrations of the middle and heavy REE originate from fluoride-rich hydrothermal fluids.^[15–17,27–29] Additionally, only these conditions may produce the mineral waimirite ($\beta\text{-YF}_3$) naturally, containing a REE content of up to 20% favoring the heavy REE.^[17] Even more striking, such fluoride-rich hydrothermal veins give rise to exceptionally high fractioning of the geochemical twins. Rock samples have been found with

an extremely enriched Y over Ho ratio from the chondritic value of 28:1^[30] to up to 928:1.^[15] It might be argued that this is linked to the almost doubled mass from the lighter to the heavier twin element. By the mass increase itself, the lighter twin should be considerably more reactive. However, exposed to the same geochemical conditions, the ratio of Zr:Hf decreases from 38:1^[30] to 2:1.^[3] That within the Zr:Hf pair, the heavier twin member enriches, as well as that both phenomena are linked to the availability of fluoride within hydrothermal veins, suggests that this is not linked to the mass but different affinities for fluoride when water is the medium of transport.^[3,31–33] A simplified scheme of a HFSE ore deposit formation by fluoride rich hydrothermal mechanism is shown in Fig. 1.2.^[34]

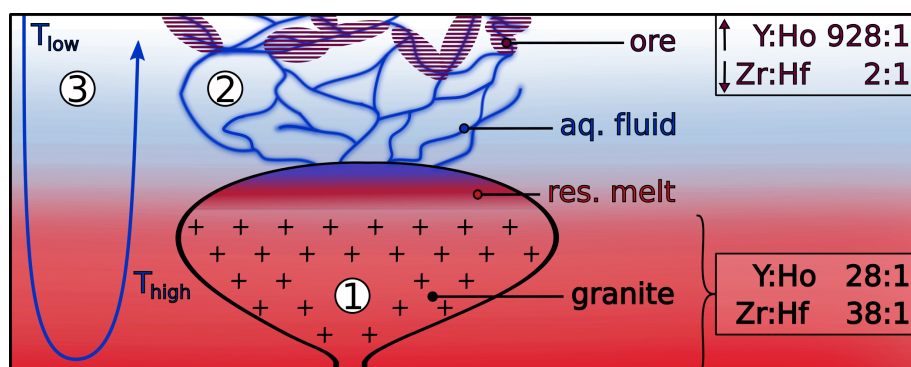
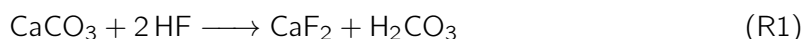


Figure 1.2 simplified scheme of a HFSE ore deposit formation as adapted from [34]; it consists of three parts: (1) the magmatic process of granite (black crosses) crystallization yielding a residual (res.) melt (red); (2) the separated aqueous (aq.) fluid (blue) giving rise to the post-magmatic, hydrothermal process; (3) the ascend of aq. fluid within the host rock. From the aq. fluids, fluoride-based hydrothermal vein ores highly enriched in HFSE precipitate (purple hatching). These show extraordinary geochemical twin ratios of 928:1^[15] (Y:Ho) or 2:1^[3] (Zr:Hf) from the chondritic ratios of 28:1^[30] (Y:Ho) or 38:1^[30] (Zr:Hf) as initially present within the melt.

The overall mechanism involves three distinct processes. First of all, there is the magmatic process (see (1) in Fig. 1.2). Initially, a granitic melt ascending from the Earth's mantle or lower crustal levels to the upper crust crystallizes to granite. Granite is mainly composed of silicates, such as feldspar (e.g., $(K, Na)AlSi_3O_8$), mica (e.g., $KAl_3Si_3O_{10}(OH)_2$), or quartz (SiO_2). Any component that is incompatible into these minerals, as e.g., water, HFSE and fluoride will accumulate within the residual (res.) melt. Once the res. melt is over-saturated with water, a phase separation occurs yielding an aq. fluid. Subsequently, this gives rise to the post-magmatic, hydrothermal processes (see (2) in Fig. 1.2). Components within the res. melt which are well water-soluble, as e.g., fluoride or HFSE fluoride complexes, fractionate into the aq. fluid.^[35] Cracks within the host rock allow the aq. fluid to escape to higher regions. By the lower temperature or by interaction with the host rock surfaces, ions precipitate from the aq. fluid forming hydrothermal vein ores. The latter plays an important role for fluoride i.e. HF, if in contact with calcium carbonate ($CaCO_3$)-based

rocks as limestone, onto which, it readily forms fluorspar (CaF_2) according to Reaction R1.



Finally, the third main process involves the surrounding aq. fluid within the host rock (see (3) in Fig. 1.2). Heated by the granite melt of process (1), the aq. fluid ascends next to the melt. Along, it carries components, which are well water-soluble at higher temperatures, as e.g., Ca(II) . These aq. fluids may mix with those of process (2) leading to further precipitation reactions forming e.g., further fluorspar in analogy to Reaction R1. Along the hydrothermal processes, HFSE are mainly transported as fluoro complexes. As the loss of solvated fluoride ions destabilizes these, they co-precipitate with fluoride forming HFSE-enriched hydrothermal vein ores.^[29] As the stability of the HFSE fluoro complexes is sensitive to more than simple ionic charge and radius, these allow the fractioning of the geochemical twins, giving rise to very enriched Y:Ho and very depleted Zr:Hf ratios.^[3,15,30] It should be stressed again, that the scheme of Fig. 1.2 is a huge simplification of the manifold and inter-dependent processes, which also include the subsequent alteration of once participated ores. This alteration also immensely affects the HFSE concentrations and thus, creates an extremely entangled, hard to trace picture of HFSE transport pathways.^[36] Consequently, it is not possible to model geochemical transports in their full complexity, neither by lab experiments nor by computation. Instead, only some of its parts can be modeled applying tremendous simplifications. So far, most such studies have focused on the anion affinities shown by the HFSE in aq. solution. These have found stronger fluoride affinities for Y than Ho,^[18,37] as well as for Hf than Zr.^[38,39] On the other hand, the solubility of REE/Y(III) fluoro complexes is very low.^[13] Consequently, a high availability of fluoride by e.g., fluorspar surfaces is required.^[28,35,36,40–42] For this reason, the complexation of chloride should also be considered. Despite the much lower affinity of HFSE for chloride,^[43] the chlorido complexes are considerably more soluble and thus more mobile than the respective fluoro complexes.^[28,42,44] Furthermore, also hydroxide ligands cannot be neglected, as it has been found that the Zr:Hf twin pair is transported as fluoro hydroxido complexes within diluted hydrofluoric acid (aq. HF).^[38,39] This leads to the first part of this thesis, devoted to the subtle differences between the geochemical twin pair of Zr:Hf. Paper **A** aims to first, investigate if the experimentally known higher affinity by Hf(IV) compared to Zr(IV) for fluoride within solution^[38,39] also shows within the cohesive energies of their respective crystals. Secondly, it compares the affinities for fluoride vs. hydroxide to finally, also investigate how these differ between the geochemical twins. Moreover, it aims to reduce the knowledge gap on fluorozirconate or fluorohafnates. Even though, these crystals are widely applied within glasses for applications in optics due to their huge adsorption free window and high thermal stability,^[45–53] their electronic structure was never before calculated by first principle methods.

Within the second, larger part of this thesis dedicated to the geochemical twin pair of Y:Ho, the focus moves from fluoride affinities within bulk to those present at the surface. Within solution, different predominant fluoride species of YF_2^+ and HoF^{2+} have been found within 0.001–0.3 molal aq. HF.^[18,37,41] According to ab initio molecular dynamics (AIMD) simulations of Y(III)^[54,55] and experimental data of Ho(III),^[37] both within chloride-bearing solutions, analogous chloride complexes are found with YCl_2^+ and $HoCl^{2+}$. If fluoride and chloride are present simultaneously, AIMD simulations have shown that only for very low fluoride concentrations, YCl_2^+ is the most prominent species.^[54] Above 0.01 molal NaF, YF_3 was predominantly formed, despite the still 100 times higher availability of chloride. Summing up, the stabilities of the solvated Y(III) and Ho(III) complexes have already been studied experimentally and computationally. Along the geochemical transport pathways, however, frequent precipitation and re-solvation occur. The mobility and enrichment of an element is, thus, not only affected by its affinity within the aq. media, but also by its interaction with the surfaces and capability of forming stable surfaces itself.

Therefore, paper **B.1–B.3** compare the fluoride affinities shown in solution to those in the solid state, based on the binary fluorides of Y(III) and Ho(III). Conveniently, these are also the easiest model crystals for fluoride affinities. Besides, these materials are worth a more detailed quantum chemical examination, as also these geochemical twin fluorides are known for their exceptional optical properties. YF_3 possesses a very low refractive index and one of the largest known absorption free windows with 12.5 eV.^[56,57] Combined with the excellent compatibility for REE, Ln-doped YF_3 is widely studied for luminescence.^[58–65] Compared to the respective REE oxides, the fluorides provide lower phonon energies and thus longer lifetimes of the excited states.^[63] In addition, the high fluoride mobility within Ln-doped YF_3 makes it a candidate for fluoride based batteries.^[66] To analyze this potential application, a comprehensive knowledge of its surface structure is required. The same applies to the fluoride-specific contact adsorptions shown by the HFSE within hydrothermal veins. However, experimentally grown thin films^[56,67–69] or nanoparticles^[61–63,66,70–73] of pure or Ln-doped YF_3 are highly dependent on the applied technique, especially the chemical nature and structure of the substrate, and/or used solvent. To pick one or a few among them all may produce an incomplete picture.

Instead, paper **B.1** predicts the intrinsic stabilities of the pristine surfaces without the influence of external effects. These are investigated for both, YF_3 and HoF_3 , independently to illuminate, whether their different electronic valence may effect the stability of unsaturated surface structures exposed to vacuum. Onto the determined most stable surfaces, paper **B.2** investigates their affinities for the adsorbates of chloride and fluoride, in reference to water. First, it aims to find the most stable adsorption sites for each surface structure. Second, for each adsorption site, it contrasts the binding affinities for a respective adsorbate between both geochemical twins of YF_3 and HoF_3 . Moreover, it compares how the adsor-

bate affinities for chloride, fluoride, and water shown by the same MF_3 vary according to the surface structure. Finally, the adsorptions onto YF_3 are analyzed further for their energetic subcontributions within paper **B.3**. Here, the reasons for the different affinities for chloride, fluoride, and water are illuminated by contrasting the different bonding natures of covalent vs. ionic character, as well as H-bond vs. direct coordination for each of the adsorption sites investigated. This allows to link these bonding natures not only to the differences between the adsorbates, but also to the found differences among the surface structures.

2. Theory

2.1. Electronic Structure Calculations

2.1.1 Schrödinger Equation

The upcoming sections introduce the essential ideas and equations behind the applied quantum chemical methods. The most fundamental subsections 2.1.1–2.1.3 are based on the textbooks "Modern Quantum Chemistry: Introduction to Advanced Electronic Structure Theory" by A. Szabo and N. Ostlund,^[74] as well as "A Chemist's Guide to Density Functional Theory" by W. Koch and M. Holthausen.^[75]

The most central quantum chemical equation is the Schrödinger equation (SE).^[76] It describes a quantum chemical system by a wave function (Φ) depending on the spatial coordinate vectors of all electrons (\mathbf{r}) and nuclei (\mathbf{R}), as well as time (t). The SE connects the outcome of applying the Hamiltonian (\hat{H}) onto this wave function with its time derivative times the imaginary unit (i) and the reduced Planck constant (\hbar).

$$\hat{H}\Phi(\mathbf{r}, \mathbf{R}, t) = i\hbar\frac{\delta}{\delta t}\Phi(\mathbf{r}, \mathbf{R}, t) \quad (2.1)$$

For multi-electron systems, Φ also depends on the electronic spin. Therefore, the electronic coordinates are extended by the magnetic spin quantum number ($m_s \in \{\frac{1}{2}, -\frac{1}{2}\}$) leading to $\Phi(\mathbf{r}, m_s, \mathbf{R}, t)$. In the following, \mathbf{r} and m_s are combined as \mathbf{x} . Generally, a non-relativistic \hat{H} is chosen, which depends solely on the spatial coordinates in absence of external fields. This allows a separation of variables yielding the stationary, or time-independent total wave function (Ψ). Thus, Eq. 2.1 reduces to the stationary, or time-independent SE, which yields the system's energy (E) as eigenvalue.

$$\hat{H}\Psi(\mathbf{x}, \mathbf{R}) = E\Psi(\mathbf{x}, \mathbf{R}) \quad (2.2)$$

In the following, SE refers to the time-independent SE of Eq. 2.2. The corresponding \hat{H} consists of operators for the kinetic energies (T) of the nuclei (N) and electrons (e), as well as operators for the potential energies (V) of their Coulomb interactions.

$$\hat{H} = \hat{T}_N + \hat{T}_e + \hat{V}_{NN} + \hat{V}_{ee} + \hat{V}_{Ne} \quad (2.3)$$

In quantum chemistry, the nuclei are generally treated as point charges with mass and the Born-Oppenheimer approximation (BOA)^[77] is applied. The BOA takes advantage of the much higher nuclear mass compared to the mass of an electron. By the subsequently, much slower motion of nuclei, the sets of electronic and nuclear coordinates are separated leading to an electronic and nuclear SE. To solve the electronic SE of Eq. 2.4, the nuclear positions are

kept constant, which corresponds to $T_N = 0$ and $V_{NN} = \text{constant}$. This leads to an electronic wave function (Ψ_e) and electronic eigenenergies (E_e), which depend parametrically on \mathbf{R} .

$$\hat{H}_e \Psi_e(\mathbf{x}; \mathbf{R}) = E_e(\mathbf{R}) \Psi_e(\mathbf{x}; \mathbf{R}) \quad (2.4)$$

By solving Eq. 2.4 for a series of different \mathbf{R} , a potential energy (hyper-)surface can be constructed, from which e.g., the equilibrium energy or transition states may be determined. The electronic Hamiltonian (\hat{H}_e) consists of sums over all i to N_e electrons and all A to N_N nuclei with nuclear charge (Z_A). In atomic units, it has the following form:

$$\hat{H}_e = \hat{T}_e + \hat{V}_{ee} + \hat{V}_{Ne}$$

$$\hat{H}_e = - \sum_i^{N_e} \frac{1}{2} \nabla_{\mathbf{r}_i}^2 + \sum_i^{N_e} \sum_{j>i}^{N_e} \frac{1}{|\mathbf{r}_i - \mathbf{r}_j|} - \sum_i^{N_e} \sum_A^{N_N} \frac{Z_A}{|\mathbf{r}_i - \mathbf{R}_A|} \quad (2.5)$$

Despite the separation of time and nuclear coordinates, Eq. 2.4 is still not analytically solvable for multi-electron systems. Consequently, further approximations are necessary. To simplify the notation of the electronic wave functions, the parametric dependency on nuclear coordinates is not explicitly stated within the following sections.

2.1.2 Hartree Fock Method

First, Ψ_e of Eq. 2.4 may be approximated by separating the total wave function depending on all electronic coordinates of $\mathbf{x}_1, \mathbf{x}_2, \dots, \mathbf{x}_{N_e}$ into i one-electron wave functions (χ_i). In the ansatz of an Hartree product (HP), the approximated total wave function is simply a product of all χ_i .

$$\Psi_e^{\text{HP}}(\mathbf{x}_1, \mathbf{x}_2, \dots, \mathbf{x}_{N_e}) = \prod_i^{N_e} \chi_i(\mathbf{x}_i) \quad (2.6)$$

The set of χ_i is chosen to be orthonormal. Following common notation, χ_i^* is the complex conjugated function of χ_i and δ_{ij} is the Kronecker delta.

$$\int_{-\infty}^{\infty} d\mathbf{x} \chi_i^*(\mathbf{x}) \chi_j(\mathbf{x}) = \delta_{ij} = \begin{cases} 1, & \text{if } i = j \\ 0, & \text{if } i \neq j \end{cases} \quad (2.7)$$

The HP ansatz would be exact for non-interacting electrons. However, it cannot reproduce the fermionic nature of electrons, which requires anti-symmetry upon exchange of two electrons.

$$\Psi_e(\mathbf{x}_1, \mathbf{x}_2, \dots, \mathbf{x}_{N_e}) = -\Psi_e(\mathbf{x}_2, \mathbf{x}_1, \dots, \mathbf{x}_{N_e}) \quad (2.8)$$

Consequently, it violates Pauli's exclusion principle, according to which two electrons bound within the same system, cannot occupy the same spin orbital.^[78] An ansatz, that reproduces the correct fermionic nature of Eq. 2.8 is a Slater determinant, in which different spin orbitals are written in each row and different electronic coordinates are written in each column.^[79]

$$\Psi_e^{\text{SD}}(\mathbf{x}_1, \mathbf{x}_2, \dots, \mathbf{x}_{N_e}) = \frac{1}{\sqrt{N_e!}} \begin{vmatrix} \chi_1(\mathbf{x}_1) & \chi_1(\mathbf{x}_2) & \dots & \chi_1(\mathbf{x}_{N_e}) \\ \chi_2(\mathbf{x}_1) & \chi_2(\mathbf{x}_2) & \dots & \chi_2(\mathbf{x}_{N_e}) \\ \vdots & \vdots & \ddots & \vdots \\ \chi_{N_e}(\mathbf{x}_1) & \chi_{N_e}(\mathbf{x}_2) & \dots & \chi_{N_e}(\mathbf{x}_{N_e}) \end{vmatrix} \quad (2.9)$$

In Dirac bra-ket notation, Eq. 2.9 may be abbreviated as a ket vector just listing the spin orbitals.

$$\Psi_e^{\text{SD}}(\Psi_e) = |\chi_1 \chi_2 \dots \chi_{N_e}\rangle = |\Psi_e^{\text{SD}}\rangle \quad (2.10)$$

Within the Hartree-Fock (HF) method, the χ_i building the total Ψ_e^{SD} are obtained by the variational principle. It says, that for any normalizable, complex, trial wave function, the respective electronic energy is higher or equal than the exact electronic ground state energy (E_0) belonging to the exact ground state wave function (Ψ_0). By this upper bound to the exact energy, Ψ_e^{SD} is constructed to minimize E .

$$\frac{\langle \Psi_e^{\text{SD}} | \hat{H}_e | \Psi_e^{\text{SD}} \rangle}{\langle \Psi_e^{\text{SD}} | \Psi_e^{\text{SD}} \rangle} = E \geq E_0 = \frac{\langle \Psi_0 | \hat{H}_e | \Psi_0 \rangle}{\langle \Psi_0 | \Psi_0 \rangle} \quad (2.11)$$

\hat{H}_e is rewritten within the HF method from Eq. 2.5 into sums of one (\hat{h}_i) and two-electron (\hat{g}_{ij}) operators.

$$\hat{H}_e = \sum_i^{N_e} \hat{h}_i + \sum_i^{N_e} \sum_{j>i}^{N_e} \hat{g}_{ij} \quad (2.12)$$

The expectation value of $\langle \hat{g}_{ij} \rangle$ may be split into a Coulomb (J_{ij}) and an exchange integral (K_{ij}). While the former corresponds to classical Coulomb repulsion, the latter has no classical interpretation. Rather, K_{ij} is a result of the permutation within the SD. It only contributes for electrons of the same spin.

$$\langle \chi_i \chi_j | \hat{g}_{ij} | \chi_i \chi_j \rangle - \langle \chi_i \chi_j | \hat{g}_{ij} | \chi_j \chi_i \rangle = J_{ij} - K_{ij} \quad (2.13)$$

Within this approximation, \hat{H}_e is simplified. Instead of using the explicit two-electron operators onto N_e electrons, N_e effective one-electron Fock operators (\hat{f}_i) are applied. The explicit electron-electron interaction is replaced by the interaction of a single electron with the averaged, effective potential of the other $N_e - 1$ electrons. Applying \hat{f}_i onto the one-electron spin orbital gives the famous HF equation. The obtained eigenvalue equals the orbital energy (ϵ_k).^[80,81]

$$\hat{f}_i \chi_k = \left(\hat{h}_i + \sum_j^{N_e} (2\hat{J}_{ij} - \hat{K}_{ij}) \right) \chi_k = \epsilon_k \chi_k \quad (2.14)$$

The total electronic HF energy (E_{HF}) of the N_e electron system is not the mere sum of all ϵ_k , but also accounts for the therein double counted electron-electron interactions.

$$E_{\text{HF}} = \sum_i^{N_e} \epsilon_i - \frac{1}{2} \sum_i^{N_e} \sum_j^{N_e} (J_{ij} - K_{ij}) \quad (2.15)$$

The χ_i may be split into a spatial orbital (ψ_i) and a spin function (σ). Again, the set of spatial orbitals is orthonormal, as are the spin functions.

$$\chi_i(\mathbf{x}_i) = \psi_i(\mathbf{r}_i) \sigma(m_s) \quad (2.16)$$

By a further approximation, ψ_i themselves are not used to solve Eq. 2.14. Instead, these are expanded in a finite set of N_ϕ basis functions (ϕ_ν) with N_ϕ coefficients ($c_{\nu i}$).

$$\psi_i(\mathbf{r}) = \sum_\nu^{N_\phi} c_{\nu i} \phi_\nu(\mathbf{r}) \quad (2.17)$$

The ψ_i may also be referred to as molecular orbitals (MO) and the ϕ_ν as atomic orbitals (AO), which are atom-centered hydrogen-like orbitals. This makes Eq. 2.17 the central equation of the molecular orbitals – linear combination of atomic orbitals (MO-LCAO) ansatz. For

multi-atomic systems, the AOs are not orthogonal leading to non-vanishing overlap matrix elements (S_{vw}).

$$S_{vw} = \langle \phi_v | \phi_w \rangle \quad (2.18)$$

The respective Fock matrix elements (F_{vw}) are obtained from applying \hat{f}_i onto the AOs.

$$F_{vw} = \langle \phi_v | \hat{f}_i | \phi_w \rangle \quad (2.19)$$

All F_{vw} are combined within the Fock matrix (\mathbf{F}). Equally is the atomic orbital coefficient matrix (\mathbf{C}) formed from all c_{vi} . Multiplying these, yields all ϵ times the overlap matrix (\mathbf{S}) of the AOs. This is the famous matrix representation of the Roothaan-Hall equations.^[82,83]

$$\mathbf{FC} = \epsilon \mathbf{SC} \quad (2.20)$$

To solve Eq. 2.20, a self-consistent field (SCF) method is necessary, which involves a set of guessed initial orbitals i.e. c_{vi} , which are iteratively optimized to yield minimal ϵ via Eq. 2.11. HF theory uses a single SD (configuration) of all occupied spin orbitals to describe the ground state of a system. However, some (nearly) degenerate ground states require a multi-configurational description. Moreover, the interactions of the ground state with higher excited states also contribute to the exact ground state energy (E_{exact}). The energy, which HF neglects is defined as the correlation energy (E_C).

$$E_C = E_{\text{exact}} - E_{\text{HF}} \quad (2.21)$$

The so-called post-HF or higher wave function methods address these problems at the price of higher computational demands. These demands quickly explode, which makes the description of a large number of electrons expanded within a sufficiently large basis set unfeasible.

2.1.3 Density Functional Theory

While the post-HF methods treat electron correlation explicitly, some of the correlation energy is also captured implicitly within density functional theory (DFT). In contrast to the high computational demand of the post-HF methods, DFT comes as cheap as HF, which makes it applicable to large systems. In the following, the fundamentals of the DFT method are addressed.

The electronic wave function of a system depends on four electronic coordinates for each of the N_e electrons (see Eq. 2.10). Instead of the massively multi-dimensional Ψ_e , DFT is based on the one-electron density (ρ), which only depends on the three spatial coordinates.

$$\rho(\mathbf{r}_1) = N_e \int d\sigma \int d\mathbf{x}_2 \cdots \int d\mathbf{x}_{N_e} \Psi_e^*(\mathbf{x}_1, \mathbf{x}_2, \dots, \mathbf{x}_{N_e}) \Psi_e(\mathbf{x}_1, \mathbf{x}_2, \dots, \mathbf{x}_{N_e}) \quad (2.22)$$

According to the first Hohenberg-Kohn theorem, the one-electron density of the ground state (ρ_0) uniquely defines an external potential (V_{ext}) (plus an arbitrary constant), which uniquely defines the total electronic Hamiltonian (\hat{H}_e), which in turn defines the ground state energy (E_0) of that system.^[84] As ρ itself is a function of the electronic coordinates, the energy is a functional of ρ .

$$\rho_0(\mathbf{r}) \rightarrow V_{\text{ext}}[\rho_0] + \text{const.} \rightarrow \hat{H}_e \rightarrow E_0[\rho_0] \quad (2.23)$$

The second Hohenberg-Kohn theorem says, that the variational principle (see Eq. 2.11) holds. Consequently, no trial electron density may result in an energy below the exact ground state energy (E_0).^[84]

$$E[\rho] \geq E_0[\rho_0] \quad (2.24)$$

To determine E , also the constant V_{NN} and thus, the nuclear positions are required, which are obtained from the cusps of the electron density at the nuclei.

$$E[\rho] = T_{\text{ee}}[\rho] + V_{\text{ee}}[\rho] + V_{\text{ext}}[\rho] + V_{\text{NN}} \quad (2.25)$$

Compared to the total energy Hamiltonian of Eq. 2.3, one finds that V_{Ne} is included within $V_{\text{ext}}[\rho]$. To differentiate the kinetic energy as a functional of the electron density of interacting electrons (T_{ee}) from the kinetic energy as a function of the spatial electron coordinates of non-interacting electrons within HF theory (T_e) of Eq. 2.5, different subscripts are chosen. The description of the former in terms of ρ is problematic. In fact, the exact functionals needed to solve Eq. 2.25 are not known. Instead, applied DFT is based on a fictitious system of non-interacting electrons exposed to an effective local potential (V_{eff}) introduced by Kohn and Sham (KF).^[85] Its electron density (ρ_S), which is the sum over all KS orbital (ψ^{KS}) densities is chosen to reproduce the ground state electron density of the interacting system.

$$\rho_S = \sum_i^{N_e} |\psi_i^{\text{KS}}|^2 = \rho \quad (2.26)$$

The kinetic energy operator acting on this ρ_S (\hat{T}_S) within KS-DFT corresponds to the kinetic energy operator \hat{T}_e in HF-theory (see Eq. 2.5). From \hat{T}_S and \hat{V}_{eff} , the KS one-electron Fock operator (\hat{f}^{KS}) is constructed. Applied onto the KS orbital, this yields the KS orbital energy (ϵ^{KS}). These are the well-known KS equations.

$$\left(-\frac{1}{2} \nabla_{\mathbf{r}_i}^2 + \hat{V}_{\text{eff}}(\mathbf{r}_i) \right) \psi_i^{\text{KS}}(\mathbf{r}_i) = \hat{f}^{\text{KS}} \psi_i^{\text{KS}}(\mathbf{r}_i) = \epsilon_i^{\text{KS}} \psi_i^{\text{KS}}(\mathbf{r}_i) \quad (2.27)$$

V_{ee} of Eq. 2.25 is split into a Coulomb and exchange integral in analogy to Eq. 2.13. The former can be written as a functional of the electron density.

$$J[\rho] = \int d\mathbf{r}_1 \int d\mathbf{r}_2 \frac{\rho(\mathbf{r}_1)\rho(\mathbf{r}_2)}{r_{12}} \quad (2.28)$$

This is not the case for K . Instead, it is implicitly treated within the exchange-correlation energy (E_{XC}), which also holds the difference between the exact and non-interacting kinetic energy.

$$E_{\text{XC}}[\rho] = T_{ee}[\rho] - T_S[\rho] + V_{ee}[\rho] - J[\rho] \quad (2.29)$$

The overall, KS ground state energy is then:

$$E[\rho] = T_S[\rho] + J[\rho] + V_{\text{ext}}[\rho] + E_{\text{XC}}[\rho] \quad (2.30)$$

While J_{ij} and K_{ij} cancel each other for $i = j$ in Eq. 2.13, this is not the case in Eq. 2.29 i.e. Eq. 2.30. This gives rise to the unphysical self-interaction error of an electron with itself. Moreover, despite the simple form of Eq. 2.29, it is not straightforward to construct these differences. This led to the creation of dozens of different density functional approximations (DFAs). These DFAs are ranked according to "Jacob's ladder" ^[86,87]. The simplest DFA, are methods based on the local density approximation (LDA) built on the homogeneous electron gas. These are solely functionals (f_{DFA}) of the electron density.

$$E_{\text{XC}}^{\text{LDA}}[\rho] = \int d\mathbf{r} f_{\text{DFA}}[\rho] \quad (2.31)$$

The next rank of DFAs consists of generalized gradient approximations (GGAs). These are also functionals of the gradient of the electron density.

$$E_{\text{XC}}^{\text{GGA}}[\rho] = \int d\mathbf{r} f_{\text{DFA}}[\rho, \nabla\rho] \quad (2.32)$$

The GGA by Perdew, Becke and Ernzerhof (PBE)^[88] is the most used DFA within the solid

state community, especially since the Materials Project.^[89] However, it also performs well for molecules,^[90] which is why PBE has also been applied within papers **A** and **B.1–B.3**. The third rank of DFAs are meta-GGAs, which are also functionals of the Laplacian of the electron density. However, more often the fourth rank DFAs are applied when higher accuracy than ordinary GGAs is desired. These DFAs are hybrid DFT methods, which replace a certain amount of exchange energy within their E_{XC} by a HF-derived one (E_X^{exact}). In contrast to the actual exchange integral in HF, E_X^{exact} is calculated from ψ^{KS} . The nature of the DFT method may be a LDA or GGA. By the addition of E_X^{exact} , the self-interaction error is partially compensated. A commonly used hybrid functional is the PBE-based PBE0.^[91]

$$E_{XC}^{\text{PBE0}} = \frac{3}{4}E_X^{\text{PBE}} + \frac{1}{4}E_X^{\text{exact}} + E_C^{\text{PBE}} \quad (2.33)$$

Finally, there exists a range separated version of PBE0, which is called HSE according to its developers Heyd, Scuseria, and Ernzerhof.^[92,93] In contrast to PBE0, it only uses E_X^{exact} within a short range (SR).

$$E_{XC}^{\text{HSE}} = \frac{3}{4}E_X^{\text{PBE,SR}}(\eta) + \frac{1}{4}E_X^{\text{exact,SR}}(\eta) + E_X^{\text{PBE,LR}}(\eta) + E_C^{\text{PBE}} \quad (2.34)$$

The SR is defined by the complementary error function of the screening parameter (η) and the radial distance to the nucleus (r). The long range (LR) is accordingly described by the error function.

$$\frac{1}{r} = \frac{\text{erfc}(\eta r)}{r} + \frac{\text{erf}(\eta r)}{r} \quad (2.35)$$

For the limit of $\eta = 0$, HSE is identical to PBE0, while for $\eta \rightarrow \infty$, it becomes equal to PBE. The recommended version of HSE06 uses $\eta = 0.11 a_0^{-1}$ with a_0 being the Bohr radius.^[93] The most computationally demanding term within hybrid DFT methods is E_X^{exact} , due to the 4-center-2-electron integrals. Given that this term is especially computational demanding within plane wave setup, HSE06 is considerably faster than PBE0 within periodic calculations.^[93] This work applied HSE06 for band gap references to validate the computational setup for HoF₃ in paper **B.1**.

In the previous equations, DFT was introduced without regard to the spin function, as the electron density itself and the energy of the system are independent of the spin. However, to describe unpaired electrons, the spin function needs to be considered. Within spin unrestricted DFT, the ψ^{KS} occupied with electrons of α -spin are separately SCF-optimized than those of β -spin (see Eq. 2.7 and 2.16). Summing over the ψ^{KS} densities for each spin separately yields the two spin-separated electron densities (ρ_σ) with $\sigma = \{\alpha, \beta\}$. Their difference is the spin density ($\rho_{\Delta\sigma}$).

$$\rho_{\Delta\sigma} = \rho_\alpha - \rho_\beta \quad \text{with} \quad \rho_\sigma = \sum_i^{N_{e,\sigma}} |\psi_i^{\text{KS}}(\mathbf{r}_i) \sigma(m_s)|^2 \quad (2.36)$$

2.1.4 Dispersion Correction

Van der Waals interactions are non-covalent interactions between two induced or permanent dipoles or higher multipoles. If both multipoles are induced, this long-range electron correlation is referred to as London dispersion. While for strong covalently bound molecules or strong ionically bound crystals, these effects are often negligible in magnitude, their importance grows with the number of atoms considered. Also, weakly adsorbed molecules onto a surface often demand the treatment of dispersion interactions. Ordinary DFT functionals fail to describe dispersion as they treat electron correlation by an approximate manner. However, the energy associated to dispersion may be retrieved easily by empirically-derived dispersion corrections as those developed by Grimme.^[94–96] This work has used the third version of Grimme’s dispersion correction (D3) with Becke-Johnson damping (BJ)^[97] as implemented within VASP^[98] (**B.2**) or within AMS-BAND (**B.3**). Within the D3-scheme, the dispersion energy (E^{D3}) is added as a correction to the KS-derived DFT energy. E^{D3} is no functional of ρ , but depending on the interatomic distances (R_{AB}).

$$E^{\text{DFT-D3}}[\rho] = E^{\text{DFT}}[\rho] + E^{\text{D3}}(R_{AB}) \quad (2.37)$$

For each atom pair A and B , it is calculated from the dispersion coefficients of sixth (C_6^{AB}) and eighth (C_8^{AB}) order, their corresponding scaling factors (s_6, s_8), and a damping function (f_D) depending on R_{AB} .

$$E^{\text{D3}}(R_{AB}) = -\frac{1}{2} \sum_{A \neq B}^{N_N} \left(\frac{s_6 C_6^{AB}}{(R_{AB})^6} + \frac{s_8 C_8^{AB}}{(R_{AB})^8} \right) f_D(R_{AB}) \quad (2.38)$$

The C_6^{AB} parameters are obtained from the averaged dipole polarizabilities ($\bar{\alpha}$) at imaginary frequency ω .

$$C_6^{AB} = \frac{3}{\pi} \int_0^\infty d\omega \bar{\alpha}_A(i\omega) \bar{\alpha}_B(i\omega) \quad (2.39)$$

These have been calculated by time-dependent DFT of the respective hydrides at different coordination numbers (CN) yielding several, CN-dependent $\bar{\alpha}_A$ for each atom A . The C_8^{AB} are derived from the C_6^{AB} . Within D3(BJ), the damping function is set to a constant (f_{BJ}) and $s_6 = 1$, while s_8 is fitted to the repulsive nature of E_{XC} at the short to medium range.

$$E^{\text{D3(BJ)}}(R_{AB}) = -\frac{1}{2} \sum_{A \neq B}^{N_N} \left(\frac{C_6^{AB}}{(R_{AB})^6 + (f_{\text{BJ}})^6} + \frac{s_8 C_8^{AB}}{(R_{AB})^8 + (f_{\text{BJ}})^8} \right) \quad (2.40)$$

$$f_{\text{BJ}} = \gamma_1 \sqrt{\frac{C_8^{AB}}{C_6^{AB}}} + \gamma_2 \quad (2.41)$$

Υ_1 and Υ_2 are global parameters fitted for each DFA. These are the reason, the energies attributed to dispersion given in paper **B.3** as ΔE_{disp} are functional-dependent.

2.1.5 Hubbard-Type Correction

This section is largely based on the chapter "The DFT+U: Approaches, Accuracy, and Applications" by Tolba et al. written for "Density Functional Calculations - Recent Progresses of Theory and Application,"^[99] to which the interested reader may be forwarded.

Ordinary DFT often fails to describe the correct electronic structures of crystals with strongly correlating electrons as e.g., from partially filled 3d or 4f-shells. While experimentally, an insulating behavior is measured, DFT predicts the materials to be conducting (see subsection 2.2.1). Such a falsely predicted conductive behavior of strongly correlated anti-ferromagnetic crystals has been described by Mott. Accordingly, these materials are called Mott insulators.^[100] One example is HoF_3 . Each Ho(III) contributes with a partially filled 4f-shell to the electronic structure. Calculating the electronic structure on a GGA level incorrectly produces a single 4f-band at the Fermi level, which results in a conducting character. However, experiments on related compounds suggest that HoF_3 is strongly insulating.^[101] When applying hybrid DFT, the 4f-shell is split in occupied and unoccupied bands with an insulating band gap (see paper **B.1**). To avoid the costly exact exchange, the results of the hybrid DFT calculations may also be approximated by applying a semiempirical on-site Coulomb interaction potential (U). This ansatz is called DFT+U and generally referred to as Hubbard-type correction, as it is derived from the Hamiltonian of the Hubbard model (\hat{H}_{Hub}) describing electron hopping at nearest neighboring atomic sites. It consists of two terms. The first term, describing the hopping, relates to a kinetic energy, while the second term describes the on-site Coulomb interaction energy.^[102]

$$\hat{H}_{\text{Hub}} = -A_{\text{Hub}} \sum_{\langle i,j \rangle, \sigma} (\hat{c}_{i,\sigma}^\dagger \hat{c}_{j,\sigma} + \hat{c}_{j,\sigma}^\dagger \hat{c}_{i,\sigma}) + U \sum_i \hat{n}_{i,\alpha} \hat{n}_{i,\beta} \quad (2.42)$$

The electrons i and j are located on two neighboring atomic sites. The amplitude of electron hopping (A_{Hub}) is proportional to the bandwidth of the valence band. The hopping is described by electron creation (\hat{c}^\dagger) and annihilation (\hat{c}) operators, as well as the number operator for electrons (\hat{n}) counting the number of α or β -electrons at the same atomic site.

$$\hat{n}_{i,\sigma} = \hat{c}_{i,\sigma}^\dagger \hat{c}_{i,\sigma} \quad (2.43)$$

Different approaches exist for the incorporation of the on-site Coulomb interaction into the overall DFT+U energy ($E^{\text{DFT+U}}$). Within paper **B.1** and **B.2**, the simple and rotationally invariant approach by Dudarev et al. was applied for HoF_3 .^[103] Their formalism is built on

the orbital-dependent method by Anisimov et al.^[104] and the rotationally invariant method by Liechtenstein et al.^[105]

The two rotationally invariant methods use the spherical averages of U (\bar{U}) and the screened Coulomb interaction (\bar{J}). Within the Dudarev approach, however, only the difference of both is considered as U_{eff} .

$$U_{\text{eff}} = \bar{U} - \bar{J} \quad (2.44)$$

The overall $E^{\text{DFT}+U}$ is then simply obtained by an additive correction term to the unrestricted DFT-derived energy as a functional of the two spin-separated electron densities (see Eq. 2.36).

$$E^{\text{DFT}+U}[\rho_{\alpha}, \rho_{\beta}] = E^{\text{DFT}}[\rho_{\alpha}, \rho_{\beta}] + \frac{U_{\text{eff}}}{2} \sum_{i,j,\sigma} P_{ij,\sigma} P_{ji,\sigma} \quad (2.45)$$

The last term sums over the density matrix elements ($P_{ij,\sigma}$) of the electrons which are affected by U_{eff} . It corrects for the double counted Coulomb repulsion given by simple additive scheme. The band splitting can be increased linearly by U_{eff} , at least up to an upper limit when the electronic structure breaks down. Therefore, any DFT+U calculations requires a reference to set an optimal U_{eff} value. Band gaps obtained by experiment or higher-level calculations may pose such references. Within paper **B.1**, we validated the DFT+U calculations against experimental crystal structure data and computed HSE06 band gaps.

2.1.6 Basis Sets and Core Potentials

This section is based on the textbooks "Introduction to Computational Chemistry" by F. Jensen^[106] and "Quantentheorie der Moleküle: Eine Einführung" by J. Reinhold.^[107] For more detailed insights, the interested reader may be referred to these textbooks.

In Eq. 2.17 within subsection 2.1.2, the concept of basis sets has been introduced with the MO-LCAO ansatz, which uses atom-centered hydrogen-like AO. Slater-type orbitals (STOs) are such a kind of basis set. The STOs are very similar to the actual solution of the hydrogen atom. Both use the same spherical harmonic functions (Y_{lm_l}) depending on the angular spherical electronic coordinates of polar (θ) and azimuth (ν) angle. The STOs are labeled according to the principal (n), angular (l), and magnetic (m_l) quantum numbers of the hydrogen-like solutions.

$$\phi_{\zeta n l m_l}^{\text{STO}}(r, \theta, \nu) = \Omega r^{(n-1)} \exp(-\zeta r) Y_{lm_l}(\theta, \nu) \quad (2.46)$$

Here, Ω is the normalization constant and ζ the exponent. In contrast to the actual hydrogen AOs, STOs possess a simplified, node-free radial part. Consequently, linear combinations of STOs are required to describe radial nodes. The electronic structures within paper **B.3** were calculated by STOs with additional numerical atomic orbitals (NAOs) as implemented in AMS-BAND.^[108] These are the numerical solutions of the KS equations (Eq. 2.27) for the isolated atoms.^[109]

Atom-centered basis sets are ranked according to the number of STOs employed per occupied AO. Within this work, the AMS-BAND-inherent TZ2P basis set was employed. This is a so-called triple- ζ (TZ) split-valence basis set, in which each valence AO is expanded by three STOs. Each core AO is expanded in two STOs. Moreover, it is doubly polarized (2P), meaning that additional STOs of higher l are included as polarization functions. It is element-dependent, which polarization functions are included. For fluorine or oxygen, for example, the applied TZ2P basis set adds one further STO of the next higher $l = d$, as well as one of the second next higher $l = f$. On the other hand, only one further STO of the next higher $l = f$ is added for the metal yttrium.^[108]

Instead of expanding all occupied AO in STOs, a certain number of the lowest-lying AOs is commonly replaced by applying the frozen core approximation. The coefficients of the frozen core orbitals (FCOs) are not updated during the SCF procedure, in which however, the STOs are orthogonalized against the FCOs. The FCOs originate from ZORA relativistic (see section 2.3) all-electron calculations on the isolated atoms applying the same basis set.^[108,109] Most reliable results are obtained, if the valence orbitals are also treated on the ZORA relativistic level.

Like the actual hydrogen-like AOs, the STOs decay exponentially with r . Consequently, a large volume needs to be considered giving rise to many possible overlaps with STOs centered

at atoms far away. Moreover, integrating over this volume is only possible by numerical methods. Due to these drawbacks, most quantum chemical codes use Gaussian-type orbitals (GTOs).

$$\phi_{\tau nlm_l}^{\text{GTO}}(r, \theta, \nu) = \Omega r^{(2n-2-l)} \exp(-\tau r^2) Y_{lm_l}(\theta, \nu) \quad (2.47)$$

The GTOs decay exponentially by r^2 . This Gaussian form allows an analytical integration, saving much computational time, especially since the product of two Gaussians is again a Gaussian. Consequently, also the overlap of two GTOs centered at any atom are easily solvable. On the other hand, a GTO cannot reproduce the nuclear cusp. Moreover, the decay badly resembles the shape of the hydrogen-like AO. Thus, instead of a single Gaussian, a linear combination of several Gaussians is used to form a single contracted GTO (cGTO). Analogous to the STOs, several of these cGTO are used to expand a single occupied AO. The GTO-based basis sets are ranked accordingly to the STO-based ones. Within in this thesis, GTOs were only used for molecular test calculation within the ORCA programme^[110] for paper **A**. These applied the def2-TZVP basis set developed by the group of Ahlrichs,^[111] also referred to as "Karlsruhe" basis set. This is again a triple- ζ (TZ) split-valence (V) basis set, in which each valence AO is expanded in three cGTOs. Within the second generation of "default" (within the Turbomole programme)^[112] basis set family (def2), the core AOs are expanded in two to three cGTOs depending on the element and basis set level. The number of additional cGTO of higher (l) as polarization functions (P) also varies. For fluorine or oxygen, for example, the applied def2-TZVP basis set adds two further cGTOs of the next higher $l = d$, as well as one of the second next higher $l = f$. On the other hand, only one further cGTO of the same $l = d$ and one of the next higher $l = f$ are added for the metals of zirconium or hafnium.

Some of our molecular calculations applied the effective core potentials (ECPs) designed for the def2 basis sets.^[113] The ECP were fitted to the valence energies of atoms at multiple states as determined by relativistic all-electron calculations. The benefits of ECPs are not only the reduced number of needed cGTOs, just as for the FCOs, they also account for the relativistic contraction of the AOs, even if the valence orbitals are treated non-relativistically.

Finally, there are non-atom-centered basis functions as plane waves. These are related to the eigenenergy of the SE for the unconstrained electron in vacuum with a rest mass (m_e).

$$E = \frac{\hbar^2}{2m_e} \mathbf{k}^2 \quad \text{with} \quad \mathbf{k} = \mathbf{p} \hbar^{-1} \quad (2.48)$$

The wave vector (\mathbf{k}) directly connects to the momentum vector (\mathbf{p}) of the electron via the De Broglie relation.^[114] This gives \mathbf{k} the unit of reciprocal space. To demonstrate this, Eq. 2.48 is not given in atomic units. Consequently, plane waves are not depending on the quantum numbers of the hydrogen atom solutions. Instead, a plane wave solely depends

on \mathbf{k} and the spatial coordinates of the electron. Within a periodic system, each unit cell (UC) is symmetrically and thus chemically equivalent. According to Bloch's theorem, the translation by the UC translation vector (\mathbf{t}) of the real-space coordinates \mathbf{r} is equal to the multiplication by the phase factor of \mathbf{k} and \mathbf{t} . From this follows that within a crystalline UC, \mathbf{k} is quantized by \mathbf{t} and thus, the reciprocal lattice vector (\mathbf{G}) (see subsection 2.2.1). Accordingly, the crystalline UC orbital ($\psi_{j,\mathbf{k}}$) for the electron band j consists of a plane wave and a unit cell part. The latter is called the Bloch orbital ($\phi_{j,\mathbf{k}}$).

$$\psi_{j,\mathbf{k}}(\mathbf{r}) = e^{i\mathbf{k}\mathbf{r}} \phi_{j,\mathbf{k}}(\mathbf{r}) \quad (2.49)$$

As a single plane wave cannot reproduce an AO, nor MO shape, a linear combination of several plane waves scaled by their respective coefficients ($c_{\mathbf{k}j}$) is necessary to expand the Bloch orbital in plane waves of all \mathbf{k} within $\mathbf{k} < \mathbf{k}_{\max}$. analogous to Eq. 2.17.

$$\phi_{j,\mathbf{k}}(\mathbf{r}) = \sum_{\mathbf{k}}^{k_{\max}} c_{\mathbf{k}j} e^{i\mathbf{k}\mathbf{r}} \quad (2.50)$$

Applying Eq. 2.48, \mathbf{k}_{\max} can be converted to an energy. It is the cutoff energy (E_{cut}) of the plane waves included within the basis set. This is the only parameter, which determines the basis set size.

$$E_{\text{cut}} = \frac{\hbar^2}{2m_e} \mathbf{k}_{\max}^2 \quad (2.51)$$

Again Eq. 2.51 is not given in atomic units. A large E_{cut} or in other words a large number of plane waves are needed to reproduce a single orbital with a complex node structure near the nucleus. On the other hand, these nodes close to the nuclei are not required to describe the bond situation between atoms. Consequently, much or even most computational time is spent on information not necessary for most chemical questions. This situation is solved by introducing a pseudopotential, in analogy to the FCOs or ECPs for the atom-centered basis sets. However, as plane waves are not originating at the nucleus, but are delocalized, the implementation of pseudopotentials is more involved. Great success was achieved with the projector augmented wave (PAW) method developed by Blöchl less than thirty years ago.^[115] This development and its implementation within the VASP code,^[98] allowed the triumph of plane waves as the most efficient and most applied solid state basis set for periodic DFT calculations.^[89,116,117] The same method was also used within paper **A**, **B.1**, and **B.2**.

Formally, the PAW method is an all-electron method as it retains all core electrons.^[115] The nodeless pseudopotential is created for and within each electronic structure calculation for the all-electron PAW function $|\Psi\rangle$ containing the full nodal structure.^[118] The all-electron wave function created by linear combination of plane waves is called pseudo wave function $|\tilde{\Psi}\rangle$. It is a continuous wave function not reproducing the correct nodal structure. The desired $|\Psi\rangle$ is constructed from $|\tilde{\Psi}\rangle$ and the respective wave functions projected onto all

single center or nuclei of $|\Psi^1\rangle$ and $|\tilde{\Psi}^1\rangle$.^[119,120]

$$|\Psi\rangle = |\tilde{\Psi}\rangle + |\Psi^1\rangle - |\tilde{\Psi}^1\rangle \quad (2.52)$$

An augmentation sphere is defined around each nucleus, which is chosen large enough to contain all nodal features. Therefore, outside each augmentation sphere, the plane waves describe the exact wave function well. Consequently, $|\Psi\rangle$ is taken to be identical to $|\tilde{\Psi}\rangle$ within these inter-atomic regions. Inside each augmentation sphere, $|\tilde{\Psi}\rangle$ is projected onto a radial function with a spherical harmonics centered at the respective nucleus. This centers the delocalized $|\tilde{\Psi}\rangle$ to a single site and reproduces the correct nodal structure. The projected function is $|\Psi^1\rangle$. To avoid double counting, the contribution of $|\tilde{\Psi}\rangle$ inside the augmentation spheres $|\tilde{\Psi}^1\rangle$ is subtracted. As the projections are performed for each nucleus (A), $|\Psi^1\rangle$ and $|\tilde{\Psi}^1\rangle$ are linear combinations over all partial waves inside the augmentation spheres of $|\psi_A\rangle$ and $|\tilde{\psi}_A\rangle$ with the respective projector function ($\tilde{\rho}_A$).

$$|\Psi^1\rangle - |\tilde{\Psi}^1\rangle = \sum_A^{N_N} (|\psi_A\rangle \langle \tilde{\rho}_A | \tilde{\Psi} \rangle) - \sum_A^{N_N} (|\tilde{\psi}_A\rangle \langle \tilde{\rho}_A | \tilde{\Psi} \rangle) \quad (2.53)$$

2.2. Periodic Systems

2.2.1 Atomic and Electronic Structure of Ideal Crystals

This section is based on the textbooks by C. Kittel translated to German "Einführung in die Festkörperphysik"^[121] and "Quantentheorie der Festkörper"^[122] to which, or to the English originals "Introduction to Solid State Physics" and "Quantum Theory of Solids," the interested reader may be forwarded.

Crystals are solids, in which the atoms are arranged in a periodic lattice. The smallest unit of periodicity is called unit cell (UC). The subset of symmetry-nonequivalent atoms within the UC form the basis. Within the crystal, any real space vector (\mathbf{R}_A) pointing to e.g., an atomic position may be described by a linear combination of the three scaled (x_A, y_A, z_A) lattice vectors (\mathbf{a}).

$$\mathbf{R}_A = x_A \mathbf{a}_1 + y_A \mathbf{a}_2 + z_A \mathbf{a}_3 \quad (2.54)$$

The lattice vectors span the UC (see Fig. 2.1). Thus, for any \mathbf{R}_A within the UC, it holds that $0 \leq x_a, y_a, z_a \leq 1$. Analogously, with the constraint that $x_t, y_t, z_t \in \mathbb{Z}$, the UC translation vector (\mathbf{t}) may be defined, which was already introduced for Bloch's theorem in Eq. 2.49 in section 2.1.6.

$$\mathbf{t} = x_t \mathbf{a}_1 + y_t \mathbf{a}_2 + z_t \mathbf{a}_3 \quad (2.55)$$

Depending on the lattice symmetry given by the number of unequal lattice vector lengths ($|\mathbf{a}|$) and the angles between them (α, β, γ), the lattices may be differentiated in seven crystal classes.

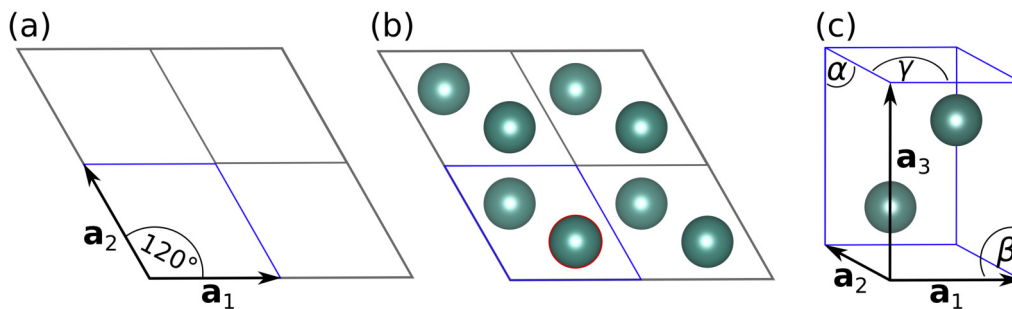


Figure 2.1 (a) 2D view along \mathbf{a}_3 onto the lattice (gray) of hexagonal closed-packed holmium with lattice vectors \mathbf{a}_1 and \mathbf{a}_2 marking the unit cell (blue); (b) with added basis (red) of a single Ho atom and its respective symmetry copies; (c) 3D view of the unit cell.

Among these, the cubic crystal has the highest symmetry with $|\mathbf{a}_1| = |\mathbf{a}_2| = |\mathbf{a}_3|$ and $\alpha = \beta = \gamma = 90^\circ$. Within this thesis, three crystal classes have been calculated. First, the orthorhombic crystals, these differ from the cubic ones by having three different lattice vector lengths. Second, hexagonal crystals, these possess two equal lengths $|\mathbf{a}_1| = |\mathbf{a}_2| \neq |\mathbf{a}_3|$ and two orthogonal angles $\alpha = \beta = 90^\circ$, together with $\gamma = 120^\circ$. Such a lattice is shown

in Fig. 2.1 for the hexagonal closed-packed (hcp) crystal of holmium. Thirdly, monoclinic crystals, in which all three lattice vector lengths are different and two orthogonal angles remain $\alpha = \gamma = 90^\circ$. The third angle, β is unconstrained. From these seven crystal classes, different UC types lead to 14 classes of Bravais lattices. The primitive UC may be found for any crystal class. It is the smallest possible unit, which contains the full symmetry of the crystal. The UC types differ by the number and arrangement of lattice points within the UC. The primitive UC possesses no further lattice points than the ones on the corners of the UC. Because these eight corner lattice points are divided into eighths by the lattice, a primitive UC contains one lattice point. For the orthorhombic crystals, e.g., all four unit cell types of primitive, body-centered, face-centered or side-centered are possible. However, within this thesis, all studied crystals show a primitive UC type.

Fig. 2.1 shows the most simple basis of a single atom, in which all other atoms of the crystal are copies by symmetry relations. In crystals with a complex stoichiometry, the basis can become much more complicated. Inserting any possible basis at the symmetry-nonequivalent positions of the 14 Bravais lattices gives rise to 230 space symmetry groups.

Computationally, a periodic lattice fulfilling Eq. 2.55 is modeled by applying periodic boundary conditions onto the UC. This means, that to any side of the UC, a periodic image of itself translated by t is adjacent. This simulates an ideal infinite crystal in any direction. This allows a couple of computational benefits when applying a plane wave basis set introduced above in subsection 2.1.6.

Within the plane wave context, Bloch's theorem was already introduced (see Eq. 2.49). It connects the electronic description in real-space with the description in reciprocal space via the reciprocal lattice vector (\mathbf{G}). The transition from real to reciprocal or Fourier space is done by a Fourier transformation (FT). According to the De Broglie relation (see Eq. 2.48), the reciprocal space is also referred to as momentum space. In analogy to the UC translation vector within real space (see Eq. 2.55), \mathbf{G} may be given as a linear combination of the reciprocal lattice vectors (\mathbf{b}) scaled by $v_1, v_2, v_3 \in \mathbb{Z}$.

$$\mathbf{G} = v_1 \mathbf{b}_1 + v_2 \mathbf{b}_2 + v_3 \mathbf{b}_3 \quad (2.56)$$

The real space and reciprocal lattice vectors relate via

$$\mathbf{b}_i \mathbf{a}_j = 2\pi \delta_{ij}. \quad (2.57)$$

Shifting the real space coordinates by the translation vector (\mathbf{t}) within the Bloch orbital, defined in Eq. 2.50 yields:

$$\phi_{j,\mathbf{k}}(\mathbf{r} + \mathbf{t}) = \sum_{\mathbf{k}}^{k_{\max}} c_{\mathbf{k}j} e^{i\mathbf{k}\mathbf{r}} e^{i\mathbf{G}\mathbf{t}}. \quad (2.58)$$

From Eq. 2.55–2.58 follows, that the Bloch orbital remains invariant upon translation, as

demanded by the periodicity of the crystal.

$$e^{i\mathbf{G}\mathbf{t}} = 1 \quad \Rightarrow \quad \phi_{j,\mathbf{k}}(\mathbf{r}) = \phi_{j,\mathbf{k}}(\mathbf{r} + \mathbf{t}) \quad (2.59)$$

Applied onto the atomic structure in real space, the FT yields the Brillouin zone. The reciprocal counterpart of the UC is the first Brillouin zone (FBZ). It is the smallest subunit of the periodic reciprocal lattice. The FBZ constrains all possible values of \mathbf{k} . Exploiting the symmetry within the FBZ, the whole reciprocal lattice may be described by even less atomic positions. The symmetry-nonequivalent subset of the FBZ is the irreducible Brillouin zone (IBZ). As the size reduction from the full FBZ to the IBZ is system-dependent, the following will introduce \mathbf{k} grids for the whole FBZ. Each FBZ centers at $\mathbf{k} = (0, 0, 0)$ named Γ -point. The shape of the FBZ of e.g. a primitive orthorhombic crystal is also orthorhombic. Its six faces are located at $\pm\pi/\mathbf{a}_i$ with \mathbf{a}_i being the respective real-space lattice vector (see Eq. 2.55). At the Γ -point, the crystalline UC orbital for band j ($\psi_{j,0}$) equals the sum of all Bloch orbitals because the multiplied plane wave part vanishes (see Eq. 2.49). Along the faces of the FBZ, the plane wave part introduced phase shift, also called perturbation is maximal. The \mathbf{k} vectors of maximal perturbation correspond to points of high symmetry within the reciprocal space. As the FBZ itself, these are determined by the Bravais lattice, namely the lattice symmetry and unit cell type within real space.

In between the Γ -point and faces of the FBZ, the phase shift varies accordingly. These \mathbf{k} vectors within the FBZ are sampled on a grid. Commonly the Monkhorst-Pack scheme is employed, which samples a \mathbf{k} grid according to Eq. 2.60.^[123]

$$\mathbf{k} = \sum_{i=1}^3 \mathbf{b}_i N_{\mathbf{k},i}^{-1} \left(n_{\mathbf{k},i} + s_{\mathbf{k},i} + \frac{1 - N_{\mathbf{k},i}}{2} \right) \quad (2.60)$$

Here, $N_{\mathbf{k}}$ is the number of \mathbf{k} grid points along the respective direction in \mathbf{b} , $n_{\mathbf{k}}$ sets each respective \mathbf{k} point according to $n_{\mathbf{k}} \in \{0, 1, \dots, N_{\mathbf{k}} - 1\}$, and $s_{\mathbf{k}}$ are optional shifting parameters, which have not been applied within this thesis. Along each \mathbf{b} direction, the produced \mathbf{k} grid is symmetrical to the Γ -point, which is included as a grid point itself for odd $N_{\mathbf{k}}$. As the $\psi_{j,\mathbf{k}}$ depend on \mathbf{k} , the grid spacing needs to be chosen small enough to obtain a converged electronic energy. Apart from the Γ -point, the other points of high symmetry, which are located at the FBZ faces, are not part of the Monkhorst-Pack \mathbf{k} grid. These $\psi_{j,\mathbf{k}}$ need to be calculated specifically. At these \mathbf{k} vectors of high symmetry, the energies of $\psi_{j,\mathbf{k}}$, the band energies possess their respective maxima and minima. Plotting the band energies against these \mathbf{k} vectors, including the paths of \mathbf{k} vectors connecting these, yields the band structure.

Within each of these bands, the energy is a continuous function of \mathbf{k} . This contrasts e.g., a single molecule possessing occupied and unoccupied MOs with discrete energy levels. Within a chain of N such molecules, N times as many energy levels exist. By attractive and repulsive

interaction between these MOs, a wide range of energy levels is spanned. Within the set of occupied MOs, as well as within the set of unoccupied ones, the energy difference between the distinct energy levels $\Delta\epsilon$ decreases with N . For $N \rightarrow \infty$, the differences in energy levels approach $\Delta\epsilon \rightarrow 0$ forming continuous bands. The energy span within a band is called electronic dispersion. It is related to the local character of orbitals. Consequently, for e.g., Ln(III)-compounds, electronic dispersion is low for the narrow bands formed by the Ln(III) 4f-electrons possessing a high local character.^[124–127] A band's width is not only observable within the band structure, but even better so within the density of states (DOS), because it is no longer a function of \mathbf{k} . To determine the DOS, the energy range is split into small, discrete bins of $\Delta\epsilon$ width. The number of states or energy levels within each bin of energy ϵ is summed over the whole \mathbf{k} space. The obtained sum is the DOS at energy ϵ . Among the occupied bands, the one with the highest energy is called valence band (VB). The band with the next higher energy is the conduction band (CB), which is the lowest energy band among the unoccupied bands. The highest occupied energy level is the Fermi energy (E_F). This corresponds to the maximum of the VB (VBM). The energy difference between VBM and the minimum of the CB (CBM) is the band gap (E_{gap}). It is a direct E_{gap} , if VBM and CBM are both located at the same \mathbf{k} vector. Otherwise, it is an indirect E_{gap} . The width of the band gap determines conductivity. Within a metal, E_F is located inside a band. Subsequently, no band gap exists, VB and CB are not separated, and electrons can easily roam within the CB. A semi-conductor is defined by a small E_{gap} , while an insulator possesses a large E_{gap} . The definitions separating these two might differ. This thesis uses the definition of $E_{\text{gap}} < 4$ eV for a semi-conductor.^[128] All geochemical twin fluorides studied within this thesis are extremely strong insulators with up to measured $E_{\text{gap}} = 12.5$ eV for YF_3 .^[57]

2.2.2 Surface Energies and Abundances

A certain plane within a bulk crystal is classified by its Miller indices (hkl) with $h, k, l \in \mathbb{Z}$ giving the multiples of the respective real space lattice vectors \mathbf{a}_1 , \mathbf{a}_2 , and \mathbf{a}_3 (see Eq. 2.55). The respective normal vectors $[hkl]$ point perpendicular to the respective plane. All seven low-lying Miller indices planes of $h, k, l \in \{0, 1\}$ are depicted in Fig. 2.2 for a $Pnma$ -symmetric crystal with MF_3 composition.

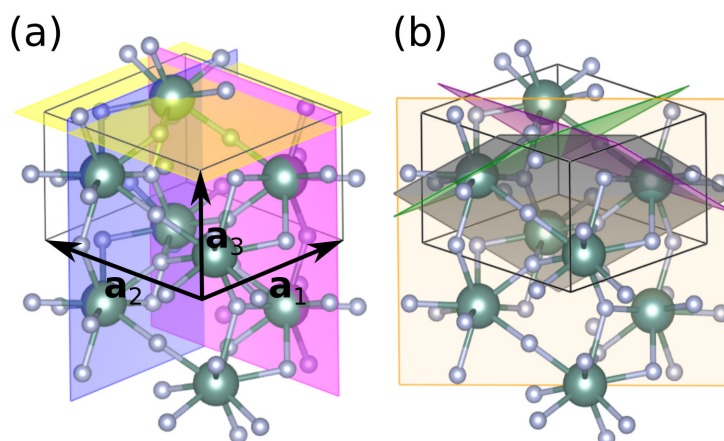


Figure 2.2 visualized Miller indices planes within a waimirite-structured crystal ($Pnma$); the black box highlights the unit cell with lattice vectors \mathbf{a}_1 , \mathbf{a}_2 and \mathbf{a}_3 containing four MF_3 formula units; **(a)** (100) in pink, (010) in blue, and (001) in yellow; **(b)** (110) in orange, (101) in purple, (011) in green, and (111) in gray.

Cutting a crystal along one of the Miller indices planes shown in Fig. 2.2 produces a surface labeled accordingly. Computationally, surfaces may be modeled within a periodic or embedded cluster framework. Within the latter, a large, layered hemisphere is built, whose outmost layer consists of thousands of point charges. This model is beneficial, if an accurate wave function-based method is desired for the core cluster or individual defects are probed.^[129,130] The main disadvantages are, that the construction of the layered hemisphere is quite challenging, as well as its enormous size, which has to be sufficiently large to avoid influences of the finite size onto the core region.

Analogous to the periodic bulk, periodic surfaces apply periodic boundary conditions allowing the use of a plane wave basis set. Since this work aims to study pristine surfaces of highly insulating crystals, which possess an electronic structure easily described qualitatively by DFT, the periodical ansatz is the better choice. Within the 3D-periodic framework, a surface is established by introducing vacuum perpendicular to the surface plane. The vacuum layer has to be sufficiently thick to exclude artificial interactions of the top surface atoms with the bottom surface atoms of its periodic copy. Thus, the vector length is converged against the total energy. Along the two lattice vectors within the surface plane, the surface expands in 2D by periodic boundary conditions. Such a surface model is commonly referred to as slab.

An example of a symmetric β -HoF₃ slab is shown in Fig.2.3. Along the non-periodic direction, the number of formula unit layers also called the slab thickness has to be sufficiently large to avoid artificial interactions of the bottom and top surface. Therefore, the slab thickness has to be converged in surface energy (E_{surf}). Symmetric slabs possess a central point of inversion or mirror plane. From this follows that the top and bottom surfaces are symmetry equivalent. This leads to two advantages. For one, the obtained E_{surf} is unambiguously linked to a single atomic surface configuration. Second, no additional dipole moments perpendicular to the surface plane are built up within the slab. These could prohibit convergence of E_{surf} with respect to the slab thickness.

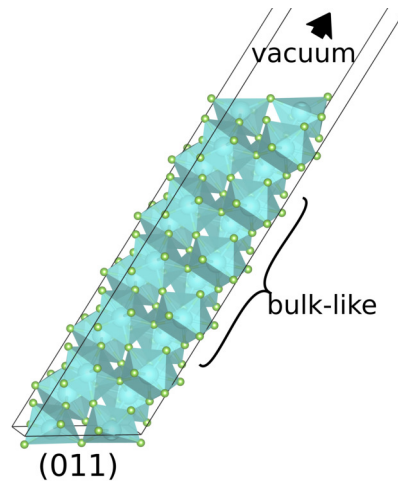


Figure 2.3 symmetric slab example of the wairirite-structured β -HoF₃; in-plane with the modeled (011) surface, the slab extends periodically; perpendicular to the surface, the slab is 12 HoF₃ layers (ca. 25 Å) thick forming a bulk-like middle part and two surfaces at the bottom / top, which are separated by a vacuum layer of ca. 25 Å.

Commonly, E_{surf} is calculated from the difference of total energies of the slab (E_{slab}) and the bulk unit cell (E_{bulk}) times the number of unit cells within the slab (N_{uc}) divided by the slab surface area (A) of the top and bottom surface.

$$E_{\text{surf}}^{\text{bd}} = \frac{E_{\text{slab}} - N_{\text{uc}}E_{\text{bulk}}}{2A} \quad (2.61)$$

As this approach uses the bulk unit cell energy, the resulting energy is referred to as bulk-derived surface energy ($E_{\text{surf}}^{\text{bd}}$) within this work. For surfaces with substoichiometric fluorine content, the numerator of Eq. 2.61 must be extended by the fluorine potential (μ_{F}) for each missing fluorine (N_{xF}).

$$E_{\text{surf}}^{\text{bd}} = \frac{E_{\text{slab}} - N_{\text{uc}}E_{\text{bulk}} + N_{\text{xF}}\mu_{\text{F}}}{2A} \quad (2.62)$$

From the bulk energy per atom of metallic yttrium or holmium, the respective metal potential (μ_{M}) is obtained. Together with E_{bulk} , the number of metal (N_{M}) and fluorine atoms (N_{F})

within the unit cell, μ_F is determined.

$$\mu_F = \frac{E_{\text{bulk}} - N_M \mu_M}{N_F} \quad (2.63)$$

Eq. 2.61 or 2.62 are applied for all β -YF₃ slabs. However, as pointed out by Boettger,^[131] $E_{\text{surf}}^{\text{bd}}$ may fail to converge with respect to N_{uc} , which can be avoided using slab-derived energies only.

$$E_{\text{surf}}^{\text{sd}} = \frac{E_{\text{slab}} - N_{\text{uc}}(E_{\text{slab}} - E_{\text{slab}-1})}{2A} \quad (2.64)$$

These slab-derived surface energy ($E_{\text{surf}}^{\text{sd}}$) use the difference in total energies of the slab and the next smaller slab ($E_{\text{slab}-1}$). Consequently, each $E_{\text{surf}}^{\text{sd}}$ needs two adjacent slab thickness. This requires one more data point within the slab thickness convergence compared to $E_{\text{surf}}^{\text{bd}}$. Indeed, linearly diverging $E_{\text{surf}}^{\text{bd}}$ were found for β -HoF₃, even though slab thicknesses of up to $N_{\text{uc}} = 7$ unit cells corresponding to Ho₂₈F₈₄ were considered. Only the relaxed slabs possessed diverging $E_{\text{surf}}^{\text{bd}}$. Unrelaxed slabs had neatly converging $E_{\text{surf}}^{\text{bd}}$. Thus, we believe that this divergence was linked to the allowed spin-polarization with PBE+U_d applied on the atomic relaxation of the whole slab. While also in β -YF₃, the whole slab was relaxed, no divergent $E_{\text{surf}}^{\text{bd}}$ were observed. However, these were performed at the PBE level without Hubbard-type correction and without allowed spin polarization. On the other hand, $E_{\text{surf}}^{\text{sd}}$ converged nicely for β -HoF₃. Therefore, all β -HoF₃ surface energies were obtained by Eq. 2.64.

The surface area of a crystal minimizes due to the missing attractive interactions of missing attractive Coulomb or orbital interactions. There is a variety of (hkl) to built the surface from. Each surface coming with a number of possible atomic configurations, called surface terminations. Within an ideal crystal in equilibrium, only the most stable termination of each (hkl) are present. Between the different (hkl) , its a interdependence of stability and geometry to generate the most stable overall crystal. This interdependence is generally solved in a Wulff plot analysis. Already in 1901, Wulff discovered that the growth of a crystal along a direction is proportional to the surface energy corresponding to this normal vector.^[132,133] Within a Wulff plot, a polar diagram is constructed, in which each surface normal vector possess the length of the respective surface energy. At the end of the normal vector, the corresponding (hkl) plane is drawn. The intersecting planes form facets, which construct the Wulff polyhedron. The ratio of each facet area among the whole crystal ($\%_{\text{surf}}$) is the abundance of that (hkl) according to its electronic energy.

2.2.3 Adsorption Energies via pEDA with NOCV Extension

An energy decomposition analysis (EDA) scheme uses separate calculations of each of the reactants A and B, as well as of the relaxed product AB. Each reactant is calculated twice, with relaxed atomic coordinates and within the atomic structure, it possesses within the relaxed product. The general scheme of EDA has been developed in the 1970s by Kitaura and Morokuma,^[134,135] as well as Ziegler and Rauk.^[136–138] The group of Ziegler also introduced the natural orbitals for chemical valence (NOCV) method as an extension to EDA.^[139] However, these were restricted to molecular systems. The transition to periodic systems calculated with DFT dates less than 10 years back, when the group of Tonner introduced their periodic energy decomposition analysis (pEDA) and NOCV schemes.^[140,141] The following section is largely based on [140, 141], onto which the interested reader is forwarded for more details.

An adsorption energy of a molecular adsorbate onto a surface is essentially the binding energy of two reactants A and B forming the product AB. If this energy is determined from the total electronic energies at the respective local minima within the potential energy surfaces of the product (E_{AB}^{AB}), as well as of reactants A (E_A^A) and B (E_B^B), it is referred to as bonding energy (ΔE_{bond}).

$$\Delta E_{\text{bond}} = E_{AB}^{AB} - E_A^A - E_B^B \quad (2.65)$$

In contrast, the interaction energy (ΔE_{int}) describes the energy gain towards the local minima product starting from reactants A (E_A^{AB}) and B (E_B^{AB}), which already possess the same atomic structures as within the product AB.

$$\Delta E_{\text{int}} = E_{AB}^{AB} - E_A^{AB} - E_B^{AB} \quad (2.66)$$

Consequently, both adsorption energies differ by the relaxation or preparation of the reactants. This difference is called preparation energy (ΔE_{prep}).

$$\Delta E_{\text{int}} = \Delta E_{\text{bond}} - \Delta E_{\text{prep}} \quad (2.67)$$

It is helpful for the understanding of chemical bonds, if ΔE_{int} is split further into its electronic subcontributions. From here on, no changes to the atomic structures are considered. All atomic structures remain as they are within the product AB (see Eq. 2.66). An easy way to quantify the energy attributed to dispersion interaction (ΔE_{disp}) is to determine ΔE_{int} with and without an additive dispersion correction as e.g., D3.^[96] This is especially useful, as this leaves the electron density unchanged (see Eq. 2.37). The remaining electronic term of the interaction energy ($\Delta E_{\text{int}}(\text{elec})$) can be decomposed into its subparts applying EDA.

$$\Delta E_{\text{int}}(\text{elec}) = \Delta E_{\text{int}} - \Delta E_{\text{disp}} \quad (2.68)$$

The EDA scheme starts from the electron densities of the isolated reactants A ($\rho_{\text{A}}^{\text{AB}}$) and B ($\rho_{\text{B}}^{\text{AB}}$). These are combined in a product ansatz, without optimization. The energetic difference between the isolated reactants and the non-optimized product of A+B is referred to as the semi-classical electrostatic energy (ΔE_{elstat}). For most bound systems, ΔE_{elstat} is attractive. In a next step, the non-optimized A+B product KS-wave function is normalized and antisymmetrized to obey the Pauli principle. This involves the orthogonalization of the reactant KS-orbitals. The corresponding energy is called Pauli energy (ΔE_{Pauli}). As the orthogonalization induces constraints on the overall wave function, ΔE_{Pauli} is strictly repulsive. Finally, the normalized, antisymmetrized KF-wave function of the product AB is SCF optimized yielding the attractive orbital energy (ΔE_{orb}).

$$\Delta E_{\text{int}}(\text{elec}) = \Delta E_{\text{elstat}} + \Delta E_{\text{orb}} + \Delta E_{\text{Pauli}} \quad (2.69)$$

The two attractive contributions of Equation 2.69 together are referred to as attractive energy (ΔE_{attr}). The ratio of ΔE_{orb} among ΔE_{attr} is used as a measure for the covalent character of a chemical bond.

$$\Delta E_{\text{attr}} = \Delta E_{\text{elstat}} + \Delta E_{\text{orb}} \quad (2.70)$$

To yield further chemical insights, ΔE_{orb} may be divided into pairwise NOCV interactions between both reactants. A deformation density matrix ($\Delta \mathbf{P}^{\text{orb}}$) is formulated from the difference in electron densities between the normalized and antisymmetrized KF wave function of the product AB before (ρ^0) and after SCF optimization (ρ_{AB}). The occupied orthonormal spin orbitals of each reactant (λ_j), as well as an additional set of non-occupied ones (λ_a) form the basis for the deformation density matrix elements ($\Delta P_{kl}^{\text{orb}}$).

$$\sum_{k,l} \Delta P_{kl}^{\text{orb}} \lambda_k \lambda_l = \Delta \rho_{\text{orb}} = \rho_{\text{AB}} - \rho^0 \quad (2.71)$$

The arithmetic mean of ρ_{AB} and ρ^0 is referred to as the transition state density (ρ^{TS}).

$$\rho^{\text{TS}} = \frac{1}{2}(\rho_{\text{AB}} + \rho^0) \quad (2.72)$$

Diagonalizing $\Delta \mathbf{P}^{\text{orb}}$ with the coefficient vectors (\mathbf{C}_i) as eigenfunctions yields the NOCV eigenvalues (ν_i).

$$\Delta \mathbf{P}^{\text{orb}} \mathbf{C}_i = \nu_i \mathbf{C}_i \quad (2.73)$$

Summing over the coefficient matrix elements (\mathbf{C}_{ij}) times the λ_j , the NOCVs (ψ_i^{NOCV}) are

obtained.

$$\Psi_i^{\text{NOCV}} = \sum_j \mathbf{C}_{ij} \lambda_j \quad (2.74)$$

The ν_i form pairs of same absolute value but opposite sign corresponding to the respective reactant's loss or gain in electron density upon interaction. With the related $\Psi_{\pm i}^{\text{NOCV}}$ pair, single interaction deformation densities ($\Delta\rho_i$) are constructed.

$$\sum_i \Delta\rho_i = \sum_i \nu_i (|\Psi_i^{\text{NOCV}}|^2 - |\Psi_{-i}^{\text{NOCV}}|^2) = \Delta\rho_{\text{orb}} \quad (2.75)$$

From ρ^{TS} defined in Eq. 2.72, the corresponding KS Fock matrix elements (F_{kl}^{TS}) are obtained. Multiplied by the respective $\Delta P_{kl}^{\text{orb}}$ and summed over all matrix elements, the overall ΔE_{orb} is reproduced.

$$\Delta E_{\text{orb}} = \sum_{k,l} \Delta P_{kl}^{\text{orb}} F_{kl}^{\text{TS}} = E[\rho_{\text{AB}}] - E[\rho^0] \quad (2.76)$$

Instead of summing over all matrix elements, ΔE_{orb} can also be retrieved from the trace of the product of $\Delta \mathbf{P}^{\text{orb}}$ and \mathbf{F}^{TS} . Via the coefficient matrix (\mathbf{C}), these are transformed from a λ_i to a Ψ_i^{NOCV} basis.

$$\Delta E_{\text{orb}} = \text{Tr}(\Delta \mathbf{P}^{\text{orb}} \mathbf{F}^{\text{TS}}) = \text{Tr}(\mathbf{C}^\dagger \Delta \mathbf{P}^{\text{orb}} \mathbf{C} \mathbf{C}^\dagger \mathbf{F}^{\text{TS}} \mathbf{C}) \quad (2.77)$$

Each summed $\pm i$ pair of the transformed Fock matrix elements (F_{ii}^{TS}) times the respective eigenvalue yields a pairwise NOCV interaction orbital energy (ΔE_{orb}^i).

$$\sum_i \Delta E_{\text{orb}}^i = \sum_i \nu_i (F_{ii}^{\text{TS}} - F_{-i-i}^{\text{TS}}) = \text{Tr}(\mathbf{C}^\dagger \Delta \mathbf{P}^{\text{orb}} \mathbf{C} \mathbf{C}^\dagger \mathbf{F}^{\text{TS}} \mathbf{C}) \quad (2.78)$$

These separated NOCV interactions are a helpful tool to interpret the chemical nature of adsorptions.

2.3. Contributions from Special Relativity

Within the very beginning of this whole chapter, the SE was introduced as the most fundamental equation of quantum chemistry (see Eq. 2.2). The whole field is rooted on the non-relativistic picture of constant mass, absolute time, as well as the separability of time and spatial coordinates. This picture is, however, incomplete and the effects of special relativity become important for heavy atoms. Considering e.g., systems without electron-electron interaction as hydrogen-like ions, the orbital energies are proportional to the squared nuclear charge (Z^2). By relativity, these are further stabilized proportional to Z^4 .^[8] Considering $Z = 67$ or 72 for the elements of holmium or hafnium, the correct electronic structure may only be described including relativistic effects. Therefore, this section introduces special relativity, relativistic quantum chemistry, and the approximation applied within this thesis. As convenient for relativistic quantum chemistry, this section uses Gaussian units, in which only the dielectric constant in vacuum is dimensionless, while in contrast to atomic units, e.g., m_e , and \hbar are explicitly given.^[142]

Dating back on experiments by Michelson and Morley in 1887,^[143] the speed of light was first suggested to be a constant. Initial explanations by Fitzgerald^[144] and Lorentz^[145] already suggested that particles moving at velocities reaching the realm of the speed of light contract linearly within the direction of motion.^[146] One fundamental principle of physics is, that the laws of physics must be the same within all inertial frames. From this, Einstein concluded in 1905, that if the speed of light in vacuum (c_0) is constant, mass and time must vary between the inertial frames.^[147] From this follows that particles moving at a high relative velocity possess an increased mass, are subject to a dilated time, and contract linearly in direction of movement.

In 1928, Dirac successfully combined these laws of special relativity with quantum theory, forming the basis of relativistic quantum chemistry.^[148,149] Within the relativistic picture, time and the three spatial coordinates are not separable. Instead, they form the Minkowski space-time vector of $\mathbf{x}^M = (c_0 t, x, y, z)^T$ with metric \mathbf{g} .^[150]

$$\mathbf{g} = \begin{pmatrix} 1 & 0 & 0 & 0 \\ 0 & -1 & 0 & 0 \\ 0 & 0 & -1 & 0 \\ 0 & 0 & 0 & -1 \end{pmatrix} \quad (2.79)$$

This requires a representation in a 4D space. These 4D wave functions are referred to as Dirac spinors (Φ^D). The name emphasizes that electronic spin is an inherent feature within Φ^D , while it enters the non-relativistic Φ of the SE (see Eq. 2.2) as the subsequently added quantum number m_s . Accordingly, the relativistic Hamiltonian is a 4×4 matrix. However, it is usually written as a 2×2 matrix of the 2×2 Pauli spin matrices ($\underline{\sigma}$). For fixed

nuclear coordinates, the one-electron Dirac-Coulomb Hamiltonian (\hat{h}_{rel}) has the following form:^[151,152]

$$\hat{h}_{\text{rel}} = \begin{pmatrix} \hat{V}_{\text{Ne}} & c_0 \underline{\sigma} \hat{p} \\ c_0 \underline{\sigma} \hat{p} & \hat{V}_{\text{Ne}} - 2 m_e c_0^2 \end{pmatrix} \quad (2.80)$$

The attractive nuclear Coulomb potential operator (\hat{V}_{Ne}) has the same form as within the non-relativistic Hamiltonian (see Eq. 2.5), apart from acting onto 4D space-time. The same applies for the quantum mechanical momentum operator $\hat{p} = -i\hbar\nabla$. Eq. 2.80 includes the relativistic correction to the kinetic energy originating from the relativistic mass increase of the electrons. This is the so-called scalar relativistic correction, as it is non-spin-dependent. Furthermore, it yields the coupling of electronic spin with the angular momentum of the spatial orbitals known as spin-orbit coupling. The relativistic kinetic energy possesses positive and negative solutions, which are separated by a large gap of $2m_e c_0^2$. For non-interacting electrons, the relativistic kinetic energy ($T_{\text{e,rel}}$) is:

$$T_{\text{e,rel}} = \pm \sqrt{-\hbar^2 \nabla^2 c_0^2 + m_e^2 c_0^4} \quad (2.81)$$

According to the interpretation by Feynman^[153] and Stückelberg,^[154] the existence of negative energy states can be explained by an antisymmetry between energy, time, and a particle (electron) vs. its respective antiparticle (positron). This antisymmetric relations are illustrated in Fig. 2.4. The eigenstates of the 4D Φ^{D} contain four components. Two are large

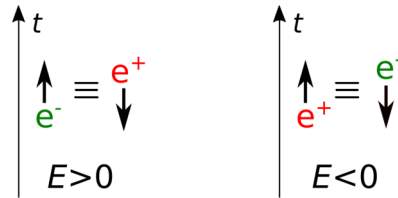


Figure 2.4 scheme visualizing the Feynman-Stückelberg interpretation of the positive and negative energy solutions of the relativistic kinetic energy (see Eq. 2.81); the positive energy solutions correspond to an electron (green) moving along the time axis (t), as well as to the positron (red) moving against t . For the negative energy solutions, the reversed is the case.

for the positive energy solutions ($\Phi_{\text{L}}^{\text{D}}$), while the other two are small ($\Phi_{\text{S}}^{\text{D}}$). According to the antisymmetry, the same components yield the reversed contributions for the negative energy solutions.^[155]

$$\Phi^{\text{D}} = \begin{pmatrix} \Phi_1^{\text{D}} \\ \Phi_2^{\text{D}} \\ \Phi_3^{\text{D}} \\ \Phi_4^{\text{D}} \end{pmatrix} = \begin{pmatrix} \Phi_{\text{L}}^{\text{D}} \\ \Phi_{\text{S}}^{\text{D}} \end{pmatrix} \quad (2.82)$$

Within the non-relativistic limit, which corresponds to $c_0 \rightarrow \infty$, the eigenvalues of $\Phi_{\text{S}}^{\text{D}}$ vanish.^[155] Approximate, relativistic Hamiltonians targeting at the full Φ^{D} are called four-

component Hamiltonians, while those only targeting at the subset of Φ_L^D are referred to as two-component Hamiltonians. The latter require to decouple Φ_L^D , or positive energy solutions from Φ_S^D , or negative energy solutions. Therefore, the relativistic kinetic energy operator is separated from the non-relativistic potential operators (\hat{V}) within the one-electron Fock operator (\hat{f}_{rel}) to obtain a field-free one-electron relativistic Hamiltonian (\hat{h}_{rel}^f).^[156]

$$\hat{f}_{\text{rel}} = \hat{h}_{\text{rel}}^f + \hat{V} \quad (2.83)$$

This ansatz assumes, that the 4×4 matrix of each potential within \hat{V} is diagonal and that the entries acting on Φ_L^D are identical to those acting on Φ_S^D . These requirements are fulfilled for the potentials within KS-DFT, but not e.g., for the exact exchange integral within HF theory.^[156] The two-component equation is obtained from the Pauli elimination by introducing an energy-dependent scaling function (Θ), which controls the relativistic correction. For the non-relativistic limit of $\Theta = 1$, Eq. 2.84 reproduces the non-relativistic SE.^[157]

$$(V - \epsilon_i)\Phi_L^D + \frac{1}{2m_e c_0^2} [(c_0 \underline{\sigma} \hat{p}) \Theta (c_0 \underline{\sigma} \hat{p})] \Phi_L^D = 0 \quad (2.84)$$

Here, V is a sum over all potentials as e.g., V_{Ne} and V_{ee} , while ϵ_i is the i -th orbital energy. Eq. 2.84 is not yet approximated and reproduces the exact large components. Here, Θ is a function of the orbital energies and the potentials. As it is only a multiplicative factor onto Φ_L^D , it allows an exact separation of spin-dependent and spin-independent contributions.^[157]

$$\Theta(V, \epsilon_i) = \frac{2m_e c_0^2}{2m_e c_0^2 - V} \left[1 + \frac{\epsilon_i}{2m_e c_0^2 - V} \right]^{-1} \quad (2.85)$$

However, instead of solving the computational demanding Eq. 2.84 with Θ of Eq. 2.85, it is more conveniently solved by a truncated Θ_k obtained from a regular approximation.^[157]

$$\Theta_k(V, \epsilon_i) = \frac{2m_e c_0^2}{2m_e c_0^2 - V} \sum_{k=0}^{\infty} \left(\frac{\epsilon_i}{V - 2m_e c_0^2} \right)^k \quad (2.86)$$

Truncating Eq. 2.86 after $k = 0$ eliminates the dependency on the orbital energy. This corresponds to the zeroth-order regular approximation (ZORA).^[158–160]

$$\Theta_{k=0}(V) = \frac{2m_e c_0^2}{2m_e c_0^2 - V} \quad (2.87)$$

Already with $\Theta_{k=0}$, a significant portion of the relativistic effects close to the nuclei are included, leading to Φ_L^D with an excellent description of the valence region.^[157] The variational ZORA Hamiltonian (\hat{H}_{ZORA}), obtained from inserting Eq. 2.87 into Eq. 2.84, may be written as a sum of scalar relativistic (sr), as well as spin-orbit coupling (SOC) contributions.

$$\hat{H}_{\text{ZORA}} = \hat{H}_{\text{ZORA}}^{\text{sr}} + \hat{H}_{\text{ZORA}}^{\text{SOC}} = V + \mathbf{p} \frac{c_0^2}{2c_0^2 - V} \mathbf{p} + \frac{c_0^2}{(2c_0^2 - V)^2} \underline{\sigma} \cdot (\nabla V \times \mathbf{p}) \quad (2.88)$$

As ZORA is applied with the KS-DFT method, the potential V includes the DFT-inherent potentials of J , V_{ext} , and the potential difference $V_{\text{ee}} - J$ associated to exchange-correlation (see Eq. 2.30).^[161] Neglecting $\underline{\sigma}$, and thus SOC, Eq. 2.88 reduces to the scalar relativistic Hamiltonian.^[161]

$$\hat{H}_{\text{ZORA}}^{\text{sr}} = V + \mathbf{p} \frac{c_0^2}{2c_0^2 - V} \mathbf{p} \quad (2.89)$$

A drawback of the originally proposed ZORA method is that it is not gauge invariant. This is practically solved by scaling the orbital energies by an expectation value over the molecular orbitals. For the scalar ZORA approach, the scaled orbital energies ($\epsilon_{i\text{-ZORA}}^{\text{sr}}$) become:^[162]

$$\epsilon_{i\text{-ZORA}}^{\text{sr}} = \frac{\epsilon_{i\text{ZORA}}^{\text{sr}}}{1 + \langle \mathbf{p} \frac{c_0^2}{(2c_0^2 - V)^2} \mathbf{p} \rangle} \quad (2.90)$$

Comparing the effect of relativity onto individual orbitals within the same atom, it is found that the closer the expectation value of the radial distance $\langle \hat{r} \rangle_{nl}$ to the nucleus, the stronger the scalar relativistic effect, and the stronger the relativistic contraction of $\langle \hat{r} \rangle_{nl}$. Due to the absence of angular nodes, the s-type orbitals possess a non-zero value at the core and are thus especially affected. Spatial orbitals of $l > 0$ split according to SOC. To describe the individual orbital energies of heavy atoms correctly, as e.g., for excitation spectra, it is vital to include SOC. Onto the overall energy, however, SOC contributes generally about one magnitude less than the relativistic kinetic energy. Hitherto unaddressed contributions from quantum electrodynamics and a finite nucleus generally contribute even two magnitudes less than the relativistic kinetic energy.^[8] As a consequence, both effects are only considered for special cases demanding an extraordinary accuracy.

For calculations predominantly aiming at atomic structures containing heavy atoms and the corresponding relative stabilities, it is a good first approximation to only include the scalar relativistic effect. This is especially true, if the valence regions is dominated by s-type orbitals as e.g., 6s in holmium or hafnium, which are the heavy atoms calculated within this thesis. As the scalar relativistic effect is strongest for the electrons closest to the core, it is common to apply ECPs (see subsection 2.1.6), instead of expanding all occupied orbitals in basis functions. The ECPs have been fitted to reproduce fully relativistic calculations. If FCOs are used instead, these FCOs need to originate from calculations applying a relativistic method. A frequently used one is the scaled scalar ZORA, because it hardly increases the computational costs. Within this work, this method has been used for the all-electron molecular test calculations in paper **A** as implemented in ORCA,^[110,161] as well as for the periodic calculations with the respective FCOs in paper **B.3** as implemented in AMS-BAND.^[108,163]

2.4. Electronic Structure of Lanthanides

After the general introduction of relativistic effects in section 2.3, this section is meant to give a deeper insight into the electronic structure of lanthanides (Ln) of lanthanum–lutetium (La–Lu). On this foundation, it is explained why the electronic structure of holmium (Ho) was calculated within this thesis without the 4f-shell. A very compact explanation of the lanthanide contraction and the little participation of the 4f-electrons within chemical bond are given in the introduction (see chapter 1).

What is particular about the shell structure of lanthanides is that, in contrast to the lighter atoms, the energetic order differs from the order of increasing $\langle \hat{r} \rangle_{nl}$.^[8] First, the energetic order is considered. For the series of atomic Ln, the energy levels of the (partially) occupied 4f, 5d, and 6s, as well as the unoccupied 6p are very close and exchange order. This creates a very complex picture of accessible electronic configurations making a multi-configurational ansatz necessary.^[8,164] To a lesser extent, this is also the case for the singly and doubly oxidized Ln(I) and Ln(II).^[164] While the former is unstable for any Ln, the latter is a stable oxidation state for Sm, Eu, Tm, and Yb. However, the most stable oxidation state and the only one, which is observed for the whole Ln-series is the triply oxidized Ln(III). For completeness sake, it should be noted that Ce, Pr, Nd, Tb, and Dy also occur in a stable oxidation state of Ln(IV).^[8] Within the Ln(III) series, the (partially) occupied 4f-energy levels are well-separated from the unoccupied 5d and 6s-energy levels.^[164] By a vacant 6s-shell, a possible transition of electron density to the 6p-shell, which is easily accessible from the 6s, is also avoided.^[8] This leaves an unambiguous ground state configuration of [Xe] 4f^{*N*_{4f}} with *N*_{4f} being the number of 4f-electrons according to the Aufbau principle from La(III) with *N*_{4f} = 0 to Lu(III) with *N*_{4f} = 14.^[6] Along the Ln(III)-series, the relative energies of the 4f-levels vary by *N*_{4f}. The occupied and unoccupied 4f-energy levels form a characteristic double zigzag curve (see orange and blue lines in Fig. 2.5 a).^[101,165] Within Ln(III), starting at Ce(III) with 4f¹, each additional 4f-electron/proton pair stabilizes the energy of the 4f-shell. The energy of the occupied 4f-levels minimizes at Gd(III) with an half-filled 4f⁷. Naturally, the surplus eighth 4f⁸ electron in Tb(III) raises the 4f-level energy considerably. From Tb(III) to Ho(III) and Tm(III) to Lu(III), each 4f-electron/proton pair stabilizes the 4f-shell again. In great contrast to these trends, the unoccupied 5d-energy levels remain largely constant with the Ln(III)-series, but are very sensitive to the chemical environment.^[101]

After the discourse on the orbital energies, now, their radial probability densities of $P_{nl} = r^2 |R_{nl}(r)|^2$ and the expectation values of the radial distance $\langle \hat{r} \rangle_{nl}$ are discussed. Each additional proton along the Ln-series decreases $\langle \hat{r} \rangle_{nl}$ and thus, the ionic radii. This is the well-known lanthanide contraction. The closer the electron density to the positive charge of the core, the less it is shielded by other electrons and the more it is affected by a charge increase within the core. From this follows that the 4f-shell contracts stronger along the Ln-series than the ones of 5d and 6s.^[8]

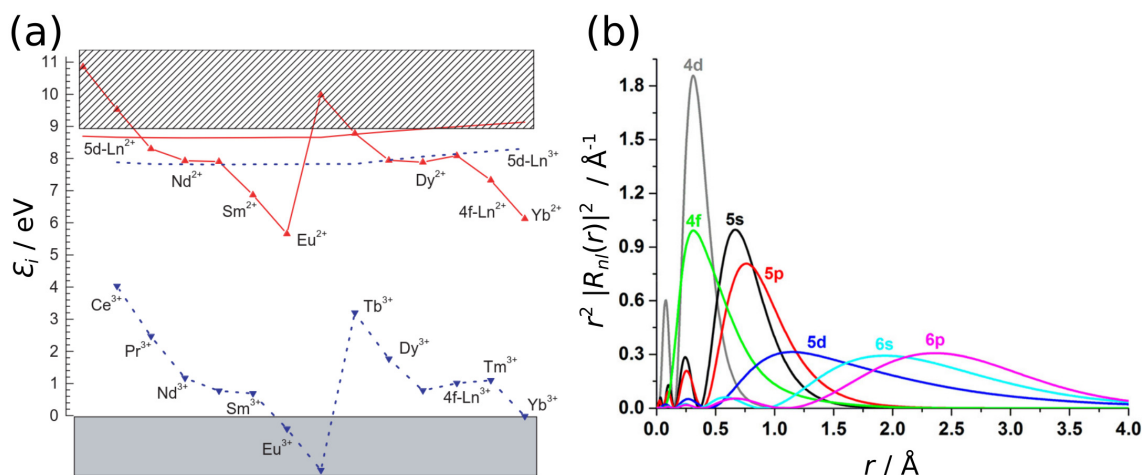


Figure 2.5 (a) Ln-doped YPO_4 : empirically-derived band energies (ϵ_i) of Ln(III) (blue) and Ln(II) (red) relative to the valence band maximum of the host crystal YPO_4 (solid gray bar); graph taken from Dorenbos;^[166] **(b)** radial probability densities ($r^2 |R_{nl}(r)|^2$) vs. radial distance (r) of atomic Sm(III) calculated at PBE/scalar ZORA/TZ2P; graph taken from Lu et al.;^[167] axis labels of both graphs have been adapted to fit nomenclature used within this thesis.

Consequently, the 4f-shell of the heavier Ln, as e.g., Ho possesses an even stronger semi-core-like character than the one within the lighter Ln.^[8,167] While this is already true within the non-relativistic picture, the effect on orbitals with a low n of predominantly s-type, but also of p-type is so strong, that the scalar relativistic effects discussed in section 2.3 become non-negligible. Due to the scalar relativistic contraction of their $\langle \hat{r} \rangle_{nl}$, these shield the nuclear charge even better. Therefore, the outer orbitals of d and f-type expand, which is also referred to as indirect relativistic effect.^[8] The expanded 4f-shell itself shields the nuclear charge less efficiently and thus, causes a subsequent expansion of the more outward shells of $n = 5, 6$.^[8] Within the same atom, $\langle \hat{r} \rangle_{nl}$ is mainly determined by n (see e.g., 4d and 5d in Fig. 2.5 b). Among orbitals of the same n , $\langle \hat{r} \rangle_{nl}$ increases slightly by l (see e.g., 5s, 5p, and 5d). From this follows that despite the higher energy of the partially filled 4f-shell, it is less accessible for bond formation as $\langle \hat{r} \rangle_{4f}$ is closer to the core, than the ones of $n = 5, 6$. Therefore, even in Ln(III), the fully occupied 5s and 5p-shells shield the 4f-shell towards the outside. Due to this radial inaccessibility or local character, the 4f-shell is attributed a core-like or semi-core-like character.^[6,8] Consequently, within a solid crystal, the ligands have little influence on the energy of the 4f-shell, which are shielded by the other electron density from the ligand field.^[6,7] Thus, the 4f-energy levels split only slightly by the ligand field and generally favoring a high spin state.^[7] However, they are hugely affected by scalar relativistic contraction and spin-orbit coupling, as well as correlation.^[6] While the impacts of the former have already been discussed, the latter will be briefly addressed in the following. The number of possible electronic states is enormous for partially filled 4f-shells. For Ho(III) with $4f^{10}$, there are

e.g., 1001 possible electronic states.^[6] The energy difference between adjacent spin-orbit-split levels is, however, very small. This allows a variety of intraconfigurational $4f \rightarrow 4f$, as well as $4f \rightarrow 5d$ transitions. For the middle Ln, both excitation series even energetically overlap.^[6] The reasons for the extraordinary optical properties of Ln-doped YF_3 , as introduced within the introduction (see chapter 1) lie within the ionic bonding nature, while keeping the unpaired 4f-electrons localized at the Ln(III) centers. This creates a large number of $4f^{N_{4f}}$ states, which allows a Kondo-like resonance of practically no barrier.^[6]

Within the Ln-series, the shells of 4f, 5d, and 6s might be only partially filled. However, due to their different n , their $\langle \hat{r} \rangle_{n,l}$ are quite different and thus, they couple only relatively weakly with each other.^[8] This means that correlation between these partially filled shells is neglectable. The effects by correlation and those by relativity are often of opposite sign, which gives rise to a lucky, partial error cancellation with relativity being the dominant effect.^[8] While correlation favors a higher 4f-occupation, relativity destabilizes the 4f-energy levels and thus, rather favors an occupation of e.g., the 6s-level.^[8]

The computational code of VASP used within paper **B.1–B.2**, offers two PAW potentials for Ho.^[98] The 4f-in-core PAW potential applied for the atomic structures expands nine electrons in plane waves. This would correspond to a nominal $5p^6 6s^2 5d^1$ valence configuration. This allows chemical bonds to form with the outmost and most reactive 5d and 6s-shells, while the 5p-shell forms the correct valence for a triply oxidized Ho(III). The fact, that the 5s-shell, which has a large radial overlap with the 5p-valence shell (see 5s and 5p in Fig. 2.5 b), is only treated within the PAW potential, might be problematic for some cases. It should be noted that the $4f^{10}$ included within the PAW potential possesses the correct N_{4f} for Ho(III). However, it is incorrect for Ho(0), Ho(I), and Ho(II), which electron configurations are measured to be $[\text{Xe}] 6s^2 4f^{11}$, $[\text{Xe}] 6s^1 4f^{11}$, and $[\text{Xe}] 4f^{11}$, respectively.^[168] The studied Ho-species within this work was HoF_3 , which is very ionic, making the Ho(III)-optimized 4f-in-core potential a valid approximation.

Nonetheless, the 4f-in-valence PAW potential was also tested within paper **B.1**. It expands 21 electrons explicitly in plane waves corresponding to a nominal valence configuration of $4f^{10} 5s^2 5p^6 6s^2 5d^1$. This 4f-in-valence PAW potential retains the flexibility of the 4f-shell, as might be required for the formal Ho(II) centers located at the studied substoichiometric surfaces. However, in analogy to the radial overlap of 5s and 5p-shells, describing the 4f-shell without the other shells of $n = 4$ might lead to an incorrect description of the 4f-shell (see 4d and 4f in Fig. 2.5 b). However, this 4f-in-valence PAW potential avoids the need of methods capturing the resulting correlation between these $n = 4$ shells overlapping with the 4f-shell.^[8]

3. Publications

3.1. Paper A

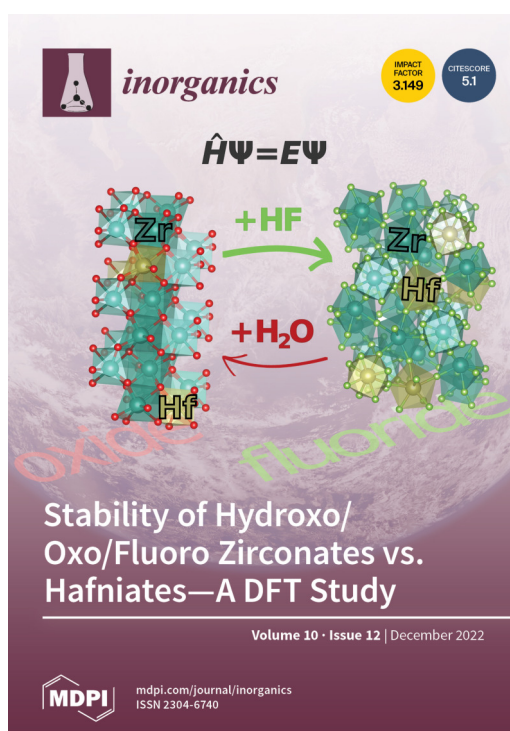
"Stability of Hydroxo/Oxo/Fluoro Zirconates vs. Hafnates—A DFT Study"

J. Anders, F. Göritz, A. Loges, T. John, B. Paulus, *Inorganics*, **2022**, 10, 259.

DOI: 10.3390/inorganics10120259

URL: <https://doi.org/10.3390/inorganics10120259>

Creative commons license: <https://creativecommons.org/licenses/by/4.0/>




coverpage of *inorganics* issue 12 featuring paper **A**.

Contributions:

The conceptualization was done by Jennifer Anders (J.A.) and Beate Paulus (B.P.) under intensive discussion with Anselm Loges (A.L.), Timm John (T.J.). The formal analysis was done by Fabian Göritz (F.G.) and J.A. Funding and resources acquisition was done by B.P. Investigations were done by F.G. and J.A. Supervision was done by J.A. and B.P. Validation was done by J.A. Visualization was done by F.G. The original draft was written by, J.A. and F.G. Review writing and editing was done by J.A., F.G., A.L., T.J. and B.P.

Article

Stability of Hydroxo/Oxo/Fluoro Zirconates vs. Hafnates—A DFT Study

Jennifer Anders ^{1,*} , Fabian Göritz ¹ , Anselm Loges ² , Timm John ² and Beate Paulus ¹¹ Institute for Chemistry and Biochemistry, Freie Universität Berlin, Arnimallee 22, 14195 Berlin, Germany² Institute for Geological Sciences, Freie Universität Berlin, Malteserstr. 74–100, 12249 Berlin, Germany

* Correspondence: jennifer.anders@fu-berlin.de

Abstract: We performed density functional theory (DFT) calculations on binary and ternary oxo/fluoro crystals of the geochemical twin pair zirconium and hafnium to evaluate and compare their stabilities. This is the first DFT study on bulk ZrF₄ or HfF₄, as well as on a hypothetical ZrOF₂ or HfOF₂ bulk crystal. For α -MO₂, β -MF₄ and MOF₂, we have found significantly higher cohesive energies for the respective hafnium species. This suggests a considerable gap in affinity toward fluorine and oxygen between the twin pair in the solid state. In agreement with experimental findings, this gap is slightly more pronounced for fluorine. This study is also the first to evaluate the theoretical, endothermic mono-hydroxylation of the respective fluorides or oxyfluorides to model the difference in affinity toward fluoride versus hydroxide. For these, we could also find a slight energetic preference for the hafnium compound.

Keywords: geochemical twins; HFSE; DFT; baddeleyite; fluorozirconate; fluorohafnate; oxofluoride



Citation: Anders, J.; Göritz, F.; Loges, A.; John, T.; Paulus, B. Stability of Hydroxo/Oxo/Fluoro Zirconates vs. Hafnates—A DFT Study. *Inorganics* **2022**, *10*, 259. <https://doi.org/10.3390/inorganics10120259>

Academic Editor: Richard Dronskowski

Received: 31 October 2022

Accepted: 5 December 2022

Published: 13 December 2022

Publisher's Note: MDPI stays neutral with regard to jurisdictional claims in published maps and institutional affiliations.



Copyright: © 2022 by the authors. Licensee MDPI, Basel, Switzerland. This article is an open access article distributed under the terms and conditions of the Creative Commons Attribution (CC BY) license (<https://creativecommons.org/licenses/by/4.0/>).

1. Introduction

1.1. Motivation

In this paper, we investigate the subtle differences between zirconium and hafnium in the solid state. Both elements form a so-called geochemical twin pair because they behave almost identically throughout most geochemical processes. This twin behavior is a simple result of the equivalent charge to radius ratio of the respective ions in their single stable oxidation state of +IV. Measured in eightfold coordination, as they occur in pure fluorides, the ionic radii are nearly identical with 0.84 Å for Zr to 0.83 Å for Hf [1]. According to these small ionic radii, combined with the high charge, both elements belong to the economically interesting class of high field strength elements (HFSE). Since the past decade, zirconia (ZrO₂) and the analogous hafnia (HfO₂) attract a lot of attention due to their ferroelectricity, which is well reviewed by Park et al. [2]. As fluorides, both elements are widely applied in optics based on ZBLAN (Zr, Ba, La, Al, Na) fluoride glasses. Depending on the glass composition, the optical window can reach from deep IR to near UV. As ultra thin fibers, ZBLAN fluoride glasses are a well-suited successor of silica in photonics, promising a much larger transmission bandwidth [3,4]. While the main component of these glasses is typically ZrF₄, some specialized ones use the analogous HfF₄. Doped with cerium, the latter shows excellent scintillating properties [5–7]. A small impurity of the respective other twin element can usually be found in all these Zr/Hf-based materials. The nuclear industry demands extremely pure, and thus very well separated, Zr/Hf because of their opposite thermal neutron-adsorption cross sections. Zr is used for materials with minimal neutron interactions, such as, e.g., for cladding of the nuclear fuel rods. The high absorption of Hf, on the other hand, makes it an ideal material for nuclear control rods [8].

Due to their twin character, fractionating Hf from Zr is not a trivial task. The behavior of ions is typically controlled primarily by their charge and radius (CHARAC) in natural geochemical systems. Therefore, and as a result of their identical charge and nearly identical

radius, Zr and Hf ions usually do not fractionate from each other in nature and are typically found in ratios close to their chondritic ratio of 37:1 in most rocks and minerals [9–11]. The rare exceptions to this rule are fluoride-rich hydrothermal veins and fluoride-rich pegmatitic melts, where much lower Zr:Hf ratios of about 2:1 have been observed [9,12–14]. It has been suggested that the cause for this Hf-enrichment is a slightly higher affinity of Hf to halogens compared to Zr [9,11,15]. The hafnium to halogen bond is generally a bit stronger than the respective zirconium to halogen bond (e.g., 240 meV for the diatomic Zr/Hf fluorides) [16,17]. Computationally, it has also been shown that the chemical adsorption of gaseous hydrogen fluoride (HF) onto the HfO₂ (111) surface is 150–210 meV stronger than for ZrO₂ [18]. On an industrial scale, the difference in halogen affinity is exploited to separate Zr/Hf, as the process relies on the isolation of the respective oxochlorides [8,19]. Another pathway to obtain the highest purities uses the fluorides (MF₄) formed from the oxides in anhydrous HF (aHF) gas according to reaction (1) [20]. Note that this reaction involves oxofluoride intermediates in varying stoichiometry. These will be further discussed in the following Section 1.2.



Furthermore, Hf also shows a higher affinity for fluorine in the liquid phase as suggested by solubility experiments in aqueous HF (aq. HF) of low concentrations (1–200 mM) [15,21]. Already at these low F-activities, only the di-fluoro HfF₂(OH)₂ complex is found for Hf, while Zr forms mono-fluoro ZrF(OH)₃, as well as di-fluoro ZrF₂(OH)₂ compounds. At a concentration of 1 molal aq. HF and elevated temperatures of 350 °C, no difference between Zr and Hf in principal complex stoichiometry was observed using X-ray spectroscopic methods, but instead slightly shorter average metal-ligand distances for the Hf complexes compared to those of Zr [22]. This may also suggest a stronger bond of Hf with fluoride. While the complex stoichiometry could not be directly observed, previous studies have shown that electrically neutral difluoro-dihydroxy complexes of Zr and Hf can be expected under these conditions [21,23].

We aim to contribute further insight on what sets the interaction of Zr/Hf to fluorine apart from Zr/Hf to oxygen and, therefore, provide a quantum-chemically-based hypothesis on the observed different solubility by solid Zr/HfO₂ in aq. HF. This requires, in a first step, to understand the respective solids. Consequently, this project will first contrast the known Zr/HfO₂ and Zr/HfF₄ to compare to the hypothetical, mixed Zr/HfOF₂. In a second step, we broaden our comparison to hydroxylation products of the respective mixed and pure fluorides. In nature, neither crystalline Zr or Hf hydroxides are known, nor simple compounds that incorporate any OH-group within the lattice. Therefore, we chose the mono-hydroxylated unit cells as a crystalline model with low OH concentration.

1.2. Known Crystal Structures

In nature, Zr is usually found as zircon (ZrSiO₄) and to a lesser extent as the binary oxide in baddeleyite (monoclinic α-ZrO₂) or zirconia (tetragonal β-ZrO₂) structure. Its less abundant twin element Hf is found as an impurity within these minerals. At ambient conditions, the oxides crystallize in the baddeleyite-structure (P2₁/c, SG 14), which is the stable phase up to (ZrO₂) or 2100 °C or 11 GPa (HfO₂), respectively [24–27]. There exist many density functional theory (DFT) studies on the phase transitions and other properties of bulk ZrO₂ and HfO₂ at the LDA [28–35] and/or GGA [18,30,31,36–43] level (see Table S1 for a full overview). However, on the corresponding binary fluorides, only a single computational study was found, which performed the ab initio perturbed ion method and configuration interaction with single excitations on the crystal clusters [44]. This leaves this study as the first DFT evaluation on fluorozirconate or fluorohafniate. β-ZrF₄ or β-HfF₄ are also monoclinic in their low temperature phase (C2/c, SG 15), which are stable up to 910 °C [45–48]. When increasing complexity by forming tertiary compounds as M(IV)-oxofluorides, no computational studies could be found and also the availability of measured crystal structures decreases significantly for Zr, while none have

been published for Hf. Two experimental crystal structures with different compositions can be found for $Zr_pO_qF_r$: a cubic ReO_3 -structured $ZrO_{0.67}F_{2.66}$ ($Pm\bar{3}m$, SG 221) [49,50] and an orthorhombic $Zr_7O_{8.79}F_{10.21}$ ($Pbam$, SG 55) [51]. It should be noted that neither of them could resolve the O/F positions unambiguously. Furthermore, the off-integer anion content suggests a considerable number of defects within the crystal structure. Recently, the Hf-analog with the approximate stoichiometry of $Hf_7O_9F_{10}$ has been found [52]. Again, they found disordered anions. Unfortunately, they could not refine the unit cell parameters distinctly, leaving the crystal structure unresolved. Despite their widely unknown crystal structures, a series of oxofluorides is described as intermediates between the two binary compounds (see reaction (1)). By XRD, the presence of zirconium oxofluorides in three further stoichiometries could be detected: $Zr_3O_2F_8$, $ZrO_{0.33}F_{3.33}$, $ZrO_{1.3}F_{1.4}$, but only one hafnium oxofluoride as Hf_2OF_6 [20]. Earlier, $Hf_3O_2F_8$ has also been reported [53]. Unfortunately, no crystal structures are published for any of these intermediates. Not only the measured, but also the calculated crystal structures, are rare for $M_pO_qF_r$. Even the comprehensive database of the Materials Project only provides three Zr and two Hf species [54]. However, none of them follow a stoichiometry to yield the desired, simple electronic structure of M(IV), O(−II) and F(−I). Most of them are instead best described as O_2 or O_3 molecules enclosed between 2D-sheets of crystalline metal fluorides. Expanding the scope further to the hydroxides such as, e.g., $Zr/Hf(OH)_4$, the same problem of unstable crystal structures is encountered. Despite F and OH being isoelectronic, their affinity to water is very different. Thus, in contrast to the crystalline fluorides, the hydroxides form gels. Only if carefully prepared from crystalline, tetragonal $[ZrOCl_2]$ ($P\bar{4}2_1c$, SG 114), its basic structural unit of double oxygen-bridged zirconium squares may be retained to some extent. In the formed $[Zr_4(OH)_8(H_2O)_{16}]Cl_8$, the neighboring tetramer units are double bridged by a pair of hydroxides [55–57]. However, according to the largest inorganic crystal structure database (ICSD) [58], actual crystalline structures built from the elements Zr, O, F, and H are exclusively made from ZrF_i lattices with crystal water as $[ZrF_4 \cdot (H_2O)_j]$ with $j = \{1, 3\}$, or if $i = \{5, 6\}$ with incorporation of oxonium ions [59–64]. No simple crystal structures are known that incorporate hydroxides into the lattice. For this study, we therefore build hypothetical crystalline oxofluorides $Zr/HfOF_2$, as well as hypothetical, mono-hydroxylated species from these structures, as well as from the stable Zr/HfF_4 . In the search for a suitable model crystal structure with resolved O/F positions and integer stoichiometry for the hypothetical crystalline oxofluoride $M_p^{IV}O_qF_r$, we chose monoclinic $TeOF_2$ ($P2_1$, SG 4) [65]. This choice is based on its stoichiometry and positions of the anions, which precisely describe local metal(IV) environments. In addition, its rather small unit cell is composed of four formula units with a corresponding unit cell volume per formula unit and lays exactly in between the narrow 1.6 \AA^3 gap of ZrF_4 and HfF_4 . We therefore consider the crystal structure of $TeOF_2$ as the most-fitting approximation to the hypothetical $Zr/HfOF_2$, despite the remaining lone-pair of Te(IV), which also contributes a 0.25 \AA bigger ionic radius compared to Zr/Hf when measured at sixfold coordination as present in $TeOF_2$ [1].

2. Computational Details

All periodic density functional theory (DFT) calculations have been performed with the Vienna Ab Initio Simulation Package (VASP, software version 5.4.4) [66] running on the supercomputer cluster HLRN in Göttingen, Germany. As the exchange-correlation functional, the generalized gradient approximation (GGA) by Perdew–Burke–Ernzerhof (PBE) has been applied [67]. A published, elaborate benchmark with different functionals (PBE, PBEsol, RPBE, and TPSS) with or without D2 or D3 dispersion correction [68,69] and/or Hubbard-type correction onto Zr-4d revealed that plain PBE performs well on the geometrical data of monoclinic ZrO_2 . It also showed that applying a Hubbard-type correction onto the conduction band (CB) forming Zr-4d does not improve the results [40]. A detailed discussion on the choice of functional is given in the SI [70–73]. Another paper on ZrO_2 and HfO_2 found that the effect of dispersion is also negligible for the

surface adsorption of two HF molecules when comparing PBE with or without dispersion correction according to the Tkatchenko–Scheffler scheme [18,74]. Therefore, we did not apply a dispersion correction for our bulk calculations of the ionic solids. Core electrons have been treated by the projector-augmented wave (PAW) method [75,76] using the VASP-inherent potential files O_h, F_h, Zr_sv, Te, and Hf_sv leaving 6, 7, 12, 6, and 12 valence electrons, respectively. The valence electrons have been described by plane waves to a kinetic energy cut-off of 773 eV. For electron smearing, Gaussian smearing with a width of 0.2 eV has been used for all ionic solids and molecular calculations. For the pure metals of Zr and Hf, a convergence test with second-order Methfessel–Paxton smearing with widths of 0.05–0.15 eV in 0.05 eV steps has been completed. A width of 0.05 eV minimized the difference between total energy and free energy for both metals. For solids of ZrO₂, HfO₂, ZrF₄, and HfF₄, the *k*-grid convergence has been tested for Monkhorst–Pack *k*-grids of $x \times x \times x$ with $x = \{1, 2, 3, 4, 5, 7, 9\}$. Convergence within 1.5 meV per unit cell in respect to the finest grid was found at $x = 4$ for all compounds. This *k*-grid was then applied on all ionic solids. The pure metals of Zr and Hf have been tested for *k*-grids with $x = \{1, 2, 3, 4, 5, 7, 9, 15, 17\}$ yielding convergence within 2.5 meV per unit cell at $x = 15$ with respect to the finest grid. The molecular calculations of H₂, HF, H₂O, O₂, and F₂ have been set up in a cubic box of 25 Å side length at the Γ -point only to avoid artificial intermolecular interactions. The structural relaxations of all solids have been conducted with the conjugate-gradient algorithm in three subsequent steps with increasing degrees of freedom. At first, only the atomic positions were relaxed. This was followed by the additional relaxation of the unit cell vectors, while keeping the volume fixed. In the third step, the positions, unit cell vectors, and unit cell volume were allowed to adapt simultaneously. The initial start structures for MF₄ [45,46], as well as TeOF₂ [65], were taken from the experimental crystal structures discussed above in Section 1.2, while the MO₂ were initiated from the PW91-relaxed structure [41]. The pure metals started from their respective experimental, hexagonal crystal structure (*P*₆₃/*mmc*, SG 194) [77,78]. To aid convergence, spin polarization was allowed and/or the ionic step width (POTIM) reduced from its default of 0.5 to 0.1 Å if needed. The accurate precision setting was used for all calculations. Geometry relaxations were performed with a self-consistent field (SCF) convergence criteria of 0.01 meV per unit cell and 0.1 meV per unit cell for the difference in total energy between two ionic steps. Final total energies and Bader charges were generated with an SCF criteria of 0.001 meV per unit cell. The atom-in-molecule-derived Bader charges were obtained by the algorithm of the Henkelman group [79–83]. Structures were built with the Python package pymatgen [84] and visualized in VESTA [85].

3. Results and Discussion

3.1. Oxo/Oxofluoro/Fluoro Crystals of Zr vs. Hf

3.1.1. Crystal Structures

We calculated the crystal structures of the geochemical twin elements Zr/Hf as binary oxides and fluorides, as well as hypothetical 1:2 oxofluorides. Table 1 shows their relaxed conventional unit cell parameters with formula units, lattice vector lengths, off-diagonal angle, and corresponding volumes. For the binary fluorides, there also exists a smaller, primitive unit cell of only six formula units. Thus, all calculations were conducted on the symmetry-translated primitive cells.

Table 1 shows good agreement between the relaxed unit cell parameters of the binary oxides and fluorides and the experimental literature data. The deviation of the unit cell vector length was less than 0.16 Å or 1.3%. The absolute and relative deviations from the experiment for all binary compounds are listed in the SI (see Table S4). For ZrO₂ and HfO₂, our PBE (cutoff energy of 773 eV) relaxed structures represent the crystal structure even better than the previously reported PB91 results (cutoff energy of 495 eV), which were used as input structures [41]. In accordance with their geochemical twin character, ZrO₂ and HfO₂ share a practically equivalent structure, just as the respective fluorides ZrF₄ and HfF₄. The relaxed structures are shown in Figure 1. Within the oxides, all metal centers

are symmetry equivalent and coordinated by seven oxygen atoms, for which two non-symmetry equivalent positions exist. The fluorides contain two metal types, each eightfold coordinated. MF_4 contains seven non-symmetry equivalent fluorine positions. Although MO_2 and MF_4 show a high similarity between the respective Zr and Hf-species, the Hf bond lengths are a bit smaller than the respective Zr bonds. The relaxed Hf–O bond lengths are 2.04–2.23 Å vs. 2.05–2.27 Å for Zr–O. Note that the latter agree perfectly with the measured bond lengths [86]. Within the fluorides, the bond lengths are generally smaller, which goes along with a smaller difference between Zr/Hf. While 2.03–2.13 Å are found for the relaxed Hf–F bonds, the range of bond lengths is increased by only 0.02 Å for Zr–F with 2.05–2.15 Å. It should be noted that the difference of Zr–F to the experimental bond lengths of 2.03–2.18 Å is of the same order of magnitude [45] (see Tables S5 and S6 for all respective bond lengths).

Table 1. Relaxed unit cell parameters vs. experimental (lit. exp.) and calculated literature (lit. PB91) values. Given are the number of formula units per unit cell ($N_{\text{f.u.}}$), unit cell vector lengths (a, b, c), unit cell volume (V), unit cell volume per formula unit ($V_{\text{f.u.}}$), and the non-orthogonal angle (β); note that $\alpha = \gamma = 90^\circ$.

Compound	$N_{\text{f.u.}}$	a (Å)	b (Å)	c (Å)	V (Å ³)	$V_{\text{f.u.}}$ (Å ³)	β (°)
ZrO ₂	4	5.154	5.224	5.332	141.56	35.39	99.55
lit. PB91 [41]	4	5.197	5.279	5.349	144.74	36.18	99.53
lit. exp. [86]	4	5.150	5.212	5.317	140.88	35.22	99.23
HfO ₂	4	5.105	5.182	5.277	137.64	34.41	99.54
lit. PB91 [41]	4	5.128	5.191	5.297	139.25	34.81	99.71
lit. exp. [87]	4	5.114	5.168	5.290	138.03	34.51	99.21
TeOF ₂	4	5.212	8.025	5.485	227.81	56.95	96.82
lit. exp. [65]	4	5.307	8.289	5.513	241.09	60.27	96.22
ZrOF ₂	4	5.305	6.879	5.318	193.88	48.47	92.63
HfOF ₂	4	5.265	6.982	5.388	197.74	49.44	93.22
ZrF ₄	12	11.694	9.889	7.660	710.40	59.20	126.68
lit. exp. [45]	12	11.845	9.930	7.730	732.53	61.04	126.32
HfF ₄	12	11.609	9.816	7.600	694.85	57.90	126.65
lit. exp. [46]	12	11.725	9.869	7.636	713.48	59.46	126.15

To investigate a simple hypothetical mixed oxofluoride, the crystal structure for TeOF₂ was taken and the metal centers replaced with Zr and Hf, respectively [65]. The Te-structure was selected because of its relatively simple, well-suited crystal structure (see discussion in Section 1.2) and the +IV oxidation state of its metal centers. However, as a p-block element, Te(IV) is left with a 5s-lone pair that leads to a six-fold coordination in the 1:2 mixed oxofluoride, while Zr(IV)/Hf(IV) have a formally vacant valence shell and can assume a higher coordination. Hence, six-fold coordinated Te(IV) has an ionic radius of 0.97 Å, while a significantly smaller radius can be found for Zr(IV) or Hf(IV) with 0.72 Å or 0.71 Å at six-fold and 0.78 Å or 0.76 Å at seven-fold coordination, respectively [1]. The missing lone pair and the overall smaller ionic radii explain that the unit cell of Zr/HfOF₂ is significantly smaller in the b -direction, more densely packed than TeOF₂ and with a β -angle closer to 90°. Yet, the resulting structure retains the same low-symmetry space group ($P2_1$, SG 4). The relaxed MOF₂ unit cells are visualized in Figure 2.

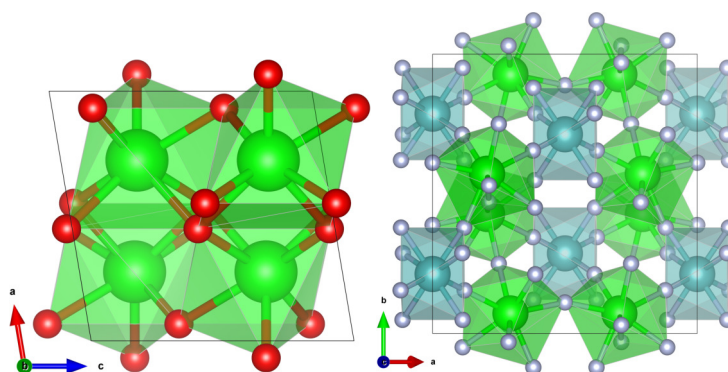


Figure 1. Visualized relaxed structures of ZrO_2 (left) and ZrF_4 (right). Structures of HfO_2 and HfF_4 closely resemble the depicted ones in geometry, but with slightly shorter bonds (see Tables S5 and S6). Atoms are colored according to: Zr in green/teal, O in red, F in gray. The fluoride structure has two different metal atoms as basis, shown in teal (center A) and green (center B), further explained in Figure 3 left. Unit cell parameters are given in Table 1.

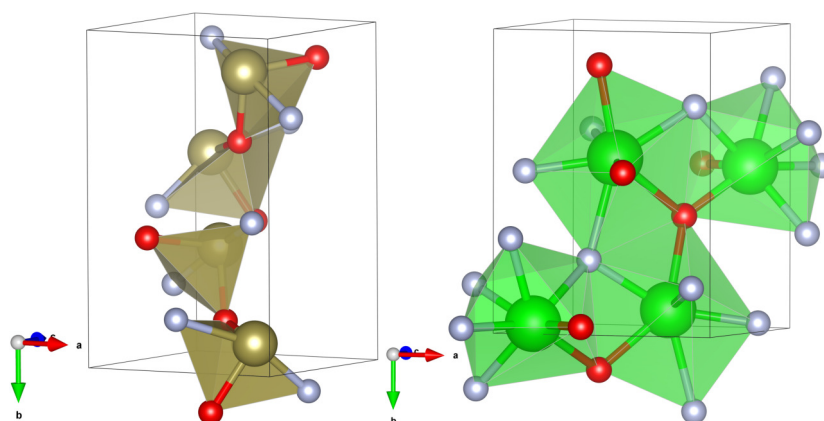


Figure 2. Relaxed unit cell of $TeOF_2$ with Te in brown (left) and $ZrOF_2$ (right). The $HfOF_2$ structure looks equivalent to the Zr-species. Unit cell parameters are given in Table 1.

Each $Zr/HfOF_2$ coordination polyhedron has a seven-fold coordinated metal center of two different types. One center is coordinated to five fluorine and two oxygen atoms, while the other center is coordinated to four fluorine and three oxygen atoms. As seen in Figure 2 (right), one fluorine and one oxygen atom form triple-coordinated bridges that connect the four polyhedra with each other. The unit cell parameters of the input structure $TeOF_2$ and $Zr/HfOF_2$ are shown in Table 1. When comparing the $V_{f.u.}$ listed in Table 1, one finds the binary fluorides to be larger than the binary oxides, in accordance with the two additional atoms per formula unit. The ternary mixed oxofluorides also contain one atom less per formula unit than the fluorides. However, when comparing the experimental $V_{f.u.}$, one finds the original $TeOF_2$ neatly positioned between HfF_4 and ZrF_4 . On the other hand, this does not hold for the relaxed $TeOF_2$, which shrinks by 3 \AA^3 . While the $V_{f.u.}$ of the relaxed HfF_4 and ZrF_4 is reduced by less than 2 \AA^3 , both hypothetical $HfOF_2$ and $ZrOF_2$ structures shrink by as much as 8 \AA^3 compared to the relaxed parent Te-structure for reasons discussed above. We found that their relaxed $V_{f.u.}$ agree very well with the respective mean of MO_2 and MF_4 . However, for the oxides and fluorides, we find $\Delta V_{f.u.}(Hf - Zr) = -1 \text{ \AA}^3$. We currently have no explanation why the volume of MOF_2 does not follow this otherwise observed trend of smaller Hf than Zr compounds. Instead, $HfOF_2$ is 1 \AA^3 bigger in $V_{f.u.}$ than its Zr-counterpart.

3.1.2. Reaction Energies

To analyze the stability of the metal oxides/fluorides and oxofluorides, the cohesive energies (ΔE_{coh}) listed in Table 2 have been calculated using the electronic energies of the relaxed structures at 0 K.

Table 2. Calculated PBE bulk solid-state cohesive energies (ΔE_{coh}) per formula unit (f.u.) for formations of different Zr/Hf-species of oxides (I), fluorides (II), and oxofluorides (III). Below, the literature values [18] for the respective bulk solid-state to gas-phase reactions (s→g) are given.

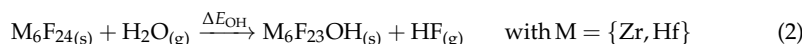
Nr.	Solid-State Reactions			ΔE_{coh} (eV/f.u.)	
				M = Zr	M = Hf
(I _a)	$M_{(s)} + O_{2(g)}$	→	$MO_{2(s)}$	−19.279	−19.545
(I _b)	$M_{(s)} + 2 H_{2}O_{(g)}$	→	$MO_{2(s)} + 2 H_{2(g)}$	−5.274	−5.540
(II _a)	$M_{(s)} + 2 F_{2(g)}$	→	$MF_{4(s)}$	−18.439	−18.718
(II _b)	$M_{(s)} + 4 HF_{(g)}$	→	$MF_{4(s)} + 2 H_{2(g)}$	−7.448	−7.727
(II _c)	$MO_{2(s)} + 4 HF_{(g)}$	→	$MF_{4(s)} + 2 H_{2}O_{(g)}$	−2.174	−2.188
(II _d)	$MOF_{2(s)} + 2 HF_{(g)}$	→	$MF_{4(s)} + H_{2}O_{(g)}$	−1.283	−1.302
(III _a)	$M_{(s)} + H_{2}O_{(g)} + 2 HF_{(g)}$	→	$MOF_{2(s)} + 2 H_{2(g)}$	−6.165	−6.425
(III _b)	$MO_{2(s)} + F_{2(g)}$	→	$MOF_{2(s)} + \frac{1}{2}O_{2(g)}$	+0.616	+0.622
(III _c)	$MO_{2(s)} + 2 HF_{(g)}$	→	$MOF_{2(s)} + H_{2}O_{(g)}$	−0.891	−0.885
lit. PBE solid to gas reactions [18]					
(II _c ^{s→g})	$MO_{2(s)} + 4 HF_{(g)}$	→	$MF_{4(g)} + 2 H_{2}O_{(g)}$	−1.14	−0.91
(III _c ^{s→g})	$MO_{2(s)} + 2 HF_{(g)}$	→	$MOF_{2(g)} + H_{2}O_{(g)}$	+2.96	+3.87

A previous computational surface study has shown that the Zr to Hf difference for bulk reactants of ZrO₂ and HfO₂ is practically equivalent when comparing the purely electronic ΔE_{coh} , or when comparing the zero point energy (ZPE) corrected free energies at 500 K ($\Delta G^{500\text{K}}$) including the volume work, the temperature-dependent enthalpic terms, as well as translational entropy [18]. The same study also found that for the corresponding (111) surfaces, a small difference between $\Delta E_{\text{coh}}(\text{Zr-Hf})$ and $\Delta G^{500\text{K}}(\text{Zr-Hf})$ occurs due to the additional surface entropy. However, even for the surfaces, this difference is one order of magnitude smaller than $\Delta E_{\text{coh}}(\text{Zr-Hf})$ itself. Published phonon spectra of ZrO₂ and HfO₂ show that their ZPE differ by as little as 0–3 meV per formula unit [33]. Measurements and calculations have shown that the shorter bond distances and thus higher force constants of Hf–O compared to Zr–O counterbalance the mass increase of the cation [33,88]. No phonon calculations exists for ZrF₄ and HfF₄. However, we expect the even stronger mass increase per single M–F bond to be counterbalanced by the additional anion-dominated vibrations with shorter interatomic Hf–F than Zr–F distances (see Section S6 in the SI for a more detailed discussion) [89]. Consequently, we consider the purely electronic quantity of ΔE_{coh} sufficient to evaluate the difference between the respective bulk Zr/Hf-compounds. The values from Table 2 show that hafnium tends to have a stronger affinity towards oxygen and fluorine, as all cohesive energies of solid-state reactions I–III are stronger for the Hf-species than for the corresponding Zr compound. The energetic difference of $\Delta E_{\text{coh}}(\text{Zr-Hf})$ is 266 meV/f.u. for the binary oxides (see I_{a-b}). For the binary fluorides, it is 279 meV/f.u. (see II_{a-b}), which means that the Zr vs. Hf difference in the fluorides is by a small amount of 13 meV/f.u. stronger than in oxides. That this value is reproduced within 1 meV/f.u. when forming from the elements or the binary oxides, indicates that electronic energies of the pure metals, as well as the ionic binary compounds are described well enough by the applied computational setup. The hypothetical 1:2 mixed oxofluoride shows similar-sized $\Delta E_{\text{coh}}(\text{Zr-Hf})$ of 260 meV/f.u. when formed from the elements (see III_a). It should be noted that this Zr vs. Hf difference is not somewhere between the binary oxide or fluoride. Instead, it is the smallest and 6 meV/f.u. less than for the oxide. This might correlate with the odd volume trend of MOF₂ discussed above. When

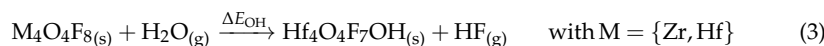
comparing the solid-state reactions II_c and III_c with the respective published bulk reactant to molecular gas-phase product reactions $\text{II}_c^{s \rightarrow g}$ and $\text{III}_c^{s \rightarrow g}$ [18], one finds the opposite Zr vs. Hf trend. In opposition to the aforementioned trend, the formation of molecular $\text{HfF}_4(g)$ is about 230 meV/f.u. less favored than for the respective $\text{ZrF}_4(g)$ (see $\text{II}_c^{s \rightarrow g}$). Even more significant is the deviation in $\Delta E_{\text{coh.}}(\text{Zr-Hf})$ for the formation of molecular $\text{HfOF}_2(g)$ (see $\text{III}_c^{s \rightarrow g}$). Here, the formation of $\text{MOF}_2(g)$ is by about 910 meV/f.u. more endothermic for the Hf-species. Accordingly, the stability of Zr and Hf compounds has to be reversed for the molecular products, for reasons that remain unclear up to now. It seems at hand that the missing ZPE correction significantly alters the gap between the two elements of different mass. On the contrary, almost the same values are obtained for the ZPE-corrected $\Delta G^{500\text{K}}(\text{Zr-Hf})$ with ca. 240 meV/f.u. ($\text{MF}_4(g)$) and 910 meV/f.u. ($\text{MOF}_2(g)$), respectively. It may be speculated whether the higher coordination of the metal center or the ligands play a further role. To investigate whether this inconsistency between bulk to bulk and bulk to gas phase reactions is caused by the gas-phase products, we performed test gas-phase calculations. Mullins et al. calculated their gas-phase ZPE with Turbomole/PBE/def-TZVPP. We performed ORCA [90]/PBE/def2-TZVP [91] test calculations with the default effective core potentials [92] or with the ZORA Hamiltonian [93,94] on all electrons. We find that only in the latter, the correct behavior of smaller Hf-F than Zr-F bond distances is reproduced (see Table S8 in the SI). As a consequence, we raise the question of whether a scalar relativistic treatment of HfF_4 or HfOF_2 is necessary to obtain the right gas-phase values. However, as this study focuses on the Zr/Hf differences within the crystal phase, we leave this question open for further studies.

3.2. Mono-Hydroxylated Oxofluoro/Fluoro Crystals of Zr vs. Hf

In the previous subsection, we compared the binary oxides and fluorides, as well as the mixed oxofluorides of Zr vs. Hf. Now, we expand the comparison to the hydroxyl group, isoelectronic to fluorine. As the pure hydroxides of Zr and Hf are too hygroscopic to form crystals, analyzing a theoretical, crystalline $\text{M}(\text{OH})_4$ is not meaningful. It is, however, plausible to consider the hydroxylation as a defect of the stable binary MO_2 or MF_4 . Within the case of oxides, each oxygen should be replaced by two hydroxyl groups to remain the metal oxidation state of +IV. This might alter the local crystal structure considerably. Moreover, since we are focusing on the differences in Zr vs. Hf affinities toward O vs. F, replacing O by OH is not target-aimed. Therefore, we only consider the substitution of F by OH. In this case, there is also no issue in generating the mono-hydroxylated species. In this theoretical substitution reaction (2), a single fluorine of the unit cell is substituted by a hydroxyl group.



Analogously, we also consider the mono-hydroxylation of the mixed oxofluorides according to reaction (3).



3.2.1. Crystal Structures

The respective relaxed unit cell parameters of the mono-hydroxylated products according to reaction (2) and (3) are summarized in Table 3. Note that only the most stable positional isomer product is given. Differences between these isomers are discussed in the following Section 3.2.2.

Table 3. Relaxed unit cell parameters for the mono-hydroxylated products. Given are the number of pseudo-formula units per unit cell when not differentiating between F and OH (“ $N_{f.u.}$ ”), unit cell vectors (a, b, c), unit cell volume (V), unit cell volume per pseudo-formula unit (“ $V_{f.u.}$ ”), and the non-orthogonal angles (β); note that all structures possess $P1$ symmetry.

Compound	$N_{f.u.}$	a (Å)	b (Å)	c (Å)	V (Å ³)	$V_{f.u.}$ (Å ³)	α (°)	β (°)	γ (°)
Zr ₆ F ₂₃ OH	6	7.649	7.666	7.681	355.54	59.26	117.43	80.48	117.02
Hf ₆ F ₂₃ OH	6	7.591	7.610	7.626	347.97	58.00	117.41	80.40	117.01
Zr ₄ O ₄ F ₇ OH	4	5.257	5.371	6.830	192.67	48.17	90.49	90.22	92.24
Hf ₄ O ₄ F ₇ OH	4	5.289	5.372	6.830	193.84	48.46	90.23	90.37	92.71

Table 3 also contains the number of pseudo-formula units per unit cell (“ $N_{f.u.}$ ”) and the resulting volume per pseudo-formula unit (“ $V_{f.u.}$ ”), which is obtained when not differentiating between the fluorine atoms and the hydroxyl group. We use these numbers to compare the volume of the mono-hydroxylated species to the respective crystalline reactants. Compared to the binary fluorides, $V_{f.u.}$ remains equivalent during mono-hydroxylation for both M₆F₂₃OH (see Table 1). Looking at the oxofluorides, both mono-hydroxylated species shrink a bit. However, while for Zr₄O₄F₇OH, this is only very marginally the case with 0.3 Å³, it is 1.0 Å³ for Hf₄O₄F₇OH. This may be connected to the unexpected large volume of HfOF₂, being bigger than the respective Zr-species by also 1.0 Å³, while the Hf-species are otherwise smaller by 1.0 Å³ (MO₂) or 1.3 Å³ (MF₄).

3.2.2. Reaction Energies and H-Bond Patterns

We use the electronic energy contribution (ΔE_{OH}) to reactions (2) and (3) as given in Table 4 as a measure to quantify the difference in affinity of the geochemical twins between fluorine and oxygen in the form of a hydroxyl group.

Table 4. Calculated electronic energy contribution (ΔE_{OH}) per unit cell (U.C.) for formations of mono-hydroxylated products according to reactions (2) or (3).

Nr.	Solid-State Reactions		ΔE_{OH} (eV/U.C.)		
			M = Zr	M = Hf	
(2)	M ₆ F _{24(s)} + H ₂ O(g)	→	M ₆ F ₂₃ OH(s) + HF(g)	+0.642	+0.628
(3)	M ₄ O ₄ F _{8(s)} + H ₂ O(g)	→	M ₄ O ₄ F ₇ OH(s) + HF(g)	+0.708	+0.649

The binary fluorides possess two non-symmetry-equivalent metal centers, labeled A and B, which are both coordinated by eight fluorine atoms. Seven non-symmetry-equivalent fluorine atoms exist (see Figure 3 left). Metal A is coordinated by fluorine positions 1–4, each twice. Metal B is coordinated by all seven fluorine positions, with only position 7 being doubly coordinated. Each two metal centers are connected via one bridging fluorine atom. A–B by fluorine 1 and B–B by fluorine 7, while A is not neighbored by another A. Mono-hydroxylation at any of these non-symmetry equivalent positions was considered. For positions 1–4 and 7, two starting M–O–H angles were tested.

The most stable conformation for each OH position is listed in Table 5. For both Zr and Hf, a hydroxylation at position 2 was found to yield the most stable reaction product. Its structure is visualized in Figure 4. However, the formation of the most stable mono-hydroxylated product according to reaction (2) was endothermic by about 0.6 eV for both metals. This is in line with the absence of the known crystal structures of Zr or Hf that actually incorporates OH (see Section 1.2). Nevertheless, already in this mono-hydroxylation of one out of 24 fluorine atoms, a small difference of 14 meV/U.C. in ΔE_{OH} was found between Zr₆F₂₃OH (642 meV/U.C.) and Hf₆F₂₃OH (628 meV/U.C.). This subtle energetic difference corresponds to 160 K. Practically the same energetic difference of 13 meV/f.u., favoring Hf over Zr, was found for the fluorination of the binary oxide MO₂ to MF₄ (see Table 2).

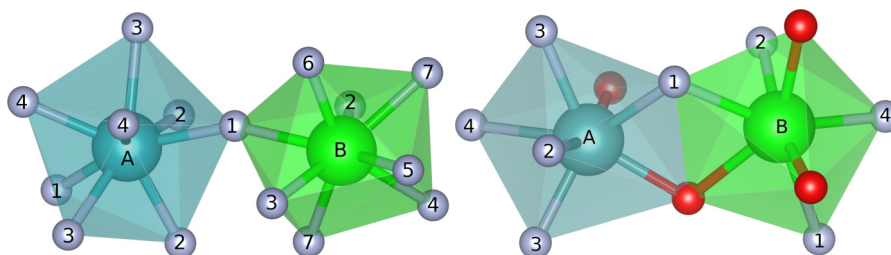


Figure 3. Visualization of the two distinct coordination polyhedrons A and B found in MF_4 (left) and MOF_2 (right). The non-symmetry equivalent fluorine atoms are labeled accordingly.

X-ray spectroscopic experiments at elevated temperatures in 1 molal aq. HF solutions have shown slightly lower average radial distances between central atom and the ligands for $\text{HfF}_2(\text{OH})_2 \cdot 2\text{H}_2\text{O}$, compared to $\text{ZrF}_2(\text{OH})_2 \cdot 2\text{H}_2\text{O}$, in a temperature window between 200 and 300 °C [22]. In light of the findings of the present contribution, this difference (e.g., 1.969 vs. 1.990 Å at 300 °C) can be interpreted to be the result of slightly tighter binding of the F and OH ligands to Hf than to Zr, or higher affinity of Hf for F.

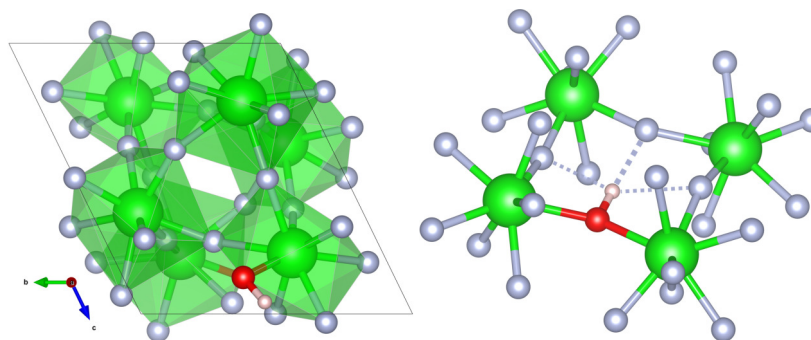


Figure 4. Relaxed unit cell of the most stable $\text{Zr}_6\text{F}_{23}\text{OH}$ structure obtained by mono-hydroxylation at position 2 (left). The $\text{Hf}_6\text{F}_{23}\text{OH}$ structure looks equivalent to the Zr species. The unit cell parameters are given in Table 3. The structural insert (right) shows the typical trifurcated H-bond with a main component (bold dashes) and two minor components (thin dashes). The structural H-bond data is listed in Table 5.

It was found in all calculated $\text{M}_6\text{F}_{23}\text{OH}$ structures that the hydroxyl group is oriented toward a polyhedral gap minimizing steric hindrance. Moreover, substitution of a fluorine atom by a hydroxyl group causes additional interaction between the added hydrogen and the surrounding fluorides by hydrogen bonding. The geometrical H-bond data is summarized in Table 5.

In all structures a trifurcated H-bond was observed. This means that one H atom establishes H-bond interactions to three different [95], yet closely located, F atoms inside a tetrameric Zr/Hf structure. A visualization of this structural motive is presented in Figure 4 (right). The major component faces the opposite side with a rather broad angle of 143–178°. The two minor components are located at the left and right. Their angles are much sharper with 99–119°. However, in most isomers, their distances are shorter than for the main component. We applied the H-bond classification introduced by Jeffrey to distinguish their main and minor components into strong, moderate, and weak H-bonds [96]. No single H-bonds may be regarded as strong and only the main component of some positional isomers classify as moderate H-bonds. All others are considered weak, as they either have a distance longer than 2.2 Å or an angle sharper than 130°. These are marked by parenthesis in Tables 5 and 6. Despite this general, non-solid-state-specific classification, the published mean O–H···F angles within transition metal compounds are 130–160° [97].

This is already much wider than for the respective other halogens. Compared to the mean O–H···F angles, the main H-bond components in Zr/Hf₆F₂₃OH already suggest the presence of rather strong O–H···F interactions for a crystalline compound. The lowest-in-energy structure (with position 2 OH-substituted) also possesses the shortest H-bond length for the main component with 2.09 Å for Zr or 2.10 Å for Hf, respectively. Additionally, it is nearly linear with an angle of 178° for Zr or 174° for Hf. This indicates a correlation with the overall energy of the structure. It should be noted that this is very close to the H-bond angle of 176° found within an infinite HF-chain [98,99]. Even though there are other positional isomers, with likewise wide angles of up to 178° for their major component, their H···F distances are much longer. Consequently, their total energies are also higher. It may be noted that R_{O-H} does not significantly change within any structure and also does so only marginally within the mono-hydroxylated oxofluorides of M₄O₄F₇OH (see Table 6).

Table 5. Position of hydroxylation (OH Pos.), energy difference per unit cell (U.C.) between the positional isomers with respect to the most stable isomer ($\Delta E_{Pos.}$), hydroxyl group bond length (R_{O-H}), H-bond length ($R_{H...F}$), and angle ($\angle_{O-H...F}$) within the mono-hydroxylated zirconium fluoride (top) or hafnium fluoride (bottom); H-bonds classified as weak by distance or angle are given in parenthesis.

Zr ₆ F ₂₃ OH				
OH Pos.	$\Delta E_{Pos.}$ (eV/U.C.)	R_{O-H} (Å)	$R_{H...F}$ (Å)	$\angle_{O-H...F}$ (°)
1	0.168	0.97	(2.53), (2.17), (2.05)	(164), (101), (107)
2	0	0.98	2.09, (2.07), (2.11)	178, (104), (107)
3	0.091	0.98	2.11, (2.16), (2.14)	154, (106), (103)
4	0.137	0.98	(2.46), (1.92), (1.86)	(176), (112), (110)
5	0.050	0.98	2.17, (2.04), (2.18)	167, (107), (106)
6	0.227	0.98	(2.59), (2.02), (1.84)	(169), (110), (116)
7	0.188	0.97	(2.46), (2.04), (1.98)	(143), (99), (107)
Hf ₆ F ₂₃ OH				
OH Pos.	$\Delta E_{Pos.}$ (eV/U.C.)	R_{O-H} (Å)	$R_{H...F}$ (Å)	$\angle_{O-H...F}$ (°)
1	0.174	0.97	2.20, (2.01), (2.18)	170, (109), (99)
2	0	0.97	2.10, (2.12), (2.04)	174, (106), (104)
3	0.091	0.97	2.11, (2.15), (2.13)	153, (106), (103)
4	0.156	0.97	(2.44), (1.91), (1.82)	(178), (112), (111)
5	0.049	0.98	2.17, (2.04), (2.17)	164, (107), (106)
6	0.273	0.98	(2.38), (2.07), (1.76)	(168), (104), (119)
7	0.093	0.97	2.11, (2.12), (2.15)	154, (104), (106)

Just as with the mono-hydroxylated fluorides, all non-symmetry-equivalent positions were considered (see Figure 3 right). The H-bonds have been analyzed likewise. In contrast to these, however, no reoccurring H-bond motive within all positional isomers was found. The positional isomers seem more diverse. What remains is the high similarity between the Zr and Hf-species. In the mono-hydroxylated oxofluorides, H-bonds can form toward oxygen or fluorine. As seen in Table 6, all positional isomers form only one moderate H-bond component. For all but isomer 3, the H-bond formed towards fluorine. The number of additional weak H-bond components varies between one (isomer 3), two (isomer 1, 4), and three (isomer 2). We note that the number of H-bond interactions does not seem to correlate with the energetic order of the positional isomers. Figure 5 (right) shows the H-bond pattern of the most stable isomer. Its trifurcated H-bond is not clearly separable into a single main component with two minor components. Despite only one O–H···F bond classifying as moderate, the absolute difference to the other O–H···F bond is not as large as in the mono-hydroxylated fluorides. Moreover, the next-stable isomer 3 is only 24 meV/U.C. less stable, but shows a very different H-bond pattern that only consists of two O–H···O interactions.

Table 6. Position of hydroxylation (OH Pos.), energy difference per unit cell (U.C.) between the positional isomers with respect to the most stable isomer ($\Delta E_{\text{Pos.}}$), hydroxyl group bond length ($R_{\text{O-H}}$), H-bond length ($R_{\text{H}\cdots\text{X}}$), and angle ($\angle_{\text{O-H}\cdots\text{X}}$) within the mono-hydroxylated zirconium oxofluoride (top) or hafnium oxofluoride (bottom); H-bonds classified as weak by distance or angle are given in parenthesis.

$\text{Zr}_4\text{O}_4\text{F}_7\text{OH}$						
OH Pos.	$\Delta E_{\text{Pos.}}$ (eV/U.C.)	$R_{\text{O-H}}$ (Å)	$R_{\text{H}\cdots\text{F}}$ (Å)	$\angle_{\text{O-H}\cdots\text{F}}$ (°)	$R_{\text{H}\cdots\text{O}}$ (Å)	$\angle_{\text{O-H}\cdots\text{O}}$ (°)
1	0	0.99	1.82, (2.21)	147.88, (130.59)	(2.98)	(137.81)
2	0.215	0.98	1.80, (2.29)	147.70, (99.21)	(2.20), (2.66)	(111.38), (100.00)
3	0.024	1.00	—	—	1.72, (2.50)	166.17, (115.74)
4	0.251	0.97	1.90, (2.33)	155.97, (98.93)	(2.78)	(95.05)
$\text{Hf}_4\text{O}_4\text{F}_7\text{OH}$						
OH Pos.	$\Delta E_{\text{Pos.}}$ (eV/U.C.)	$R_{\text{O-H}}$ (Å)	$R_{\text{H}\cdots\text{F}}$ (Å)	$\angle_{\text{O-H}\cdots\text{F}}$ (°)	$R_{\text{H}\cdots\text{O}}$ (Å)	$\angle_{\text{O-H}\cdots\text{O}}$ (°)
1	0	0.99	1.87, (2.37)	147.41, (131.32)	(2.91)	(140.75)
2	0.248	0.98	1.87, (2.32)	150.33, (96.44)	(2.21), (2.61)	(112.13), (107.42)
3	0.022	1.00	—	—	1.71, (2.56)	165.59, (116.82)
4	0.284	0.97	1.95, (2.28)	162.72, (98.86)	(2.46)	(91.40)

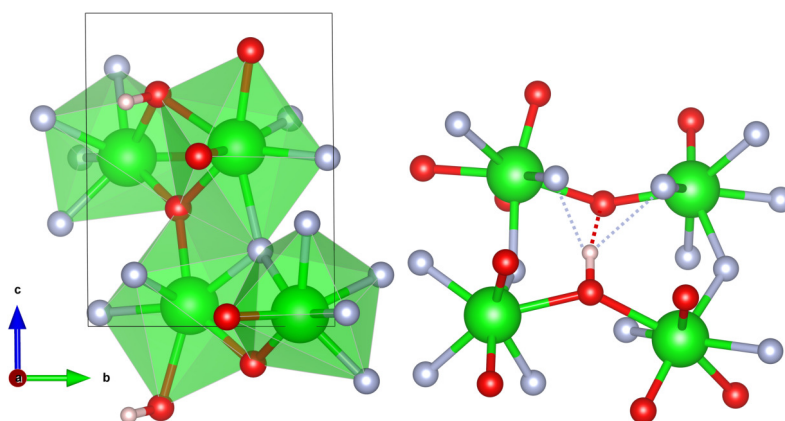


Figure 5. Relaxed unit cell of the most stable $\text{Zr}_4\text{O}_4\text{F}_7\text{OH}$ structure obtained by the mono-hydroxylation at position 1 (left). The $\text{M}_4\text{O}_4\text{F}_7\text{OH}$ structure looks practically equivalent to the Zr-species. The unit cell parameters are given in Table 3. The structural insert (right) shows the trifurcated H-bond with three components (dashes). The structural H-bond data is listed in Table 5.

3.3. Partial Charges

To compare the electronic structures, Bader charges were calculated. Within the MO_2 , we find -1.3 e for oxygen and 2.6 e for Zr, as well as Hf. In MF_4 , the metal centers were slightly more charged by 2.8 e, with -0.7 e for fluorine. This marginally more positive charge of the metal centers in the fluorides indicates a slightly higher ionic character for the metal-F-bond compared to the oxides. The situation is similar in the oxofluorides, but two slightly different charges of $-(1.2-1.3)$ e for oxygen and fluorine $-(0.7-0.8)$ e were found. The metal centers have a Bader charge of 2.7 e, which is equivalent to the mean value of metal charges within the pure oxide and fluoride. At this point, we already compare the mono-hydroxylated species for their partial charges. Within $\text{M}_6\text{F}_{23}\text{OH}$, we find -1.2 e for oxygen, -0.7 e for fluorine, 0.6 e for hydrogen, and 2.8 e for both Zr and Hf. For $\text{M}_4\text{O}_4\text{F}_7\text{OH}$, the Bader charges are varying a bit more, however they all range between $-(1.1-1.3)$ e for oxygen, $-(0.7-0.8)$ e for fluorine, $0.6-0.7$ e for hydrogen, and $2.6-2.7$ e for both metals. Consequently, we cannot see differences in the Bader charges between the geochemical twin pair for any of the calculated crystals. Moreover, the effect of the

anions onto the metal center is rather subtle with max. 0.2 e. Furthermore, no significant differences are detectable after mono-hydroxylation; even the hydroxyl oxygen charge resembles the other oxygen atoms.

4. Conclusions

In this paper, we investigated the subtle differences in the solid state between the geochemical twin elements Zr/Hf as binary oxides and fluorides, as well as the hypothetical 1:2 mixed oxofluorides. We found that the cohesive energies to form any of these three products from the elements is significantly larger for hafnium than for zirconium. Consequently, within the solid-state, hafnium seems to have a considerably higher affinity for oxygen as well as for fluorine. However, as shown by the fluorination of the respective oxides, the affinity gap between the geochemical twins is slightly larger for fluorine. This might explain the different solubility products of the oxides in diluted aq. HF. In the second part of this study, we explored the hypothetical, endothermic mono-hydroxylated fluorides and oxofluorides of both metals. For the mono-hydroxylated fluorides, interesting trifurcated H-bonds toward three fluorines were found. Although zirconium and hafnium fluorides prefer the same position for hydroxylation, they do show a small energetic difference, again slightly favoring the reaction with the hafnium species. On the other side, according to their Bader charges, no significant difference between Zr/Hf could be found within any of these compounds. Their partial charges hardly changed, whether they were coordinated with the oxygen of fluorine. Consequently, the topology of their electron density is hardly affected.

Supplementary Materials: The following supporting information can be downloaded at: <https://www.mdpi.com/article/10.3390/inorganics10120259/s1>, Figure S1: k -grid convergence for ionic unit cells. Plotted is the difference in total energy per unit cell to the finest grid (ΔE_0). The convergence area of $\Delta E_0 \leq 1.5$ meV is visualized by two horizontal lines. Values for $n = 1, 2$ are not included in this zoomed-in plot due to their high deviation. Figure S2: k -grid convergence for metallic unit cells. Plotted is the difference in total energy per unit cell to the finest grid (ΔE_0). The convergence area of $\Delta E_0 \leq 2.5$ meV is visualized by two horizontal lines. Values for $n = 1, 2$ are not included in this zoomed-in plot due to their high deviation. Figure S3: Second-order Methfessel–Paxton smearing convergence for different smearing widths (σ) in meV per unit cell. Plotted is the difference of free energy at 0 K (F) minus the total energy (E_0). Figure S4: Bonding situation in a subunit of Zr/HfO₂. The oxygen atoms are labeled in accordance with the bond lengths given in Table S5. Figure S5: Bonding situation in a subunit of Zr/HfF₄. The fluorine atoms are labeled in accordance with the bond length in Table S6. Table S1: Literature overview on calculated bulk MO₂ and MF₄ monoclinic crystals with M = Zr or Hf. For plain wave calculations the cutoff energy is given in eV. The k -grid is given as $k_a \times k_b \times k_c$ or if not available in number of irreducible k -points (k_{irred}). The main aims are abbreviated as phase transitions (PT), band structure or gap (BS), elastic (EP), and dielectric properties (DP) or phonon spectra (Ph). Table S2: k -grid converged total energies (E_0) in eV for ionic unit cells. Given are the values for the finest grid, the within 1.5 meV converged grid size, and their difference (ΔE_0). The latter is also plotted in Figure S1. Table S3: k -grid converged total energies (E_0) in eV for metallic unit cells. Given are the values for the finest grid, the within 2.5 meV converged grid size, and their difference (ΔE_0). The latter is also plotted in Figure S2. Table S4: Relaxed unit cell parameters versus experimental (lit. exp.) and calculated literature (lit. PB91) values. Given are the unit cell vector lengths (a, b, c), unit cell volume (V), unit cell volume per formula unit ($V_{\text{f.u.}}$), and the non-orthogonal angle (β), each relaxed parameter is also given as absolute difference to the experimental literature value ($\Delta \text{exp.}$) and the deviation from experiment in percentage ($\Delta\% \text{ exp.}$); note that $\alpha = \gamma = 90^\circ$. Table S5: Bond lengths between metal center and oxygen atoms ($R_{\text{M-O}}$) in relaxed ZrO₂/HfO₂ with the absolute difference in bond length between the two M-species ($\Delta R_{\text{M-O}}$). For comparison, also the experimental bond lengths for ZrO₂ ($R_{\text{Zr-O}}^{\text{exp.}}$) [86] are given together with the absolute difference to the relaxed values ($\Delta R_{\text{Zr-O}}^{\text{exp.}}$). All values are given in Å. Table S6: Bond lengths between metal center and fluorine atoms ($R_{\text{M-F}}$) in relaxed ZrF₄/HfF₄ with the absolute difference in bond length between the two M-species ($\Delta R_{\text{M-F}}$). For comparison, also the experimental bond lengths for ZrF₄ ($R_{\text{Zr-F}}^{\text{exp.}}$) [45] are given together with the absolute difference to the relaxed

values ($\Delta R_{Zr-F}^{exp.}$). All values are given in Å. Table S7: ZPE energies per formula unit (f.u.) obtained from the published optical phonon frequencies at the Γ -point calculated with the PBE, LDA, or PW91 functional. Table S8: Comparison of M–F bond length in Å and ZPE in meV per formula unit for molecular ZrF_4 and HfF_4 with or without ZORA. References [25,27–48,68–73,77,78,86–94] are cited in the supplementary materials.

Author Contributions: Conceptualization, A.L., T.J., J.A. and B.P.; formal analysis, F.G. and J.A.; funding acquisition, B.P.; investigation, F.G. and J.A.; resources, B.P.; supervision, J.A. and B.P.; validation, J.A.; visualization, F.G.; writing—original draft, J.A. and F.G.; writing—review and editing, J.A., F.G., A.L., T.J. and B.P. All authors have read and agreed to the published version of the manuscript.

Funding: The project was funded by the Freie Universität Berlin and the Deutsche Forschungsgemeinschaft (DFG, German Research Foundation) – Project-ID 387284271 – CRC 1349—fluorine-specific interactions.

Institutional Review Board Statement: Not applicable.

Informed Consent Statement: Not applicable.

Data Availability Statement: See supplementary materials. Further data can be requested from the authors.

Acknowledgments: The authors thank the North-German Supercomputing Alliance (Norddeutscher Verbund zur Förderung des Hoch- und Höchstleistungsrechnens HLRN) and the Zentraleinrichtung für Datenverarbeitung (ZEDAT) at the Freie Universität Berlin for computational resources, the German Science Foundation (DFG) for funding within the CRC 1349—Fluorine-Specific Interactions.

Conflicts of Interest: The authors declare no conflict of interest.

References

- Shannon, R.D. Revised effective ionic radii and systematic studies of interatomic distances in halides and chalcogenides. *Acta Cryst. A* **1976**, *32*, 751–767. [\[CrossRef\]](#)
- Park, M.H.; Lee, Y.H.; Mikolajick, T.; Schroeder, U.; Hwang, C.S. Review and perspective on ferroelectric HfO_2 -based thin films for memory applications. *MRS Commun.* **2018**, *8*, 795–808. [\[CrossRef\]](#)
- Cozmuta, I.; Cozic, S.; Poulain, M.; Poulain, S.; Martini, J.R.L. Breaking the Silica Ceiling: ZBLAN-Based Opportunities for Photonics Applications. In Proceedings of the SPIE OPTO, San Francisco, CA, USA, 1–6 February 2020; Volume 11276; p. 112760R. [\[CrossRef\]](#)
- He, Z.; Li, W.; Yu, A.; Wu, Y.; Cai, Z. Efficient UV-visible emission enabled by 532 nm CW excitation in an Ho^{3+} -doped ZBLAN fiber. *Opt. Express* **2022**, *30*, 10414. [\[CrossRef\]](#) [\[PubMed\]](#)
- Hasz, W.C.; Whang, J.H.; Moynihan, C.T. Comparison of physical properties of ZrF_4 - and HfF_4 based melts and glasses. *J. Non Cryst. Solids* **1993**, *161*, 127–132. [\[CrossRef\]](#)
- Dmitruk, L.; Vinogradova, N.; Kozlov, V.; Machov, V.; Devitsin, E.; Fyodorov, V. Scintillating HfF_4 -based glasses doped cerium chloride and cerium oxide compounds. *J. Non Cryst. Solids* **1997**, *213–214*, 311–314. [\[CrossRef\]](#)
- Brekhovskikh, M.; Sukhoverkhov, V.; Fedorov, V.; Batygov, S.; Dmitruk, L.; Vinogradova, N.; Devitsin, E.; Kozlov, V.; Provorova, A. Influence of fluorooxidizers on scintillation properties of fluorohafnate glass doped with Ce^{3+} . *J. Non Cryst. Solids* **2000**, *277*, 68–71. [\[CrossRef\]](#)
- Jones, J.V., III; Piatak, N.M.; Bedinger, G.M. *Zirconium and Hafnium, Professional Paper 1802-V*; Technical report; US Geological Survey: Reston, VA, USA, 2017. [\[CrossRef\]](#)
- Bau, M. Controls on the fractionation of isovalent trace elements in magmatic and aqueous systems: Evidence from Y/Ho, Zr/Hf, and lanthanide tetrad effect. *Contrib. Mineral. Petrol.* **1996**, *123*, 323–333. [\[CrossRef\]](#)
- Ellison, A.J.; Hess, P.C. Solution behavior of +4 cations in high silica melts: Petrologic and geochemical implications. *Contrib. Mineral. Petrol.* **1986**, *94*, 343–351. [\[CrossRef\]](#)
- Linnen, R.L.; Keppler, H. Melt composition control of Zr/Hf fractionation in magmatic processes. *Geochim. Cosmochim. Acta* **2002**, *66*, 3293–3301. [\[CrossRef\]](#)
- Neves, J.M.C.; Nunes, J.E.L.; Sahama, T.G. High hafnium members of the zircon-hafnon series from the granite pegmatites of Zambézia, Mozambique. *Contrib. Mineral. Petrol.* **1974**, *48*, 73–80. [\[CrossRef\]](#)
- Yin, R.; Wang, R.C.; Zhang, A.C.; Hu, H.; Zhu, J.C.; Rao, C.; Zhang, H. Extreme fractionation from zircon to hafnon in the Koktokay No. 1 granitic pegmatite, Altai, northwestern China. *Am. Mineral.* **2013**, *98*, 1714–1724. [\[CrossRef\]](#)
- Kudryashov, N.M.; Skublov, S.G.; Galankina, O.L.; Udoratina, O.V.; Voloshin, A.V. Abnormally high-hafnium zircon from rare-metal pegmatites of the Vasin-Mylk deposit (the northeastern part of the Kola Peninsula). *Geochemistry* **2020**, *80*, 125489. [\[CrossRef\]](#)

15. Loges, A.; Migdisov, A.A.; Wagner, T.; Williams-Jones, A.E.; Markl, G. Fluoride complexation of hafnium under hydrothermal conditions. *Mineral. Mag.* **2012**, *76*, 2030.
16. Haynes, W.M. (Ed.) *CRC Handbook of Chemistry and Physics*, 97th ed.; CRC Press: Boca Raton, FL, USA, 2016. [CrossRef]
17. Luo, Y.R. *Comprehensive Handbook of Chemical Bond Energies*, 1st ed.; CRC Press: Boca Raton, FL, USA, 2007. [CrossRef]
18. Mullins, R.; Kondati Natarajan, S.; Elliott, S.D.; Nolan, M. Self-Limiting Temperature Window for Thermal Atomic Layer Etching of HfO₂ and ZrO₂ Based on the Atomic-Scale Mechanism. *Chem. Mater.* **2020**, *32*, 3414–3426. [CrossRef]
19. Skaggs, R.L.; Rogers, D.T.; Hunter, D.B. *Review of Anhydrous Zirconium-Hafnium Separation Techniques*; Technical report; US Department of the Interior, Bureau of Mines: Washington, DC, USA, 1984.
20. Vilakazi, B.M.; Monnahela, O.S.; Wagener, J.B.; Carstens, P.A.B.; Ntsoane, T. A thermogravimetric study of the fluorination of zirconium and hafnium oxides with anhydrous hydrogen fluoride gas. *J. Fluor. Chem.* **2012**, *141*, 64–68. [CrossRef]
21. Migdisov, A.; Williams-Jones, A.E.; van Hinsberg, V.; Salvi, S. An experimental study of the solubility of baddeleyite (ZrO₂) in fluoride-bearing solutions at elevated temperature. *Geochim. Cosmochim. Acta* **2011**, *75*, 7426–7434. [CrossRef]
22. Loges, A.; Louvel, M.; Wilke, M.; Jahn, S.; Klemme, S.; Welter, E.; Borchert, M.; Qiao, S.; Manni, M.; Keller, B.; et al. Fluoride Complexation of Zr and Hf in Hydrothermal Aqueous Fluids. Online Resource on ResearchGate. 2022. Available online: https://www.researchgate.net/publication/359514094_Fluoride_complexation_of_Zr_and_Hf_in_hydrothermal_aqueous_fluids?channel=doi&linkId=62421da67931cc7ccf00a78c&showFulltext=true (accessed on 30 October 2022).
23. Ryzhenko, B.N.; Kovalenko, N.I.; Prisyagina, N.I.; Starshinova, N.P.; Krupskaya, V.V. Experimental determination of zirconium speciation in hydrothermal solutions. *Geochem. Int.* **2008**, *46*, 328–339. [CrossRef]
24. Boysen, H.; Frey, F.; Vogt, T. Neutron powder investigation of the tetragonal to monoclinic phase transformation in undoped zirconia. *Acta Crystallogr. B* **1991**, *47*, 881–886. [CrossRef]
25. Block, S.; Da Jornada, J.A.H.; Piermarini, G.J. Pressure-Temperature Phase Diagram of Zirconia. *J. Am. Ceram. Soc.* **1985**, *68*, 497–499. [CrossRef]
26. Shin, D.; Arroyave, R.; Liu, Z.k. Thermodynamic modeling of the Hf–Si–O system. *Calphad* **2006**, *30*, 375–386. [CrossRef]
27. Al-Khatatbeh, Y.; Lee, K.K.M.; Kiefer, B. Phase diagram up to 105 GPa and mechanical strength of HfO₂. *Phys. Rev. B* **2010**, *82*, 144106. [CrossRef]
28. Králik, B.; Chang, E.K.; Louie, S.G. Structural properties and quasiparticle band structure of zirconia. *Phys. Rev. B* **1998**, *57*, 7027–7036. [CrossRef]
29. Demkov, A.A. Investigating Alternative Gate Dielectrics: A Theoretical Approach. *Phys. Status Solidi B* **2001**, *226*, 57–67. [CrossRef]
30. Zhao, X.; Vanderbilt, D. First-principles study of structural, vibrational, and lattice dielectric properties of hafnium oxide. *Phys. Rev. B* **2002**, *65*, 233106. [CrossRef]
31. Zhao, X.; Vanderbilt, D. Phonons and lattice dielectric properties of zirconia. *Phys. Rev. B* **2002**, *65*, 75105. [CrossRef]
32. Debernardi, A.; Fanciulli, M. Structural and vibrational properties of high-dielectric oxides, HfO₂ and TiO₂: A comparative study. *Mater. Sci. Semicond. Process.* **2006**, *9*, 1014–1019. [CrossRef]
33. Luo, X.; Zhou, W.; Ushakov, S.V.; Navrotsky, A.; Demkov, A.A. Monoclinic to tetragonal transformations in hafnia and zirconia: A combined calorimetric and density functional study. *Phys. Rev. B* **2009**, *80*, 134119. [CrossRef]
34. Li, J.; Meng, S.; Niu, J.; Lu, H. Electronic structures and optical properties of monoclinic ZrO₂ studied by first-principles local density approximation + U approach. *J. Adv. Ceram.* **2017**, *6*, 43–49. [CrossRef]
35. Li, J.; Han, J.; Meng, S.; Lu, H.; Tohyama, T. Optical properties of monoclinic HfO₂ studied by first-principles local density approximation + U approach. *Appl. Phys. Lett.* **2013**, *103*, 071916. [CrossRef]
36. Jomard, G.; Petit, T.; Pasturel, A.; Magaud, L.; Kresse, G.; Hafner, J. First-principles calculations to describe zirconia pseudopolymorphs. *Phys. Rev. B* **1999**, *59*, 4044–4052. [CrossRef]
37. Kuwabara, A.; Tohei, T.; Yamamoto, T.; Tanaka, I. Ab initio lattice dynamics and phase transformations of ZrO₂. *Phys. Rev. B* **2005**, *71*, 64301. [CrossRef]
38. Fadda, G.; Colombo, L.; Zanzotto, G. First-principles study of the structural and elastic properties of zirconia. *Phys. Rev. B* **2009**, *79*, 214102. [CrossRef]
39. Fadda, G.; Zanzotto, G.; Colombo, L. First-principles study of the effect of pressure on the five zirconia polymorphs. II. Static dielectric properties and Raman spectra. *Phys. Rev. B* **2010**, *82*, 64106. [CrossRef]
40. Delarmelina, M.; Quesne, M.G.; Catlow, C.R.A. Modelling the bulk properties of ambient pressure polymorphs of zirconia. *Phys. Chem. Chem. Phys.* **2020**, *22*, 6660–6676. [CrossRef]
41. Jaffe, J.E.; Bachorz, R.A.; Gutowski, M. Low-temperature polymorphs of ZrO₂ and HfO₂: A density-functional theory study. *Phys. Rev. B* **2005**, *72*, 144107. [CrossRef]
42. Laudadio, E.; Stipa, P.; Pierantoni, L.; Mencarelli, D. Phase Properties of Different HfO₂ Polymorphs: A DFT-Based Study. *Crystals* **2022**, *12*, 90. [CrossRef]
43. Low, J.J.; Paulson, N.H.; D’Mello, M.; Stan, M. Thermodynamics of monoclinic and tetragonal hafnium dioxide (HfO₂) at ambient pressure. *Calphad* **2021**, *72*, 102210. [CrossRef]
44. Rivas-Silva, J.F.; Flores-Riveros, A.; Durand-Niconoff, J.S.; Aquino, N. Ab initio analysis of some fluoride and oxide structures doped with Pr and Yb. *Int. J. Quantum Chem.* **2004**, *97*, 815–825. [CrossRef]

45. Legein, C.; Fayon, F.; Martineau, C.; Body, M.; Buzaré, J.Y.; Massiot, D.; Durand, E.; Tressaud, A.; Demourgues, A.; Péron, O.; et al. ^{19}F High Magnetic Field NMR Study of $\beta\text{-ZrF}_4$ and CeF_4 : From Spectra Reconstruction to Correlation between Fluorine Sites and ^{19}F Isotropic Chemical Shifts. *Inorg. Chem.* **2006**, *45*, 10636–10641. [[CrossRef](#)]
46. Benner, G.; Müller, B.G. Zur Kenntnis binärer Fluoride des ZrF_4 -Typs: HfF_4 und ThF_4 . *Z. Anorg. Allg. Chem.* **1990**, *588*, 33–42. [[CrossRef](#)]
47. McDonald, R.A.; Sinke, G.C.; Stull, D.R. High Temperature Enthalpy, Heat Capacity, Heat of Fusion, and Melting Point of Zirconium Tetrafluoride. *J. Chem. Eng. Data* **1962**, *7*, 83. [[CrossRef](#)]
48. Sicius, H. (Ed.) Titangruppe: Elemente der vierten Nebengruppe. In *Handbuch der chemischen Elemente*; Springer: Berlin/Heidelberg, Germany, 2021; pp. 483–529. [[CrossRef](#)]
49. Joubert, P.; Gaudreau, B. Sur quelques oxyfluorures de zirconium tetravalent. *Rev. Chim. Mine.* **1975**, *12*, 289–302.
50. Papiernik, R.; Frit, B. Structure cristalline d'une phase cubique desordonnée de type ReO_3 excédentaire en anions: $\text{ZrF}_{2.67}\text{O}_{0.67}$. *Mater. Res. Bull.* **1984**, *19*, 509–516. [[CrossRef](#)]
51. Holmberg, B. The crystal structure of $\text{Zr}_7\text{O}_9\text{F}_{10}$. *Acta Crystallogr. B* **1970**, *26*, 830–835. [[CrossRef](#)]
52. Flynn, S.; Zhang, C.; Griffith, K.J.; Shen, J.; Wolverson, C.; Dravid, V.P.; Poeppelmeier, K.R. Fluoridation of HfO_2 . *Inorg. Chem.* **2021**, *60*, 4463–4474. [[CrossRef](#)] [[PubMed](#)]
53. Rickard, C.E.F.; Waters, T.N. The hafnium tetrafluoride-water system. *J. Inorg. Nucl. Chem.* **1964**, *26*, 925–930. [[CrossRef](#)]
54. Jain, A.; Ong, S.P.; Hautier, G.; Chen, W.; Richards, W.D.; Dacek, S.; Cholia, S.; Gunter, D.; Skinner, D.; Ceder, G.; et al. Commentary: The Materials Project: A materials genome approach to accelerating materials innovation. *APL Mater.* **2013**, *1*, 11002. [[CrossRef](#)]
55. Clearfield, A.; Vaughan, P.A. The crystal structure of zirconyl chloride octahydrate and zirconyl bromide octahydrate. *Acta Crystallogr.* **1956**, *9*, 555–558. [[CrossRef](#)]
56. Scholz, J.; Scholz (nee Böhme), K.; McQuillan, A.J. In Situ Infrared Spectroscopic Analysis of the Water Modes of $[\text{Zr}_4(\text{OH})_8(\text{H}_2\text{O})_{16}]^{8+}$ during the Thermal Dehydration of $\text{ZrOCl}_2 \cdot 8\text{H}_2\text{O}$. *J. Phys. Chem. A* **2010**, *114*, 7733–7741. [[CrossRef](#)]
57. Zhukov, A.V.; Chizhevskaya, S.V.; Phyto, P.; Panov, V.A. Heterophase Synthesis of Zirconium Hydroxide from Zirconium Oxychloride. *Inorg. Mater.* **2019**, *55*, 994–1000. [[CrossRef](#)]
58. Bergerhoff, G.; Brown, I. *Crystallographic Databases*; International Union of Crystallography: Chester, UK, 1987.
59. Gabela, F.; Kojić-Prodić, B.; Šljukić, M.; Ružić-Toroš, Z. Refinement of the crystal structure of di- μ -fluoro-hexafluorohexaaqua-dizirconium(IV), $\text{Zr}_2\text{F}_8(\text{H}_2\text{O})_6$. *Acta Crystallogr. B* **1977**, *33*, 3733–3736. [[CrossRef](#)]
60. Kojić-Prodić, B.; Gabela, F.; Ružić-Toroš, Z.; Šljukić, M. Structure of aquatetrafluorozirconium(IV). *Acta Crystallogr. B* **1981**, *37*, 1963–1965. [[CrossRef](#)]
61. Davidovich, R.; Gerasimenko, A.; Bukvetskii, B.; Logvinova, V.; Buslaev, Y. Crystal structure of hydroxonium hexafluorozirconate. *Russ. J. Coord. Chem./Koord. Khimiya* **1987**, *13*, 706–709.
62. Charpin, P.; Lance, M.; Nierlich, M.; Vigner, J.; Lambard, J. Structures of oxonium pentafluorozirconate mono- and dihydrates. *Acta Crystallogr. C* **1988**, *44*, 1698–1701. [[CrossRef](#)]
63. Marsh, R.E. Structure of oxonium pentafluorozirconate dihydrate. Corrigendum. *Acta Crystallogr. C* **1989**, *45*, 980. [[CrossRef](#)]
64. Davidovich, R.L.; Pushilin, M.A.; Logvinova, V.B.; Gerasimenko, A.V. Crystal structure of monoclinic modifications of zirconium and hafnium tetrafluoride trihydrates. *J. Struct. Chem.* **2013**, *54*, 541–546. [[CrossRef](#)]
65. Guillet, L.; Ider, A.; Laval, J.P.; Frit, B. Crystal structure of TeOF_2 . *J. Fluor. Chem.* **1999**, *93*, 33–38. [[CrossRef](#)]
66. Kresse, G.; Hafner, J. Norm-conserving and ultrasoft pseudopotentials for first-row and transition elements. *J. Phys. Condens. Matter* **1994**, *6*, 8245–8257. [[CrossRef](#)]
67. Perdew, J.P.; Burke, K.; Ernzerhof, M. Generalized Gradient Approximation Made Simple. *Phys. Rev. Lett.* **1996**, *77*, 3865–3868. [[CrossRef](#)]
68. Grimme, S. Semiempirical GGA-type density functional constructed with a long-range dispersion correction. *J. Comput. Chem.* **2006**, *27*, 1787–1799. [[CrossRef](#)]
69. Grimme, S.; Antony, J.; Ehrlich, S.; Krieg, H. A consistent and accurate ab initio parametrization of density functional dispersion correction (DFT-D) for the 94 elements H–Pu. *J. Chem. Phys.* **2010**, *132*, 154104. [[CrossRef](#)] [[PubMed](#)]
70. Balog, M.; Schieber, M.; Michman, M.; Patai, S. Chemical vapor deposition and characterization of HfO_2 films from organo-hafnium compounds. *Thin Solid Films* **1977**, *41*, 247–259. [[CrossRef](#)]
71. Lucovsky, G.; Fulton, C.C.; Zhang, Y.; Zou, Y.; Luning, J.; Edge, L.F.; Whitten, J.L.; Nemanich, R.J.; Ade, H.; Schlom, D.G.; et al. Conduction band-edge States associated with the removal of d-state degeneracies by the Jahn-Teller effect. *IEEE Trans. Device Mater. Reliab.* **2005**, *5*, 65–83. [[CrossRef](#)]
72. French, R.H.; Glass, S.J.; Ohuchi, F.S.; Xu, Y.N.; Ching, W.Y. Experimental and theoretical determination of the electronic structure and optical properties of three phases of ZrO_2 . *Phys. Rev. B* **1994**, *49*, 5133–5142. [[CrossRef](#)]
73. Smith, D.K.; Newkirk, W. The crystal structure of baddeleyite (monoclinic ZrO_2) and its relation to the polymorphism of ZrO_2 . *Acta Cryst.* **1965**, *18*, 983–991. [[CrossRef](#)]
74. Tkatchenko, A.; Scheffler, M. Accurate Molecular Van Der Waals Interactions from Ground-State Electron Density and Free-Atom Reference Data. *Phys. Rev. Lett.* **2009**, *102*, 73005. [[CrossRef](#)] [[PubMed](#)]
75. Blöchl, P.E. Projector augmented-wave method. *Phys. Rev. B* **1994**, *50*, 17953–17979. [[CrossRef](#)]
76. Kresse, G.; Joubert, D. From ultrasoft pseudopotentials to the projector augmented-wave method. *Phys. Rev. B* **1999**, *59*, 1758–1775. [[CrossRef](#)]

77. Maimaitiyili, T.; Steuwer, A.; Blomqvist, J.; Bjerken, C.; Blackmur, M.S.; Zanellato, O.; Andrieux, J.; Ribeiro, F. Observation of the δ to ϵ Zr-hydride transition by in-situ synchrotron X-ray diffraction. *Cryst. Res. Technol.* **2016**, *51*, 663–670. [[CrossRef](#)]
78. Romans, P.A.; Paasche, O.G.; Kato, H. The transformation temperature of hafnium. *J. Less-Common Met.* **1965**, *8*, 213–215. [[CrossRef](#)]
79. Bader, R.F.W. Atoms in molecules. *Acc. Chem. Res.* **1985**, *18*, 9–15. [[CrossRef](#)]
80. Henkelman, G.; Arnaldsson, A.; Jónsson, H. A fast and robust algorithm for Bader decomposition of charge density. *Comp. Mat. Sci.* **2006**, *36*, 354–360. [[CrossRef](#)]
81. Sanville, E.; Kenny, S.D.; Smith, R.; Henkelman, G. Improved grid-based algorithm for Bader charge allocation. *J. Comput. Chem.* **2007**, *28*, 899–908. [[CrossRef](#)] [[PubMed](#)]
82. Tang, W.; Sanville, E.; Henkelman, G. A grid-based Bader analysis algorithm without lattice bias. *J. Phys. Condens. Matter* **2009**, *21*, 84204. [[CrossRef](#)] [[PubMed](#)]
83. Yu, M.; Trinkle, D.R. Accurate and efficient algorithm for Bader charge integration. *J. Chem. Phys.* **2011**, *134*, 64111. [[CrossRef](#)]
84. Tran, R.; Xu, Z.; Radhakrishnan, B.; Winston, D.; Sun, W.; Persson, K.A.; Ong, S.P. Surface energies of elemental crystals. *Sci. Data* **2016**, *3*, 160080. [[CrossRef](#)] [[PubMed](#)]
85. Momma, K.; Izumi, F. VESTA 3 for three-dimensional visualization of crystal, volumetric and morphology data. *J. Appl. Crystallogr.* **2011**, *44*, 1272–1276. [[CrossRef](#)]
86. Howard, C.J.; Hill, R.J.; Reichert, B.E. Structures of ZrO₂ polymorphs at room temperature by high-resolution neutron powder diffraction. *Acta Crystallogr. B* **1988**, *44*, 116–120. [[CrossRef](#)]
87. Pathak, S.; Das, P.; Das, T.; Mandal, G.; Joseph, B.; Sahu, M.; Kaushik, S.D.; Siruguri, V. Crystal structure of monoclinic hafnia (HfO₂) revisited with synchrotron X-ray, neutron diffraction and first-principles calculations. *Acta Crystallogr. C* **2020**, *76*, 1034–1042. [[CrossRef](#)]
88. Quintard, P.E.; Barb eris, P.; Mirgorodsky, A.P.; Merle-M ejean, T. Comparative Lattice-Dynamical Study of the Raman Spectra of Monoclinic and Tetragonal Phases of Zirconia and Hafnia. *J. Am. Ceram. Soc.* **2002**, *85*, 1745–1749. [[CrossRef](#)]
89. Goldstein, M.; Hughes, R.J.; Unsworth, W.D. Vibrational spectra of some heavy metal tetrafluorides in the solid state. *Spectrochim. Acta A* **1975**, *31*, 621–624. [[CrossRef](#)]
90. Neese, F. Software update: The ORCA program system—Version 5.0. *WIREs Comput Mol Sci.* **2022**, *12*, e1606. [[CrossRef](#)]
91. Weigend, F.; Ahlrichs, R. Balanced basis sets of split valence, triple zeta valence and quadruple zeta valence quality for H to Rn: Design and assessment of accuracy. *Phys. Chem. Chem. Phys.* **2005**, *7*, 3297–3305. [[CrossRef](#)] [[PubMed](#)]
92. Andrae, D.; H au er mann, U.; Dolg, M.; Stoll, H.; Preu , H. Energy-adjusted ab initio pseudopotentials for the second and third row transition elements. *Theoret. Chim. Acta* **1990**, *77*, 123–141. [[CrossRef](#)]
93. van W ullen, C. Molecular density functional calculations in the regular relativistic approximation: Method, application to coinage metal diatomics, hydrides, fluorides and chlorides, and comparison with first-order relativistic calculations. *J. Chem. Phys.* **1998**, *109*, 392–399. [[CrossRef](#)]
94. Pantazis, D.A.; Chen, X.Y.; Landis, C.R.; Neese, F. All-Electron Scalar Relativistic Basis Sets for Third-Row Transition Metal Atoms. *J. Chem. Theory Comput.* **2008**, *4*, 908–919. [[CrossRef](#)]
95. Steiner, T. The Hydrogen Bond in the Solid State. *Angew. Chem. Int. Ed.* **2002**, *41*, 48–76. [[CrossRef](#)]
96. Jeffrey, G. *An Introduction to Hydrogen Bonding*; Oxford University Press: Oxford, UK, 1997.
97. Brammer, L.; Bruton, E.A.; Sherwood, P. Fluoride ligands exhibit marked departures from the hydrogen bond acceptor behavior of their heavier halogen congeners. *New J. Chem.* **1999**, *23*, 965–968. [[CrossRef](#)]
98. Hirata, S.; Iwata, S. Ab Initio Hartree–Fock and Density Functional Studies on the Structures and Vibrations of an Infinite Hydrogen Fluoride Polymer. *J. Phys. Chem. A* **1998**, *102*, 8426–8436. [[CrossRef](#)]
99. Johnson, M.W.; S andor, E.; Arzi, E. The crystal structure of deuterium fluoride. *Acta Crystallogr. B* **1975**, *31*, 1998–2003. [[CrossRef](#)]

Supplementary Materials: Stability of Hydroxo/Oxo/Fluoro Zirconates vs. Hafnates — A DFT Study

Jennifer Anders¹ *, Fabian Göritz¹, Anselm Loges², Timm John², Beate Paulus¹

Contents

1	Literature Overview	1	2
2	Choice of Functional	1	3
3	Convergence of Computational Setup	2	4
	3.1 k -grid Convergence	2	5
	3.2 Electronic Smearing Convergence	4	6
4	Validation on Known Crystal Structures.	5	7
	4.1 Unit Cells of Known Crystals	5	8
	4.2 Bonding Situation in Known Crystals	6	9
5	Literature ZPE Energies on MO ₂	8	10
6	Discussion on Zr/Hf differences in ΔE vs. ΔG	8	11
	6.1 Test Calculations in the Gas-Phase	9	12
	References	10	13

1. Literature Overview

Table S1. Literature overview on calculated bulk MO₂ and MF₄ monoclinic crystals with M = Zr or Hf. For plain wave calculations the cutoff energy is given in eV. The k -grid is given as $k_a \times k_b \times k_c$ or if not available in number of irreducible k -points ($k_{\text{irred.}}$). The main aims are abbreviated as phase transitions (PT), band structure or gap (BS), elastic (EP) and dielectric properties (DP) or phonon spectra (Ph):

	system	setup	aim
Králík et al.[1]	ZrO ₂	LDA+GW(-/1361 eV/2 $k_{\text{irred.}}$)	BS
Jomard et al. [2]	ZrO ₂	LDA+PW91+PB(VASP/300 eV/4x4x4)	PT
Kuwabara et al. [3]	ZrO ₂	PW91(VASP/500 eV/3x3x3)	PT
Fadda et al.[4,5]	ZrO ₂	LDA+PBE(ABINIT/1633 eV/4x4x4)	EP+DP+Ph
Delarmelina et al.[6]	ZrO ₂	PBE+PBEsol+RPBE+TPSS w/o +U w/o D2/D3(VASP/550 eV/5x5x5)	PT+BS+EP+DP
Demkov[7]	ZrO ₂ +HfO ₂	LDA(CASTEP/750 eV/4x4x4)	BS
Zhao and Vanderbilt[8,9]	ZrO ₂ +HfO ₂	LDA+PBE(-/340 eV/4x4x4)	Ph+DP
Jaffe et al.[10]	ZrO ₂ +HfO ₂	LDA+PW91(VASP/495 eV/9x9x9)	PT+BS
Luo et al.[11]	ZrO ₂ +HfO ₂	LDA(VASP/800 eV/8x8x8)	PS+Ph
Mullins et al.[12]	ZrO ₂ +HfO ₂	PBE(VASP/550 eV/6x6x6)	surface etching
Debernardi and Fanciulli[13]	HfO ₂	LDA(PWSCF/476 eV/4x4x4)	PT+Ph
Li et al.[14]	HfO ₂	LDA+8eV Hf-5d +6eV O-2p (CASTEP/380 eV/24x24x24)	BS
Li et al.[15]	HfO ₂	LDA+8eV Hf-5d +4.35 eV O-2p (CASTEP/380 eV/6x6x6)	BS
Laudadio et al.[16]	HfO ₂	PBE+6eV Hf-5d +4eV O-2p (QuantumATK/1200 eV/15x15x15)	
Low et al.[17]	HfO ₂	PBEsol(ABINIT/2721 eV/6x6x6)	PT+Ph
Rivas-Silva et al. [18]	ZrF ₄ +HfF ₄	CIS(Gaussian/STO/cluster)	BS

2. Choice of Functional

Delarmelina et al.[6] published a very elaborate benchmark on various properties for the three phases of ZrO₂ with different functionals (PBE, PBEsol, RPBE and TPSS) with/without D2 or D3 dispersion correction and/or Hubbard-type correction (+U) onto Zr-4d. For the performance onto the atomic structure of monoclinic ZrO₂, they found that the relative error versus experiment for each lattice vector varies just from 0.2–0.3% (PBEsol) to 1.2–2.2% (RPBE). For the original PBE, the relative errors are in between with 0.7–1.2%.

Thus, there is little variation between these meta-/GGA functionals onto the very ionic bulk crystal. When comparing the +U correction, the relative lattice vector errors even grow with U. At the highest U = 8 eV, these are 1.7–3.3% (PBEsol+U 8 eV) to 2.9–4.9% (RPBE+U 8 eV). By applying D3 on a smaller U of 2 eV, the relative errors are considerably lower again with 0.1–0.6% (PBEsol+U 2 eV + D3) to 1.5–1.6% (RPBE+U 2 eV +D3), but still higher than PBEsol without any addition. It should also be noted that Delarmelina et. al. refer their results to an older experimental value with lattice vectors of $a = 5.145 \text{ \AA}$, $b = 5.207 \text{ \AA}$ and $c = 5.242 \text{ \AA}$ [19]. When instead referencing to the slightly larger values of $a = 5.150 \text{ \AA}$, $b = 5.212 \text{ \AA}$ and $c = 5.317 \text{ \AA}$ measured 23 years later by high-resolution neutron powder diffraction [20], the relative errors of their reported PBE (550 eV cutoff/5x5x5 *k*-grid) are significantly smaller with 0.2–0.8%. Compared to this newer experimental value, their tested 0.1–1.8% (PBEsol+U 2 eV + D3) performs equally in relative errors as simple PBEsol but worse than simple PBE. By using the hard PAW-potential on oxygen, the accurate numerical setting and a larger cutoff, our now reported PBE (773 eV cutoff/4x4x4 *k*-grid) vectors are even closer with only 0.1–0.3%. Summing up, on geometrical data of monoclinic ZrO₂, applying a dispersion correction or +U correction onto the Zr-4d does not improve the results.

The reason behind the non-observed enhancement by +U onto the crystal structure lies within the nominal IV oxidation state, which is present in all the studied bulk crystals within this paper. Formally, Zr(IV) possesses the electronic configuration of krypton and Hf(IV) of xenon. Measurements on MO₂ have shown, that the Zr(IV)-4d and Hf(IV)-5d form the conduction band (CB) instead of the valence band (VB), which is constructed from the O-2p suggesting that there are no correlated d-electrons to localize by +U [21,22]. For a longer discussion we would also like to refer to a study on HfO₂ by Low et al. [17].

We have seen that other authors use LDA+U on MO₂ with a big +U of 8 eV on Zr-4d (or 6–8 eV on Hf-5d), in combination with another 4.35 eV (or 4-6 eV for HfO₂) on O-2p to obtain better band gap agreement [14–16]. However, for the reasons above, we chose to not apply a large +U onto non-occupied orbitals and to simultaneously apply two empirical +U parameters on a binary compound.

Moreover, we do not expect that the Zr-4d and Hf-5d CB significantly mixes into the bonding to oxide or fluoride, as the band gaps of these materials are far in the insulating regime (ZrO₂: 5.83 eV [21]; HfO₂: 5.86 eV [23]; ZrF₄: 9.4 eV [18]; HfF₄: 10.3 eV [18]). It is well known, that GGAs generally underestimate band gaps as the electronic structure is too delocalized. However, given the high band gaps of these ionic crystals, there is a large tolerance before the underestimation would severely change the nature of conductivity. As our paper does not discuss band structures, electronic excitations or other optical properties but merely relative stabilities between the bulk solids, we chose the simple GGA approach.

3. Convergence of Computational Setup

Unless stated differently, the computational details given in the main paper apply.

3.1. *k*-grid Convergence

The *k*-grid has been tested for convergence by single point calculations on the respective experimental crystal structures. All grids are Monkhorst-Pack-type and possess an equal number of *k*-points in all three dimensions. For the metallic unit cells, the converged smearing width of 0.05 eV has been applied. As the metallic unit cells are just needed for the cohesive energies with elemental reactants (see main paper Table 2), we considered the convergence of $\Delta E_0 \leq 2.5 \text{ meV}$ per unit cell enough and chose to not increase the *k*-grid further than $n = 17$.

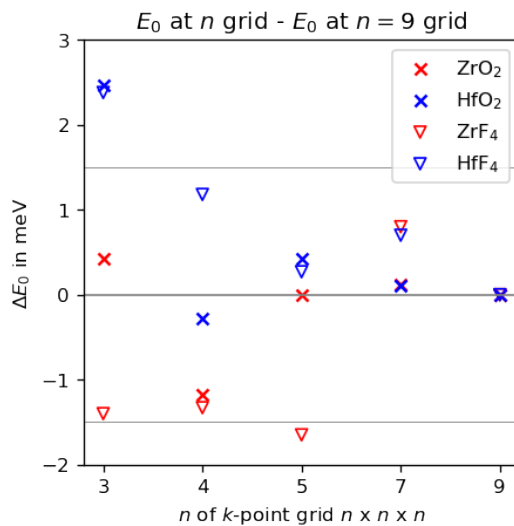


Figure S1. *k*-grid convergence for ionic unit cells. Plotted is the difference in total energy in meV per unit cell to the finest grid (ΔE_0). The convergence area of $\Delta E_0 \leq 1.5$ meV is visualized by two horizontal lines. Values for $n = 1, 2$ are not included in this zoomed-in plot due to their high deviation.

Table S2. *k*-grid converged total energies (E_0) in eV for ionic unit cells. Given are the values for the finest grid, the within 1.5 meV converged grid size and their difference (ΔE_0). The latter is also plotted in Figure S1:

compound	$E_0 (n = 4)$	$E_0 (n = 9)$	ΔE_0
ZrO ₂	-115.13051	-115.12933	-118×10^{-5}
HfO ₂	-133.12904	-133.12876	-28×10^{-5}
ZrF ₄	-205.28538	-205.28405	-133×10^{-5}
HfF ₄	-232.20100	-232.20218	118×10^{-5}

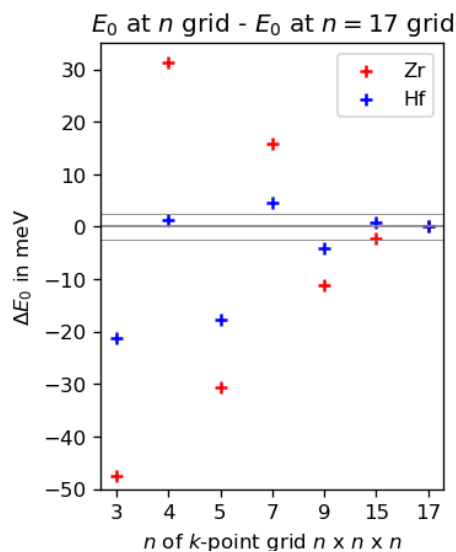


Figure S2. *k*-grid convergence for metallic unit cells. Plotted is the difference in total energy in meV per unit cell to the finest grid (ΔE_0). The convergence area of $\Delta E_0 \leq 2.5$ meV is visualized by two horizontal lines. Values for $n = 1, 2$ are not included in this zoomed-in plot due to their high deviation.

Table S3. *k*-grid converged total energies (E_0) in eV for metallic unit cells. Given are the values for the finest grid, the within 2.5 meV converged grid size and their difference (ΔE_0). The latter is also plotted in Figure S2:

compound	E_0 ($n = 15$)	E_0 ($n = 17$)	ΔE_0
Zr	-17.042727	-17.040550	-218×10^{-5}
Hf	-25.479629	-25.480518	89×10^{-5}

3.2. Electronic Smearing Convergence

For the two metallic unit cells of Zr and Hf, the second order Methfessel-Paxton smearing has been tested for different smearing widths (σ) by single point calculations on the respective experimental crystal structures applying the converged *k*-grid of $n = 15$. The σ -value of 0.05 eV has been selected for both metals as it yields the smallest deviation between total energy (E_0) and free energy at 0 K (F), which differ by the electronic entropy. However, for the set of tested values, all give a much smaller deviation than the *k*-grid convergence error. Therefore, as well as we only need the total energy of the metal unit cell to construct the cohesion energies, we did not sample further σ -values.

69

70

71

72

73

74

75

76

77

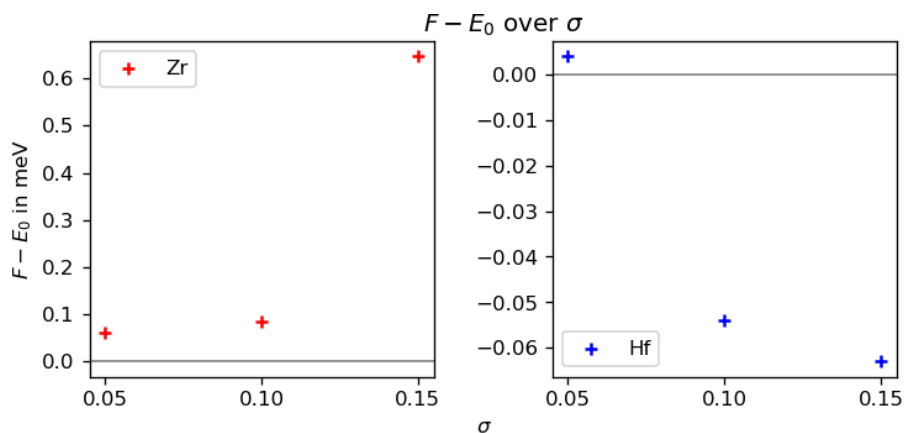


Figure S3. Second order Methfessel-Paxton smearing convergence for different smearing widths (σ) in meV per unit cell. Plotted is the difference of free energy at 0 K (F) minus the total energy (E_0).

4. Validation on Known Crystal Structures

4.1. Unit Cells of Known Crystals

To evaluate the performance of our computational setup on the geometrical parameters, Table S4 gives the calculated and literature unit cell parameters for all experimentally known crystal structures used within the main paper. It also gives the absolute difference to the experimental literature value (Δ_{exp}) and the deviation from experiment in percentage ($\Delta_{\% \text{exp}}$) according to Equation 1.

$$\Delta_{\% \text{exp}} = \frac{|\text{calc} - \text{exp}|}{\text{exp}} \times 100\% = \frac{\Delta_{\text{exp}}}{\text{exp}} \times 100\% \quad (1)$$

78

79

Table S4. Relaxed unit cell parameters versus experimental (lit. exp) and calculated literature (lit. PB91) values. Given are the unit cell vector lengths (a, b, c), unit cell volume (V), unit cell volume per formula unit ($V_{\text{f.u.}}$) and the non-orthogonal angle (β), each relaxed parameter is also given as absolute difference to the experimental literature value (Δ exp) and the deviation from experiment in percentage ($\Delta\%$ exp); note, that for monoclinic oxides and fluorides: $\alpha = \gamma = 90^\circ$, while for hcp metals: $\alpha = \beta = 90^\circ$ and $\gamma = 120^\circ$:

Compound	a (Å)	b (Å)	c (Å)	V (Å ³)	β (°)
ZrO₂	5.154	5.224	5.332	141.56	99.55
lit. PB91 [10]	5.197	5.279	5.349	144.74	99.53
lit. exp [20]	5.150	5.212	5.317	140.88	99.23
Δ exp	0.004	0.012	0.015	0.68	0.32
$\Delta\%$ exp	0.1	0.2	0.3	0.5	0.3
HfO₂	5.105	5.182	5.277	137.64	99.54
lit. PB91 [10]	5.128	5.191	5.297	139.25	99.71
lit. exp [24]	5.114	5.168	5.290	138.03	99.21
Δ exp	0.009	0.014	0.013	0.39	0.33
$\Delta\%$ exp	0.2	0.3	0.2	2.9	0.3
ZrF₄	11.694	9.889	7.660	710.40	126.68
lit. exp [25]	11.845	9.930	7.730	732.53	126.32
Δ exp	0.151	0.041	0.070	22.13	0.36
$\Delta\%$ exp	1.3	0.4	0.9	3.0	0.3
HfF₄	11.609	9.816	7.600	694.85	126.65
lit. exp [26]	11.725	9.869	7.636	713.48	126.15
Δ exp	0.116	0.053	0.036	18.63	0.50
$\Delta\%$ exp	1.0	0.5	0.5	2.6	0.4
Zr	3.234	3.234	5.168	46.82	
lit. exp. [27]	3.242	3.242	5.166	47.03	
Δ exp	0.008	0.008	0.002	0.21	
$\Delta\%$ exp	0.2	0.2	0.03	0.4	
Hf	3.202	3.202	5.056	44.91	
lit. exp. [28]	3.198	3.198	5.061	44.83	
Δ exp	0.004	0.004	0.005	0.08	
$\Delta\%$ exp	0.1	0.1	0.1	0.2	

4.2. Bonding Situation in Known Crystals

We also tested our computational method on the bond lengths published for the Zr- species. The bonding situation within the oxides is shown in Figure S4. The bond lengths between the metal center and each of the seven oxygen atoms are listed in Table S5. For any of the seven bond lengths, the difference to experiment ($\Delta R_{\text{Zr-O}}^{\text{exp}}$) is only 0.000–0.011 Å. By that, $\Delta R_{\text{Zr-O}}^{\text{exp}}$ is one order of magnitude smaller than the difference between the two relaxed geochemical twins $\Delta R_{\text{M-O}}$, with one exception. For M–O₄, $\Delta R_{\text{M-O}_4}$ and $\Delta R_{\text{Zr-O}_4}^{\text{exp}}$ possess the same order of magnitude.

80
81
82
83
84
85
86
87

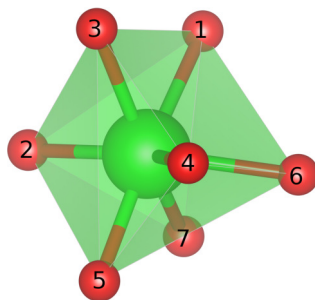


Figure S4. Bonding situation in a subunit of Zr/HfO₂. The oxygen atoms are labeled in accordance to the bond lengths given in Table S5.

Table S5. Bond lengths between metal center and oxygen atoms (R_{M-O}) in relaxed ZrO₂/HfO₂ with the absolute difference in bond length between the two M-species (ΔR_{M-O}). For comparison, also the experimental bond lengths for ZrO₂ (R_{Zr-O}^{exp}) [20] are given together with the absolute difference to the relaxed values ($\Delta R_{Zr-O}^{\text{exp}}$). All values are given in Å.

bond	R_{Zr-O}	R_{Hf-O}	ΔR_{M-O}	R_{Zr-O}^{exp} [20]	$\Delta R_{Zr-O}^{\text{exp}}$
$M - O_1$	2.265	2.228	0.037	2.267	0.002
$M - O_2$	2.070	2.051	0.019	2.063	0.007
$M - O_3$	2.155	2.138	0.017	2.153	0.002
$M - O_4$	2.253	2.236	0.017	2.242	0.011
$M - O_5$	2.052	2.041	0.011	2.052	0.000
$M - O_6$	2.175	2.165	0.010	2.176	0.001
$M - O_7$	2.163	2.137	0.026	2.157	0.006

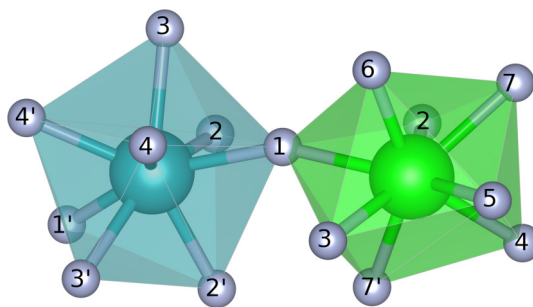


Figure S5. Bonding situation in a subunit of Zr/HfF₄. The fluorine atoms are labeled in accordance to the bond length in Table S6.

The bonding situation of the fluorides is shown in Figure S6 and listed in Table S6. In contrast to the oxides, the relaxed bond lengths differ stronger to the experimental bond lengths with 0.003–0.049 Å. Thus, $\Delta R_{Zr-F}^{\text{exp}}$ and ΔR_{M-F} are about the same order of magnitude for most bonds.

Table S6. Bond lengths between metal center and fluorine atoms (R_{M-F}) in relaxed ZrF_4/HfF_4 with the absolute difference in bond length between the two M-species (ΔR_{M-F}). For comparison, also the experimental bond lengths for ZrF_4 (R_{Zr-F}^{exp}) [25] are given together with the absolute difference to the relaxed values ($\Delta R_{Zr-F}^{\text{exp}}$). All values are given in Å.

bond	R_{Zr-F}	R_{Hf-F}	ΔR_{M-F}	R_{Zr-F}^{exp} [25]	$\Delta R_{Zr-F}^{\text{exp}}$
$M_A - F_1$	2.082	2.067	0.015	2.072	0.010
$M_A - F'_1$	2.082	2.067	0.015	2.072	0.010
$M_A - F_2$	2.082	2.068	0.014	2.072	0.010
$M_A - F'_2$	2.082	2.068	0.014	2.072	0.010
$M_A - F_3$	2.151	2.133	0.018	2.180	0.029
$M_A - F'_3$	2.151	2.133	0.018	2.180	0.029
$M_A - F_4$	2.069	2.054	0.015	2.052	0.017
$M_A - F'_4$	2.069	2.054	0.015	2.052	0.017
$M_B - F_1$	2.097	2.033	0.064	2.132	0.035
$M_B - F_2$	2.110	2.093	0.017	2.159	0.049
$M_B - F_3$	2.096	2.083	0.013	2.127	0.031
$M_B - F_4$	2.085	2.068	0.017	2.088	0.003
$M_B - F_5$	2.126	2.111	0.015	2.148	0.022
$M_B - F_6$	2.051	2.035	0.016	2.048	0.003
$M_B - F_7$	2.095	2.076	0.019	2.118	0.023
$M_B - F'_7$	2.047	2.083	0.036	2.031	0.016

5. Literature ZPE Energies on MO_2

92

Table S7. ZPE energies per formula unit (f.u.) obtained from the published optical phonon frequencies at the Γ -point calculated with the PBE, LDA or PW91 functional:

		ZPE(MO_2) in eV/f.u.	
		M = Zr	M = Hf
Zhao and Vanderbilt[8]	PBE	—	0.190
Luo et al.[11]	LDA	0.203	0.206
Kuwabara et al. [3]	PW91	0.192	—
Fadda et al.[5]	LDA	0.202	—
	PBE	0.190	—

6. Discussion on Zr/Hf differences in ΔE vs. ΔG

93

The main focus of our paper is to compare the affinity of Zr(IV) vs. Hf(IV) to form oxide or fluorides. We do not strive to accurately predict the formation energy released under experimental conditions, but rather the relative energy difference between Zr and Hf. For the comparison of the respective Zr(IV) and Hf(IV) reaction in Table 2, only the solid bulk compound changes. The molecular reactants or products remain identical when comparing the same reaction. Within this study, we compare Zr(IV) and Hf(IV) bulk materials. Within the bulk crystals itself, we do expect little temperature and due to their hardness very little pressure dependent contributions. A pressure induced phase transition would only occur at 3 GPa for ZrO_2 [29] and even 11 GPa for HfO_2 [30]. Thermally, all studied Zr and Hf oxides and fluorides are stable until at least 910°C [29,31,32]. Ab initio molecular dynamics calculations on the monoclinic to tetragonal phase transition of HfO_2 found a linear temperature dependence of ΔG up to 730°C [17]. This suggests that the anharmonic contributions are only decisive for temperatures beyond. Within their surface etching study, Mullins et al.[12] did calculate their ΔG as:

$$\Delta G = \Delta E_{\text{DFT}} + \Delta \text{ZPE} + \Delta W(T) - T\Delta S + RT\ln(Q)$$

The last term of volume work ($RT\ln(Q)$) is included, as they considered a variable number of gaseous molecules and thus variable pressures for reactants and products. Most

108

109

importantly, they considered a bulk or surface to gas-phase reaction. Q is the quotient of partial pressures of gaseous products divided by gaseous reactants. As entropic contributions (ΔS), they included the translational entropy of the gaseous molecules, as well as the surface entropy. Both do not play a role when comparing the Zr vs. Hf difference in bulk to bulk reactions. The enthalpic contributions ($\Delta W(T)$) and the difference in zero point energy (ΔZPE) have been calculated for the gaseous molecules by the rigid rotator, harmonic oscillator model, as well as for the first layer of surface atoms by a harmonic phonon calculation. They do not clarify, whether they also performed a phonon calculation for the bulk compounds.

Table S7 lists all found harmonic phonon DFT calculations by literature. No phonon calculations could be found for the fluorides. The only found measured spectra could only resolve 20 vibrations for ZrF_4 but 29 for HfO_2 , while by symmetry the monoclinic unit cell should have 27 optical phonons [33]. The ZPE of ZrO_2 at the LDA-level from Luo et al.[11] and Fadda et al.[5] agree very well, just do the two GGAs PBE and PW91 on ZrO_2 . One also sees that the ZPE at the PBE-level is identical to at least 1 meV per formula unit between ZrO_2 and HfO_2 when comparing from two sources. The only source calculating the full phonon spectra of both compounds at the LDA-level of Luo et al.[11] gives a slightly higher ZPE for the heavier HfO_2 by 3 meV per formula unit.

Harmonic vibrations are proportional to the force constant and anti-proportional to the square root of the reduced mass. Judged by the mass, the vibrational frequencies of HfO_2 should be lower than for the much lighter ZrO_2 . However, the Hf–O bond distances and thus the force constants of HfO_2 are significantly stronger. Because the mass difference dominates, the low frequency modes are considerably higher in energy for ZrO_2 than for HfO_2 as shown by calculations of Luo et al.[11] and measurements by Quintard et al. [34]. Within the high frequency regime of oxygen-dominated vibrations, both found slightly higher frequencies for HfO_2 than for ZrO_2 due to the stronger force constants.

Based on these observations on MO_2 , we make the following assumptions for the ZPE of MF_4 . Because of the slightly higher mass of F than O, the reduced masses of a single Hf–F bond grows stronger than the Zr one compared to the oxides. This should decrease the vibrational frequencies and thus lower the ZPE of HfF_4 vs. ZrF_4 . Comparing the ZPE per formula unit of the oxides vs. the fluorides, we expect a considerably higher value for the latter, because the formula unit contains 5 instead of 3 atoms. However, all additional atoms are fluorine and all Hf–F bonds are also shorter and thus expected to have stronger force constant than Zr–F. Consequently, these should add more high frequency vibrations dominated by fluorine. These could make the possible difference between Hf and Zr-species even smaller than the found 0–3 meV per formula unit for the oxides. Summing up, we expect the effect of stronger mass increase per single M–F bond within the fluorides on the one side and more anion-dominated vibrations with shorter interatomic distance Hf–F than Zr–F on the other side to counterbalance as they did in the oxides.

6.1. Test Calculations in the Gas-Phase

To invest why the bulk to gas-phase reactions reported by Mullins et al. [12] predict the opposite Zr to Hf trend as our bulk to bulk reactions, we performed additional gas-phase calculations.

We relaxed tetrahedral ZrF_4 and HfF_4 in the gas-phase by ORCA 5.0.3[35] at the PBE/def2-TZVP[36] level applying D_2 symmetry, a TightSCF and a final DFT grid of 5. When applying the Karlsruhe basis of def or def2, most programs use the corresponding Stuttgart effective core potentials (ECP) per default. For Zr, this default ECP contains 28 core electrons, while for Hf, this default ECP is a very large core with 60 electrons [37]. For comparison, we performed the same relaxation as all-electron calculation with additional ZORA [38,39] to account for the scalar relativistic effects. By the analytical Hessian, we obtain the ZPE. The relaxed bond lengths and ZPE are given in Table S8.

Table S8. Comparison of M–F bond length in Å and ZPE in meV per formula unit for molecular ZrF₄ and HfF₄ with or without ZORA:

	PBE/def2-TZVP		PBE/def2-TZVP/ZORA	
	R_{M-F}	ZPE	R_{M-F}	ZPE
ZrF ₄	1.103	217.5	1.100	214.3
HfF ₄	1.104	209.7	1.097	214.3

Table S8 shows that with the default ECP, PBE predicts a too large Hf–F bond distance, which results in a too small ZPE. Note that this is not observed in the solid state calculations, that are giving a smaller Hf–F than Zr–F distance. These test calculations suggest that for the gas-phase, it is vital not to use the default large core on Hf but to include all electrons and treat the scalar relativistic effects more explicitly than by ECP. However, according to their paper, Mullins et al. [12] did not include any relativistic correlation. They also do not state if they used a non-default smaller core on Hf.

References

- Králik, B.; Chang, E.K.; Louie, S.G. Structural properties and quasiparticle band structure of zirconia. *Phys. Rev. B* **1998**, *57*, 7027–7036. <https://doi.org/10.1103/PhysRevB.57.7027>.
- Jomard, G.; Petit, T.; Pasturel, A.; Magaud, L.; Kresse, G.; Hafner, J. First-principles calculations to describe zirconia pseudopolymorphs. *Phys. Rev. B* **1999**, *59*, 4044–4052. <https://doi.org/10.1103/PhysRevB.59.4044>.
- Kuwabara, A.; Tohei, T.; Yamamoto, T.; Tanaka, I. Ab initio lattice dynamics and phase transformations of ZrO₂. *Phys. Rev. B* **2005**, *71*, 64301. <https://doi.org/10.1103/PhysRevB.71.064301>.
- Fadda, G.; Colombo, L.; Zanzotto, G. First-principles study of the structural and elastic properties of zirconia. *Phys. Rev. B* **2009**, *79*, 214102. <https://doi.org/10.1103/PhysRevB.79.214102>.
- Fadda, G.; Zanzotto, G.; Colombo, L. First-principles study of the effect of pressure on the five zirconia polymorphs. II. Static dielectric properties and Raman spectra. *Phys. Rev. B* **2010**, *82*, 64106. <https://doi.org/10.1103/PhysRevB.82.064106>.
- Delarmelina, M.; Quesne, M.G.; Catlow, C.R.A. Modelling the bulk properties of ambient pressure polymorphs of zirconia. *Phys. Chem. Chem. Phys.* **2020**, *22*, 6660–6676. <https://doi.org/10.1039/D0CP00032A>.
- Demkov, A.A. Investigating Alternative Gate Dielectrics: A Theoretical Approach. *Phys. Status Solidi B* **2001**, *226*, 57–67. [https://doi.org/10.1002/1521-3951\(200107\)226:1<57::AID-PSSB57>3.0.CO;2-L](https://doi.org/10.1002/1521-3951(200107)226:1<57::AID-PSSB57>3.0.CO;2-L).
- Zhao, X.; Vanderbilt, D. Phonons and lattice dielectric properties of zirconia. *Phys. Rev. B* **2002**, *65*, 75105. <https://doi.org/10.1103/PhysRevB.65.075105>.
- Zhao, X.; Vanderbilt, D. First-principles study of structural, vibrational, and lattice dielectric properties of hafnium oxide. *Phys. Rev. B* **2002**, *65*, 233106. <https://doi.org/10.1103/PhysRevB.65.233106>.
- Jaffe, J.E.; Bachorz, R.A.; Gutowski, M. Low-temperature polymorphs of ZrO₂ and HfO₂: A density-functional theory study. *Phys. Rev. B* **2005**, *72*, 144107. <https://doi.org/10.1103/PhysRevB.72.144107>.
- Luo, X.; Zhou, W.; Ushakov, S.V.; Navrotsky, A.; Demkov, A.A. Monoclinic to tetragonal transformations in hafnia and zirconia: A combined calorimetric and density functional study. *Phys. Rev. B* **2009**, *80*, 134119. <https://doi.org/10.1103/PhysRevB.80.134119>.
- Mullins, R.; Kondati Natarajan, S.; Elliott, S.D.; Nolan, M. Self-Limiting Temperature Window for Thermal Atomic Layer Etching of HfO₂ and ZrO₂ Based on the Atomic-Scale Mechanism. *Chem. Mater.* **2020**, *32*, 3414–3426. <https://doi.org/10.1021/acs.chemmater.9b05021>.
- Debernardi, A.; Fanciulli, M. Structural and vibrational properties of high-dielectric oxides, HfO₂ and TiO₂: A comparative study. *Mater. Sci. Semicond. Process.* **2006**, *9*, 1014–1019. <https://doi.org/10.1016/j.mssp.2006.10.036>.
- Li, J.; Han, J.; Meng, S.; Lu, H.; Tohyama, T. Optical properties of monoclinic HfO₂ studied by first-principles local density approximation + U approach. *Appl. Phys. Lett.* **2013**, *103*, 071916. <https://doi.org/10.1063/1.4818765>.
- Li, J.; Meng, S.; Niu, J.; Lu, H. Electronic structures and optical properties of monoclinic ZrO₂ studied by first-principles local density approximation + U approach. *J. Adv. Ceram.* **2017**, *6*, 43–49. <https://doi.org/10.1007/s40145-016-0216-y>.
- Laudadio, E.; Stipa, P.; Pierantoni, L.; Mencarelli, D. Phase Properties of Different HfO₂ Polymorphs: A DFT-Based Study. *Crystals* **2022**, *12*. <https://doi.org/10.3390/cryst12010090>.
- Low, J.J.; Paulson, N.H.; D’Mello, M.; Stan, M. Thermodynamics of monoclinic and tetragonal hafnium dioxide (HfO₂) at ambient pressure. *Calphad* **2021**, *72*, 102210. <https://doi.org/j.calphad.2020.102210>.
- Rivas-Silva, J.F.; Flores-Riveros, A.; Durand-Niconoff, J.S.; Aquino, N. Ab initio analysis of some fluoride and oxide structures doped with Pr and Yb. *Int. J. Quantum Chem.* **2004**, *97*, 815–825. <https://doi.org/10.1002/qua.10779>, <https://doi.org/10.1002/qua.10779>.
- Smith, D.K.; Newkirk, W. The crystal structure of baddeleyite (monoclinic ZrO₂) and its relation to the polymorphism of ZrO₂. *Acta Cryst.* **1965**, *18*, 983–991. <https://doi.org/10.1107/S0365110X65002402>.

20. Howard, C.J.; Hill, R.J.; Reichert, B.E. Structures of ZrO₂ polymorphs at room temperature by high-resolution neutron powder diffraction. *Acta Crystallogr. B* **1988**, *44*, 116–120. <https://doi.org/10.1107/S0108768187010279>. 210
21. French, R.H.; Glass, S.J.; Ohuchi, F.S.; Xu, Y.N.; Ching, W.Y. Experimental and theoretical determination of the electronic structure and optical properties of three phases of ZrO₂. *Phys. Rev. B* **1994**, *49*, 5133–5142. <https://doi.org/10.1103/PhysRevB.49.5133>. 211
22. Lucovsky, G.; Fulton, C.C.; Zhang, Y.; Zou, Y.; Luning, J.; Edge, L.F.; Whitten, J.L.; Nemanich, R.J.; Ade, H.; Schlom, D.G.; et al. Conduction band-edge States associated with the removal of d-state degeneracies by the Jahn-Teller effect. *IEEE Trans. Device Mater. Reliab.* **2005**, *5*, 65–83. <https://doi.org/10.1109/TDMR.2005.845804>. 212
23. Balog, M.; Schieber, M.; Michman, M.; Patai, S. Chemical vapor deposition and characterization of HfO₂ films from organo-hafnium compounds. *Thin Solid Films* **1977**, *41*, 247–259. [https://doi.org/10.1016/0040-6090\(77\)90312-1](https://doi.org/10.1016/0040-6090(77)90312-1). 213
24. Pathak, S.; Das, P.; Das, T.; Mandal, G.; Joseph, B.; Sahu, M.; Kaushik, S.D.; Siruguri, V. Crystal structure of monoclinic hafnia (HfO₂) revisited with synchrotron X-ray, neutron diffraction and first-principles calculations. *Acta Crystallogr. C* **2020**, *76*, 1034–1042. <https://doi.org/10.1107/S2053229620013960>. 214
25. Legein, C.; Fayon, F.; Martineau, C.; Body, M.; Buzaré, J.Y.; Massiot, D.; Durand, E.; Tressaud, A.; Demourgues, A.; Péron, O.; et al. 19F High Magnetic Field NMR Study of β -ZrF₄ and CeF₄: From Spectra Reconstruction to Correlation between Fluorine Sites and 19F Isotropic Chemical Shifts. *Inorg. Chem.* **2006**, *45*, 10636–10641. <https://doi.org/10.1021/ic061339a>. 215
26. Benner, G.; Müller, B.G. Zur Kenntnis binärer Fluoride des ZrF₄-Typs: HfF₄ und ThF₄. *Z. anorg. allg. Chem.* **1990**, *588*, 33–42. <https://doi.org/10.1002/zaac.19905880105>. 216
27. Maimaitiyili, T.; Steuwer, A.; Blomqvist, J.; Bjerkén, C.; Blackmur, M.S.; Zanellato, O.; Andrieux, J.; Ribeiro, F. Observation of the δ to ϵ Zr-hydride transition by in-situ synchrotron X-ray diffraction. *Cryst. Res. Technol.* **2016**, *51*, 663–670. <https://doi.org/10.1002/crat.201600234>. 217
28. Romans, P.A.; Paasche, O.G.; Kato, H. The transformation temperature of hafnium. *J. Less-Common Met.* **1965**, *8*, 213–215. [https://doi.org/10.1016/0022-5088\(65\)90048-2](https://doi.org/10.1016/0022-5088(65)90048-2). 218
29. Block, S.; Da Jornada, J.A.H.; Piermarini, G.J. Pressure-Temperature Phase Diagram of Zirconia. *J. Am. Ceram. Soc.* **1985**, *68*, 497–499. <https://doi.org/10.1111/j.1151-2916.1985.tb15817.x>. 219
30. Al-Khatatbeh, Y.; Lee, K.K.M.; Kiefer, B. Phase diagram up to 105 GPa and mechanical strength of HfO₂. *Phys. Rev. B* **2010**, *82*, 144106. <https://doi.org/10.1103/PhysRevB.82.144106>. 220
31. McDonald, R.A.; Sinke, G.C.; Stull, D.R. High Temperature Enthalpy, Heat Capacity, Heat of Fusion, and Melting Point of Zirconium Tetrafluoride. *J. Chem. Eng. Data* **1962**, *7*, 83. <https://doi.org/10.1021/je60012a026>. 221
32. Sicius, H. Titangruppe: Elemente der vierten Nebengruppe. In *Handbuch der chemischen Elemente*; Sicius, H., Ed.; Springer Berlin Heidelberg: Berlin, Heidelberg, 2021; pp. 483–529. https://doi.org/10.1007/978-3-662-55939-0_19. 222
33. Goldstein, M.; Hughes, R.J.; Unsworth, W.D. Vibrational spectra of some heavy metal tetrafluorides in the solid state. *Spectrochim. Acta A* **1975**, *31*, 621–624. [https://doi.org/10.1016/0584-8539\(75\)80055-9](https://doi.org/10.1016/0584-8539(75)80055-9). 223
34. Quintard, P.E.; Barbéris, P.; Mirgorodsky, A.P.; Merle-Méjean, T. Comparative Lattice-Dynamical Study of the Raman Spectra of Monoclinic and Tetragonal Phases of Zirconia and Hafnia. *J. Am. Ceram. Soc.* **2002**, *85*, 1745–1749. <https://doi.org/10.1111/j.1151-2916.2002.tb00346.x>. 224
35. Neese, F. Software update: The ORCA program system—Version 5.0. *WIREs Comput Mol Sci.* **2022**, *12*, e1606. <https://doi.org/10.1002/wcms.1606>, <https://doi.org/10.1002/wcms.1606>. 225
36. Weigend, F.; Ahlrichs, R. Balanced basis sets of split valence, triple zeta valence and quadruple zeta valence quality for H to Rn: Design and assessment of accuracy. *Phys. Chem. Chem. Phys.* **2005**, *7*, 3297–3305. <https://doi.org/10.1039/B508541A>. 226
37. Andrae, D.; Häußermann, U.; Dolg, M.; Stoll, H.; Preuß, H. Energy-adjusted ab initio pseudopotentials for the second and third row transition elements. *Theoret. Chim. Acta* **1990**, *77*, 123–141. <https://doi.org/10.1007/BF01114537>. 227
38. van Wüllen, C. Molecular density functional calculations in the regular relativistic approximation: Method, application to coinage metal diatomics, hydrides, fluorides and chlorides, and comparison with first-order relativistic calculations. *J. Chem. Phys.* **1998**, *109*, 392–399. doi: 10.1063/1.476576, <https://doi.org/10.1063/1.476576>. 228
39. Pantazis, D.A.; Chen, X.Y.; Landis, C.R.; Neese, F. All-Electron Scalar Relativistic Basis Sets for Third-Row Transition Metal Atoms. *J. Chem. Theory Comput.* **2008**, *4*, 908–919. doi: 10.1021/ct800047t, <https://doi.org/10.1021/ct800047t>. 229

3.2. Paper B.1

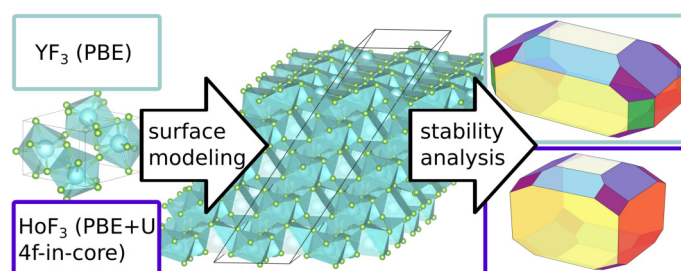
"First Principle Surface Analysis of YF_3 and Isostructural HoF_3 "

J. Anders, N. Limberg, B. Paulus, *Materials*, **2022**, 15, 6048.

DOI: 10.3390/ma15176048

URL: <https://doi.org/10.3390/ma15176048>

Creative commons license: <https://creativecommons.org/licenses/by/4.0/>



graphical abstract of paper **B.1**.

Contributions:

The conceptualization was done by Jennifer Anders (J.A.) and Beate Paulus (B.P.). The formal analysis was done by J.A. and Niklas Limberg (N.L.). Funding acquisition was done by B.P. Resources acquisition was done by J.A. and B.P. Investigations were done by J.A. Supervision was done by B.P. Validation and visualization was done by J.A. The original draft was written by, J.A. Review writing and editing was done by J.A., N.L., and B.P.

Article

First Principle Surface Analysis of YF_3 and Isostructural HoF_3

Jennifer Anders , Niklas Limberg , Beate Paulus

Institute for Chemistry and Biochemistry, Freie Universität Berlin, Arnimallee 22, 14195 Berlin, Germany

* Correspondence: jennifer.anders@fu-berlin.de

Abstract: The trifluorides of the two high field strength elements yttrium and holmium are studied by periodic density functional theory. As a lanthanide, holmium also belongs to the group of rare earth elements (REE). Due to their equivalent geochemical behavior, both elements form a geochemical twin pair and consequently, yttrium is generally associated with the REE as REE+Y. Interestingly, it has been found that DFT/DFT+U describe bulk HoF_3 best, when the 4f-electrons are excluded from the valence region. An extensive surface stability analysis of YF_3 (PBE) and HoF_3 (PBE+ $U_d/3$ eV/4f-in-core) using two-dimensional surface models (slabs) is performed. All seven low-lying Miller indices surfaces are considered with all possible stoichiometric or substoichiometric terminations with a maximal fluorine-deficit of two. This leads to a scope of 24 terminations per compound. The resulting Wulff plots consists of seven surfaces with 5–26% abundance for YF_3 and six surfaces with 6–34% for HoF_3 . The stoichiometric (010) surface is dominating in both compounds. However, subtle differences have been found between these two geochemical twins.

Keywords: geochemical twins; REE; HFSE; waimirite; DFT; DFT+U; Hubbard; surface energy; Wulff plots



Citation: Anders, J.; Limberg, N.; Paulus, B. First Principle Surface Analysis of YF_3 and Isostructural HoF_3 . *Materials* **2022**, *15*, 6048. <https://doi.org/10.3390/ma15176048>

Academic Editor: Anastasios J. Tasiopoulos

Received: 3 August 2022

Accepted: 24 August 2022

Published: 1 September 2022

Corrected: 14 July 2023

Publisher's Note: MDPI stays neutral with regard to jurisdictional claims in published maps and institutional affiliations.



Copyright: © 2022 by the authors. Licensee MDPI, Basel, Switzerland. This article is an open access article distributed under the terms and conditions of the Creative Commons Attribution (CC BY) license (<https://creativecommons.org/licenses/by/4.0/>).

1. Introduction

Yttrium and holmium form a geochemical twin pair. The term emphasizes their identical geochemical behavior caused by the equal ratio of charge to radius in their only stable oxidation state +III. According to their small ionic radii of 1.075 Å (Y) and 1.072 Å (Ho) in nine-fold coordination [1] and their high oxidation state, both belong to the interesting group of high field strength elements (HFSE). As a lanthanide, holmium also belongs to the rare earth elements (REE). Due to their twin character, yttrium is also often associated with that group [2–4].

As fluorides, both metals can be used for different specific applications. The wide-band-gap material YF_3 has very good properties for laser applications [5–8]. Doped with trivalent REE cations, YF_3 is also applicable as an optical filter in 157-nm photolithography [9]. Another emerging field of application is solid-state fluoride batteries, resulting from the very high conductivity of fluoride anions [10–14]. HoF_3 is interesting for magnetic high-field applications as, e.g., a contrast agent, due to the very high magnetic moment of holmium [15,16]. Moreover, YF_3 and HoF_3 are important precursors for the synthesis of the respective pure metallic compounds [17,18]. In nature, YF_3 is found within the mineral waimirite-(Y), which contains high concentrations of other REE [8]. Fluoride plays a significant role in accumulating HFSE and REE within hydrothermal fluids, as these cations do not form such stable complexes with chloride [2,19–21]. Interestingly, those fluoride-rich hydrothermal fluids produce ores with a non-chondritic excess of yttrium over holmium. It is suggested that one underlying reason for the twin separation is their different affinity to fluorine, which was found in dissolving experiments of YF_3 and HoF_3 in diluted hydrofluoric acid [20]. To lay one foundation for future quantum chemical studies on the different fluorine-affinity of yttrium and holmium, we started with an investigation of the respective trifluorides and their surfaces.

In accordance with their twin behavior, solid YF_3 and HoF_3 occur in the same crystal structure type of $\beta\text{-YF}_3$ (space group $Pnma$, fully occupied Wyckoff positions (Y) 4c, (F) 4c, (F) 8d (Figure 1)) [18,22,23]. This is their only stable phase up to 1343 K (HoF_3) or 1350 K (YF_3), which is well beyond the temperature regime of hydrothermal fluids of typically 323–873 K [7,18,24,25]. The ionic radii of the middle and late lanthanides Sm(III)–Lu(III) differ by only ≤ 6 pm compared to Y(III) [1]. Consequently, all their trifluorides crystallize as well in $\beta\text{-YF}_3$ [18,22,23,26–31]. The same low-temperature phase is also found for the two actinides Bk(III) and Cf(III) [32–34]. Due to the often observed analogy of actinides to lanthanides, the same crystal structure is assumed for the, so far, experimentally unknown heavier actinide trifluorides of Es(III)–Lr(III) [35]. Interestingly, the known orthorhombic low-temperature phase of plutonium trihydride is also reasoned to be an exotic example of a $\beta\text{-YF}_3$ structure [36]. Outside the f-block, the $\beta\text{-YF}_3$ -structure is experimentally known for bismuth trifluoride [23,37,38] and predicted as an accessible meta-stable phase for the trichlorides of Y(III) and Bi(III) [38].

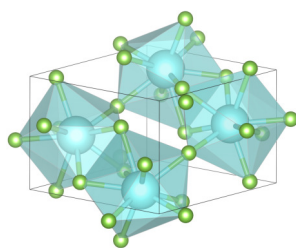


Figure 1. The orthorhombic unit cell of $\beta\text{-YF}_3$ with $Pnma$ symmetry. Lattice constants are given in Table 1. The distorted tricapped trigonal prisms formed by nine fluorides (green) around each yttrium (cyan) are visualized by transparent, cyan planes.

Table 1. Comparison of the relaxed unit cells to experiment including standard deviation in parentheses [22,23]. Given is the absolute difference (Δ), as well as the deviation from experiment in percentage ($\Delta\%$).

	YF_3 (PBE)				HoF_3 (PBE+ $U_d/3$ eV/4f-in-Core)			
	a (Å)	b (Å)	c (Å)	V (Å ³)	a (Å)	b (Å)	c (Å)	V (Å ³)
calc.	6.3215	6.8059	4.3300	186.29	6.4164	6.8796	4.3440	191.76
exp. [22]	6.353(3)	6.850(3)	4.393(3)	191.2	6.404(3)	6.875(3)	4.379(3)	192.8
Δ	0.032	0.044	0.063	4.9	0.012	0.005	0.035	1.0
$\Delta\%$	0.5%	0.6%	1.4%	2.6%	0.2%	0.1%	0.8%	0.5%
exp. [23]	6.3537(7)	6.8545(7)	4.3953(5)	191.42				
Δ	0.0322	0.0486	0.0653	5.13				
$\Delta\%$	0.5%	0.7%	1.5%	2.7%				

To the best knowledge of the authors, no first principle surface stability analysis of any compound within the whole structure type is available in the literature. The only surface calculation of any compound of $\beta\text{-YF}_3$ structure was published in 2013 by Ye et al. [39] on two selected surfaces of DyF_3 (001) and (101). They only calculated the surfaces matching their experimentally obtained nano-plates. However, these and other experiments on this class of compounds clearly demonstrate that the obtained surface structures are very dependent on the experimental conditions, especially on the utilized nature and geometry of the substrate, as well as on the solvent and fluoride concentration [14,16,40–45]. The present work analyzes the inherent quantum chemical stability of all of the seven low Miller indices (hkl) surfaces, namely (001), (010), (100), (011), (101), (110) and (111). A previous study on another metal trifluoride, AlF_3 revealed stoichiometric or substoichiometric surfaces with a small fluorine-deficit as the most stable terminations [46]. Additionally, a substoichiometric fluorine content has also been found for YbF_3 thin films made from

ion assisted deposition [47]. Consequently, this study includes all possible stoichiometric terminations and those with a small-to-moderate fluorine-deficit of 1–2 fluorine atoms per surface unit cell. This results in a scope of 24 terminations. The obtained surface energy results are combined with the geometry of the surface cut by a Wulff analysis to examine the expected surface abundance [48,49].

2. Methodology

2.1. Computational Details

All calculations were performed in the Vienna Ab Initio Simulation Package (VASP, version 5.4.4) [50] on the supercomputer cluster HLRN in Berlin and Göttingen, Germany, using periodic density functional theory (DFT) with a generalised gradient approximation (GGA). As an exchange–correlation functional, the one of Perdew–Burke–Ernzerhof (PBE) is applied [51]. The inner shell electrons were described by the projector augmented wave (PAW) method [52,53]. The outer shell electrons were expanded in plane waves.

For converged YF₃ total bulk energies, the VASP potential files F_h (“hard”, 7 electrons) and Y_sv (11 electrons) were applied together with a 9 × 9 × 9 Monkhorst–Pack grid. In accordance with the F_h potential file, a kinetic energy cut-off of 772.6 eV was used. For HoF₃, both available Ho potential files Ho_3 (9 electrons, 4f-in-core) and Ho (21 electrons, 4f-in-valence) were evaluated with respective grid sizes of 7 × 7 × 7 and 3 × 3 × 3. On holmium, the Hubbard-type correction in the simple Dudarev formalism was applied [54]. In a test series of 1–10 eV in 1 eV steps with U_d (with Ho_3) and U_f (with Ho), PBE+U_d with 3 eV agreed best with the crystal structure and the presumed electronic structure (Table 1 and Figures S1 and S2). As an electronic structure reference, bulk HoF₃ was also calculated with the Heyd–Scuseria–Ernzerhof hybrid functional (HSE06) [55].

For electron smearing, tests on several bulk and slabs structures of both trifluorides were performed, comparing Gaussian smearing with the tetrahedron method with Blöchl correction [56]. No energy difference within the applied self-consistent field (SCF) convergence criteria could be found. We therefore used Gaussian smearing on our insulating trifluorides.

Apart from the trifluorides, molecular fluorine, as well as metallic yttrium and holmium, were also considered. The first was calculated in a cubic box of 25 Å length. For the latter two, Gaussian smearing could not be applied. A convergence test with 1st and 2nd-order Methfessel–Paxton smearing with widths of 0.05–0.35 eV yielded 2nd-order Methfessel–Paxton smearing with a width of 0.10 eV (Y) or 0.15 eV (Ho) as the best combination to minimize the difference between total energy and free energy.

Each bulk structure started from the respective, experimental crystal structure (YF₃[23], HoF₃ [22], Y [57], Ho [58]) and was fully relaxed in atomic positions, lattice constants and volume. The accurate precision setting was applied. As convergence criteria, 0.01 meV per unit cell was used for SCF total energies and 0.1 meV per unit cell for the difference in total energy between two ionic steps. Final total energies, density of states (DOS) and Bader charges were performed with an SCF criteria of 0.001 meV. All DOS plots and Bader charges, as well as all HoF₃ data, were calculated with allowed spin polarization. To aid SCF convergence, an additional support grid (.ADDGRID.) and/or a reduced minimal mixing parameter for Kerker’s initial approximation [59] (AMIN) of <0.01 were applied on most slabs.

Symmetric slabs were built from the relaxed bulk structure with the Python package pymatgen [60,61]. The vacuum height perpendicular to the surface was tested for one stoichiometric termination of YF₃ (001). The converged value of 25 Å was applied for all slabs. For slab calculations, only one *k*-point was used perpendicular to the surface. For the other two directions, we applied the same *k*-point grid size as in bulk. The complete slabs were relaxed in atomic positions.

DOS plots and band structures were generated with pymatgen. Wulff plots were constructed with the WulffPack Python package [62]. Atomic structures were visualized in VESTA [63].

2.2. Choice of Electronic Structure Method

The effect of dispersion was tested by applying Grimme's dispersion correction with Becke–Johnson damping (D3(BJ)) [64]. From PBE to PBE+D3(BJ), the lattice constants changed only by 1.9–4.5 pm or 0.3–1.0% during the full optimization of atomic positions, lattice constants and volume of YF₃. Due to this small deviation, we neglected dispersion correction for our highly ionic systems.

For HoF₃, a test series was performed to decide whether to treat the 4f-electrons inside the core or at the valence level. Hubbard-type Coulomb parameters of 1–10 eV were scanned for the 4f-in-core with U_d acting on Ho-d orbitals, as well as for 4f-in-valence with U_f acting on Ho-f orbitals. It should be noted that the Ho-5d orbitals mainly constituted the broad conduction band in both approaches. Yet, they also hybridized in the valence band mainly constructed by F-2p (Figure S3). The PBE+U benchmark plots for unit cell parameters and band gaps are given in the SI with further discussion (Figures S1 and S2). All HoF₃ (PBE+U_d/4f-in-core) band structures resembled the YF₃ (PBE) one and produced comparable F-2p to Ho-5d or Y-4d charge transfer band gaps of 7–8 eV (Figure S3). By adding exact exchange via HSE06/4f-in-core, these bands were further separated to 11 eV. Whereas, HSE06/4f-in-valence predicted an Ho-4f to Ho-4f transition of 8 eV. In contrast, PBE/4f-in-valence was not able to separate the partially filled 4f¹⁰ into un-/occupied bands. Instead, it placed the Fermi-level (E_F) inside the 4f band, predicting a pseudo-metal. When introducing the additional Coulomb potential of 1–10 eV onto the 4f in PBE+U_f, this 4f–4f gap was tuneable from 1 eV to a maximum of 6 eV. At U_f ≥ 5 eV, the nature of the band gap changed to a charge transfer of F-2p to Ho-4f. Unfortunately, no measured band gap exists in the literature for HoF₃. Therefore, it was not possible to pin-point the true band gap, nor to evaluate the correct nature of that transition. Nevertheless, based on a purely empirical model derived from other lanthanide compounds, HoF₃ is expected to have a band gap of ca. 9 eV [65]. This empirically estimated band gap, as well as the calculated HSE06 reference, were best reproduced without including the 4f-electrons explicitly.

Another quantity upon which to judge the applied electronic structure method was the Bader charges obtained by applying the atoms in molecules (AIM) population analysis [66–70]. For both bulk materials of YF₃ and HoF₃, all tested methods predicted a metal charge of 2.2–2.4 e and fluorine charge of −(0.7–0.8) e. The Bader charges of all applied methods with 4f-in-core or valence agreed well with each other and thus suggested that including 4f explicitly was not necessary for HoF₃.

Furthermore, all methods used with 4f-in-valence predicted a high-spin bulk unit cell with all four holmium aligned resulting in an electronic magnetic moment of 16 μ_B. This ferromagnetic result was obtained even when starting from anti-ferromagnetic spin arrangements. According to the experimentally known magnetic structures, the physically correct spin arrangement is anti-ferromagnetic below 0.53 K or paramagnetic above [71].

To summarize, not including the 4f-electrons explicitly provided the best electronic structure results. The differences between simple PBE and PBE+U_d were minor. When considering the unit cell parameters given in Table 1, PBE+U_d/3 eV/4f-in-core performed best with deviations of as little as 0.1–0.8%.

2.3. Surface Energy

The surface formation energy (E_{surf}) is generally calculated from the total energy of the 2D-periodic slab (E_n), the energy of the 3D-periodic bulk unit cell (E_{bulk}) and the surface area of the slab (A):

$$E_{\text{surf}}^{\text{bd}} = \frac{E_n - nE_{\text{bulk}}}{2A}. \quad (1)$$

n is the slab thickness measured in unit cells. We label this bulk-derived surface energy E_{surf}^{bd}. Equation (1) is used for all YF₃ surface energies. In this work, we also considered surfaces with a substoichiometric amount of fluorine. For these, the fluorine potential μ_F for each missing fluorine was added to the numerator of Equation (1). μ_F was obtained from

E_{bulk} , the bulk energy per atom of the pure metal of yttrium or holmium (μ_{M}), as well as the number of metal ($n_{\text{M}} = 4$) and fluorine ($n_{\text{F}} = 12$) atoms within the bulk MF_3 unit cell:

$$\mu_{\text{F}} = \frac{E_{\text{bulk}} - n_{\text{M}}\mu_{\text{M}}}{n_{\text{F}}}. \quad (2)$$

Yet, as pointed out by Boettger, this bulk-derived surface energy ($E_{\text{surf}}^{\text{bd}}$) can lead to diverging E_{surf} with respect to n [72]. This can be avoided by using slab-derived (sd) energies only:

$$E_{\text{surf}}^{\text{sd}} = \frac{E_n - n(E_n - E_{n-1})}{2A}. \quad (3)$$

E_{bulk} is then replaced by the difference of E_n to the total energy of the next smaller slab (E_{n-1}). For HoF_3 , we indeed observed linearly diverging $E_{\text{surf}}^{\text{bd}}$ when applying Equation (1), despite system sizes of up to 7 UC or $\text{Ho}_{28}\text{F}_{84}$. Depending on the (hkl) , this stoichiometry corresponds to 12, 24 or 26 HoF_3 -layers. Likely, this is a result of the allowed spin-polarization with Hubbard-type correction and atomic relaxation of the whole slab. It can be seen in Table S3, that this linear divergence only appears after relaxation in $E_{\text{surf,opt}}^{\text{bd}}$. The unrelaxed surface energies $E_{\text{surf,SP}}^{\text{bd}}$ show no divergence. In YF_3 , no divergent $E_{\text{surf,opt}}^{\text{bd}}$ are observed. Here, no Hubbard-type correction is applied and the atomic relaxation is performed without spin polarization. A comparison of slab convergence by both equations is given in Tables S2 and S3. Due to the divergence issue, all HoF_3 surface energies given within this paper are slab-derived using Equation (3), which nicely converge. As each $E_{\text{surf}}^{\text{sd}}$ is derived from two slabs differing by one unit cell in size, at least three slabs are needed to determine convergence. Whereas for $E_{\text{surf}}^{\text{bd}}$, these are just two. Due to the observed convergence of $E_{\text{surf}}^{\text{bd}}$ in YF_3 , only two slab thicknesses are modeled for many terminations. Therefore, the convergence of the respective $E_{\text{surf}}^{\text{sd}}$ cannot be evaluated. As a consequence, we used the converged $E_{\text{surf}}^{\text{bd}}$ for YF_3 to compare with the converged HoF_3 $E_{\text{surf}}^{\text{sd}}$. All YF_3 bulk-derived surface energies converged within 0.03 J m^{-2} at slab thickness of about 5–5.5 UC or 10–22 YF_3 -layers (Table S2). The HoF_3 slab-derived surface energies of 14 terminations, including all of the most stable ones per Miller indices, converged to 0.01 J m^{-2} or less within a slab thickness of about 6–6.5 UC or 12–26 HoF_3 -layers (Table S3). Some of the higher energy terminations converged only to $0.02\text{--}0.04 \text{ J m}^{-2}$ at that thickness, while four high energy terminations did not converge even to 0.1 J m^{-2} . Fortunately, it is clear from their surface energies that even within the present uncertainty, those high energy terminations do not compete with the lowest energy ones. The slab thickness convergence for HoF_3 is visualized by error bars in Figure S5.

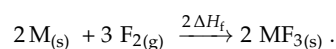
3. Results and Discussion

3.1. Bulk Properties

For YF_3 , the PBE relaxed lattice constants, given in Table 1, agree very well with both experimental values, which are underestimated by as little as 0.5–1.5% [22,23]. The resulting unit cell volume is underestimated by 2.6–2.7%, which is still in good agreement for a GGA functional. The best performing HoF_3 method against the only available experimental unit cell data and the calculated HSE06 band gaps was found to be $\text{PBE} + \text{U}_d / 3 \text{ eV} / 4\text{f-in-core}$. The resulting unit cell parameters deviate by as little as 0.1–0.8%.

The respective F–M bond length on the PBE (YF_3) and $\text{PBE} + \text{U}_d$ level (HoF_3) are $R_{\text{F-Y}} = \{2.28; 2.29; 2.46\} \text{ \AA}$ and $R_{\text{F-Ho}} = \{2.30; 2.32; 2.45\} \text{ \AA}$. These agree perfectly with the measured interatomic distances of 2.3–2.6 \AA [22,23].

Before we come to the surfaces, we evaluate possible energetic differences between the two geochemical twins as bulk materials. We calculate the electronic contribution to the formation enthalpies (ΔH_f) according to:



The electronic energies are taken from the bulk metals in hcp ($P63/mmc$) structure and the bulk trifluorides, as well as molecular fluorine. For YF_3 , we obtained an electronic contribution of $-1591.1 \text{ kJ mol}^{-1}$ versus $-1587.3 \text{ kJ mol}^{-1}$ for HoF_3 . Thus, judged by the electronic energies only, both trifluorides are equally strong bound with a very small favor of -3.7 kJ mol^{-1} or 0.2% for YF_3 over HoF_3 .

3.2. Surface Energies

The surface energies of all calculated terminations are given in Table 2. The given metal surface coordination number (CN_{surf}) is determined with a bond length cut-off of $R_{F-M} \leq 2.60 \text{ \AA}$. Table 2 also includes the nominal net surface charge (q_{surf}) caused by substoichiometric fluoride. Finally, the last column includes the surface abundance for each respective most stable termination predicted by Wulff construction ($\%_{surf}$).

Table 2. The YF_3 (PBE) and HoF_3 (PBE+ $U_d/3 \text{ eV}/4f$ -in-core) surfaces with respective terminations (term.), slab thickness in layers of formula units without terminal F-deficit (L_{MF_3}), nominal surface net charge (q_{surf}) in e, surface energies of relaxed (E_{surf}) and unrelaxed slabs ($E_{surf}^{unrel.}$) in J m^{-2} , as well as the relaxed surface metal coordination number (CN_{surf}). The lowest surface energies per (hkl) cut are highlighted in bold. For these, also the abundance obtained by the Wulff plot ($\%_{surf}$) is given.

(hkl)	term.	q_{surf}	L_{MF_3}		CN_{surf}		$E_{surf} (E_{surf}^{unrel.})$		$\%_{surf}$	
			YF_3	HoF_3	YF_3	HoF_3	YF_3	HoF_3	YF_3	HoF_3
(100)	1	0	20	24	5,9		1.61 (2.87)	0.93 (1.48)	7%	25%
	2	0	22	26	6,9		1.03 (2.02)	0.58 (0.96)		
	3	+1	20	24	5,8		1.24 (1.61)	0.62 (0.68)		
	4	+2	22	26	4,7		1.79 (2.14)	0.87 (0.90)		
(010)	1	0	10	12	8,8		0.58 (0.84)	0.47 (0.49)	26%	34%
	2	+2	10	12	6,6		1.80 (2.05)	1.52 (1.52)		
(001)	1	0	20	24	5,8,8,9		1.23 (2.45)	1.37 (2.25)	10%	6%
	2	0	22	26	6,7,8,9		0.58 (1.39)	0.67 (1.16)		
	3	+2	22	26	4,5,8,9		1.27 (1.70)	1.23 (1.29)		
(110)	1	0	20	24	6,8,8		1.01 (1.80)	0.99 (1.59)	5%	0%
	2	0	22	26	6,8,8		1.00 (2.41)	1.00 (2.18)		
	3	+2	22	26	4,6,9	4,6,8	1.42 (1.73)	2.09 (1.36)		
(101)	1	0	20	24	6,7,8,8		0.82 (1.48)	0.89 (1.33)	20%	14%
	2	0	20	24	6,6,8,8		0.82 (3.34)	0.88 (3.17)		
	3	+1	20	24	6,7,8,8		0.76 (1.16)	0.69 (0.89)		
	4	+1	22	26	5,6,7,9	5,6,8,8	1.07 (2.10)	1.03 (1.70)		
	5	+2	20	24	4,5,8,8	5,6,8,8	0.98 (1.39)	0.99 (0.99)		
(011)	1	0	10	12	7,7,9,9		0.78 (1.30)	0.81 (1.14)	22%	13%
	2	0	10	12	6,6,8,8		0.61 (1.32)	0.68 (1.15)		
	3	+2	10	12	4,4,8,8		1.25 (1.68)	1.35 (1.38)		
(111)	1	0	20	24	6,7,7,8	7,7,8,8	1.02 (3.46)	0.87 (3.29)	10%	7%
	2	+1	20	24	5,6,8,8		0.83 (1.30)	0.82 (1.04)		
	3	+1	22	26	6,6,7,9		1.05 (1.70)	0.75 (1.11)		
	4	+2	20	24	5,5,7,7		0.93 (1.22)	0.95 (1.13)		

The two terminations, (110)-1 and -2 greatly illustrate the importance of atomic relaxation of the surface prior analysis. Before relaxation, nothing but the very surface layer differs within each (hkl) cut. As both terminations are stoichiometric, they are also identical in composition. However, for both trifluorides, the unrelaxed (110)-1 surface is by 0.6 J m^{-2} more stable than the one of (110)-2 (see $E_{surf}^{unrel.}$ in Table 2). When allowed to relax in atomic positions, the {5,9,8} surface coordinations of (110)-2 rearrange into {6,8,8} (Table S1 and Figure S4). Hence, the surface energy reduces by as much as 1.41 J m^{-2} for YF_3 or 1.18 J m^{-2} for HoF_3 . In contrast, termination (110)-1 already starts at a higher surface coordination of {6,9,8}, before it also rearranges into {6,8,8}. According to the lesser degree of rearrangement, its surface energy only reduces by 0.79 J m^{-2} for YF_3 or 0.60 J m^{-2} for HoF_3 . Both rearranged terminations are structurally equivalent.

The argumentation in CN_{surf} cannot only be applied to explain the high $E_{surf}^{unrel.}$ of some terminations, but is also partially applicable to the relaxed E_{surf} . Within all YF_3 (hkl) subsets, except those of (101) and (111), the respective smallest CN_{surf} value correlates with E_{surf} . Thus, the smaller the smallest coordination polyhedron, the less stable the surface and the

higher its surface energy. For example, a 4-fold coordination, as present in many surfaces with a fluorine-deficit of two, is only found for the highest E_{surf} within the (hkl) subset. Yet, this correlation holds only for the very minimal value within a set of CN_{surf} . No correlation can be found for the remaining, higher CN_{surf} values of the same surface. Therefore, these cannot explain the energetic order of two terminations showing the same smallest CN_{surf} value (as seen e.g., in YF_3 (100)-1 and -3 in Table 2). For HoF_3 , this correlation of surface coordination and stability has two more exceptions. Here, the stability of the least and second-least stable (100) and (001) terminations flip compared to YF_3 , without any change in CN_{surf} . Prior to surface relaxation, all coordination polyhedrons of YF_3 and HoF_3 are identical as they share the same crystal bulk structure. After relaxation, this is still true for twenty terminations (Table S1). Only four rearranged terminations differ slightly in surface coordination between YF_3 and HoF_3 . All of these four terminations belong to the less stable surfaces within the respective (hkl) . All most or second-most stable terminations are identical in surface coordination between YF_3 and HoF_3 . The most stable surface structure termination for each of the seven Miller indices is shown in Figure 2.

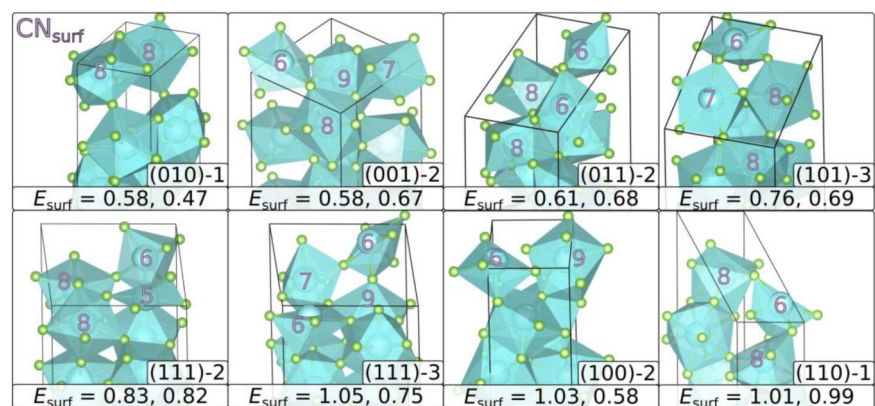


Figure 2. Most stable terminations of the relaxed surface structures: the coordination number of the surface metals (CN_{surf}) and the surface energies in J m^{-2} (E_{surf}) are given. The first entry corresponds to YF_3 and the second to HoF_3 . The mean of both values corresponds to the given order from top left to bottom right. Each (hkl) slab is rotated in a way to show the surface coordination best. For (111), two surfaces are given, as (111)-2 is preferred by YF_3 and (111)-3 by HoF_3 .

As shown in Figure 3, the obtained E_{surf} are similar in magnitude and, within most Miller indices, the order of terminations is equal between YF_3 and HoF_3 . Within convergence, this is also true for the two stoichiometric terminations of (110) and (101), which are very similar in surface energy. For (100) and (001), the least and second-least stable terminations switch their order between YF_3 and HoF_3 . Here, HoF_3 prefers the surface with a nominal surface net charge of +2 over the stoichiometric one. The only difference in termination order between the two compounds, which also affects the most stable surface, is found in (111). For YF_3 , the most stable surface is (111)-2, which shows a surface coordination of $\text{CN}_{\text{surf}} = \{6, 5, 8, 8\}$. Whereas, HoF_3 prefers (111)-3 with $\text{CN}_{\text{surf}} = \{6, 7, 6, 9\}$ (Figure 2). However, both of these terminations are equal in constitution with a fluorine-deficit of 1 per surface.

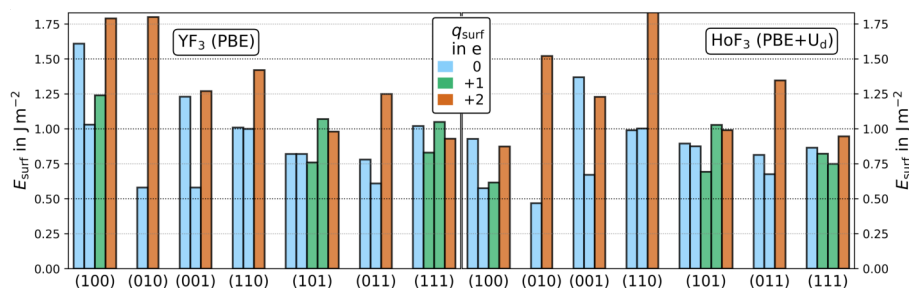


Figure 3. Relaxed surface energies of YF₃ (left, PBE) and HoF₃ (right, PBE+U_d/3 eV/4f-in-core) of all 24 terminations. The surfaces are color-coded to their nominal surface net charge (q_{surf}) in e of 0 (blue), +1 (green) or +2 (orange). This magnified plot does not show the HoF₃ (110)-3 value of 2.09 J m⁻².

Even though the order within one (hkl) is largely the same between YF₃ and HoF₃, the order between the different (hkl) does change. For YF₃, the overall two most stable surfaces are (010)-1 and (001)-2, which are both stoichiometric and give a surface energy of 0.58 J m⁻². This is closely followed by the stoichiometric surface (011)-2. Medium stable surfaces are found for (101)-3 and (111)-2, which are both substoichiometric surfaces missing a single fluorine. The two least stable surfaces (110)-1/-2 and (100)-2 prefer a stoichiometric termination again.

(010)-1 is also the overall most stable surface for HoF₃, but the remaining surfaces differ in order. (100)-2, which is the most unstable (hkl) in YF₃, is the second-most stable one in HoF₃. The moderately stable surfaces (001)-2, (011)-2 and (101)-3 have equivalent surface energies within the slab thickness convergence of 0.01 J m⁻². (111)-3 is the second least stable surface. The least stable surface is stoichiometric (110)-1/-2, which is not even part of the Wulff plot (Figure 4).

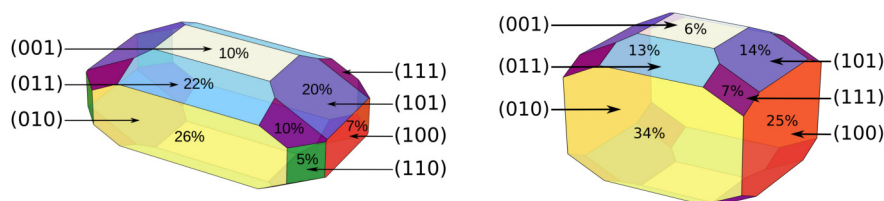


Figure 4. Wulff Plots of YF₃ (left, PBE) and HoF₃ (right, PBE+U_d/3 eV/4f-in-core) from relaxed surfaces. The percentage shows the relative abundance of each surface, which is also given in Table 2.

From the corresponding energies of the respective most stable surfaces shown in Figure 2, the Wulff plots are constructed. A Wulff plot visualizes the thermodynamically most stable crystal shape at quantum chemical conditions of 0 K and vacuum. To test the dependence of surface ratios on the slab thickness convergence, an estimation on the maximum possible error is given in the SI (Table S4).

The largest surface area of over one quarter in YF₃ or one third in HoF₃ is formed by (010). That HoF₃ prefers (010) even stronger is a consequence of its surface energy being 0.11 J m⁻² more stable than any other. This contrasts YF₃, for which (001) has the same surface energy as (010), as well as a very closely (0.03 J m⁻²) following (011). Nonetheless, the geometric interdependence of surfaces cause a much smaller abundance of only 10% for (001) versus more than double for (011) in YF₃. The third most abundant surface in YF₃ is (101) with 20%, which is one of the two obtained substoichiometric surfaces. As these same three surfaces (001), (011) and (101) are only medium stable in HoF₃, they also only constitute 6%, 13% and 14% of the overall surface. The second substoichiometric surface present in both Wulff plots is (111), which forms an area of 10% in YF₃ and 7% in HoF₃. Thus, almost one third of the YF₃ crystal is made from terminations with a nominal positive

net charge of +1. Whereas for HoF_3 , these are only about a fifth. The two least stable surfaces of YF_3 are (100) and (110), which constitute about 7% and 5%. In HoF_3 , the latter is to such an extent energetically unstable, that it is completely excluded from the Wulff plot. (100), on the other hand, turns to be the second most stable and second most abundant surface in HoF_3 . It constitutes one quarter of the total surface.

The overall scale of most stable surface energies per Miller indices is comparable between YF_3 and HoF_3 . The respective ranges are $0.58\text{--}1.03\text{ J m}^{-2}$ for YF_3 and $0.47\text{--}1.00\text{ J m}^{-2}$ for HoF_3 . However, the resulting average by the Wulff plot is 16% higher for YF_3 with $\varnothing E_{\text{surf}} = 0.70\text{ J m}^{-2}$ than for HoF_3 with $\varnothing E_{\text{surf}} = 0.59\text{ J m}^{-2}$. This means, that forming surfaces from the bulk crystal involves a higher thermodynamic barrier in YF_3 than in HoF_3 . This is interesting, as there is no significant difference within the formation enthalpies of the bulk. The difference in average surface energy also hints, that the thermodynamic barrier of crystal nucleation is also higher in YF_3 than in HoF_3 . Though, to accurately predict the nucleation, the nature of the respective precursors and the media needs to be considered.

3.2.1. Bader Charges

Figure 5 shows the partial charges obtained by Bader analysis for all 24 thickness-converged slabs of YF_3 or HoF_3 . As these slabs are built from up to 104 atoms, a large number of very similar charges are obtained. To ease comparison, the Bader charges given in Figure 5 are rounded to 0.1 e. The Bader charges of the central slab atoms reproduce the bulk values with 2.4 e for yttrium, 2.3 e for holmium, as well as -0.8 e for fluorine in both compounds. Only HoF_3 (011)-3 shows a marginally increased central slab value of 2.4 e for holmium. In general, the Miller indices do not seem to affect the Bader charges within the analyzed accuracy. The highly ionic partial charge on fluorine does not significantly change for any slab with an overall range of $-(0.7\text{--}1.0)\text{ e}$. Moreover, all stoichiometric surfaces have practically the same metal partial charges with 2.3–2.4 e. On the contrary, substoichiometric surfaces with a fluorine-deficit of one do all have at least one metal center charged less at the surface. These might be as low as 1.7 e, as found for the third termination of (100) in both trifluorides. Subsequently, surfaces with a fluorine-deficit of two contain even less ionic metal centers at the surface. The least charged metal center is observed again in (100) with only 1.2–1.3 e by the fourth termination. The Bader charges suggest that all substoichiometric surfaces missing two fluorine have at least a single surface metal center in an oxidation state of +II.

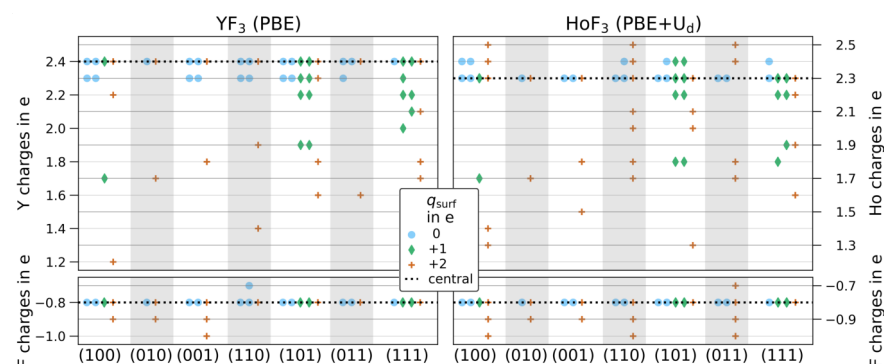


Figure 5. Bader charges rounded to 0.1 e for all slabs of YF_3 (left, PBE) and HoF_3 (right, PBE+ $U_d/3\text{ eV}/4f\text{-in-core}$): the Bader charges of the bulk are highlighted by the dotted line (Y: 2.4 e, Ho: 2.3 e, F: -0.8 e). Terminations are differently colored by their formal surface net charge (q_{surf}) in e for 0 (blue circle), +1 (green diamond) and +2 (orange cross).

3.2.2. Surface Band Gaps

Investigating the electronic properties, we found that the band gap, total DOS and projected DOS of atoms central within the slab converged already at the smallest slab

thickness. All band gaps are plotted in Figure S6. For the most stable termination of each (*hkl*), the DOS near the Fermi level are also shown in Figure S7. The surface DOS narrow the band gap within all terminations. For stoichiometric slabs, the direct band gap is reduced from the bulk value of ca. 8 eV to 4–7 eV. Thus, all stoichiometric surfaces remain fully within the insulating regime. In contrast, for substoichiometric terminations, the direct band gap collapses to 0–1 eV, predicting a pseudo-metallic or narrow-band-gap surface. For HoF₃ (101) and (111), only one spin direction shows a nearly metallic character. The other stays insulating (5–6 eV). It should be noted that this pseudo-metallic or narrow-band-gap electronic structure at the substoichiometric surfaces might be strongly effected by the chosen neutral 2D-periodic model. However, as this paper is focusing on the relative stability of surfaces, we are not investigating the nature of the band gaps, nor the observed surface magnetism or spin-asymmetric band gaps of some HoF₃ surfaces further.

4. Conclusions

The aim of this study was to obtain the relative surface stabilities, in order to find the most abundant surfaces of the two REE trifluorides, YF₃ and HoF₃ according to their inherent quantum chemical stability. While YF₃ can be treated on the DFT level, the 4f-electrons of HoF₃ required an extensive electronic structure benchmark evaluating DFT, DFT+U and hybrid DFT against the crystal unit cell, band gaps and Bader charges. On the DFT or DFT+U level, our results show that including the 4f-electrons explicitly within the plane wave expansion worsens the geometrical and band gap results, while the Bader charges stay unaffected. Considering also the experimentally not observed high-spin preference of the 4f-electrons, as well as the strongly increased computational demand, we treated HoF₃ by a 4f-in-core DFT+U approach, in which the Hubbard-type correction is applied on the Ho-5d orbitals, which mix into the valence band mainly constructed by F-2p.

From the relaxed bulk, surface models were created for any of the seven low-lying Miller indices. Our analysis included all possible stoichiometric terminations, as well as those showing a small to moderate fluorine-deficit. The surfaces were quantified by Bader charges, band gaps and DOS. From the resulting scope of 24 surfaces, we constructed the first Wulff plots for the whole class of β -YF₃-structured compounds.

We found that, within each Miller indices, both trifluorides prefer the same termination with the exception of (111), in which different surface coordinations are favored.

Comparing the different Miller indices, both compounds clearly show stoichiometric (010) as the most stable surface. The preference of the other surfaces, though, varies between the two. The greatest difference is found for (100), which is the second-most stable surface for HoF₃, but the second-least stable one for YF₃. On average, the surface energy predicted by the Wulff plot is higher for YF₃ than for HoF₃. This suggests a higher thermodynamical barrier for the formation of YF₃ surfaces from the bulk.

In total, one third of the predicted equilibrium crystal shape of YF₃ is made from the substoichiometric terminations of (101) and (111) missing a single fluorine per surface. In HoF₃, these only constitute a fifth. In the search for the underlying reason between the different fluorine affinity of the two compounds, this different availability of substoichiometric surfaces is an interesting finding. However, to evaluate possible effects, further studies are needed that actually model binding interactions with these surfaces. These should also apply more elaborate binding analysis tools than simple population analysis.

Supplementary Materials: The following supporting information can be downloaded at: <https://www.mdpi.com/article/10.3390/ma15176048/s1>, Figure S1: Calculated HoF₃ direct band gaps with HSE06 (blue), PBE+U (green) and pure PBE (red) applied on 4f-in-core (full markers) or 4f-in-valence (crosses); HSE06/4f-in-valence is not relaxed but done on-top of the crystal structure; the area between the two HSE06 values is highlighted in blue; Figure S2: Calculated HoF₃ relaxed unit cell parameters with HSE06 (blue), PBE+U (green) and pure PBE (red) applied on 4f-in-core (full markers) or 4f-in-valence (crosses) compared to the experimental values (horizontal line); Figure S3: Bulk band structure, total DOS (tDOS: gray) and DOS projected onto the metal d band (blue) or fluorine 2p band (green): (a) YF₃ (PBE) and (b) HoF₃ (PBE+U_d/3 eV/4f-in-core); Table S1: Comparison of

unrelaxed versus relaxed (or rearranged) slabs in metal coordination number at the surface (CN_{surf}), as well as in metal centers of the non-surface layers ($CN_{\text{non-surf}}$) as determined with a bond distance cut-off of 2.6 Å; Figure S4: Effect of surface rearrangement on the stoichiometric surface terminations of (110)-1 (left), (110)-2 (middle) and (101)-2 (right). Atomic positions are shown before (gray) and after relaxation (M: blue, F: green). For the latter, all polyhedra are shown but the one from the initially lowest surface coordination number ($CN_{\text{surf}}^{\text{unrel}}$). Given are the surface energies in J m^{-2} of the unrelaxed surfaces ($E_{\text{surf}}^{\text{unrel}}$) for YF_3 (first) and HoF_3 (second); Table S2: YF_3 (PBE) bulk-derived ($E_{\text{surf}}^{\text{bd}}$) and slab-derived ($E_{\text{surf}}^{\text{sd}}$) surface energies without (SP) and with atomic position relaxation (OPT); all energies in J m^{-2} ; the $E_{\text{surf,opt}}^{\text{bd}}$ values are used within the main paper; Table S3: HoF_3 (PBE+ $U_d/3$ eV/4f-in-core) bulk-derived ($E_{\text{surf}}^{\text{bd}}$) and slab-derived ($E_{\text{surf}}^{\text{sd}}$) surface energies without (SP) and with atomic position relaxation (OPT); all energies in J m^{-2} ; all magnetic moments in μ_B ; the $E_{\text{surf,opt}}^{\text{sd}}$ values are used within the main paper; Figure S5: Relaxed slab-derived surface energies of HoF_3 (PBE+ $U_d/3$ eV/4f-in-core). The uncertainty due to slab thickness convergence is given by error bars on each termination; Table S4: Effect of maximal error accumulation due to the convergence in slab thickness of maximal $\pm 0.03 \text{ J m}^{-2}$ for YF_3 and $\pm 0.01 \text{ J m}^{-2}$ for HoF_3 onto Wulff construction; i denotes the initial value of average surface energy ($\varnothing E_{\text{surf}}$) or surface abundance ($\%_{\text{surf}}$) given by the Wulff plots in the main paper Figure 4; Figure S6: YF_3 (left, PBE) and HoF_3 (right, PBE+ $U_d/3$ eV/4f-in-core) band gaps of surfaces compared with the respective bulk value (gray). Minimal band gaps, direct or indirect are given by solid bars. In the case, the minimal band gap was found to be indirect, also the direct band gap is given by a transparent bar. For HoF_3 (101) and (111) with +1 nominal charges, the band gaps are not spin-symmetric and both direct transitions are given; Figure S7: DOS comparison between the most stable surfaces ordered by their abundance (in %): YF_3 (left, PBE), HoF_3 (right, PBE+ $U_d/3$ eV/4f-in-core), total DOS (tDOS: gray, downscaled to the bulk tDOS) and projected DOS of a single surface atom (Y, Ho: blue; F: green). Substoichiometric slabs with a fluorine-deficit of 1 per surface are framed in green. The top row gives the bulk tDOS with projected DOS of a single bulk atom as reference.

Author Contributions: Conceptualization, B.P.; Formal analysis, J.A. and N.L.; Funding acquisition, B.P.; Investigation, J.A.; Resources, J.A. and B.P.; Supervision, B.P.; Validation, J.A.; Visualization, J.A.; Writing - original draft, J.A.; Writing-review & editing, N.L. and B.P. All authors have read and agreed to the published version of the manuscript.

Funding: The project was funded by the Freie Universität Berlin and the Deutsche Forschungsgemeinschaft (DFG, German Research Foundation)—Project-ID 387284271—CRC 1349—fluorine-specific interactions. funded by the Freie Universität Berlin and the German Science Foundation (DFG) via CRC 1349—Fluorine-Specific Interactions.

Institutional Review Board Statement: Not applicable.

Informed Consent Statement: Not applicable.

Data Availability Statement: See supplementary materials. Further data can be requested from the authors.

Acknowledgments: The authors thank the North-German Supercomputing Alliance (Norddeutscher Verbund zur Förderung des Hoch- und Höchstleistungsrechnens HLRN) and the Zentraleinrichtung für Datenverarbeitung (ZEDAT) at the Freie Universität Berlin for computational resources, the German Science Foundation (DFG) for funding within the CRC 1349—Fluorine-Specific Interactions, as well as Anselm Loges for scientific discussions.

Conflicts of Interest: The authors declare no conflict of interest.

References

1. Shannon, R.D. Revised effective ionic radii and systematic studies of interatomic distances in halides and chalcogenides. *Acta Cryst. A* **1976**, *32*, 751–767. [[CrossRef](#)]
2. Bau, M.; Dulski, P. Comparative study of yttrium and rare-earth element behaviours in fluorine-rich hydrothermal fluids. *Contrib. Mineral. Petrol.* **1995**, *119*, 213–223. [[CrossRef](#)]
3. Minuzzi, O.R.R.; Bastos Neto, A.C.; Formoso, M.L.L.; Andrade, S.; Janasi, V.A.; Flores, J.A. Rare earth element and yttrium geochemistry applied to the genetic study of cryolite ore at the Pitinga Mine (Amazon, Brazil). *An. Acad. Bras. Cienc.* **2008**, *80*, 719–733. [[CrossRef](#)]

4. Goodenough, K.M.; Schilling, J.; Jonsson, E.; Kalvig, P.; Charles, N.; Tuduri, J.; Deady, E.A.; Sadeghi, M.; Schiellerup, H.; Müller, A.; et al. Europe's rare earth element resource potential: An overview of REE metallogenetic provinces and their geodynamic setting. *Ore Geol. Rev.* **2016**, *72*, 838–856. [[CrossRef](#)]
5. Kaminski, A. *Laser Crystals: Their Physics and Properties*, 2nd ed.; Springer: Berlin/Heidelberg, Germany, 1990.
6. Kollia, Z.; Sarantopoulou, E.; Cefalas, A.C.; Nicolaides, C.A.; Naumov, A.K.; Semashko, V.V.; Abdulsabirov, R.Y.; Korableva, S.L.; Dubinskii, M.A. Vacuum-ultraviolet interconfigurational 4f₃ → 4f₂5d absorption and emission studies of the Nd³⁺ ion in KYF₃, YF₃, and YLF crystal hosts. *J. Opt. Soc. Am. B* **1995**, *12*, 782–785. [[CrossRef](#)]
7. Lage, M.M.; Righi, A.; Matinaga, F.M.; Gesland, J.Y.; Moreira, R.L. Raman-spectroscopic study of lanthanide trifluorides with the -YF₃ structure. *J. Phys. Condens. Matter* **2004**, *16*, 3207–3218. [[CrossRef](#)]
8. Atencio, D.; Bastos Neto, A.C.; Pereira, V.P.; Ferron, J.T.M.M.; Hoshino, M.; Moriyama, T.; Watanabe, Y.; Miyawaki, R.; Coutinho, J.M.V.; Andrade, M.B.; et al. Waimirite-(Y), orthorhombic YF₃, a new mineral from the Pitinga mine, Presidente Figueiredo, Amazonas, Brazil and from Jabal Tawlah, Saudi Arabia: Description and crystal structure. *Mineral. Mag.* **2015**, *79*, 767–780. [[CrossRef](#)]
9. Sarantopoulou, E.; Kollia, Z.; Cefalas, A.C. YF₃:Nd³⁺, Pr³⁺, Gd³⁺ wide band gap crystals as optical materials for 157-nm photolithography. *Opt. Mater.* **2001**, *18*, 23–26. [[CrossRef](#)]
10. O'Keeffe, M. Ionic Conductivity of Yttrium Fluoride and Lutetium Fluoride. *Science* **1973**, *180*, 1276–1277. [[CrossRef](#)]
11. Pogorenko, Y.V.; Pshenychnyi, R.M.; Lutsyk, V.I.; Omel'chuk, A.O. Transport Properties of Alivalent Substitution Solid Solutions of the System (1-x)PbF₂-xYF₃-SnF₂. *IOP Conf. Ser. Mater. Sci. Eng.* **2017**, *175*, 012039. [[CrossRef](#)]
12. Fedorov, P.P.; Sorokin, N.I. Stabilization of the α-YF₃ structure type by isomorphous substitutions. *Inorg. Mater.* **2017**, *53*, 1307–1311. [[CrossRef](#)]
13. Cui, X.; Hu, T.; Wang, J.; Zhang, J.; Zhong, X.; Chen, Y.; Li, X.; Yang, J.; Gao, C. Ionic transportation and dielectric properties of YF₃:Eu³⁺ nanocrystals. *Nanomaterials* **2018**, *8*, 995. [[CrossRef](#)] [[PubMed](#)]
14. Dai, X.; Komatsu, Y.; Shimizu, R.; Hitosugi, T. Diffusion of F atoms from fluoride substrates promotes the epitaxial growth of metal fluorides. *Appl. Phys. Express* **2020**, *13*, 85507. [[CrossRef](#)]
15. Hoard, R.; Mance, S.; Leber, R.; Dalder, E.; Chaplin, M.; Blair, K.; Nelson, D.; Dyke, D.V. Field enhancement of a 12.5-T magnet using holmium poles. *IEEE Trans. Magn.* **1985**, *21*, 448–450. [[CrossRef](#)]
16. González-Mancebo, D.; Becerro, A.I.; Rojas, T.C.; García-Martín, M.L.; de la Fuente, J.M.; Ocaña, M. HoF₃ and DyF₃ Nanoparticles as Contrast Agents for High-Field Magnetic Resonance Imaging. *Part. Part. Syst. Character.* **2017**, *34*, 1700116. [[CrossRef](#)]
17. Rudzitis, E.; Feder, H.M.; Hubbard, W.N. Fluorine bomb calorimetry. XI. The enthalpy of formation of yttrium trifluoride. *J. Phys. Chem.* **1965**, *69*, 2305–2307. [[CrossRef](#)]
18. Spedding, F.H.; Henderson, D.C. High-temperature heat contents and related thermodynamic functions of seven trifluorides of the rare earths: Y, La, Pr, Nd, Gd, Ho, and Lu. *J. Chem. Phys.* **1971**, *54*, 2476–2483. [[CrossRef](#)]
19. Loges, A.; Migdisov, A.A.; Wagner, T.; Williams-Jones, A.E.; Markl, G. Fluoride complexation of hafnium under hydrothermal conditions. In Proceedings of the Goldschmidt Conference, Montréal, QC, Canada, 24–29 June 2012; p. 2030.
20. Loges, A.; Migdisov, A.A.; Wagner, T.; Williams-Jones, A.E.; Markl, G. An experimental study of the aqueous solubility and speciation of Y(III) fluoride at temperatures up to 250°C. *Geochim. Cosmochim. Acta* **2013**, *123*, 403–415. [[CrossRef](#)]
21. Bau, M. Controls on the fractionation of isoivalent trace elements in magmatic and aqueous systems: Evidence from Y/Ho, Zr/Hf, and lanthanide tetrad effect. *Contrib. Mineral. Petrol.* **1996**, *123*, 323–333. [[CrossRef](#)]
22. Zalkin, A.; Templeton, D.H. The Crystal Structures of YF₃ and Related Compounds. *J. Am. Chem. Soc.* **1953**, *75*, 2453–2458. [[CrossRef](#)]
23. Cheetham, A.K.; Norman, N. The Structures of Yttrium and Bismuth Trifluorides by Neutron Diffraction. *Acta Chem. Scand.* **1974**, *28*, 55–60. [[CrossRef](#)]
24. Khairulin, R.A.; Stankus, S.V.; Lyapunov, K.M. The Thermal Properties of Holmium Trifluoride at High Temperatures. *High Temp.* **2000**, *38*, 149–151. [[CrossRef](#)]
25. Loges, A. (Freie Universität Berlin, Berlin, Germany). Private communication, 2020.
26. Vologzhanina, A.V.; Pushkin, D.V.; Serezhkin, V.N. Coordination polyhedra LnFn (Ln = La-Lu) in crystal structures. *Russ. J. Inorg. Chem.* **2006**, *51*, 747–758. [[CrossRef](#)]
27. Rotereau, K.; Daniel, P.; Desert, A.; Gesland, J.Y. The high-temperature phase transition in samarium fluoride: Structural and vibrational investigation. *J. Phys. Condens. Matter* **1998**, *10*, 1431–1446. [[CrossRef](#)]
28. Zinchenko, V.; Efrushina, N.; Eryomin, O.; Markiv, V.; Belyavina, N.; Mozkova, O.; Zakharenko, M. Synthesis, structure and optical properties of EuF₃ film-forming material. *J. Alloys Compd.* **2002**, *347*, L1–L3. [[CrossRef](#)]
29. Piotrowski, M.; Murasik, A. Exchange and Dipolar Interactions in TbF₃. *Phys. Status Solidi A* **1985**, *89*, 571–580. [[CrossRef](#)]
30. Piotrowski, M.; Ptasiwicz-bąk, H.; Murasik, A. The crystal structures of HoF₃ and TbF₃ by neutron diffraction. *Phys. Status Solidi A* **1979**, *55*, K163–K166. [[CrossRef](#)]
31. Bukvetskii, B.; Garashina, L. Crystal-chemical investigation of the orthorhombic trifluorides of samarium, holmium, and ytterbium. *Russ. J. Coord. Chem.* **1977**, *3*, 1024–1029.
32. Peterson, J.R.; Cunningham, B.B. Crystal structures and lattice parameters of the compounds of berkelium—IV berkelium trifluoride. *J. Inorg. Nucl. Chem.* **1968**, *30*, 1775–1784. [[CrossRef](#)]
33. Cunningham, B.; Ehrlich, P. *USAEC Report UCRL-20426*; Technical Report; USAEC: Houston, TX, USA, 1970.

34. Stevenson, J.N.; Peterson, J.R. The trigonal and orthorhombic crystal structures of CfF_3 and their temperature relationship. *J. Inorg. Nucl. Chem.* **1973**, *35*, 3481–3486. [[CrossRef](#)]
35. Morss, L.R.; Edelstein, N.M.; Fuger, J. (Eds.) *The Chemistry of the Actinide and Transactinide Elements*, 3rd ed.; Springer International Publishing: Dordrecht, The Netherlands, 2008; p. 1468.
36. Haschke, J.M.; Hodges, A.E.; Lucas, R.L. Equilibrium and structural properties of the PuH system. *J. Less-Common Met.* **1987**, *133*, 155–166. [[CrossRef](#)]
37. Greis, O.; Martinez-Ripoll, M. Darstellung, Temperaturverhalten und Kristallstruktur von BiF_3 . *Z. Anorg. Allg. Chem.* **1977**, *436*, 105–112. [[CrossRef](#)]
38. Deng, Z.; Wei, F.; Wu, Y.; Seshadri, R.; Cheetham, A.K.; Canepa, P. Understanding the Structural and Electronic Properties of Bismuth Trihalides and Related Compounds. *Inorg. Chem.* **2020**, *59*, 3377–3386. [[CrossRef](#)]
39. Ye, X.; Chen, J.; Engel, M.; Millan, J.A.; Li, W.; Qi, L.; Xing, G.; Collins, J.E.; Kagan, C.R.; Li, J.; et al. Competition of shape and interaction patchiness for self-assembling nanoplates. *Nat. Chem.* **2013**, *5*, 466–473. [[CrossRef](#)]
40. Griffiths, C.L.; Macdonald, J.E.; Williams, R.H. The growth and characterisation of epitaxial insulating HoF_3 layers on silicon. *Appl. Surf. Sci.* **1992**, *56–58*, 782–788. [[CrossRef](#)]
41. Guo, F.; Li, H.; Zhang, Z.; Meng, S.; Li, D. Synthesis of mesoporous YF_3 nanoflowers via solvent extraction route. *Mater. Sci. Eng. B* **2009**, *163*, 134–137. [[CrossRef](#)]
42. Wen, C.; Sun, L.; Yan, J.; Liu, Y.; Song, J.; Zhang, Y.; Lian, H.; Kang, Z. Mesoporous rare earth fluoride nanocrystals and their photoluminescence properties. *J. Colloid Interface Sci.* **2011**, *357*, 116–120. [[CrossRef](#)]
43. Tian, Y.; Chen, B.; Li, X.; Zhang, J.; Tian, B.; Sun, J.; Cheng, L.; Zhong, H.; Zhong, H.; Hua, R. Solvothermal synthesis and tunable luminescence of Tb^{3+} , Eu^{3+} codoped YF_3 nano- and micro-crystals with uniform morphologies. *J. Solid State Chem.* **2012**, *196*, 187–196. [[CrossRef](#)]
44. Chen, J.x.; Wang, X.p.; Wang, L.J.; Yang, X.w.; Yang, Y. White electroluminescence of diamond— HoF_3 - diamond composite film. *J. Lumin.* **2020**, *224*, 117310. [[CrossRef](#)]
45. Nanda, S.S.; Nayak, P.; Goutam, U.K.; Dash, S. Influence of Eu^{3+} on the Structure and Photophysical Properties in $(\text{Y,Gd})\text{F}_3$ Nanophosphors. *J. Fluoresc.* **2021**, *31*, 129–139. [[CrossRef](#)]
46. Pandharkar, R.; Becker, C.; Budau, J.; Kaawar, Z.; Paulus, B. A Computational Study of AlF_3 and ACF Surfaces. *Inorganics* **2018**, *6*, 124. [[CrossRef](#)]
47. Schnellbügel, A.; Anton, R. On background subtraction for quantitative analysis of X-ray photoelectron spectra of rare earth fluorides. *Surf. Sci.* **2001**, *492*, 305–314. [[CrossRef](#)]
48. Wulff, G. XXV. Zur Frage der Geschwindigkeit des Wachstums und der Auflösung der Krystallflächen. *Z. Kristallogr.-Cryst. Mater.* **1901**, *34*, 449–530. [[CrossRef](#)]
49. Laue, M.V. Der Wulffsche Satz für die Gleichgewichtsform von Kristallen. *Z. Kristallogr.-Cryst. Mater.* **1943**, *105*, 124–133. [[CrossRef](#)]
50. Kresse, G.; Hafner, J. Norm-conserving and ultrasoft pseudopotentials for first-row and transition elements. *J. Phys. Condens. Matter* **1994**, *6*, 8245–8257. [[CrossRef](#)]
51. Perdew, J.P.; Burke, K.; Ernzerhof, M. Generalized Gradient Approximation Made Simple. *Phys. Rev. Lett.* **1996**, *77*, 3865–3868. [[CrossRef](#)] [[PubMed](#)]
52. Blöchl, P.E. Projector augmented-wave method. *Phys. Rev. B* **1994**, *50*, 17953–17979. [[CrossRef](#)]
53. Kresse, G.; Joubert, D. From ultrasoft pseudopotentials to the projector augmented-wave method. *Phys. Rev. B* **1999**, *59*, 1758–1775. [[CrossRef](#)]
54. Dudarev, S.L.; Botton, G.A.; Savrasov, S.Y.; Humphreys, C.J.; Sutton, A.P. Electron-energy-loss spectra and the structural stability of nickel oxide: An LSDA+U study. *Phys. Rev. B* **1998**, *57*, 1505–1509. [[CrossRef](#)]
55. Krukau, A.V.; Vydrov, O.A.; Izmaylov, A.F.; Scuseria, G.E. Influence of the exchange screening parameter on the performance of screened hybrid functionals. *J. Chem. Phys.* **2006**, *125*, 224106. [[CrossRef](#)]
56. Blöchl, P.E.; Jepsen, O.; Andersen, O.K. Improved tetrahedron method for Brillouin-zone integrations. *Phys. Rev. B* **1994**, *49*, 16223–16233. [[CrossRef](#)]
57. Evans, D.S.; Baynor, G.V. Lattice spacings in thorium—Yttrium alloys. *J. Nucl. Mater.* **1960**, *2*, 209–215. [[CrossRef](#)]
58. Pechan, M.J.; Stassis, C. Magnetic structure of holmium. *J. Appl. Phys.* **1984**, *55*, 1900–1902. [[CrossRef](#)]
59. Kerker, G.P. Efficient iteration scheme for self-consistent pseudopotential calculations. *Phys. Rev. B* **1981**, *23*, 3082–3084. [[CrossRef](#)]
60. Sun, W.; Ceder, G. Efficient creation and convergence of surface slabs. *Surf. Sci.* **2013**, *617*, 53–59. [[CrossRef](#)]
61. Tran, R.; Xu, Z.; Radhakrishnan, B.; Winston, D.; Sun, W.; Persson, K.A.; Ong, S.P. Surface energies of elemental crystals. *Sci. Data* **2016**, *3*, 160080. [[CrossRef](#)]
62. Rahm, J.M.; Erhart, P. WulffPack: A Python package for Wulff constructions. *J. Open Source Softw.* **2020**, *5*, 1944. [[CrossRef](#)]
63. Momma, K.; Izumi, F. VESTA 3 for three-dimensional visualization of crystal, volumetric and morphology data. *J. Appl. Crystallogr.* **2011**, *44*, 1272–1276. [[CrossRef](#)]
64. Grimme, S.; Ehrlich, S.; Goerigk, L. Effect of the damping function in dispersion corrected density functional theory. *J. Comput. Chem.* **2011**, *32*, 1456–1465. [[CrossRef](#)]

65. Rogers, E.; Dorenbos, P.; van der Kolk, E. Systematics in the optical and electronic properties of the binary lanthanide halide, chalcogenide and pnictide compounds: An overview. *New J. Phys.* **2011**, *13*, 093038. [[CrossRef](#)]
66. Bader, R.F.W. Atoms in molecules. *Acc. Chem. Res.* **1985**, *18*, 9–15. [[CrossRef](#)]
67. Henkelman, G.; Arnaldsson, A.; Jónsson, H. A fast and robust algorithm for Bader decomposition of charge density. *Comp. Mat. Sci.* **2006**, *36*, 354–360. [[CrossRef](#)]
68. Sanville, E.; Kenny, S.D.; Smith, R.; Henkelman, G. Improved grid-based algorithm for Bader charge allocation. *J. Comput. Chem.* **2007**, *28*, 899–908. [[CrossRef](#)] [[PubMed](#)]
69. Tang, W.; Sanville, E.; Henkelman, G. A grid-based Bader analysis algorithm without lattice bias. *J. Phys. Condens. Matter* **2009**, *21*, 84204. [[CrossRef](#)] [[PubMed](#)]
70. Yu, M.; Trinkle, D.R. Accurate and efficient algorithm for Bader charge integration. *J. Chem. Phys.* **2011**, *134*, 64111. [[CrossRef](#)]
71. Brown, P.J.; Forsyth, J.B.; Hansen, P.C.; Leask, M.J.M.M.; Ward, R.C.C.C.; Wells, M.R. Neutron diffraction determination of magnetic order in holmium trifluoride, HoF₃. *J. Phys. Condens. Matter* **1990**, *2*, 4471–4484. [[CrossRef](#)]
72. Boettger, J.C. Nonconvergence of surface energies obtained from thin-film calculations. *Phys. Rev. B* **1994**, *49*, 16798–16800. [[CrossRef](#)] [[PubMed](#)]

Supplementary Materials: First Principle Surface Analysis of β -YF₃-Structured Rare Earth Element Trifluorides

Jennifer Anders¹*, Niklas Limberg², Beate Paulus

Contents

1	Properties of the Bulk	1
1.1	HoF ₃ Bulk Benchmark	1
1.2	Bulk Band Structures	3
2	Relaxation Effect on Coordination Polyhedrons	3
3	Convergence against Slab Thickness	5
4	Error Estimation	7
4.1	Error Estimation in Slab Thickness Convergence	7
4.2	Error Estimation in Wulff Plots	7
5	Electronic Properties of Surfaces	8
5.1	Surface Band Gaps.	8
5.2	Surface DOS	9

1. Properties of the Bulk

1.1. HoF₃ Bulk Benchmark

As for HoF₃, no experimental, but a purely empirically predicted band gap of ca. 9 eV exists, we calculated HSE06/4f-in-core and HSE06/4f-in-valence as references (Figure S1). Considering the computational demands and SCF convergence issues, only HSE06/4f-in-core was relaxed in unit cell parameters. The HSE06/4f-in-valence band gap is calculated on the experimental crystal structure. The difference between the two HSE06 direct band gaps is 3.24 eV. All 4f-in-core values of PBE and PBE+U_d with U = 1–7 eV are found within that range of both HSE06 values. However, all PBE+U_f/4f-in-valence band gaps stay below. Note the non-linear behavior of PBE+U_f/4f-in-valence at 6 eV. Here, the nature of the valence band maximum (VBM) changes from Ho-4f to F-2p. At 10 eV, the band structure collapses to a pseudo-metallic one.

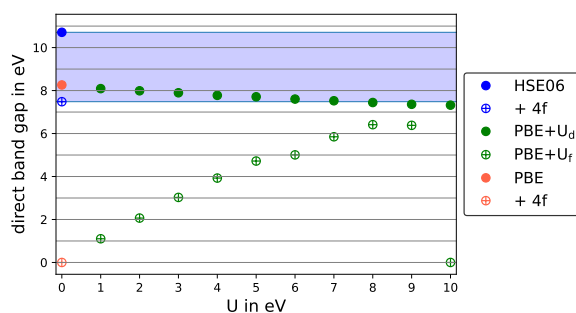


Figure S1. Calculated HoF₃ direct band gaps with HSE06 (blue), PBE+U (green) and pure PBE (red) applied on 4f-in-core (full markers) or 4f-in-valence (crosses); HSE06/4f-in-valence is not relaxed but done on-top of the crystal structure; the area between the two HSE06 values is highlighted in blue.

Pure PBE/4f-in-core performs already quite well on the band gap, as well as on the unit cell parameters (Figure S2). All PBE+U_f/4f-in-valence values perform worse with the exception of U_f = 6 eV. By increasing the potential in PBE+U_d, the unit cell parameters increase almost linearly up to U_d = 8 eV. At U_d = 3 eV, the relaxed unit cell volume

deviates by as little as 0.5% from the experimental value. HSE06/4f-in-core gives a much more shrunken unit cell, which is 15.6 \AA^3 below the experimental value.

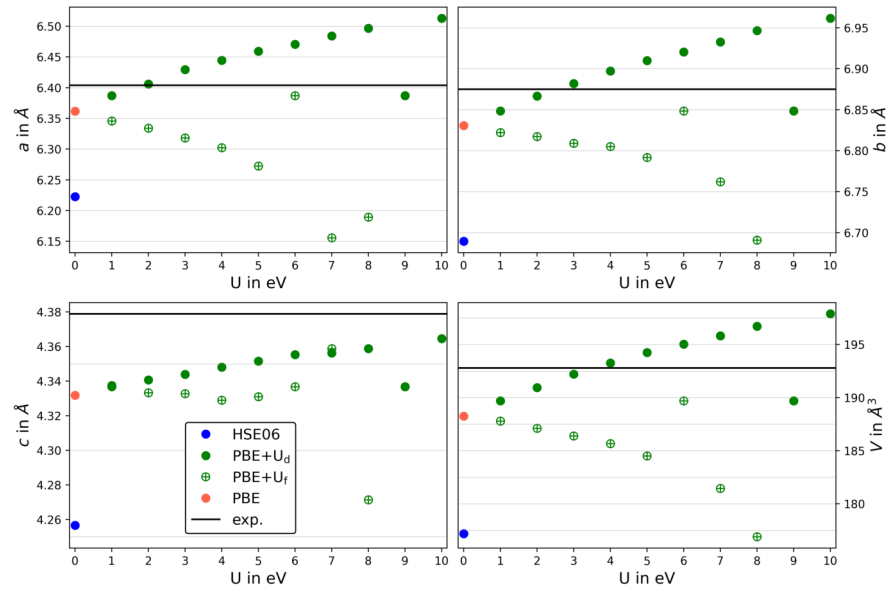


Figure S2. Calculated HoF₃ relaxed unit cell parameters with HSE06 (blue), PBE+U (green) and pure PBE (red) applied on 4f-in-core (full markers) or 4f-in-valence (crosses) compared to the experimental values (horizontal line).

In conclusion, the 4f-in-core approach reduces the computational demand and general SCF convergence issues inherent to the 4f-in-valence method, considerably. Moreover, it leaves the Bader charges practically unchanged and does not suffer from wrong spin arrangements (see main paper). In addition, it gives larger band gaps, which are closer to the predicted value and the calculated HSE06 ones. Finally, it yields the least structure derivation from experimental crystal structure (Figure S2 and main paper Table 1). Consequently, all HoF₃ slabs are obtained by PBE+U_d with 3 eV on 4f-in-core.

1.2. Bulk Band Structures

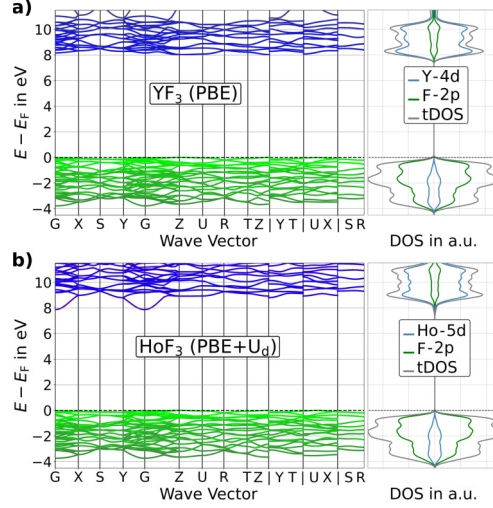


Figure S3. Bulk band structure, total DOS (tDOS: gray) and DOS projected onto the metal d band (blue) or fluorine 2p band (green): (a) YF_3 (PBE) and (b) HoF_3 (PBE+ $U_d/3$ eV/4f-in-core).

Band structure calculations on the 3D-bulk show, that, typical for such ionic compounds, the bands are very localized or flat in k -space. This is especially true for the valence band (VB) of both compounds, which is mostly made from the 2p band of fluorine. The conduction band (CB) is mostly made from d band of holmium or yttrium. In YF_3 , the CB is also very flat and featureless. In HoF_3 , the CB has a slightly pronounced minimum (CBM) at the Γ -point.

2. Relaxation Effect on Coordination Polyhedrons

Table S1. Comparison of unrelaxed versus relaxed (or rearranged) slabs in metal coordination number at the surface (CN_{surf}), as well as in metal centers of the non-surface layers ($\text{CN}_{\text{non-surf}}$) as determined with a bond distance cut-off of 2.6 Å:

(hkl)	term.	unrelaxed				relaxed			
		CN_{surf}		$\text{CN}_{\text{non-surf}}$		CN_{surf}		$\text{CN}_{\text{non-surf}}$	
		YF_3	HoF_3	YF_3	HoF_3	YF_3	HoF_3	YF_3	HoF_3
(100)	1	5,9	9		5,9	9			
	2	6,9	9		6,9 (2 nd 8,8)	9			
	3	5,8	9		5,8	9			
	4	4,7	9		4,7 (2 nd 8,9)	9			
(010)	1	8,8	9		8,8	9			
	2	6,6	9		6,6	9			
(001)	1	6,8,9,9	9		5,8,8,9	8			
	2	6,8,9,9	9		6,7,8,9	8			
	3	4,6,9,9	9		4,5,8,9	8			
(110)	1	6,8,9	9		6,8,8	9			
	2	5,8,9	9		6,8,8	9			
	3	4,6,9	9		4,6,9 4,6,8	9			
(101)	1	6,8,8,9	9		6,7,8,8	8			
	2	4,6,9,9	9		6,6,8,8	8			
	3	6,8,8,8	9		6,7,8,8	8			
	4	5,6,8,9	9		5,6,7,9 5,6,8,8	8,9			
	5	5,7,8,8	9		4,5,8,8 5,6,8,8	8 9			
(011)	1	6,6,9,9	9		6,6,8,8	8			
	2	7,7,9,9	9		7,7,9,9	8			
	3	4,4,9,9	9		4,4,8,8	8			
(111)	1	4,6,9,9	9		6,7,7,8 7,7,8,8	8,(9) 8,9			
	2	6,6,7,9	9		5,6,8,8	8,(9)			
	3	6,6,7,9	9		6,6,7,9	8,9			
	4	5,6,8,8	9		5,5,7,7	8,9			

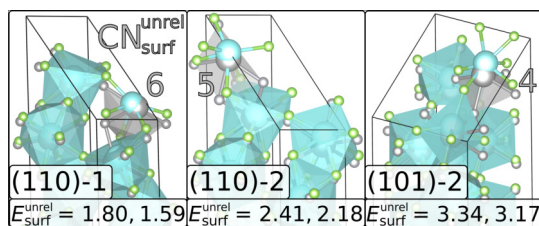


Figure S4. Effect of surface rearrangement on the stoichiometric surface terminations of (110)-1 (left), (110)-2 (middle) and (101)-2 (right). Atomic positions are shown before (gray) and after relaxation (M: blue, F: green). For the latter, all polyhedra are shown but the one from the initially lowest surface coordination number ($CN_{\text{surf}}^{\text{unrel}}$). Given are the surface energies in J m^{-2} of the unrelaxed surfaces ($E_{\text{surf}}^{\text{unrel}}$) for YF_3 (first) and HoF_3 (second).

Table S1 shows the change in surface coordination numbers (CN_{surf}). For three exemplary surfaces, these are also visualized in Figure S4. The 6-fold coordination polyhedron of (110)-1 reminds vaguely of a distorted pentagonal pyramid with the metal center cut by the pseudo-equatorial plane. Four out of five pseudo-equatorial fluorine have an angle of only $65\text{--}75^\circ$ towards the axial fluorine. The 5-fold polyhedron of (110)-2 is obtained by removing one pseudo-equatorial fluorine from the 6-fold coordination polyhedron. When allowed to rearrange in atomic positions, both terminations converged into an equivalent surface arrangement. Both show the same surface coordination and an identical surface energy within slab thickness convergence (Tables S2 and S3). In (101), the unrelaxed stoichiometric terminations (101)-1 and -2 mainly differ in a 4-fold versus 6-fold coordination (Figure S4 and Table S1). The latter is constructed as in (110)-1. Within the 4-fold polyhedron, all four fluorine point towards the second slab layer in a distorted 4-fold umbrella shape. After relaxation, (101)-1 and (101)-2, both, have six as their lowest coordination number and are also equivalent in surface energy. In contrast to (110), the relaxed polyhedron keeps a clear exposure of the metal ion similar to substoichiometric (101)-3 shown in main paper Figure 2.

Apart from the coordination at the surface layer, Table S1 also gives the coordination numbers of the non-surface metal centers ($CN_{\text{non-surf}}$). However, no correlation to E_{surf} could be found. During relaxation, the slabs expand in vacuum-direction. For some slabs, this leads to a reduction of some fully coordinated metal centers from 9 to 8 inside the non-surface layers. Within the non-surface layers of (111)-3 and -4, the 8-fold and 9-fold polyhedrons are both present in roughly the same ratio. Whereas in (111)-2, the 8-fold coordination strongly dominates within the non-surface layers. This is denoted by the parenthesis in Table S1. If only the coordination within the second layer is different from the other non-surface coordinations, as e.g. in (100)-2 and -4, this is denoted by (2nd). However, none of these changes in non-surface layers from 9-fold to 8-fold coordination does effect the Bader charges, discussed in the main paper (Figure 5).

Considering the surface layers, the very exposed $CN_{\text{surf}} = 4$ is only found for 4 (HoF_3) or 5 (YF_3) relaxed substoichiometric slabs missing two fluorine per surface. Initially, prior to relaxation, also stoichiometric (101)-2 and (111)-1 show a 4-fold coordination. Accordingly, their unrelaxed surface energies are among the highest ones. During relaxation, their surface energies reduce considerably while the surface coordination increases to $CN_{\text{surf}} = 6$.

3. Convergence against Slab Thickness

The bulk- and slab-derived surface energies of all calculated slab thicknesses are given in Table S2 for YF_3 and Table S3 for HoF_3 . The respective stoichiometry is given in respect to the unit cell (UC) of M_4F_{12} .

Table S2. YF_3 (PBE) bulk-derived ($E_{\text{surf}}^{\text{bd}}$) and slab-derived ($E_{\text{surf}}^{\text{sd}}$) surface energies without (SP) and with atomic position relaxation (OPT); all energies in J m^{-2} ; the $E_{\text{surf,opt}}^{\text{bd}}$ values are used within the main paper:

(hkl)	stoichiometry	SP		OPT	
		$E_{\text{surf,SP}}^{\text{bd}}$	$E_{\text{surf,SP}}^{\text{sd}}$	$E_{\text{surf,opt}}^{\text{bd}}$	$E_{\text{surf,opt}}^{\text{sd}}$
(100)-1	3 UC	2.72	—	1.56	—
	4 UC	2.79	2.50	1.59	1.47
	5 UC	2.87	2.51	1.61	1.48
(100)-2	4.5 UC	1.95	—	1.01	—
	5.5 UC	2.02	1.62	1.03	0.88
(100)-3	4 UC-2F	1.53	—	1.21	—
	5 UC-2F	1.61	1.25	1.24	1.11
	4.5 UC-4F	2.07	—	1.76	—
(100)-4	5.5 UC-4F	2.14	1.74	1.79	1.63
(010)-1	3 UC	0.68	—	0.51	—
	4 UC	0.76	0.45	0.54	0.40
	5 UC	0.84	0.45	0.58	0.40
(010)-2	4 UC-4F	1.97	—	1.77	—
	5 UC-4F	2.05	1.66	1.80	1.63
(001)-1	3 UC	2.35	—	1.25	—
	4 UC	2.40	2.20	1.24	1.28
	5 UC	2.45	2.20	1.23	1.26
(001)-2	4.5 UC	1.34	—	0.59	—
	5.5 UC	1.39	1.12	0.58	0.62
(001)-3	4.5 UC-4F	1.65	—	1.28	—
	5.5 UC-4F	1.70	1.42	1.27	1.31
(110)-1	3 UC	1.69	—	0.90	—
	4 UC	1.74	1.53	0.98	0.66
	5 UC	1.80	1.53	1.01	0.90
(110)-2	4.5 UC	2.35	—	0.98	—
	5.5 UC	2.41	2.11	1.00	0.88
(110)-3	4.5 UC-4F	1.68	—	1.40	—
	5.5 UC-4F	1.73	1.44	1.42	1.30
(101)-1	3 UC	1.40	—	0.78	—
	4 UC	1.44	1.27	0.81	0.72
	5 UC	1.48	1.27	0.82	0.76
(101)-2	3 UC	3.34	—	0.78	—
	4 UC	3.30	3.13	0.80	0.71
	5 UC	3.34	3.13	0.82	0.75
(101)-3	4 UC-2F	1.11	—	0.75	—
	5 UC-2F	1.16	0.95	0.76	0.68
(101)-4	4.5 UC-2F	2.06	—	1.07	—
	5.5 UC-2F	2.10	1.87	1.07	1.05
(101)-5	4 UC-4F	1.35	—	0.96	—
	5 UC-4F	1.39	1.18	0.98	0.89
(011)-1	3 UC	1.21	—	0.76	—
	4 UC	1.26	1.09	0.77	0.72
	5 UC	1.30	1.09	0.78	0.73
(011)-2	3 UC	1.23	—	0.59	—
	4 UC	1.27	1.10	0.60	0.56
	5 UC	1.32	1.10	0.61	0.57
(011)-3	4 UC-4F	1.64	—	1.24	—
	5 UC-4F	1.68	1.18	1.25	0.93
(111)-1	3 UC	3.37	—	0.59	—
	4 UC	3.42	3.24	1.00	-0.62
	5 UC	3.46	3.27	1.02	0.89
	6 UC	3.49	3.27	1.03	0.96
(111)-2	4 UC-2F	1.26	—	0.82	—
	5 UC-2F	1.30	1.11	0.83	0.77
(111)-3	4.5 UC-2F	1.66	—	1.03	—
	5.5 UC-2F	1.70	1.49	1.05	0.97
(111)-4	4 UC-4F	1.37	—	0.92	—
	5 UC-4F	1.40	1.22	0.93	0.85

Table S3. HoF₃ (PBE+U_d/3 eV/4f-in-core) bulk-derived ($E_{\text{surf}}^{\text{bd}}$) and slab-derived ($E_{\text{surf}}^{\text{sd}}$) surface energies without (SP) and with atomic position relaxation (OPT); all energies in J m⁻²; all magnetic moments in μ_B ; the $E_{\text{surf,opt}}^{\text{sd}}$ values are used within the main paper:

(hkl)	stoichiometry	SP			OPT		
		$E_{\text{surf,SP}}^{\text{bd}}$	$E_{\text{surf,SP}}^{\text{sd}}$	μ_{SP}	$E_{\text{surf,opt}}^{\text{bd}}$	$E_{\text{surf,opt}}^{\text{sd}}$	μ_{opt}
(100)-1	4 UC	1.47	—	0.00	0.77	—	0.00
	5 UC	1.46	1.48	0.00	0.73	0.93	0.00
	6 UC	1.46	1.48	0.00	0.69	0.93	0.00
	7 UC	1.46	1.48	0.00	0.66	0.93	0.00
(100)-2	4.5 UC	0.95	—	0.00	0.40	—	0.00
	5.5 UC	0.94	0.96	0.00	0.36	0.58	0.00
	6.5 UC	0.94	0.96	0.00	0.33	0.58	0.00
(100)-3	4 UC-2F	0.67	—	0.00	0.46	—	0.00
	5 UC-2F	0.67	0.68	0.00	0.43	0.62	0.00
	6 UC-2F	0.66	0.68	0.00	0.39	0.62	0.00
(100)-4	4.5 UC-4F	0.88	—	0.01	0.70	—	0.00
	5.5 UC-4F	0.88	0.90	0.00	0.66	0.88	0.00
	6.5 UC-4F	0.88	0.90	0.00	0.62	0.87	0.00
(010)-1	4 UC	0.47	—	0.00	0.22	—	0.00
	6 UC	0.45	0.49	0.00	0.10	0.47	0.00
	7 UC	0.45	0.48	0.00	0.05	0.39	0.00
(010)-2	4 UC-4F	1.51	—	4.03	1.28	—	3.53
	5 UC-4F	1.49	1.60	3.57	1.22	1.53	3.53
	6 UC-4F	1.48	1.52	3.57	1.16	1.52	3.53
(001)-1	4 UC	2.22	—	0.00	1.14	—	0.00
	5 UC	2.22	2.24	0.00	1.09	1.33	0.00
	6 UC	2.22	2.25	0.00	1.04	1.37	0.00
	7 UC	2.21	2.24	0.00	0.99	1.33	0.00
(001)-2	4.5 UC	1.15	—	0.00	0.43	—	0.00
	5.5 UC	1.14	1.16	0.00	0.38	0.67	0.00
	6.5 UC	1.14	1.16	0.00	0.33	0.67	0.00
(001)-3	4.5 UC-4F	1.24	—	0.00	0.95	—	0.00
	5.5 UC-4F	1.27	1.10	-0.01	0.93	1.08	0.00
	6.5 UC-4F	1.26	1.29	0.00	0.87	1.23	0.00
(110)-1	4 UC	1.57	—	0.00	0.81	—	0.00
	5 UC	1.56	1.58	0.00	0.76	1.00	0.00
	6 UC	1.56	1.59	0.00	0.71	0.99	0.00
	7 UC	1.55	1.59	0.00	0.66	1.01	0.00
(110)-2	4.5 UC	2.16	—	0.00	0.79	—	0.00
	5.5 UC	2.16	2.18	0.00	0.74	1.00	0.00
	6.5 UC	2.15	2.18	0.00	0.69	1.00	0.00
(110)-3	4.5 UC-4F	1.34	—	0.00	1.06	—	0.19
	5.5 UC-4F	1.34	1.36	0.47	1.01	1.27	0.27
	6.5 UC-4F	1.33	1.36	0.47	0.82	2.09	0.00
(101)-1	4 UC	1.32	—	0.00	0.75	—	0.00
	5 UC	1.14	1.33	0.00	0.72	0.87	0.00
	6 UC	1.13	1.33	0.00	0.69	0.89	0.00
	7 UC	1.13	1.33	0.00	0.65	0.90	0.00
(101)-2	4 UC	3.16	—	0.00	0.74	—	0.00
	5 UC	3.16	3.17	0.00	0.71	0.86	0.00
	6 UC	3.16	3.17	0.00	0.67	0.88	0.00
	7 UC	3.15	3.18	0.00	0.64	0.89	0.00
(101)-3	4 UC-2F	0.87	—	2.00	0.55	—	2.00
	5 UC-2F	0.87	0.88	2.00	0.52	0.68	2.00
	6 UC-2F	0.86	0.89	2.00	0.48	0.69	2.00
(101)-4	4.5 UC-2F	1.85	—	1.96	0.88	—	2.00
	5.5 UC-2F	1.84	1.87	2.00	0.84	1.05	2.00
	6.5 UC-2F	1.87	1.70	0.00	0.81	1.03	2.00
(101)-5	4 UC-4F	1.08	—	0.00	0.76	—	0.00
	5 UC-4F	1.08	1.09	0.00	0.74	0.83	0.00
	6 UC-4F	1.09	0.99	0.00	0.69	0.99	0.00
(011)-1	4 UC	1.12	—	0.00	0.65	—	0.00
	5 UC	1.12	1.14	0.00	0.62	0.81	0.00
	6 UC	1.12	1.14	0.00	0.58	0.81	0.00
	7 UC	1.12	1.14	0.00	0.54	0.79	0.00
(011)-2	4 UC	1.14	—	0.00	0.52	—	0.00
	5 UC	1.14	1.15	0.00	0.48	0.67	0.00
	6 UC	1.13	1.15	0.00	0.44	0.68	0.00
	7 UC	1.13	1.15	0.00	0.40	0.67	0.00
(011)-3	4 UC-4F	1.37	—	0.00	1.04	—	0.00
	5 UC-4F	1.36	1.38	0.00	1.01	1.19	0.00
	6 UC-4F	1.36	1.38	0.00	0.94	1.35	0.00
(111)-1	4 UC	3.27	—	0.00	0.72	—	0.00
	5 UC	3.25	3.36	1.95	0.72	0.71	0.00
	6 UC	3.24	3.29	0.00	0.70	0.87	0.00
	7 UC	3.25	3.23	1.84	0.67	0.88	0.00
(111)-2	4 UC-2F	1.03	—	2.00	0.70	—	2.00
	5 UC-2F	1.02	1.04	2.00	0.67	0.82	2.00
	6 UC-2F	1.02	1.04	2.00	0.64	0.82	2.00
(111)-3	4.5 UC-2F	1.46	—	2.00	0.86	—	2.00
	5.5 UC-2F	1.46	1.11	2.00	0.83	0.75	2.00
	6.5 UC-2F	1.46	1.11	2.00	0.80	0.75	2.00
(111)-4	4 UC-4F	1.15	—	0.04	0.79	—	0.00
	5 UC-4F	1.15	1.12	1.31	0.78	0.80	0.00
	6 UC-4F	1.16	1.13	2.92	0.75	0.95	0.00
	7 UC-4F	1.11	1.44	0.00	0.72	0.92	0.00

4. Error Estimation

The error in final total energy is maximum 10^{-6} eV. Compared to the the one in slab thickness convergence, this error is negligible. Of course, there might be considerable errors inherent to the applied electronic structure methods. However, these cannot be quantified without reference value. Therefore, we focus on the slab thickness convergence error.

4.1. Error Estimation in Slab Thickness Convergence

For YF_3 , all surface energies slab-thickness-converged within 0.03 J m^{-2} at thicknesses of about 5–5.5 UC. For HoF_3 , 14 terminations including all of the most stable ones per Miller indices converged to 0.01 J m^{-2} or less within slab thickness of about 6–6.5 UC. Some of the higher energy terminations converged only to 0.02 – 0.04 J m^{-2} at that thickness, whereas four high energy terminations did not converge even to 0.1 J m^{-2} . The difference in surface energy between the two largest adjacent slab thickness are visualized as error bars in Figure S5.

In HoF_3 , the surface energy of (110)-3 with a fluorine-deficit of two per surface is much higher with 2.09 J m^{-2} than any other. It also contains the highest uncertainty due to slab thickness convergence as shown in Table S3 and Figure S5. The large difference to the next smaller slab thickness seems to correlate with the change in magnetic structure from $\mu_{\text{opt}} = 0.27 \mu_{\text{B}}$ to none.

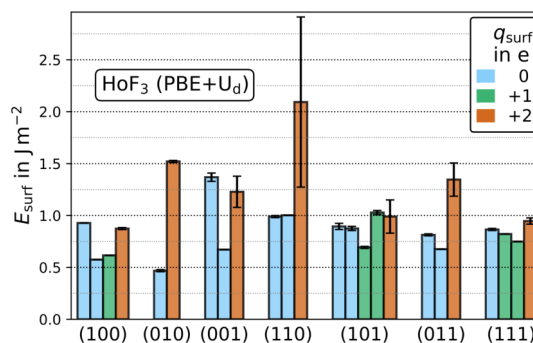


Figure S5. Relaxed slab-derived surface energies of HoF_3 (PBE+ $U_d/3 \text{ eV}/4f$ -in-core). The uncertainty due to slab thickness convergence is given by error bars on each termination.

4.2. Error Estimation in Wulff Plots

The Wulff plot is constructed by the lowest energy termination of each Miller indices. These have a slab thickness convergence error of maximum 0.03 J m^{-2} or 0.01 J m^{-2} for YF_3 or HoF_3 , respectively. The error margins for the Wulff plots given in Table S4 come from a very conservative view and give the maximum of possible error accumulation. For the very tiny surface percentages this gives huge relative errors of 46–100%. For the two most important surfaces, with 25% or 34% surface abundance, the relative errors are 8% or 12%. Note that, due to the geometrical interdependence of the surfaces, the absolute errors are not simply symmetrical around each initial value, but might be generally over- or underestimating.

Table S4. Effect of maximal error accumulation due to the convergence in slab thickness of maximal $\pm 0.03 \text{ J m}^{-2}$ for YF_3 and $\pm 0.01 \text{ J m}^{-2}$ for HoF_3 onto Wulff construction; i denotes the initial value of average surface energy ($\varnothing E_{\text{surf}}$) or surface abundance ($\%_{\text{surf}}$) given by the Wulff plots in the main paper Figure 4:

	YF_3		HoF_3	
	i	± 0.03	i	± 0.01
$\varnothing E_{\text{surf}}$ in J m^{-2}	0.70	0.66–0.73	0.59	0.57–0.60
$\%_{\text{surf}}(100)$	7	4–10	25	25–27
$\%_{\text{surf}}(010)$	26	21–30	34	32–36
$\%_{\text{surf}}(001)$	10	5–17	6	5–8
$\%_{\text{surf}}(110)$	5	2–10	0	0
$\%_{\text{surf}}(101)$	20	11–29	14	11–18
$\%_{\text{surf}}(011)$	22	12–33	13	10–16
$\%_{\text{surf}}(111)$	10	2–23	7	4–11

5. Electronic Properties of Surfaces

5.1. Surface Band Gaps

The direct and indirect band gaps of all slabs are given in Figure S6. It should be noted, that these values are directly obtained from the k -point grid of $9 \times 9 \times 1$ for YF_3 or $7 \times 7 \times 1$ for HoF_3 . No band structures have been calculated for the 2D-slab models. In agreement with the rather flat band structures of bulk YF_3 and HoF_3 shown in Figure S3, most slabs also show a direct Γ - Γ band gap. The Γ -point is included within our k -grids. However, some show indirect band gaps including a k -point, which is not explicitly included within the k -grid. For these, the actual band gaps might slightly differ from the ones given.

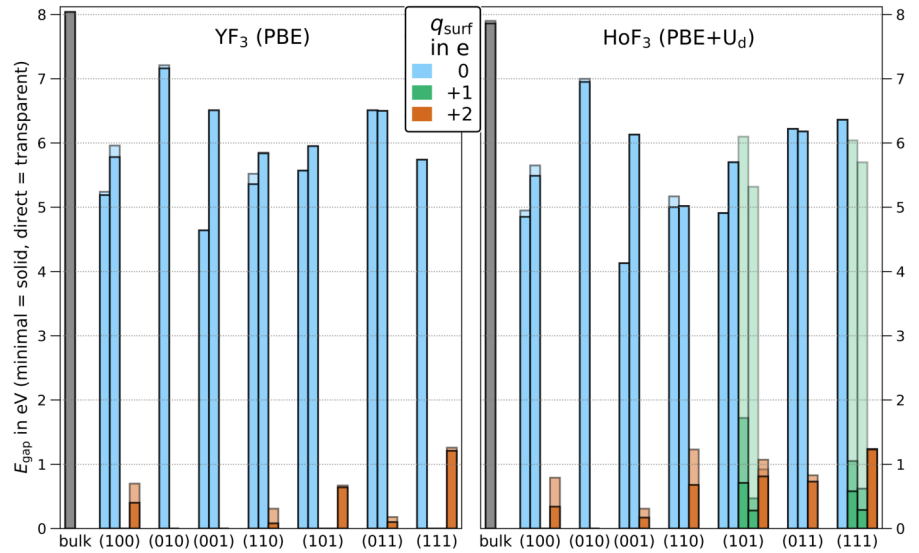


Figure S6. YF_3 (left, PBE) and HoF_3 (right, PBE+ $U_d/3 \text{ eV}/4f$ -in-core) band gaps of surfaces compared with the respective bulk value (gray). Minimal band gaps, direct or indirect are given by solid bars. In the case, the minimal band gap was found to be indirect, also the direct band gap is given by a transparent bar. For HoF_3 (101) and (111) with +1 nominal charges, the band gaps are not spin-symmetric and both direct transitions are given.

5.2. Surface DOS

Slab convergence was tested against the direct band gaps, total DOS and projected DOS onto central-slab atoms. We found that the valence band and near conduction band are already converged at our smallest slab sizes. A comparison of the total DOS between the most stable termination of each (hkl) is shown in Figure S7.

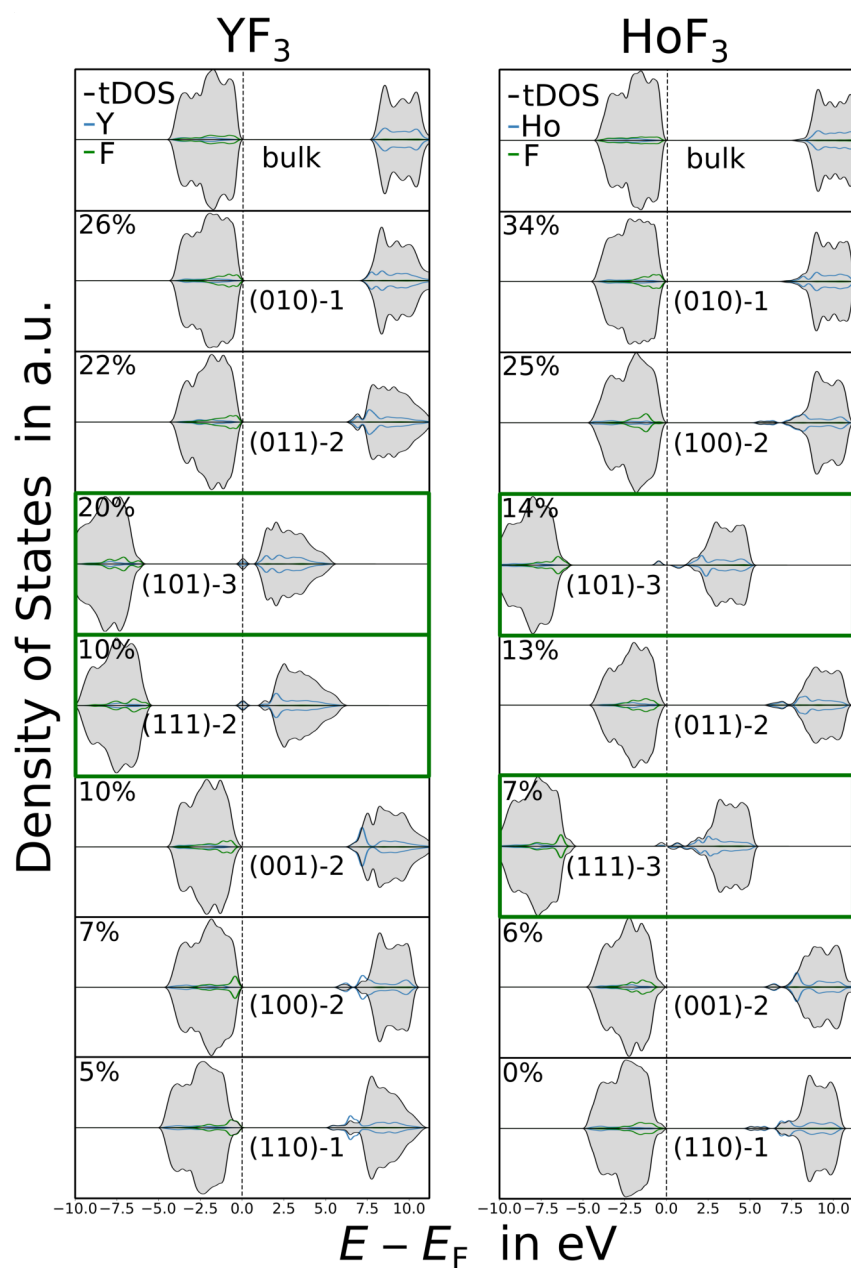


Figure S7. DOS comparison between the most stable surfaces ordered by their abundance (in %): YF_3 (left, PBE), HoF_3 (right, PBE+ $U_d/3$ eV/4f-in-core), total DOS (tDOS: gray, downscaled to the bulk tDOS) and projected DOS of a single surface atom (Y, Ho: blue; F: green). Substoichiometric slabs with a fluorine-deficit of 1 per surface are framed in green. The top row gives the bulk tDOS with projected DOS of a single bulk atom as reference.

3.3. Paper B.2

"Chemical Adsorption of HF, HCl, and H₂O onto YF₃ and Isostructural HoF₃ Surfaces by First Principles"

J. Anders, H. Wiedenhaupt, B. Paulus, *Crystals*, **2023**, 13, 555.

DOI: 10.3390/cryst13040555

URL: <https://doi.org/10.3390/cryst13040555>

Creative commons license: <https://creativecommons.org/licenses/by/4.0/>

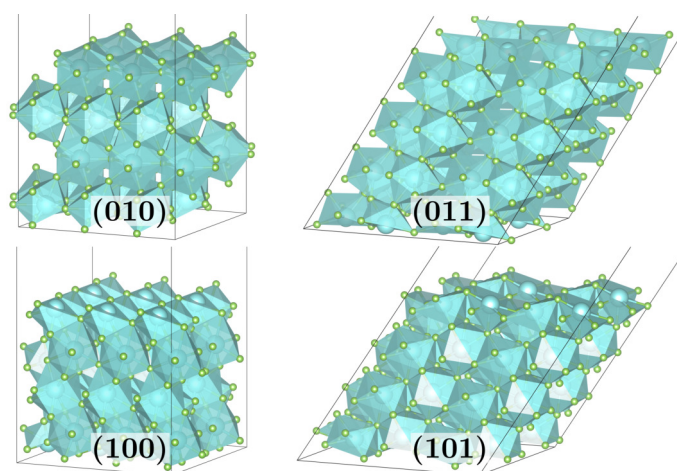


Fig. 1 of paper **B.2**.

Contributions:

The conceptualization was done by Jennifer Anders (J.A.) and Beate Paulus (B.P.). The formal analysis was done by Henrik Wiedenhaupt (H.W.) and J.A. Funding and resources acquisition was done by B.P. Investigations were done by H.W. and J.A. Supervision was done by B.P. Validation and visualization was done by J.A. The original draft was written by, J.A. Review writing and editing was done by J.A. and B.P.

Article

Chemical Adsorption of HF, HCl, and H₂O onto YF₃ and Isostructural HoF₃ Surfaces by First Principles

Jennifer Anders ^{*} , Henrik Wiedenhaupt and Beate Paulus

Institute for Chemistry and Biochemistry, Freie Universität Berlin, Arnimallee 22, 14195 Berlin, Germany

* Correspondence: jennifer.anders@fu-berlin.de

Abstract: The two elements, yttrium and holmium, form a geochemical twin pair as their cations possess equivalent ratios of charge to radius. However, despite their equal electrostatics, a subtle difference in their fluoride or chloride affinity is known within solutions. In this work, we investigated whether this affinity gap is also present within the solid phase and how it depends on the surface configuration. We modeled adsorptions onto β -YF₃ (waimirite) and isostructural β -HoF₃ by periodic density functional theory. To draw conclusions on the affinity toward fluoride and chloride vs. water, adsorbates of HF, HCl, or H₂O onto any of the four highly abundant surfaces of (010), (100), (011), and (101) were studied. Among others, the conformational landscape was explored by 200 ps of ab initio molecular dynamics. For stoichiometric surfaces of both MF₃, we indeed found stronger adsorptions for HF than HCl. All (*hkl*)-H₂O showed slightly stronger adsorption energies for HoF₃, while for HF and HCl, the metal preferences varied by the surface. While (100) showed the strongest preference for HoF₃, (101) preferred YF₃ by the same magnitude.

Keywords: fluorides; geochemical twins; rare earth elements; high-field strength elements; surface adsorption; waimirite; DFT



Citation: Anders, J.; Wiedenhaupt, H.; Paulus, B. Chemical Adsorption of HF, HCl, and H₂O onto YF₃ and Isostructural HoF₃ Surfaces by First Principles *Crystals* **2023**, *13*, 555. <https://doi.org/10.3390/cryst13040555>

Academic Editor: Sergio Brutti

Received: 3 March 2023

Revised: 16 March 2023

Accepted: 20 March 2023

Published: 23 March 2023



Copyright: © 2023 by the authors. Licensee MDPI, Basel, Switzerland. This article is an open access article distributed under the terms and conditions of the Creative Commons Attribution (CC BY) license (<https://creativecommons.org/licenses/by/4.0/>).

1. Introduction

In nature, the elements yttrium and holmium are trivalent cations of practically identical sizes (107.5 pm for Y(III) vs. 107.2 pm for Ho(III) measured at nine-fold coordination, e.g., as present in waimirite) [1,2]. As most geochemical transport processes are driven by the ratio of charge to radius, both high-field strength elements (HFSE) behave alike and are, therefore, referred to as geochemical twin pairs [3]. However, despite the equal electrostatic behavior, subtle differences between both twin elements have been found in solutions within their affinities toward fluoride or chloride [4–6]. It is believed that these small differences are the key forces for the significant decrease in Ho and increase in Y concentrations found in fluoride-rich ores originating from hydrothermal veins [3–5,7–10]. Within these hydrothermal zones, a continuous interplay of dissolving vs. precipitation from the aqueous phase occurs. Modeling this complex system involving a great number of elements in an unknown number of chemical species is a too demanding task to be tackled in its entirety by quantum chemical methods. However, to begin this long journey of understanding these processes in a step-wise manner, we start with the interfaces of the simple, binary fluorides with the most simple, charge-neutral species of fluoride and chloride, HF and HCl, and contrast them with H₂O. Even this simplistic model contains open-ended questions that need to be answered before moving on to more realistic ones. First, due to the absence of such surface studies, it is unknown how the choice of the surface plane affects the halide affinity, or whether the effect is the same for both twin elements. Second, even the pristine surfaces offer plenty of adsorption structural isomers and conformations leading to a potential energy hypersurface with numerous local minima. We, therefore, scanned these by two methods—ab initio molecular dynamics (AIMD) simulations and a systematic generation of initial molecular arrangements. Moreover, the obtained adsorption

energies of well-defined MF_3 -Ads structures pose an excellent theoretical foundation for future spectroscopic measurements of any waimirite-structured rare earth element (REE) trifluoride. To the best of our knowledge, not a single computational study of molecular interactions to a yttrium trihalide surface exists for any rare earth element trihalide or waimirite structure type surface.

2. Methodology

2.1. Crystal Structure and Surfaces

The mineral waimirite-Y is constituted of orthorhombic β - YF_3 , the low-temperature phase of all middle and late lanthanide trifluorides of SmF_3 – LuF_3 [2,11,12]. Its $Pnma$ symmetric unit cell contains four formula units forming distorted tricapped trigonal antiprisms of nine fluorides around each metal center. Analyzing the stability of the bare surfaces for the prototype structure YF_3 and its geochemical twin compound HoF_3 at quantum chemical conditions, in a previous study we found that 75% (YF_3) or 86% (HoF_3) of the total crystal surface was made from the four low Miller index surfaces of (010), (100), (011), and (101) [13]. For the former three, a stoichiometric, non-polar termination was favored, while (101) preferred a substoichiometric composition, in which each surface unit cell was missing one fluorine atom. For the larger supercells used within the isolated setup shown in Figure 1, this resulted in a nominal surface net charge of +4. However, as the applied periodic boundary conditions prohibited a charged surface, each fluorine vacancy instead produced a nominal M(II) center. The most stable and abundant surface of (010) forms a very flat surface of an eight-fold coordinated M(III). The second most abundant surfaces are (011) for YF_3 and (100) for HoF_3 containing M(III) in a six-fold coordination. However, these six-fold polyhedrons possess different shapes and leave M(III) less covered in the case of (100). Both MF_3 agree again on (101) as the third most abundant surface, whose six-fold coordinated M(II) are the most accessible ones within the study.

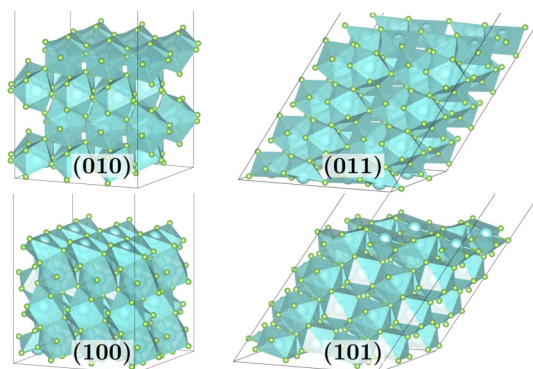


Figure 1. Bare surface supercells as used for the isolated adsorption setup for (010) and (100) of $(4 \times 3 \times 4)$ MF_3 -layers, as well as (011) and (101) of $(4 \times 4 \times 4)$ MF_3 -layers for $M = \text{Y, Ho}$.

The bare surfaces are modeled by sufficiently large supercells to avoid artificial adsorbate–adsorbate interactions (see Figure 1). Molecular adsorbates (Ads) of HF, HCl, and H_2O were adsorbed onto these to study the adsorption energy and structure.

2.2. Scan of Conformational Adsorption Space

The vast conformational spaces of possible adsorbate structural isomers and conformations of MF_3 ·(Ads) were scanned by AIMD and a systematic input generation script. In both, full coverage of the surfaces was probed to directly capture the conformations of multiple adsorbates. Because the atomic structures of YF_3 and HoF_3 surfaces are practically equivalent, we chose to scan the conformational spaces of possible adsorptions using YF_3 ·(Ads) only. We further limited the conformational space scan to the three major

contributing surfaces, as the (100) surface possesses only a minor abundance in YF_3 . Onto these surface slabs, a single layer of four HF or H_2O molecules was added. Relaxed slab supercells of the converged thickness of $(2 \times 2 \times 5)$ YF_3 -layers for (011) and (101) (see Figure 2a) or $(2 \times 1 \times 10)$ YF_3 -layers for (010) were used (see Figure 2b) [13]. For the 1:1 mixed monolayer setup of four HF or HCl with four H_2O molecules onto (010), the surface unit cell was doubled using supercells of $(2 \times 2 \times 4)$ YF_3 -layers (see Figure 2c).

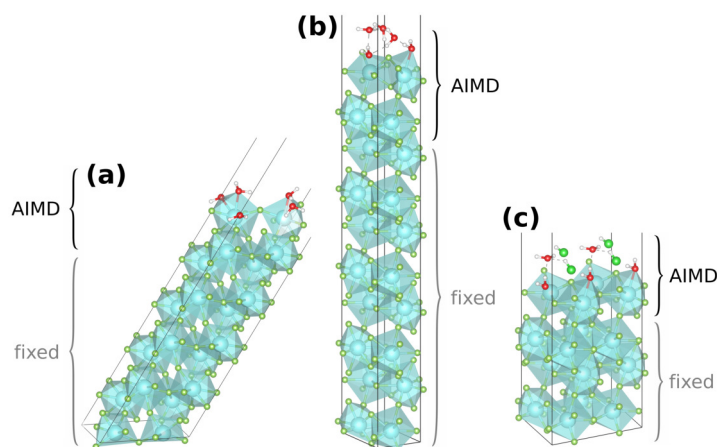


Figure 2. Generic AIMD start structures of the pure monolayer setups of (011)·(H_2O) (a) and (010)· H_2O (b), as well as of the mixed monolayer setup of (010)·HCl: H_2O (c); the region of atoms not fixed (top four YF_3 and adsorbates) is labeled AIMD.

Initial temperature tests of up to 873 K onto (010)·(HF) revealed that at higher temperatures some molecules diffuse into the vacuum because their kinetic energies outweigh the rather weak adsorption. Therefore, the AIMD runs were performed at rather cold temperatures of 50–300 K with the majority of simulation time obtained at 200 K (see Table S3). Summing over all respective trajectories, about 60 ps AIMD simulation time was created for the pure monolayer onto each surface of (010), (011), and (101). About 30 ps was produced for the mixed monolayer onto (010). Within the AIMD simulations, adsorption events were judged by distance to the surface atoms (≤ 260 pm) and visualization. Long-living (≥ 2 ps) coordination events for each surface and adsorbate were selected as starting conformations for further studies. Moreover, the coordination of short lifetimes (≥ 350 fs) was also considered if showing structural features not already within the scope.

In a second approach, input structures for atomic structure relaxation were script-generated, varying the adsorbate position perpendicular and in-plane to the surface, as well as rotating the adsorbate. Monolayer structures of $YF_3 \cdot 4 HF$, $YF_3 \cdot 4 H_2O$ and $YF_3 \cdot 2 HF \cdot 2 H_2O$ were created for the surfaces of (010), (011), and (101), all as supercells in analogy to Figure 2a,b. For each combination of monolayer and surface 36 start structures were generated. From the relaxed 324 structures, the most stable ones were selected for further studies. From both approaches sampling the full monolayer, single adsorbate conformations were extracted and transferred to the isolated adsorption setup of $(4 \times 3 \times 4)$ MF_3 -layers for (010) and (100) or $(4 \times 4 \times 4)$ MF_3 -layers for (011) and (101) (see Figure 1). All (100)·Ads initial structures originated from transferring adsorbate conformations from the other three surfaces. Each selected $YF_3 \cdot HF$ adsorption also posed a starting structure for the respective $YF_3 \cdot HCl$ one. The same applied to the YF_3 analogous HoF_3 , for which the adsorbate coordinates were transferred from the respective $YF_3 \cdot (Ads)$ structures. Overall, an isolated adsorption structural scope of 61 YF_3 and 59 HoF_3 structures were considered. Several of these relaxed into chemically equivalent structures or nearly equivalent conformers of the same structural isomer. Thus, our results are based on a total scope of 44 single

adsorbate structural isomers for each MF₃. The respective scopes for each surface and adsorbate are listed in Table S4 and all structural isomers are depicted in Figures S2–S13.

2.3. Computational Details

The same computational setup of Perdew–Burke–Ernzerhof (PBE) functional [14] at a kinetic cutoff of 773 eV was used within the Vienna Ab Initio Simulation Package (VASP) [15–18] as applied to the surface energies evaluated in [13]. The hard projector augmented wave potentials of H, O, and Cl were applied with valence electron numbers of 6 and 7 for the latter two. The effect of hard vs. normal potential files was tested (see SI Section 1.1 [19,20]). All calculations were performed at the Γ -point. The surface supercells were built with the python packages pymatgen [21,22] and ASE [23]. A minimum of a 25 Å vacuum was applied to all isolated molecules and perpendicular to the surface plane in all supercells to avoid artificial interaction.

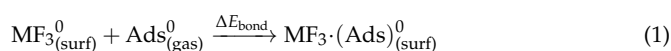
For the first conformational scan approach by AIMD, the NVT ensemble with the Verlet algorithm and the Nosé–Hoover thermostat with a coupling parameter of 1 were applied at a 1 fs time step [24–26]. See Table S3 for an overview of the runtimes at temperatures of 50–300 K. To keep the computational time of the AIMD feasible, the monolayer AIMD (setup a and b) were conducted at low precision, applying the RMM-DIIS [27,28] algorithm with preconditioned residuum-minimization (VeryFast) as well as a default self-consistent field (SCF) convergence criteria. The mixed monolayer AIMD (setup c) was conducted with the default (Kosugi) blocked-Davidson algorithm at normal precision with SCF criteria of 10^{−5} eV.

For the second conformational scan approach of script-generated input structures, the atomic relaxation was conducted via a conjugate gradient algorithm at normal precision with the default convergence criteria.

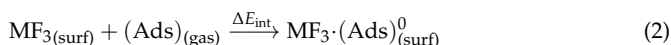
For the isolated adsorption setup used for the analysis, converged surface supercell sizes were found at (4 × 3 × 4) MF₃-layers for (010) and (100) or (4 × 4 × 4) MF₃-layers for (101) and (011) (see Figure S1 and Tables S1 and S2). The top two MF₃-layers of each surface (48 atoms for (010) and (100) or 64 atoms for (101) and (011)), as well as the adsorbates were relaxed in atomic coordinates with allowed spin polarization, Gaussian smearing with a width of 0.2 eV, Grimme’s dispersion correction with Becke–Johnson damping (D3(BJ)) [29,30], and accurate precision. SCF criteria of 10^{−5} eV were applied for geometry optimizations and 10^{−6} eV for final energies. For difficult SCF cases, symmetry was turned off (ISYM = −1), and/or an additional DFT support grid (.ADDGRID.), and/or a reduced minimal mixing parameter of Kerker’s initial approximation [31] (AMIN) of <0.01 was used. If geometric convergence was neither achieved by the conjugated gradient nor by the RMM-DIIS algorithm [27], the ionic step width (POTIM) was reduced from its default of 0.5 to 0.1 Å. All atomic structure visualizations were conducted in VESTA [32]. Trajectories were visualized in VMD [33].

3. Results

All given results were obtained using the isolated adsorption setup shown in Figure 1. We differentiate two kinds of adsorption energies referred to as bonding energies (ΔE_{bond}) according to Reaction (1) and interaction energy (ΔE_{int}) according to Reaction (2). The former is calculated with respect to the relaxed (superscript 0) reactants. Consequently, ΔE_{bond} is obtained from the total energy of the relaxed adsorption structure minus the total energy of the relaxed, bare surface supercell and the relaxed isolated adsorbate in vacuum.



ΔE_{int} is obtained analogously from non-relaxed reactants, which already possess the same atomic structure as inside the relaxed adsorption product.



Thus, the difference in both adsorption energies is the atomic structure relaxation of the separated reactants from the relaxed structure of the adsorption product. It is, therefore, labeled as preparation energy (ΔE_{prep})

$$\Delta E_{\text{prep}} = \Delta E_{\text{bond}} - \Delta E_{\text{int}} \quad (3)$$

By the atomic structure relaxation of the adsorbed product, spontaneous dissociations of some adsorbate molecules were observed. These can be classified into two categories. For one, there are the H-bond induced dissociations onto stoichiometric surfaces of several strong HCl adsorptions, whose final hydrogen-to-surface fluorine ($\text{H}-\text{F}_{\text{surf}}$) distance is considerably shorter than the H-Cl one (see Figure S17). In one case, this was followed by a subsequent movement of the Cl atom across the surface leading to a final H-Cl distance of 7 Å (see Figure S6e). However, in all of these H-bond-induced dissociations, the $\text{MF}_3 \cdot \text{Ads}$ stay diamagnetic and no change in the surface metal (M_{surf}) or partial charges occur.

On the other hand, several adsorptions of HF or HCl onto the electron-rich, sub-stoichiometric (101) surface spontaneously dissociate in a hydride-forming mechanism leading to separately adsorbed halide and hydride ($q(\text{H}) = -0.6 \text{ e}$) anions. By formal oxidation state, two electrons are transferred from the surface to the adsorbate, agreeing with a total change in Bader charges of about 1.4 e. A clear difference is also shown by the spin arrangement. The collinear magnetic moment of $8 \mu_{\text{B}}$ is found for bare (101) produced by the ferromagnetic arrangement of the eight formal M(II) centers (four each on the top/bottom surfaces), each with an unpaired electron. While this magnetic moment is retained for all non-dissociated (101)·Ads, it reduces to $6 \mu_{\text{B}}$ within the hydride-forming ones. Within the final structures, these two anions remain either coordinated to the same M_{surf} ((101)· $\text{H}_{3\text{Å}}\text{F}/\text{Cl}$, see Figure S19a), coordinated to two neighboring M_{surf} , ((101)· $\text{H}_{3.5\text{Å}}\text{F}$, see Figure S19b), or with one other M_{surf} in-between ((101)· $\text{H}_{7\text{Å}}\text{F}/\text{Cl}$, see Figure S19c). Due to the charge repulsion, the stability and, thus, the absolute adsorption energy increase by the distance of halide to hydride (see Table 1). (101)· $\text{H}_{3.5\text{Å}}\text{F}$ was not found to be stable for the respective HCl adsorption. Starting from that structure, the chloride moved across the surface, converging into (101)· $\text{H}_{7\text{Å}}\text{Cl}$. On the used ($2 \times 2 \times 4$) supercell, this is the maximum distance that the two anions can adopt while being coordinated to the six-fold coordinated M(II) centers. Compared to all other $\text{MF}_3 \cdot \text{Ads}$, their adsorption energies are much larger and their properties are very different. We, therefore, analyzed them as a separate class of adsorption.

Table 1. Comparison of the different hydride-forming adsorptions by coordination number ($\text{CN}_{\text{surf}}^{\text{M}}$) and the maximum change in partial charge for one M_{surf} ($\Delta q_{\text{surf}}^{\text{M}}$) of the coordination sites(s) vs. the bare (101) charges of $q_{\text{surf}}^{\text{M(II)}} = 1.7\text{--}1.8 \text{ e}$ for six-fold coordinated and $q_{\text{surf}}^{\text{M(III)}} = 2.2\text{--}2.4 \text{ e}$ for seven-fold coordinated M_{surf} , together with the halide to hydride distances ($R_{\text{Cl}\dots\text{H}}$) in pm and adsorption energies in $\text{kJ}\cdot\text{mol}^{-1}$.

	$\text{CN}_{\text{surf}}^{\text{M}}$	M	HF			HCl				
			$R_{\text{F}\dots\text{H}}$	$\Delta q_{\text{surf}}^{\text{M}}$	ΔE_{int}	ΔE_{bond}	$R_{\text{Cl}\dots\text{H}}$	$\Delta q_{\text{surf}}^{\text{M}}$	ΔE_{int}	ΔE_{bond}
(101)· $\text{H}_{3\text{Å}}\text{F}/\text{Cl}$	6	Y	257	+0.5	−973	−315	285	+0.4	−829	−311
		Ho	262	+0.5	−938	−290	292	+0.4	−807	−296
(101)· $\text{H}_{3.5\text{Å}}\text{F}$	6; 7	Y	352	+0.5	−1036	−349			—	
		Ho	357	+0.5	−1003	−324				
(101)· $\text{H}_{7\text{Å}}\text{F}/\text{Cl}$	6; 6	Y	681	+0.5	−1081	−485	684	+0.5	−937	−482
		Ho	688	+0.5	−1079	−483	691	+0.5	−937	−481

The ΔE_{bond} values of Table 1 are plotted separately in Figure 3 to the respective strongest adsorptions of the other $\text{MF}_3 \cdot \text{Ads}$ giving an impression on how large ΔE_{bond} is affected by the interplay of the adsorbate type and surface cut, while the metal type only has a minor impact.

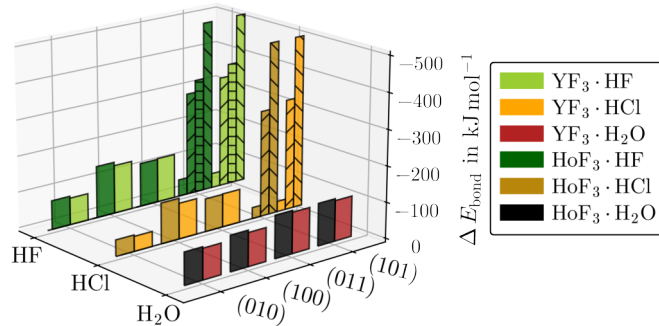


Figure 3. ΔE_{bond} for the respective strongest adsorptions of YF_3 -Ads and HoF_3 -Ads for each (hkl) and adsorbate. The hydride-forming adsorptions of $(101)\cdot\text{H}_{3\text{\AA}}\text{F}/\text{Cl}$ (upward stripes), $(101)\cdot\text{H}_{3.5\text{\AA}}\text{F}$ (horizontal stripes), or $(101)\cdot\text{H}_{7\text{\AA}}\text{F}/\text{Cl}$ (downward stripes) are given separately.

The most striking variation in adsorption energies is found along $(hkl)\cdot\text{HF}$ and $(hkl)\cdot\text{HCl}$. The differences between the respective strongest adsorptions onto the same MF_3 ($\Delta\Delta E_{\text{bond}}^{\text{Cl-F}}$) according to Equation (4) are depicted in Figure 4.

$$\Delta\Delta E_{\text{bond}}^{\text{Cl-F}} = \Delta E_{\text{bond}}^{(hkl)\cdot\text{HCl}} - \Delta E_{\text{bond}}^{(hkl)\cdot\text{HF}} \quad (4)$$

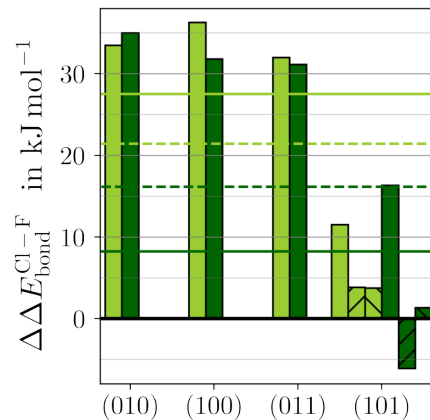


Figure 4. The difference in ΔE_{bond} between $\text{MF}_3\cdot\text{HCl}$ and $\text{MF}_3\cdot\text{HF}$ ($\Delta\Delta E_{\text{bond}}^{\text{Cl-F}}$) (see Equation (4)) for $M = \text{Y}$ (light green) and $M = \text{Ho}$ (dark green) is given for the respective strongest adsorption of each (hkl) (bars) and as the average overall (hkl) with (solid lines) or without the hydride-forming adsorptions (dashed lines) of $(101)\cdot\text{H}_{3\text{\AA}}\text{F}/\text{Cl}$ (upward stripes) or $(101)\cdot\text{H}_{7\text{\AA}}\text{F}/\text{Cl}$ (downward stripes).

Both MF_3 bind HF significantly stronger than HCl. The preference for HF over HCl is similar in the three stoichiometric surfaces. Within the F-substoichiometric surface of (101), the preference is considerably smaller. The averages of ΔE_{bond} over all surfaces are 8–28 $\text{kJ}\cdot\text{mol}^{-1}$ stronger for HF, suggesting that the F– M_{surf} bond is slightly stronger than the respective chloride one. Consequently, the surface mobility of chloride should be slightly higher. This, together with chloride's more diffuse electron density resulting in higher spacious demands considering the repulsion with the hydride, indicates why the $(101)\cdot\text{H}_{3.5\text{\AA}}\text{F}/\text{Cl}$ was not found to be stable.

The ΔE_{bond} for each non-hydride-forming adsorption is related to ΔE_{int} in Figure 5. Naturally, the difference of ΔE_{prep} is very low for the weakly adsorbed structures. However, it remains very low for any $\text{MF}_3\cdot\text{H}_2\text{O}$, while it becomes significant for strong HF adsorptions onto (100) or (011) and even larger than the final ΔE_{bond} itself for the respective

HCl adsorptions. The latter is caused by the strong H–Cl bond elongation introduced above as H-bond dissociated structures.

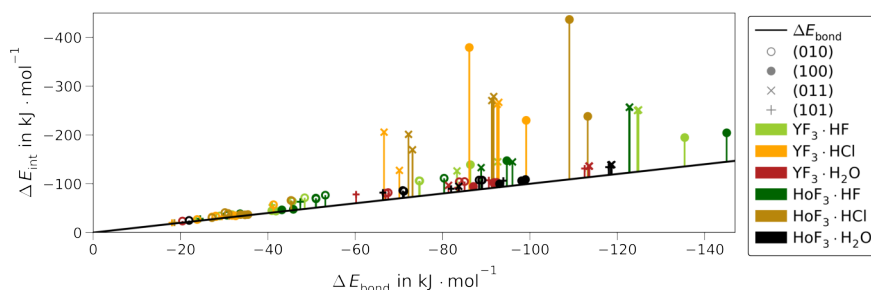


Figure 5. Interaction energy (ΔE_{int}) vs. bonding energy (ΔE_{bond}) for all non-hydride-forming $\text{MF}_3 \cdot \text{Ads}$ for each surface (marker) of YF_3 (light green/orange/red) or HoF_3 (dark green/brown/black) without the 7 Å-wide dissociated (100)·HCl. The difference (ΔE_{prep} , see Equation (3)) is emphasized by bars.

In the next step, the effect of the metal type on ΔE_{prep} is considered (see Figures S14–S16). While most $\text{HoF}_3 \cdot \text{H}_2\text{O}$ adsorb slightly stronger than the respective $\text{YF}_3 \cdot \text{H}_2\text{O}$ already prior to relaxation, the preference for HoF_3 very mildly increases further upon relaxation by up to $4 \text{ kJ} \cdot \text{mol}^{-1}$. Moreover, all non-hydride-forming $\text{MF}_3 \cdot \text{HF}$ prefer HoF_3 over YF_3 before relaxation by up to $10 \text{ kJ} \cdot \text{mol}^{-1}$. However, for most of these, ΔE_{prep} hardly affects this preference, with the exception of (011)·HF, for which ΔE_{prep} shifts twice that initial preference for HoF_3 to a final preference for YF_3 . Finally, the non-hydride-forming $\text{MF}_3 \cdot \text{HCl}$ show the strongest preference for HoF_3 of up to 50 or $57 \text{ kJ} \cdot \text{mol}^{-1}$ with or without the relaxation of the reactants. However, the effect of ΔE_{prep} decreases or increases the preference depending on the adsorption isomer.

In the following, the quantities determining ΔE_{bond} are further analyzed. The dependency on the atomic structure parameters of the H-bond angle and distance toward F_{surf} , as well as the direct coordination of O/F/Cl toward Y/Ho_{surf} are visualized in Figure 6. See Table S5 for a comparison of non-/weighted averages over each or all surfaces, as well as Figure S18 for a version of Figure 6 including the hydride-forming adsorptions.

As by the lanthanide contraction, the ionic radii of Y(III) and Ho(III) differ by as little as 0.3 pm [1]; any difference in coordination originates from a different bonding situation. However, we found that the difference in the $\Delta \Delta E_{\text{bond}}^{\text{Y-Ho}}$ (see Figure S24) is too weak to affect the intra-adsorbate bond lengths, as these stay insensitive to the metal center. By closer contact to the surface, the H-bond angles and distances, as well as the direct coordination distances of O/F/Cl to M_{surf} show notable differences between $\text{YF}_3 \cdot \text{Ads}$ and $\text{HoF}_3 \cdot \text{Ads}$ when analyzing each surface separately. On the other hand, the signs of these differences vary by surface. As a result, averaging over all surfaces, the metal-type correlated differences do not persist. Considering all surfaces, only those between the adsorbates survive. These emphasize the considerable distinction between weak H_2O H-bonds vs. strong HF and HCl ones. Moreover, they reveal the high similarity between the latter two, which is also present in the direct coordination when accounting for the gap in ionic radii [1].

Linked to the ionic radii and electronegativities, differences between the adsorbates appear within the partial Bader charges. Due to the high electronegativity of F and, thus, little variance of its strongly negative partial charge, which is already very low (-0.7 e) for molecular HF, the adsorption onto MF_3 shows no further reduction (see Figures 7 and S20).

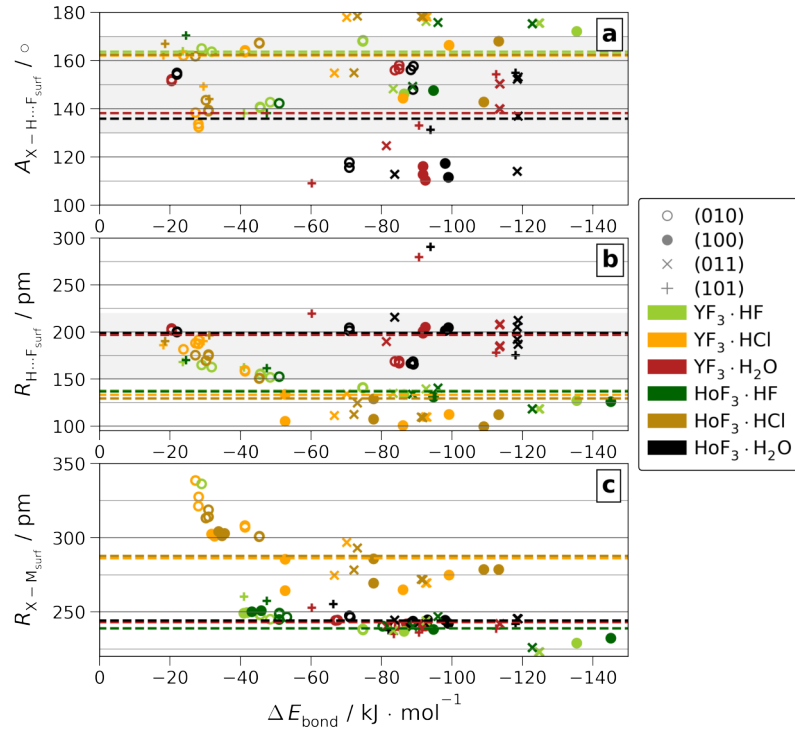


Figure 6. H-bond angles ($A_{X-H \cdots F_{\text{surf}}}$ (a)) and distances ($R_{H \cdots F_{\text{surf}}}$ (b)) or direct surface coordination distances of $X = O/F/Cl$ ($R_{X-M_{\text{surf}}}$ (c)) vs. ΔE_{bond} for all non-hydrate-forming adsorptions. The respective ΔE_{bond} -weighted means over all surfaces are given as dashed lines. The area of H-bonds classified as moderate [34] is shaded.

However, for HCl adsorption, the partial charges change significantly compared to molecular HCl due to the low ionic character of the H–Cl bond (see Figure S21). This allows the bonding character of $MF_3 \cdot HCl$ to be surface-dependent. For adsorptions toward six-fold coordinated M_{surf} as present in (100) and (011), the partial charges suggest a strong ionic character comparable to $MF_3 \cdot HF$. This is linked to the formation of the H-bond dissociated $Cl \cdots H - F_{\text{surf}}$ introduced above, for which we find no significant differences between both MF_3 (see Figure S17). Finally, the partial charges of H_2O are only marginally affected by the adsorption (see Figures S22 and S23). Onto all stoichiometric surfaces, the positive charge of H slightly increases by 0.1 e, regardless of CN_{surf} . Adsorbed at the substoichiometric, electron-rich (101), the positive charge of H is reduced slightly by up to -0.2 e. However, in contrast to HF and HCl, no dissociation is observed.

Despite the high similarity between the two MF_3 for the properties discussed above, subtle differences appear within the adsorption energies. The differences between both MF_3 for all adsorptions are weighed with the respective surface abundance ratios ($\%_{\text{surf}}$, Equation (5)) of the ideal crystals taken from [13] and compared in Figure 8.

$$\Delta \Delta E_{\text{bond}, \%}^{Y-Ho} = \left(\Delta E_{\text{bond}}^{YF_3 \cdot \text{Ads}} \cdot \%_{\text{surf}}^{YF_3} \right) - \left(\Delta E_{\text{bond}}^{HoF_3 \cdot \text{Ads}} \cdot \%_{\text{surf}}^{HoF_3} \right) \quad (5)$$

Note that HoF_3 possesses higher $\%_{\text{surf}}$ than YF_3 for the surfaces of (010) and (100) but lower ones for (011) and (101). See Figure S24 for the corresponding non-weighted differences ($\Delta \Delta E_{\text{bond}}^{Y-Ho}$) together with the respective $\%_{\text{surf}}$.

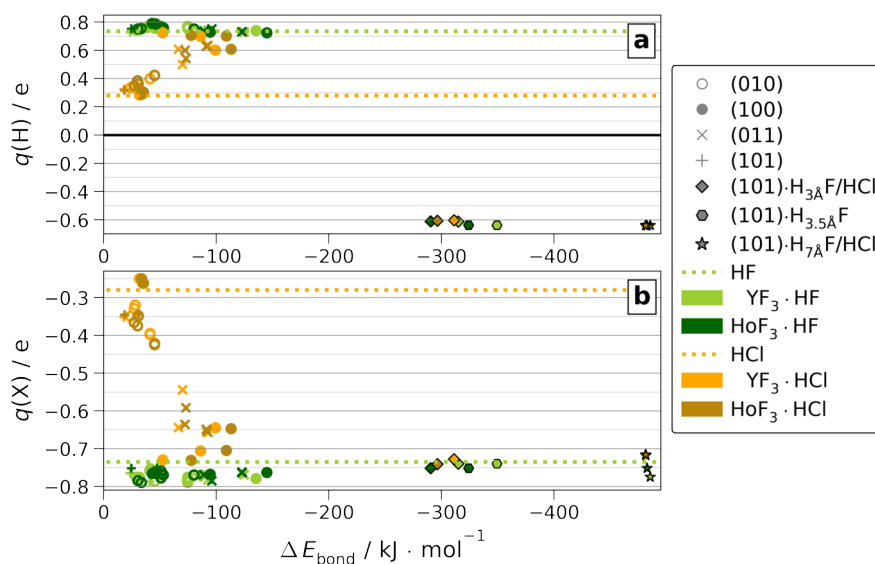


Figure 7. Partial Bader charges ($q(\text{H})$ (a) and $q(\text{Cl})/q(\text{F})$ (b)) of molecular HF or HCl (dotted lines) or adsorbed onto MF₃ (markers).

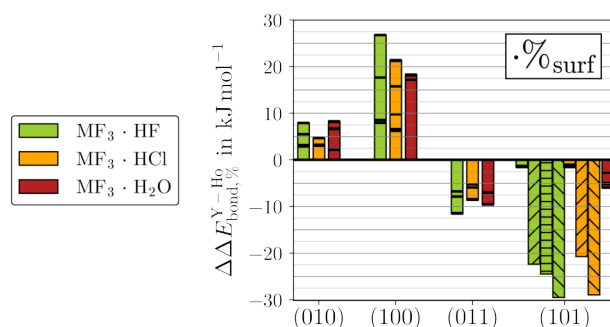


Figure 8. The %_{surf}-weighted differences in ΔE_{bond} between YF₃ and HoF₃ ($\Delta\Delta E_{\text{bond}, \%}^{\text{Y-Ho}}$) (see Equation (5)) is given for all adsorptions (black lines). The bar plots highlight the respective strongest adsorptions. The hydride-forming adsorptions of (101)·H_{3Å}F/Cl (upward stripes), (101)·H_{3.5Å}F (horizontal stripes), or (101)·H_{7Å}F/Cl (downward stripes) are given separately.

Even though the non-weighted H₂O adsorptions bind slightly stronger to HoF₃ than YF₃ regardless of the surface cut, the different %_{surf} of the two MF₃ impose a surface dependency for $\Delta\Delta E_{\text{bond}, \%}^{\text{Y-Ho}}$. In contrast, the binding preference for HoF₃ or YF₃ shown by HF or HCl varies inherently between the different surfaces. At the eight-fold coordinated M_{surf} of (010), HF and HCl, both slightly prefer HoF₃. While the $\Delta\Delta E_{\text{bond}, \%}^{\text{Y-Ho}}$ of HF is about the same as H₂O, it is lowest for HCl. By the better accessible M_{surf} of (100), the %_{surf}-weighted preferences for HoF₃ grow considerably, yielding the strongest for (100)·HF within all (hkl) -Ads. In contrast, all $\Delta\Delta E_{\text{bond}, \%}^{\text{Y-Ho}}$ at (011) prefer YF₃ due to the flipped order in surface abundances. Although (011) also contains six-fold coordinated M_{surf}, these are less accessible (see Figure 1). In agreement with the metal accessibility, the magnitude of $\Delta\Delta E_{\text{bond}, \%}^{\text{Y-Ho}}$ is only marginally larger than in (010). Finally, for the hydride-forming adsorptions of (101), the higher %_{surf} of YF₃ amplifies the inherent preference for the lighter twin element. We believe that this difference primarily originates from the ionization potentials (IP) of M(II), which are measured to be 20.5 eV for Y(II) and 22.8 eV for Ho(II) in the gas phase [35,36]. It may be assumed that the qualitative relation of considerably

easier Y(II) than Ho(II) oxidation remains the same for six-fold coordinated metal centers. It should be noted that Ho(II) is measured to have a $4f^{11}$ configuration [36], which is not possible with the applied $4f^{10}$ -in-core potential developed for the stable oxidation state of Ho(III). Therefore, no quantitative relation of ΔIP to $\Delta \Delta E_{\text{bond}}^{Y-\text{Ho}}$ may be drawn.

Comparing our quantum chemical results with experiments and theoretical studies in solutions at elevated temperatures, we find an agreement of the preference for fluoride over chloride found for Y(III) in aqueous solutions by AIMD simulations [6]. This suggests that the preference is present in different phases of Y(III). A solubility study in aqueous HF compared the fluoride affinity of Y(III) vs. Ho(III) [4]. At high HF concentrations, they found a higher fluoride affinity by Y(III). In another study applying AIMD and in situ X-ray experiments onto aqueous NaCl solutions, the chloride affinity of Y(III) was also found to be higher compared to Ho(III) [5]. Within our study, however, the marginal difference in fluoride or chloride affinity shown between the two metals is much lower than between the surfaces. This demonstrates that, compared to the free ions in solution, the difference in binding affinity at the surface is very sensitive to the surface geometry and termination, even when the respective ions are as similar as Y(III) vs. Ho(III). Apparently, the change in the local environment between the surfaces affects the two twin elements differently and, thus, shifts the small gap in halide affinities between the two. Comparable experimental and computational studies of Y(III) and Ho(III) affinities in solutions containing both HF and HCl could give more insight into these subtle differences and would be the next step to elucidate the composition in fluoride-rich ores originating from hydrothermal veins.

4. Conclusions

The adsorptions of HF, HCl, and H₂O onto the four most abundant surfaces of YF₃ and HoF₃ were studied by applying periodic density functional theory. Comparing the two halides, we found that both MF₃ bind HF notably stronger than HCl for all three stoichiometric surfaces. We found that the adsorption energy of H₂O is insensitive to the surface cut. Due to this surface insensitivity, the slight preference for HoF₃ over YF₃ remains constant. On the contrary, the adsorption energies of HF and HCl are sensitive to the surface. For the latter, this also shows within the partial charges. For the rather bulk-like surface of (010) with low metal accessibility, the preference for HoF₃ is comparable to that shown by H₂O. The adsorptions of HF and HCl onto stoichiometric surfaces with more accessible M_{surf} are considerably stronger, showing the strongest H-bonds and, thus, the largest structural changes upon adsorption. These also show varying metal affinities. HF and HCl both show the strongest preference for HoF₃ over YF₃ within (100), a surface that is also much more abundant in the heavier twin trifluoride. On the other hand, (011) prefers YF₃. Finally, the largest preference for YF₃ is found for the hydride-forming adsorptions onto the F-substoichiometric (101).

Supplementary Materials: The following supporting information can be downloaded at <https://www.mdpi.com/article/10.3390/cryst13040555/s1>, Table S1: Scope of supercell size convergence onto the (010) YF₃ surface with a single adsorbate. Each column gives the supercell thickness in unit cell copies (UC) and YF₃-layers perpendicular to the surface. The supercells of 1 UC thickness are done for a single adsorbate of HF or H₂O. Figure S1: Supercell size convergence of ΔE_{bond} for the (010) YF₃ surface with a single adsorbate of HF (top left) or H₂O (top right). The x-axis gives the thickness perpendicular to the surface (p) in YF₃-layers. The difference to the biggest supercell ($\Delta E_{\text{bond}} - \Delta E_{\text{bond}}(6 \times 3 \times 4)$) is plotted for YF₃-HF (bottom). The green dotted lines and shaded areas visualize ± 1.0 and $\pm 0.5 \text{ kJ}\cdot\text{mol}^{-1}$, respectively. Table S2: Converged supercell sizes of all surface cuts with their corresponding surface area (A_{surf}), the total number of formula units ($N_{\text{f.u.}}$) and atoms within the supercell (N_{atoms}). Table S3: Overview of AIMD simulation at different temperatures for pure monolayers of YF₃-(Ads)₄ and 1:1 mixed monolayers of YF₃-(Ads₁)₄-(Ads₂)₄ with summed-up simulation times over all respective runs. Table S4: Structural scope of MF₃-(Ads) giving the total number of different final conformers with the total number of all respective starting structures in parenthesis. Figure S2: Relaxed adsorption structures of (010)-1HF in order of increasing $|\Delta E_{\text{bond}}|$ viewing onto the surface unit cell (black frame) made from $(2 \times 3 \times 2)$ bulk unit cells.

Two YF₃ structures were conducted for structural isomer c and five for structural isomer e. Three HoF₃ structures were conducted for structural isomer c and two for structural isomer e. Figure S3: Relaxed adsorption structures of (010)·1HCl in order of increasing $|\Delta E_{\text{bond}}|$ viewing onto the surface unit cell (black frame) made from $(2 \times 3 \times 2)$ bulk unit cells. Three structures were conducted for structural isomer b and two for structural isomer c. Figure S4: Relaxed adsorption structures of (010)·1H₂O in order of increasing $|\Delta E_{\text{bond}}|$ viewing onto the surface unit cell (black frame) made from $(2 \times 3 \times 2)$ bulk unit cells. Three structures were conducted for structural isomers b and c. Figure S5: Relaxed adsorption structures of (100)·1HF in order of increasing $|\Delta E_{\text{bond}}|$ viewing onto the surface unit cell (black frame) made from $(2 \times 3 \times 2)$ bulk unit cells. Figure S6: Relaxed adsorption structures of (100)·1HCl in order of increasing $|\Delta E_{\text{bond}}|$ viewing onto the surface unit cell (black frame) made from $(2 \times 3 \times 2)$ bulk unit cells. Figure S7: Relaxed adsorption structures of (100)·1H₂O in order of increasing $|\Delta E_{\text{bond}}|$ viewing onto the surface unit cell (black frame) made from $(2 \times 3 \times 2)$ bulk unit cells. Two YF₃ structures were conducted for structural isomer a. Figure S8: Relaxed adsorption structures of (011)·1HF in order of increasing $|\Delta E_{\text{bond}}|$ viewing onto the surface unit cell (black frame) made from $(2 \times 2 \times 4)$ bulk unit cells. Two structures were conducted for structural isomer c. Figure S9: Relaxed adsorption structures of (011)·1HCl in order of increasing $|\Delta E_{\text{bond}}|$ viewing onto the surface unit cell (black frame) made from $(2 \times 2 \times 4)$ bulk unit cells. Two structures were conducted for structural isomer c. Figure S10: Relaxed adsorption structures of (011)·1H₂O in order of increasing $|\Delta E_{\text{bond}}|$ viewing onto the surface unit cell (black frame) made from $(2 \times 2 \times 4)$ bulk unit cells. Two structures were conducted for structural isomer b. Figure S11: Relaxed adsorption structures of (101)·1HF in order of increasing $|\Delta E_{\text{bond}}|$ viewing onto the surface unit cell (black frame) made from $(2 \times 2 \times 4)$ bulk unit cells. The hydride-forming configurations c, d, and e are called MF₃·H_{3.5Å}F, MF₃·H_{3.5Å}F and MF₃·H_{7Å}F within the main paper according to the H–F distance. Figure S12: Relaxed adsorption structures of (101)·1HCl in order of increasing $|\Delta E_{\text{bond}}|$ viewing onto the surface unit cell (black frame) made from $(2 \times 2 \times 4)$ bulk unit cells. The hydride-forming configurations c and d are called MF₃·H_{3Å}Cl and MF₃·H_{7Å}Cl within the main paper according to the H–Cl distance. For configuration d, two structures were conducted for HoF₃·H_{7Å}Cl. Figure S13: Relaxed adsorption structures of (101)·1H₂O in order of increasing $|\Delta E_{\text{bond}}|$ viewing onto the surface unit cell (black frame) made from $(2 \times 2 \times 4)$ bulk unit cells. Figure S14: Difference in the adsorption energies of YF₃·HF and HoF₃·HF with $(\Delta \Delta E_{\text{bond}}^{Y-\text{Ho}})$ or without $(\Delta \Delta E_{\text{int}}^{Y-\text{Ho}})$ relaxed reactants. An area of $\pm 2 \text{ kJ}\cdot\text{mol}^{-1}$ is shaded. Figure S15: Difference in the adsorption energies of YF₃·HCl and HoF₃·HCl with $(\Delta \Delta E_{\text{bond}}^{Y-\text{Ho}})$ or without $(\Delta \Delta E_{\text{int}}^{Y-\text{Ho}})$ relaxed reactants. An area of $\pm 10 \text{ kJ}\cdot\text{mol}^{-1}$ is shaded. Figure S16: Difference in the adsorption energies of YF₃·H₂O and HoF₃·H₂O with $(\Delta \Delta E_{\text{bond}}^{Y-\text{Ho}})$ or without $(\Delta \Delta E_{\text{int}}^{Y-\text{Ho}})$ relaxed reactants. An area of $\pm 2 \text{ kJ}\cdot\text{mol}^{-1}$ is shaded. Table S5: Calculated means of intra-adsorbate bond length ($R_{\text{X-H}}$), H-bond angles ($A_{\text{X-H}\dots\text{F}_{\text{surf}}}$) and distances ($R_{\text{H}\dots\text{F}_{\text{surf}}}$), direct O/F/Cl to metal coordination ($R_{\text{X-Y}/\text{Ho}_{\text{surf}}}$) without weight (\bar{n}) or weighted by ΔE_{bond} as given in Equation 1 (\bar{n}_E) for all non-hydride-forming single adsorptions and without the 7 Å dissociated (100)·HCl structural isomer e; the \bar{n}_E over all (*hkl*) are plotted in Figure 6 within the main paper. Figure S17: $R_{\text{H}\dots\text{F}_{\text{surf}}}$ vs. $R_{\text{X-H}}$ for HoF₃·Ads (a) and YF₃·Ads (b) for all non-hydride-forming adsorptions but the 7 Å wide H-bond dissociated (100)·HCl. $R_{\text{H}\dots\text{F}_{\text{surf}}} = R_{\text{X-H}} - \Delta R_x$ pm is highlight for $\Delta R_x = 0$ (solid line) and $\Delta R_x = 30$ (dotted line). Figure S18: Coordination distances toward the surface by the adsorbate for H ($R_{\text{H}\dots\text{F}/\text{M}_{\text{surf}}}$, a) and X = O/F/Cl ($R_{\text{X-M}_{\text{surf}}}$, b) vs. ΔE_{bond} for all single adsorptions. Figure S19: Changes in partial Bader charges (≥ 0.05 e) of M_{surf} upon adsorbate dissociation for (101)·H_{3Å}F/Cl (a), (101)·H_{3.5Å}F (b) and (101)·H_{7Å}F/Cl (c) for YF₃·HF (1a–1c), HoF₃·HF (2a–2c), YF₃·HCl (3a–3c) and HoF₃·HCl (4a–4c). Figure S20: Change of partial Bader charges of HF adsorbed onto YF₃ or HoF₃ ($\Delta q(\text{H})$ a with zoom b and $\Delta q(\text{F})$ c) vs. molecular HF. Figure S21: Change of partial Bader charges of HCl adsorbed onto YF₃ or HoF₃ ($\Delta q(\text{H})$ a and $\Delta q(\text{Cl})$ b) vs. molecular HCl. Figure S22: Partial Bader charges of molecular H₂O (dotted line) and adsorbed onto YF₃ or HoF₃ ($q(\text{H})$ a and $q(\text{O})$ b). Figure S23: Change of partial Bader charges of H₂O adsorbed onto YF₃ or HoF₃ ($\Delta q(\text{H})$ a and $\Delta q(\text{O})$ b) vs. molecular H₂O. Figure S24: The difference in ΔE_{bond} between YF₃ and HoF₃ ($\Delta \Delta E_{\text{bond}}^{Y-\text{Ho}}$) (see Equation (2)) is given for all single adsorptions (black lines). The bar plots highlight the respective strongest adsorbed structures. The hydride-forming adsorptions of (101)·H_{3Å}F/Cl (upward stripes), (101)·H_{3.5Å}F (horizontal stripes) or (101)·H_{7Å}F/Cl (downward stripes) are given separately. The surface abundance ratios ($\%_{\text{surf}}$) for the ideal crystals are taken from [13].

Author Contributions: Conceptualization, J.A. and B.P.; formal analysis, H.W. and J.A.; funding acquisition, B.P.; investigation, H.W. and J.A.; resources, B.P.; supervision, B.P.; validation, J.A.; visualization, J.A.; writing—original draft, J.A.; writing—review and editing, J.A. and B.P. All authors have read and agreed to the published version of the manuscript.

Funding: The project was funded by the Freie Universität Berlin and the Deutsche Forschungsgemeinschaft (DFG, German Research Foundation)—Project-ID 387284271—CRC 1349—fluorine-specific interactions.

Institutional Review Board Statement: Not applicable.

Informed Consent Statement: Not applicable.

Data Availability Statement: See supplementary materials. All relaxed surface structures are available within the NOMAD repository (ID: xoipefEvRGOWfNV5x_R1MA). Further data can be requested from the authors.

Acknowledgments: The authors thank the North-German Supercomputing Alliance (Norddeutscher Verbund zur Förderung des Hoch- und Höchstleistungsrechnens HLRN) and the Zentraleinrichtung für Datenverarbeitung (ZEDAT) at the Freie Universität Berlin for the computational resources, as well as the Freie Universität Berlin and the German Science Foundation (DFG) for funding within the CRC 1349—Fluorine-Specific Interactions.

Conflicts of Interest: The authors declare no conflict of interest.

References

1. Shannon, R.D. Revised effective ionic radii and systematic studies of interatomic distances in halides and chalcogenides. *Acta Cryst. A* **1976**, *32*, 751–767. [[CrossRef](#)]
2. Atencio, D.; Bastos Neto, A.C.; Pereira, V.P.; Ferron, J.T.M.M.; Hoshino, M.; Moriyama, T.; Watanabe, Y.; Miyawaki, R.; Coutinho, J.M.V.; Andrade, M.B.; et al. Waimirite-(Y), orthorhombic YF₃, a new mineral from the Pitinga mine, Presidente Figueiredo, Amazonas, Brazil and from Jabal Tawlah, Saudi Arabia: Description and crystal structure. *Mineral. Mag.* **2015**, *79*, 767–780. [[CrossRef](#)]
3. Bau, M. Controls on the fractionation of isoivalent trace elements in magmatic and aqueous systems: Evidence from Y/Ho, Zr/Hf, and lanthanide tetrad effect. *Contrib. Mineral. Petrol.* **1996**, *123*, 323–333. [[CrossRef](#)]
4. Loges, A.; Migdisov, A.A.; Wagner, T.; Williams-Jones, A.E.; Markl, G. An experimental study of the aqueous solubility and speciation of Y(III) fluoride at temperatures up to 250 °C. *Geochim. Cosmochim. Acta* **2013**, *123*, 403–415. [[CrossRef](#)]
5. Guan, Q.; Mei, Y.; Etschmann, B.; Testemale, D.; Louvel, M.; Brugger, J. Yttrium complexation and hydration in chloride-rich hydrothermal fluids: A combined ab initio molecular dynamics and in situ X-ray absorption spectroscopy study. *Geochim. Cosmochim. Acta* **2020**, *281*, 168–189. [[CrossRef](#)]
6. Stefanski, J.; Jahn, S. Yttrium speciation in subduction-zone fluids from ab initio molecular dynamics simulations. *Solid Earth* **2020**, *11*, 767–789. [[CrossRef](#)]
7. Bau, M.; Dulski, P. Comparative study of yttrium and rare-earth element behaviours in fluorine-rich hydrothermal fluids. *Contrib. Mineral. Petrol.* **1995**, *119*, 213–223. [[CrossRef](#)]
8. Schönenberger, J.; Köhler, J.; Markl, G. REE systematics of fluorides, calcite and siderite in peralkaline plutonic rocks from the Gardar Province, South Greenland. *Chem. Geol.* **2008**, *247*, 16–35. [[CrossRef](#)]
9. Loges, A. (Freie Universität Berlin, Berlin, Germany). Private Communication, 2020.
10. Zhang, W.; Yan, T. A molecular dynamics investigation of La³⁺ and Lu³⁺-ligand speciation in aqueous solution. *J. Mol. Liq.* **2022**, *347*, 118367. [[CrossRef](#)]
11. Zalkin, A.; Templeton, D.H. The Crystal Structures of YF₃ and Related Compounds. *J. Am. Chem. Soc.* **1953**, *75*, 2453–2458. [[CrossRef](#)]
12. Spedding, F.H.; Henderson, D.C. High-temperature heat contents and related thermodynamic functions of seven trifluorides of the rare earths: Y, La, Pr, Nd, Gd, Ho, and Lu. *J. Chem. Phys.* **1971**, *54*, 2476–2483. [[CrossRef](#)]
13. Anders, J.; Limberg, N.; Paulus, B. First Principle Surface Analysis of YF₃ and Isostructural HoF₃. *Materials* **2022**, *15*, 6048. [[CrossRef](#)] [[PubMed](#)]
14. Perdew, J.P.; Burke, K.; Ernzerhof, M. Generalized Gradient Approximation Made Simple. *Phys. Rev. Lett.* **1996**, *77*, 3865–3868. [[CrossRef](#)] [[PubMed](#)]
15. Kresse, G.; Hafner, J. Ab initio molecular dynamics for liquid metals. *Phys. Rev. B* **1993**, *47*, 558–561. [[CrossRef](#)]
16. Kresse, G.; Furthmüller, J. Efficiency of ab-initio total energy calculations for metals and semiconductors using a plane-wave basis set. *Comput. Mat. Sci.* **1996**, *6*, 15–50. [[CrossRef](#)]
17. Kresse, G.; Furthmüller, J. Efficient iterative schemes for ab initio total-energy calculations using a plane-wave basis set. *Phys. Rev. B* **1996**, *54*, 11169–11186. [[CrossRef](#)] [[PubMed](#)]

18. Kresse, G.; Hafner, J. Norm-conserving and ultrasoft pseudopotentials for first-row and transition elements. *J. Phys. Condens. Matter* **1994**, *6*, 8245–8257. [CrossRef]
19. NIST Computational Chemistry Comparison and Benchmark Database, NIST Standard Reference Database Number 101. 2022. Available online: <http://cccbdb.nist.gov/> (accessed on 05 December 2022).
20. NIST Diatomic Spectral Database, NIST Standard Reference Database 114. Available online: <https://www.nist.gov/pml/diatomic-spectral-database> (accessed on 5 December 2022).
21. Sun, W.; Ceder, G. Efficient creation and convergence of surface slabs. *Surf. Sci.* **2013**, *617*, 53–59. [CrossRef]
22. Tran, R.; Xu, Z.; Radhakrishnan, B.; Winston, D.; Sun, W.; Persson, K.A.; Ong, S.P. Surface energies of elemental crystals. *Sci. Data* **2016**, *3*, 160080. [CrossRef]
23. Larsen, A.H.; Mortensen, J.J.; Blomqvist, J.; Castelli, I.E.; Christensen, R.; Dułak, M.; Friis, J.; Groves, M.N.; Hammer, B.; Hargus, C.; et al. The atomic simulation environment—a Python library for working with atoms. *J. Phys. Condens. Matter* **2017**, *29*, 273002. [CrossRef]
24. Nosé, S. A unified formulation of the constant temperature molecular dynamics methods. *J. Chem. Phys.* **1984**, *81*, 511–519. [CrossRef]
25. Hoover, W.G. Canonical dynamics: Equilibrium phase-space distributions. *Phys. Rev. A* **1985**, *31*, 1695–1697. [CrossRef] [PubMed]
26. Nosé, S. Constant Temperature Molecular Dynamics Methods. *Prog. Theor. Phys. Suppl.* **1991**, *103*, 1–46. [CrossRef]
27. Pulay, P. Convergence acceleration of iterative sequences. the case of scf iteration. *Chem. Phys. Lett.* **1980**, *73*, 393–398. [CrossRef]
28. Wood, D.M.; Zunger, A. A new method for diagonalising large matrices. *J. Phys. A Math. Gen.* **1985**, *18*, 1343. [CrossRef]
29. Grimme, S.; Antony, J.; Ehrlich, S.; Krieg, H. A consistent and accurate ab initio parametrization of density functional dispersion correction (DFT-D) for the 94 elements H-Pu. *J. Chem. Phys.* **2010**, *132*, 154104. [CrossRef] [PubMed]
30. Grimme, S.; Ehrlich, S.; Goerigk, L. Effect of the damping function in dispersion corrected density functional theory. *J. Comput. Chem.* **2011**, *32*, 1456–1465. [CrossRef]
31. Kerker, G.P. Efficient iteration scheme for self-consistent pseudopotential calculations. *Phys. Rev. B* **1981**, *23*, 3082–3084. [CrossRef]
32. Momma, K.; Izumi, F. VESTA 3 for three-dimensional visualization of crystal, volumetric and morphology data. *J. Appl. Crystallogr.* **2011**, *44*, 1272–1276. [CrossRef]
33. Humphrey, W.; Dalke, A.; Schulten, K. VMD: Visual molecular dynamics. *J. Mol. Graph.* **1996**, *14*, 33–38. [CrossRef]
34. Jeffrey, G. *An Introduction to Hydrogen Bonding*; Oxford University Press: New York, NY, USA; Oxford, UK, 1997.
35. Epstein, G.L.; Reader, J. Spectrum of doubly ionized yttrium (YIII). *J. Opt. Soc. Am.* **1975**, *65*, 310–314. [CrossRef]
36. Johnson, D.A.; Nelson, P.G. Lanthanide Ionization Energies and the Sub-Shell Break. Part 2. The Third and Fourth Ionization Energies. *J. Phys. Chem. Ref. Data* **2017**, *46*, 013109. [CrossRef]

Disclaimer/Publisher’s Note: The statements, opinions and data contained in all publications are solely those of the individual author(s) and contributor(s) and not of MDPI and/or the editor(s). MDPI and/or the editor(s) disclaim responsibility for any injury to people or property resulting from any ideas, methods, instructions or products referred to in the content.

Supplementary Materials: Chemical Adsorption of HF, HCl, and H₂O onto YF₃ and Isostructural HoF₃ Surfaces by First Principles

Jennifer Anders, Henrik Wiedenhaupt, Beate Paulus

Contents

	1
1 Computational Method Validation	1 2
1.1 Potential Files	1 3
1.2 Supercell Size	2 4
2 AIMD	3 5
3 Structural Scope	4 6
3.1 (010)	4 7
3.1.1 HF	4 8
3.1.2 HCl	5 9
3.1.3 H ₂ O	5 10
3.2 (100)	5 11
3.2.1 HF	5 12
3.2.2 HCl	6 13
3.2.3 H ₂ O	6 14
3.3 (011)	6 15
3.3.1 HF	6 16
3.3.2 HCl	7 17
3.3.3 H ₂ O	7 18
3.4 (101)	7 19
3.4.1 HF	7 20
3.4.2 HCl	8 21
3.4.3 H ₂ O	8 22
4 Effect of Relaxation	8 23
5 Averages over Structural Properties	9 24
6 H-Bond Dissociated Structures	10 25
7 Hydride Forming Dissociated Structures	11 26
8 Partial Charges	12 27
9 Y vs. Ho Surface Dependence of Adsorption Energy	14 28
References	15 29

1. Computational Method Validation

1.1. Potential Files

We used the hard potential files for atoms available as recommended by VASP for very small bond distances, as e.g. the case for H–F, a central molecule of this study. We tested the effect of the hard potential files F_h and H_h vs. the normal ones F and H while keeping all other parameters, including the kinetic cutoff value constant as given in computational details. The first test system is the simple free, molecular HF in vacuum, which we need to calculate ΔE_{bond} of the adsorbed systems. When using the hard potential files, a bond distance of $R_{\text{H-F}} = 93.15$ pm is obtained. With the normal potential files, the bond elongates significantly by 0.62 pm. According to NIST, the experimental bond length is $R_{\text{H-F}} = 91.68$ pm [2] or by calculation e.g. 91.7 pm at the CCSD(T)/aug-cc-pVQZ level [1]. Consequently, the bond elongation equals a worse description.

We also tested the effect onto the surfaces by single point calculations with the normal potential files onto bare (100) and adsorbed (100)-HF isomer c (see Figure S5 c) built and relaxed at the hard potential file setup as described in the computational details. The adsorption energy obtained by applying the normal potential files is by -3.4 kJ·mol⁻¹ or

4% stronger. Thus the normal vs. hard potential files also have a considerable effect on the adsorption energies.

1.2. Supercell Size

To ensure isolated adsorptions with non-interacting adsorbates, we tested supercell sizes ($n \times m \times p$) with $n, m, p = \{1 - 3\}$ UC onto the (010) surface with a single HF or H₂O molecule adsorbed. Note that each (010) UC corresponds to $(2 \times 1 \times 2)$ YF₃-layers. The atomic positions of the adsorbate and the first YF₃-layer are relaxed. All other parameters equal those given within in the computational details for the isolated adsorption setup of the main paper.

Table S1. Scope of supercell size convergence onto the (010) YF₃ surface with a single adsorbate. Each column gives the supercell thickness in unit cell copies (UC) and YF₃-layers perpendicular to the surface. The supercells of 1 UC thickness are done for a single adsorbate of HF or H₂O:

YF ₃ ·HF + YF ₃ ·H ₂ O		YF ₃ ·HF		YF ₃ ·HF	
UC	layer	UC	layer	UC	layer
1 × 1 × 1	2 × 1 × 2	1 × 1 × 2	2 × 1 × 4	1 × 1 × 3	2 × 1 × 6
2 × 2 × 1	4 × 2 × 2	2 × 2 × 2	4 × 2 × 4	2 × 2 × 3	4 × 2 × 6
2 × 3 × 1	4 × 3 × 2	2 × 3 × 2	4 × 3 × 4	2 × 3 × 3	4 × 3 × 6
		3 × 3 × 2	6 × 3 × 4		

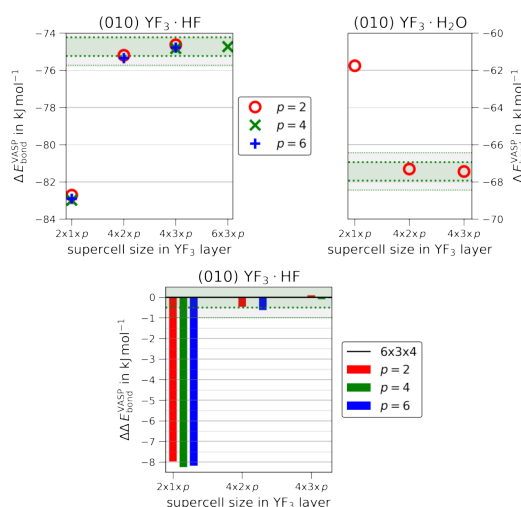


Figure S1. Supercell size convergence of ΔE_{bond} for the (010) YF₃ surface with a single adsorbate of HF (top left) or H₂O (top right). The x-axis gives the thickness perpendicular to the surface (p) in YF₃-layers. The difference to the biggest supercell ($\Delta E_{\text{bond}} - \Delta E_{\text{bond}}(6 \times 3 \times 4)$) is plotted for YF₃·HF (bottom). The green dotted lines and shaded areas visualize ± 1.0 and ± 0.5 kJ·mol⁻¹, respectively.

Comparing the two in-surface-plane lattice vectors, we find that the effect onto YF₃·H₂O is smaller than on YF₃·HF. Therefore, the bigger supercell tests were only done for the slower converging YF₃·HF. When increasing from the unit cell of (2×1) YF₃ layers to a (2×2) supercell of (4×2) YF₃ layers, the difference in ΔE_{bond} is as large as 7–8 kJ·mol⁻¹. A further increase to the square-like supercell of (4×3) YF₃ layers, only changes ΔE_{bond} by 0.5 kJ·mol⁻¹. The next possible supercell of (6×3) YF₃ layers alters the ΔE_{bond} by as little as 0.1 kJ·mol⁻¹. We thus consider a supercell size of $(2 \times 3 \times 2)$ in UC or $(4 \times 3 \times 4)$ in YF₃-layers as converged. This corresponds to almost square-like dimensions

of $12.6430 \text{ \AA} \times 12.9900 \text{ \AA} \times 13.6118 \text{ \AA}$. The ΔE_{bond} differed by as little as $0.5 \text{ kJ}\cdot\text{mol}^{-1}$ compared to the largest tested supercell area of $18.9645 \text{ \AA} \times 12.9900 \text{ \AA} \times 13.6118 \text{ \AA}$ by $(6 \times 3 \times 4)$ YF_3 -layers. For the other surface cuts, supercells have been chosen that keep the dimensions similar.

Upon increasing the supercell thickness, the changes in relaxed adsorption energy ΔE_{bond} are very low. 2 YF_3 -layers perpendicular to the surface give already a converged ΔE_{bond} . However, for the substoichiometric (101) surfaces, these were found to be unstable within the atomic position relaxations. Consequently, a thickness of 4 MF_3 -layers is used for all supercells.

Table S2. Converged supercell sizes of all surface cuts with their corresponding surface area (A_{surf}), the total number of formula units ($N_{\text{f.u.}}$) and atoms within the supercell (N_{atoms}):

(hkl)	in UC	in layers	A_{surf} in \AA^2	$N_{\text{f.u.}}$	N_{atoms}
(010)	$(2 \times 3 \times 2)$	$(4 \times 3 \times 4)$	(12.6430×12.9900)	48	192
(100)	$(2 \times 3 \times 2)$	$(4 \times 3 \times 4)$	(13.6117×12.9900)	48	192
(101)	$(2 \times 2 \times 4)$	$(4 \times 4 \times 4)$	(13.6117×15.3245)	64–8F	248
(011)	$(2 \times 2 \times 4)$	$(4 \times 4 \times 4)$	(12.6430×16.1330)	64	256

2. AIMD

An overview of all AIMD runtimes and temperatures is given in Table S3. Within the pure HF monolayers, the issue of infinite HF-chains forming by the periodic boundary conditions was frequently encountered due to the relatively small lattice vectors within the surface plane. These Ads-Ads interactions gave a more favorable energy than the interaction towards the surface. Accordingly, it was not helpful to judge adsorption events by the energy time series of the trajectory.

Table S3. Overview of AIMD simulation at different temperatures for pure monolayers of $\text{YF}_3\cdot(\text{Ads})_4$ and 1:1 mixed monolayers of $\text{YF}_3\cdot(\text{Ads}_1)_4\cdot(\text{Ads}_2)_4$ with summed up simulation times over all respective runs:

(hkl)	Ads	setup	T in K	runtime in ps
(010)	HF	a	50	1
	HF	a	100	2.5
	HF	a	200	25
	H_2O	a	50	1
	H_2O	a	100	2.5
	H_2O	a	200	25
	HF: H_2O 1:1	c	200	20
	HCl: H_2O 1:1	c	200	8
(011)	HF	b	50	1
	HF	b	100	2.5
	HF	b	200	25
	HF	b	300	1
	H_2O	b	50	1
	H_2O	b	100	2.5
	H_2O	b	200	25
	H_2O	b	300	1
(101)	HF	b	50	1
	HF	b	100	2.5
	HF	b	200	25
	HF	b	300	1
	H_2O	b	50	1
	H_2O	b	100	2.5
	H_2O	b	200	25

3. Structural Scope

This section visualizes all found 44 single adsorption conformations grouped from 60 relaxed structures for YF_3 and 58 for HoF_3 done in the isolated setup. All final electronic structure data used to calculate ΔE_{int} and ΔE_{bond} are available within the NOMAD repository (ID: xoipefEvRGOWfNVSx_R1MA).

Table S4. Structural Scope of $\text{MF}_3 \cdot (\text{Ads})$ giving the total number of different final conformers with the total number of all respective starting structures in parenthesis:

(hkl)	n Ads	YF_3	HoF_3
(010)	1 HF	5 (10)	5 (8)
	1 HCl	3 (6)	3 (6)
	1 H_2O	3 (7)	3 (7)
(100)	1 HF	4 (4)	4 (4)
	1 HCl	5 (5)	5 (5)
	1 H_2O	3 (4)	3 (3)
(011)	1 HF	3 (4)	3 (4)
	1 HCl	3 (4)	3 (4)
	1 H_2O	2 (3)	2 (3)
(101)	1 HF	5 (5)	5 (5)
	1 HCl	4 (4)	4 (5)
	1 H_2O	4 (4)	4 (4)

3.1. (010)

3.1.1. HF

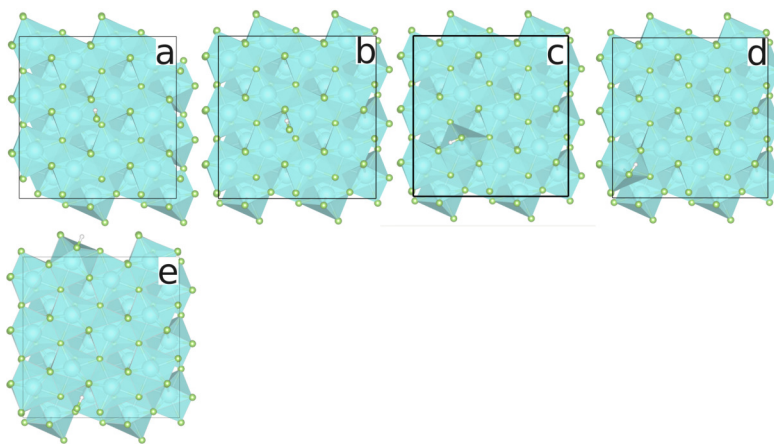


Figure S2. Relaxed adsorption structures of $(010) \cdot 1\text{HF}$ in order of increasing $|\Delta E_{\text{bond}}|$ viewing onto the surface unit cell (black frame) made from $(2 \times 3 \times 2)$ bulk unit cells. Two YF_3 structures were done for structural isomer c and five for structural isomer e. Three HoF_3 structures were done for structural isomer c and two for structural isomer e.

3.1.2. HCl

86

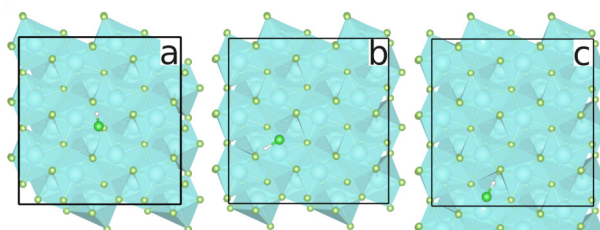


Figure S3. Relaxed adsorption structures of (010)-1HCl in order of increasing $|\Delta E_{\text{bond}}|$ viewing onto the surface unit cell (black frame) made from $(2 \times 3 \times 2)$ bulk unit cells. Three structures were done for structural isomer **b** and two for structural isomer **c**.

3.1.3. H₂O

87

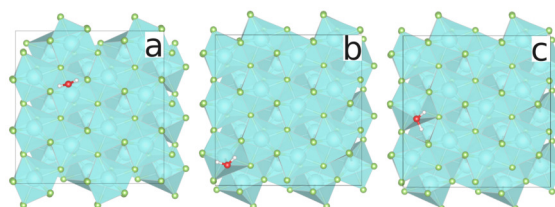


Figure S4. Relaxed adsorption structures of (010)-1H₂O in order of increasing $|\Delta E_{\text{bond}}|$ viewing onto the surface unit cell (black frame) made from $(2 \times 3 \times 2)$ bulk unit cells. Three structures were done for structural isomer **b** and **c**.

3.2. (100)

88

3.2.1. HF

89

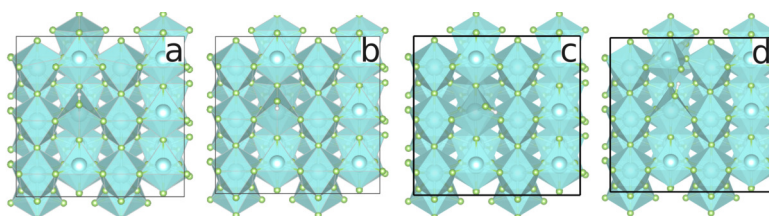


Figure S5. Relaxed adsorption structures of (100)-1HF in order of increasing $|\Delta E_{\text{bond}}|$ viewing onto the surface unit cell (black frame) made from $(2 \times 3 \times 2)$ bulk unit cells.

3.2.2. HCl

90

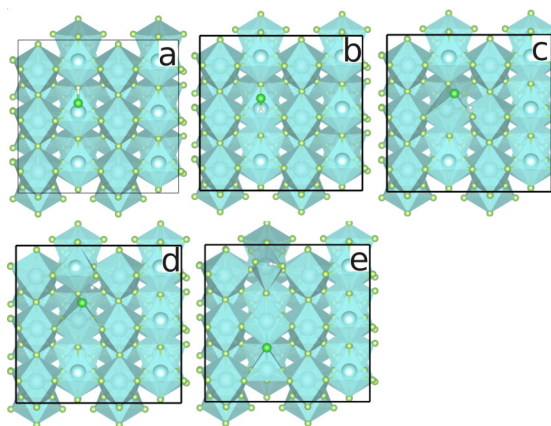


Figure S6. Relaxed adsorption structures of (100)-1HCl in order of increasing $|\Delta E_{\text{bond}}|$ viewing onto the surface unit cell (black frame) made from $(2 \times 3 \times 2)$ bulk unit cells.

3.2.3. H₂O

91

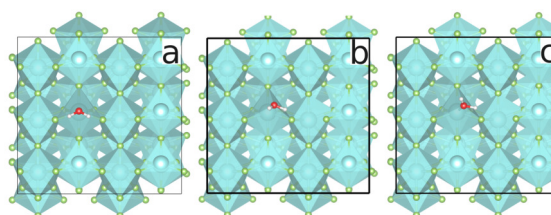


Figure S7. Relaxed adsorption structures of (100)-1H₂O in order of increasing $|\Delta E_{\text{bond}}|$ viewing onto the surface unit cell (black frame) made from $(2 \times 3 \times 2)$ bulk unit cells. Two YF₃ structures were done for structural isomer a.

3.3. (011)

92

3.3.1. HF

93

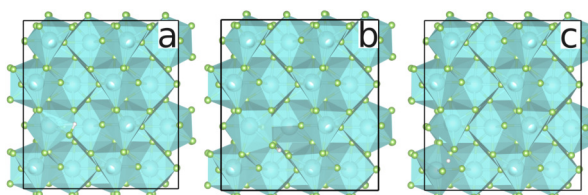


Figure S8. Relaxed adsorption structures of (011)-1HF in order of increasing $|\Delta E_{\text{bond}}|$ viewing onto the surface unit cell (black frame) made from $(2 \times 2 \times 4)$ bulk unit cells. Two structures were done for structural isomer c.

3.3.2. HCl

94

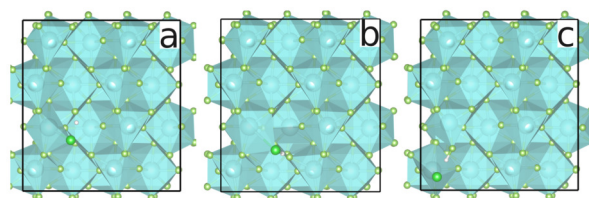


Figure S9. Relaxed adsorption structures of (011)·1HCl in order of increasing $|\Delta E_{\text{bond}}|$ viewing onto the surface unit cell (black frame) made from $(2 \times 2 \times 4)$ bulk unit cells. Two structures were done for structural isomer c.

3.3.3. H₂O

95

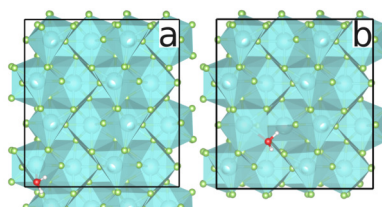


Figure S10. Relaxed adsorption structures of (011)·1H₂O in order of increasing $|\Delta E_{\text{bond}}|$ viewing onto the surface unit cell (black frame) made from $(2 \times 2 \times 4)$ bulk unit cells. Two structures were done for structural isomer b.

3.4. (101)

96

3.4.1. HF

97

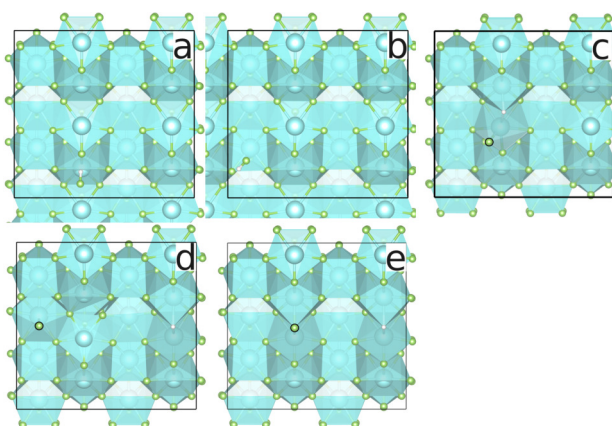


Figure S11. Relaxed adsorption structures of (101)·1HF in order of increasing $|\Delta E_{\text{bond}}|$ viewing onto the surface unit cell (black frame) made from $(2 \times 2 \times 4)$ bulk unit cells. The hydride forming configurations c, d and e are called $\text{MF}_3 \cdot \text{H}_{3\text{Å}}\text{F}$, $\text{MF}_3 \cdot \text{H}_{3.5\text{Å}}\text{F}$ and $\text{MF}_3 \cdot \text{H}_{7\text{Å}}\text{F}$ within the main paper according to the H–F distance.

3.4.2. HCl

98

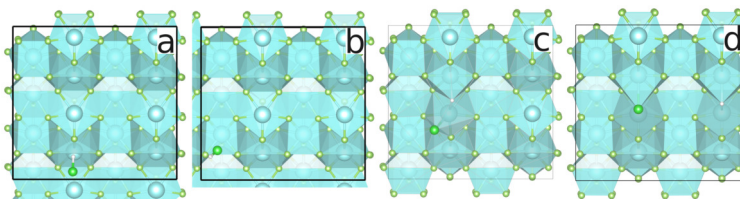


Figure S12. Relaxed adsorption structures of (101)·1HCl in order of increasing $|\Delta E_{\text{bond}}|$ viewing onto the surface unit cell (black frame) made from $(2 \times 2 \times 4)$ bulk unit cells. The hydride forming configurations **c** and **d** are called $\text{MF}_3 \cdot \text{H}_{3\text{A}}\text{Cl}$ and $\text{MF}_3 \cdot \text{H}_{7\text{A}}\text{Cl}$ within the main paper according to the H–Cl distance. For configuration **d**, two structures were done for $\text{HoF}_3 \cdot \text{H}_{7\text{A}}\text{Cl}$.

3.4.3. H₂O

99

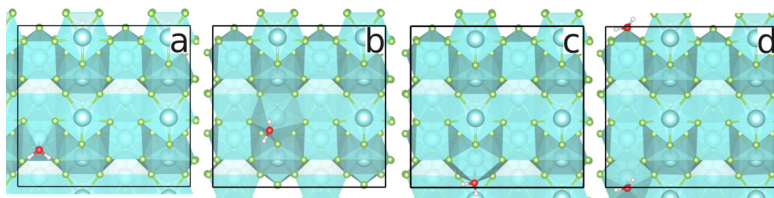


Figure S13. Relaxed adsorption structures of (101)·1H₂O in order of increasing $|\Delta E_{\text{bond}}|$ viewing onto the surface unit cell (black frame) made from $(2 \times 2 \times 4)$ bulk unit cells.

4. Effect of Relaxation

100

Figures S14–S16 illustrate how the difference in adsorption energy between $\text{YF}_3 \cdot \text{Ads}$ and $\text{HoF}_3 \cdot \text{Ads}$ is affected by the relaxation energy of the reactants. $\Delta\Delta E_{\text{int}}^{\text{Y-Ho}}$ is defined analogously to $\Delta\Delta E_{\text{bond}}^{\text{Y-Ho}}$ (see Equation 5 of the main paper). The central, black diagonal plots $\Delta\Delta E_{\text{bond}}^{\text{Y-Ho}}$ against itself. A positive $\Delta\Delta E_{\text{int}}^{\text{Y-Ho}}$ (or $\Delta\Delta E_{\text{bond}}^{\text{Y-Ho}}$) means that the $\text{HoF}_3 \cdot \text{Ads}$ is stronger bound than the respective $\text{YF}_3 \cdot \text{Ads}$. Therefore, values within the lower right triangle correspond to an increased difference between the two MF_3 upon reactant relaxation. 101
102
103
104
105
106

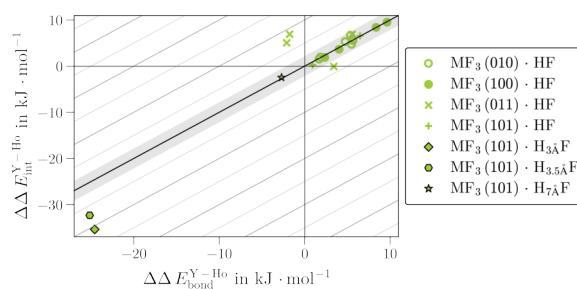


Figure S14. Difference of adsorption energies of $\text{YF}_3 \cdot \text{HF}$ and $\text{HoF}_3 \cdot \text{HF}$ with $(\Delta\Delta E_{\text{bond}}^{\text{Y-Ho}})$ or without $(\Delta\Delta E_{\text{int}}^{\text{Y-Ho}})$ relaxed reactants. An area of $\pm 2 \text{ kJ} \cdot \text{mol}^{-1}$ is shaded.

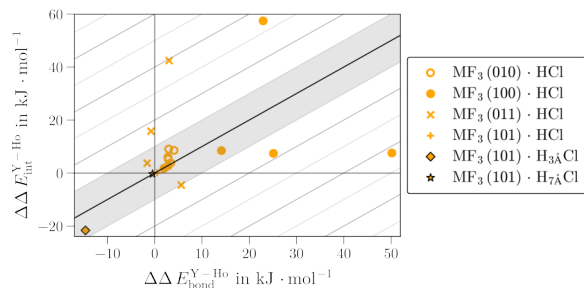


Figure S15. Difference of adsorption energies of $\text{YF}_3 \cdot \text{HCl}$ and $\text{HoF}_3 \cdot \text{HCl}$ with ($\Delta\Delta E_{\text{bond}}^{\text{Y-Ho}}$) or without ($\Delta\Delta E_{\text{int}}^{\text{Y-Ho}}$) relaxed reactants. An area of $\pm 10 \text{ kJ} \cdot \text{mol}^{-1}$ is shaded.

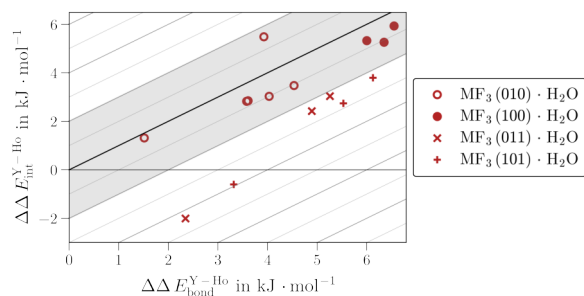


Figure S16. Difference of adsorption energies of $\text{YF}_3 \cdot \text{H}_2\text{O}$ and $\text{HoF}_3 \cdot \text{H}_2\text{O}$ with ($\Delta\Delta E_{\text{bond}}^{\text{Y-Ho}}$) or without ($\Delta\Delta E_{\text{int}}^{\text{Y-Ho}}$) relaxed reactants. An area of $\pm 2 \text{ kJ} \cdot \text{mol}^{-1}$ is shaded.

5. Averages over Structural Properties

107

The coordination of an adsorbate towards the surface has been considered a H-bond, if either the angle or distance satisfies at least the criteria of moderate H-bonds with $A_{\text{X-H} \cdots \text{F}_{\text{surf}}} \geq 130^\circ$ or $R_{\text{H} \cdots \text{F}_{\text{surf}}} \leq 220 \text{ pm}$ [3].

108

109

110

For the structural properties (a) of bond distances and H-bond angle, its arithmetic mean and linearly weighted mean by ΔE_{bond} (\bar{a}_E) is given in Table S5 for each surface and over all surfaces. Note that the intra-adsorbate bond length ($R_{\text{O-H}}$) for $\text{MF}_3 \cdot \text{H}_2\text{O}$ is given as the mean over both O–H bonds.

111

112

113

114

$$\bar{a}_E = \frac{\sum_i (-\Delta E_{\text{int},i} a_i)}{\sum_i (-\Delta E_{\text{bond},i})} \quad (1)$$

Table S5. Calculated means of intra-adsorbate bond length (R_{X-H}), H-bond angles ($A_{X-H \cdots F_{\text{surf}}}$) and distances ($R_{H \cdots F_{\text{surf}}}$), direct O/F/Cl to metal coordinations ($R_{X-Y/\text{Ho}_{\text{surf}}}$) without weight (\bar{a}) or weighted by ΔE_{bond} as given in Equation 1 (\bar{a}_E) for all non-hydride forming single adsorptions and without the 7 Å dissociated (100)-HCl structural isomer e; the \bar{a}_E over all (*hkl*) are plotted in Figure 6 within the main paper:

<i>(hkl)</i>	MF ₃	\bar{R}_{X-H} / pm		$\bar{A}_{X-H \cdots F_{\text{surf}}}$ / °		$\bar{R}_{H \cdots F_{\text{surf}}}$ / pm		$\bar{R}_{X-Y/\text{Ho}_{\text{surf}}}$ / pm			
		\bar{a}	\bar{a}_E	\bar{a}	\bar{a}_E	\bar{a}	\bar{a}_E	\bar{a}	\bar{a}_E		
HF	(010)	Y	98	99	159	161	149	146	252	246	
		Ho	98	98	156	157	152	149	244	244	
	(100)	Y	100	103	159	162	130	130	241	237	
		Ho	100	103	160	162	128	128	243	239	
	(011)	Y	107	108	169	170	128	126	232	230	
		Ho	107	108	169	170	128	126	235	234	
	(101)	Y	95	96	151	148	165	165	260	260	
		Ho	96	96	154	149	166	165	257	257	
	all	Y	100	102	160	164	144	138	246	239	
		Ho	100	103	160	162	144	137	242	239	
	HCl	(010)	Y	131	131	149	151	178	175	321	318
			Ho	132	133	153	155	166	164	310	308
(100)		Y	149	163	155	156	107	107	289	277	
		Ho	148	161	155	156	106	106	293	286	
(011)		Y	157	157	172	173	116	115	278	277	
		Ho	158	158	172	173	114	113	279	278	
(101)		Y	130	130	156	154	188	189	—	—	
		Ho	130	130	156	153	193	194	—	—	
all		Y	143	151	158	162	151	133	297	286	
		Ho	143	152	159	162	147	129	295	288	
H ₂ O		(010)	Y	98	98	155	156	182	173	262	248
			Ho	98	98	143	142	187	181	245	245
	(100)	Y	97	97	113	113	202	202	241	241	
		Ho	97	97	114	114	203	203	244	244	
	(011)	Y	98	98	141	142	195	195	241	241	
		Ho	98	98	134	135	203	202	245	245	
	(101)	Y	99	99	132	137	226	223	241	240	
		Ho	98	99	143	144	233	226	244	243	
	all	Y	98	98	138	138	198	197	249	243	
		Ho	98	98	137	136	199	199	244	244	

The non-/weighted averages of \bar{R}_{X-H} hardly differ (≤ 2 pm) between Y and Ho. Which MF₃·Ads possesses the smaller \bar{R}_{X-H} is surface dependent. Only those H-bonds have been included that are either by distance (≤ 220 pm) or by angle ($\geq 130^\circ$) at least within the moderate regime. By that criteria (101)·H₂O isomer a (see Figure S13 a) is just (hardly) included within YF₃ but (hardly) not in HoF₃.

The H-bond angles also hardly differ between the two metals for MF₃·HF, as well as MF₃·HCl with a maximum difference of 4°. Interestingly for adsorptions of H₂O, the weighted averages for (010) and (011)·H₂O are 14° and 7° wider for YF₃ than for HoF₃, while no such difference is observed for (100) and even the opposite for non-hydride forming (101)·H₂O. The F–H···F_{surf} distance is equivalent for YF₃ and HoF₃. For (010), however, the respective Cl–H···F_{surf} distance is significantly shorter in HoF₃. This is supported by the little bit wider H-bonds angles.

6. H-Bond Dissociated Structures

Adsorbates have been classified as H-bond dissociated if the distance within the adsorbate molecule is at least by 30 pm larger than the H-bond distance to a surface. This cutoff is illustrated in Figure S17 as dotted line.

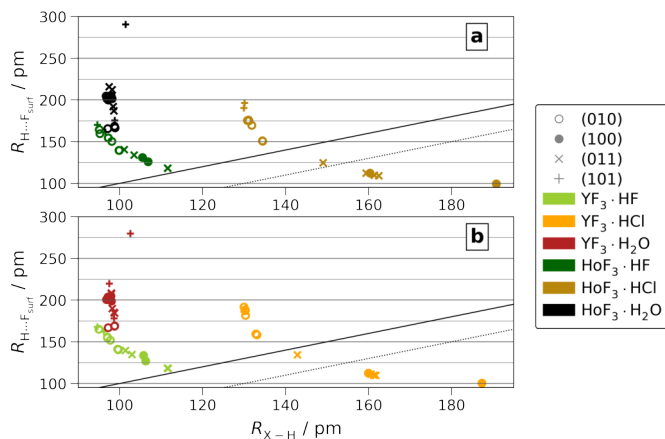


Figure S17. $R_{H...F_{surf}}$ vs. R_{X-H} for HoF_3 -Ads (a) and YF_3 -Ads (b) for all non-hydride forming adsorptions but the 7 Å wide H-bond dissociated (100)·HCl. $R_{H...F_{surf}} = R_{X-H} - \Delta R_x$ pm is highlight for $\Delta R_x = 0$ (solid line) and $\Delta R_x = 30$ (dotted line).

7. Hydride Forming Dissociated Structures

Figure S18 gives a version of Figure 6 b and c of the main paper including the hydride forming adsorptions of (101)·HF/HCl. Their negatively charged hydrogen forms no H-bond to F_{surf} but directly coordinates to M_{surf} . Thus, the distances of hydrogen towards the surface given in Figure S18 a are $R_{H...M_{surf}}$ for the hydride forming adsorptions, while for any other, these are $R_{H...F_{surf}}$, as in the main paper.

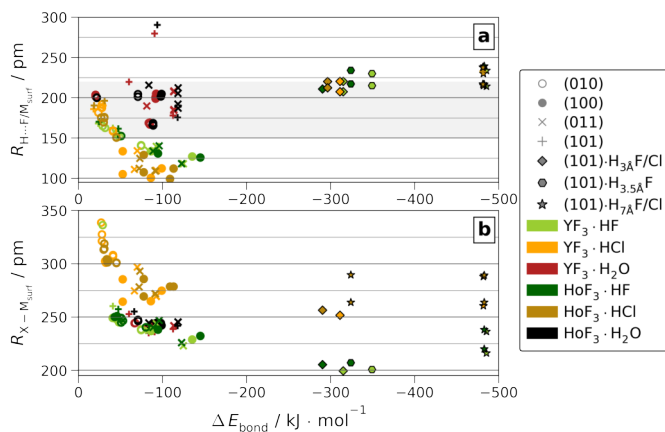


Figure S18. Coordination distances towards the surface by the adsorbate for H ($R_{H...F/M_{surf}}$, a) and X = O/F/Cl ($R_{X-M_{surf}}$, b) vs. ΔE_{bond} for all single adsorptions.

Figure S19 gives the changes in partial Bader charges of ≥ 0.05 e upon adsorption for all metal centers. The partial charges of all F_{surf} remain unchanged compared to the bare surface. Upon hydride formation, the surface metal partial charges are increased by 0.4–0.5 e for each of the two $M_{surf}(II)$ (next to) coordination sites for (101)· $H_{7A}F/Cl$ and (101)· $H_{3.5A}F$. In (101)· $H_{3A}F/Cl$, with the halide and hydride coordinating to the same $M_{surf}(II)$, again increased by 0.5 e, the remaining charge is split over two further $M_{surf}(II)$.

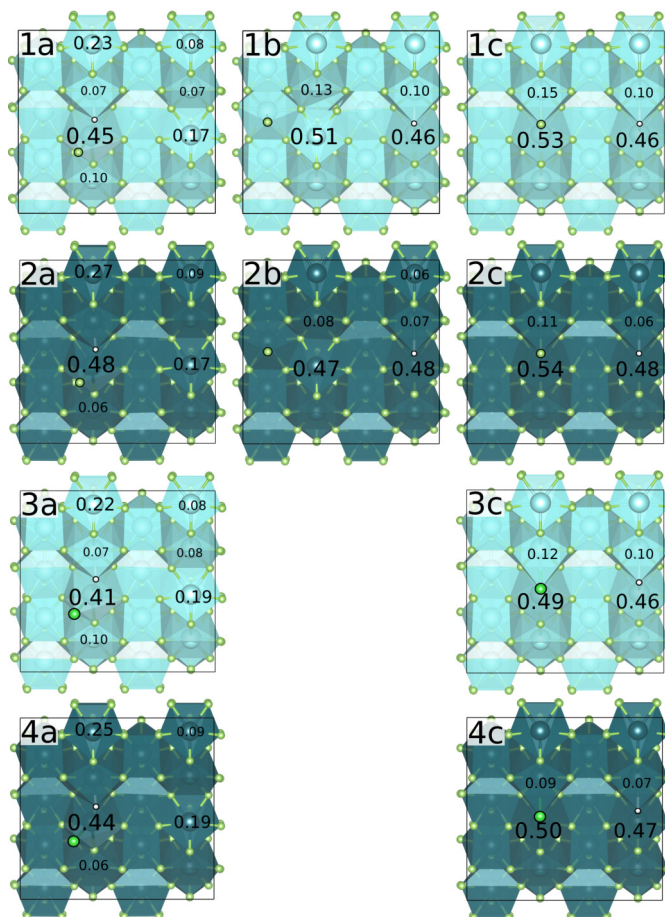


Figure S19. Changes in partial Bader charges ($\geq 0.05 e$) of M_{surf} upon adsorbate dissociation for $(101)\cdot\text{H}_{3\text{\AA}}\text{F}/\text{Cl}$ (a), $(101)\cdot\text{H}_{3.5\text{\AA}}\text{F}$ (b) and $(101)\cdot\text{H}_{7\text{\AA}}\text{F}/\text{Cl}$ (c) for $\text{YF}_3\cdot\text{HF}$ (1a–1c), $\text{HoF}_3\cdot\text{HF}$ (2a–2c), $\text{YF}_3\cdot\text{HCl}$ (3a–3c) and $\text{HoF}_3\cdot\text{HCl}$ (4a–4c).

8. Partial Charges

The partial charges of the adsorbed structure, as well as their differences compared to the free molecule are given in Figure S20–S23. See the main paper Figure 7 for the final partial charges of HF and HCl adsorptions.

143

144

145

146

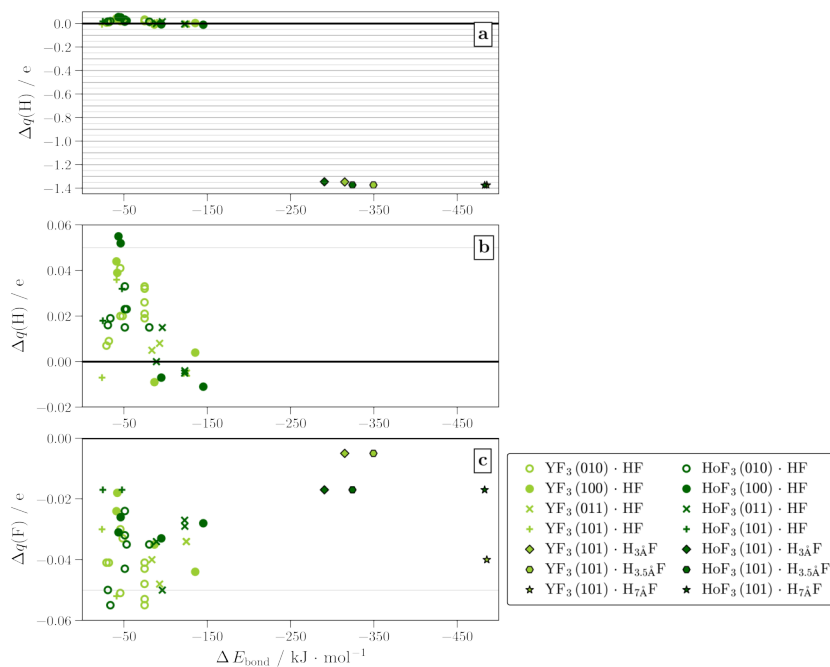


Figure S20. Change of partial Bader charges of HF adsorbed onto YF₃ or HoF₃ ($\Delta q(\text{H})$ a with zoom b and $\Delta q(\text{F})$ c) vs. molecular HF.

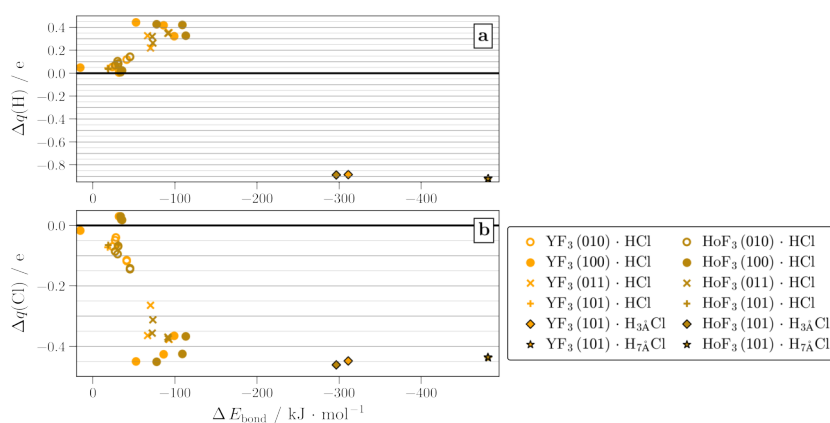


Figure S21. Change of partial Bader charges of HCl adsorbed onto YF₃ or HoF₃ ($\Delta q(\text{H})$ a and $\Delta q(\text{Cl})$ b) vs. molecular HCl.

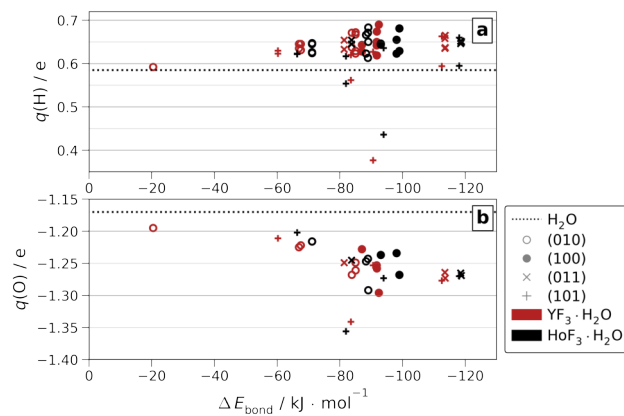


Figure S22. Partial Bader charges of molecular H₂O (dotted line) and adsorbed onto YF₃ or HoF₃ ($q(\text{H})$ a and $q(\text{O})$ b).

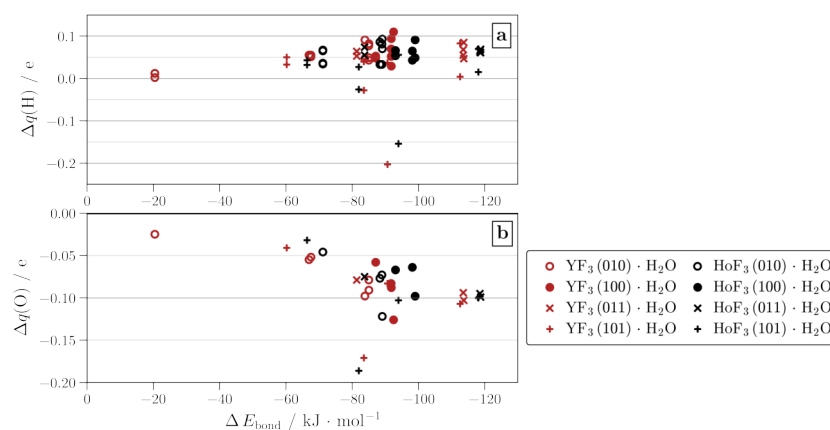


Figure S23. Change of partial Bader charges of H₂O adsorbed onto YF₃ or HoF₃ ($\Delta q(\text{H})$ a and $\Delta q(\text{O})$ b) vs. molecular H₂O.

9. Y vs. Ho Surface Dependence of Adsorption Energy

147

Figure S24 gives the difference in ΔE_{bond} between YF₃ and HoF₃ with the surface abundance ratios used to calculate the surface-weighted $\Delta \Delta E_{\text{bond},\%}^{\text{Y-Ho}}$ of main paper Figure 8. 148

$$\Delta \Delta E_{\text{bond}}^{\text{Y-Ho}} = \Delta E_{\text{bond}}^{\text{YF}_3 \cdot \text{Ads}} - \Delta E_{\text{bond}}^{\text{HoF}_3 \cdot \text{Ads}} \quad (2) \quad 149$$

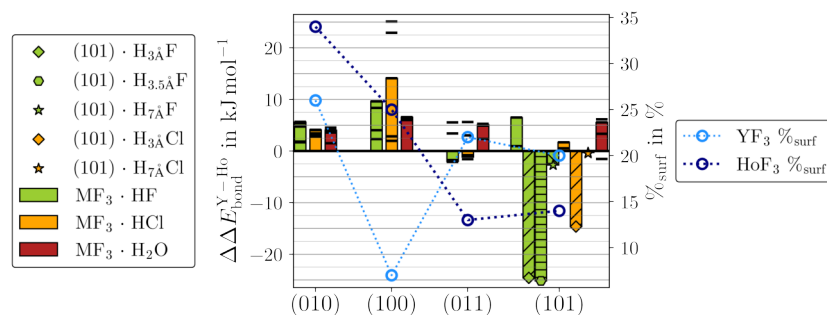


Figure S24. The difference in ΔE_{bond} between YF_3 and HoF_3 ($\Delta\Delta E_{\text{bond}}^{Y-Ho}$) (see Equation 2) is given for all single adsorptions (black lines). The bar plots highlight the respective strongest adsorbed structures. The hydride forming adsorptions of $(101)\text{-H}_{3\bar{A}}\text{F/Cl}$ (upward stripes), $(101)\text{-H}_{3,5\bar{A}}\text{F}$ (horizontal stripes) or $(101)\text{-H}_{7\bar{A}}\text{F/Cl}$ (downward stripes) are given separately. The surface abundance ratios ($\%_{\text{surf}}$) for the ideal crystals are taken from [4].

References

1. NIST Computational Chemistry Comparison and Benchmark Database, NIST Standard Reference Database Number 101. 2022. Available online: <http://cccbdb.nist.gov/> (accessed on 05 December 2022). 150
2. NIST Diatomic Spectral Database, NIST Standard Reference Database 114. Available online: <https://doi.org/10.18434/T4T59X> (accessed on 05 December 2022). 151
3. Jeffrey, G. *An Introduction to Hydrogen Bonding*; Oxford University Press: New York, NY, USA; Oxford, UK, 1997. 152
4. Anders, J.; Limberg, N.; Paulus, B. First Principle Surface Analysis of YF_3 and Isostructural HoF_3 . *Materials* **2022**, *15*, 6048. <https://doi.org/10.3390/ma15176048>. 153

150
151
152
153
154
155
156
157

3.4. Paper B.3

"Chemical Bonding of HF, HCl, and H₂O onto YF₃ Surfaces
– Quantification by First Principles"

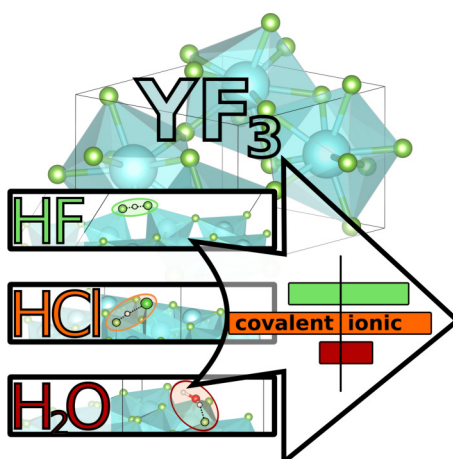
J. Anders, H. Wiedenhaupt, F. Kreuter, R. Tonner-Zech, B. Paulus, *J. Comput. Chem.*, **2023**, accepted and published online.

To the date of handing in this thesis, the issue and page number have not been assigned, yet.

DOI: 10.1002/jcc.27168

URL: <https://doi.org/10.1002/jcc.27168>

Creative commons license: <https://creativecommons.org/licenses/by/4.0/>



graphical abstract of paper **B3**.

Contributions:

The conceptualization was done by Jennifer Anders (J.A.) and Beate Paulus (B.P.). The formal analysis was done by Henrik Wiedenhaupt (H.W.) and J.A. Funding and resources acquisition was done by B.P. Investigations were done by H.W., Florian Kreuter (F.K.), and J.A. Supervision was done by Ralf Tonner-Zech (R.T.-Z.) and B.P. Validation and visualization was done by J.A. The original draft was written by, J.A. Review writing and editing was done by J.A., F.K., R.T. and B.P.

Chemical bonding of HF, HCl, and H₂O onto YF₃ surfaces: Quantification by first principles

Jennifer Anders¹ | Henrik Wiedenaupt¹ | Florian Kreuter² |
Ralf Tonner-Zech² | Beate Paulus¹

¹Institut für Chemie und Biochemie, Freie Universität Berlin, Berlin, Germany

²Wilhelm-Ostwald-Institut für Physikalische und Theoretische Chemie, Universität Leipzig, Leipzig, Germany

Correspondence

Jennifer Anders, Institut für Chemie und Biochemie, Freie Universität Berlin, Arnimallee 22, 14195 Berlin, Germany.
Email: jennifer.anders@fu-berlin.de

Funding information

Deutsche Forschungsgemeinschaft

Abstract

The surfaces of wairerite β -YF₃ have been studied for their fluorine and chlorine versus water affinity. Bonding patterns of HF, HCl, and H₂O chemically adsorbed onto surfaces of (010), (100), (011), and (101) have been quantified by density functional theory applying energy decomposition analysis. We found that the adsorption of H₂O is dominated by about 65% of electrostatics, which causes a low surface sensitivity and weak interactions. On the contrary, the adsorptions of HF and HCl are driven by strong hydrogen bonds resulting in a highly surface-dependent ratio of 30–60% electrostatic versus orbital contribution. Among the stoichiometric surfaces, the shortest and strongest hydrogen bonds and consequently most covalent bonding patterns are found within YF₃·HCl. However, when including the preparation energy, each surface favors the adsorption of HF over HCl, which reproduces the higher affinity of yttrium towards fluoride over chloride, previously known for solutions, also for the solid state.

KEYWORDS

DFT, HFSE, pEDA, surface adsorption, wairerite

1 | INTRODUCTION

Current research suggests that subtle differences within the fluoride and chloride affinities of solvated rare earth element or yttrium (REE +Y) cations have a major impact on their hydrothermal transport.^{1–8} However, little is known how these translate to the solid phase and which impact the surface structure has. The prototype structure for most REE+Y fluorides is β -YF₃, an interesting host material for laser applications due to its huge absorption-free window.^{9–15} Moreover, by its extraordinary high F[−] conductivity, it is a promising candidate for the upcoming field of solid state fluoride batteries.^{16–20} In nature, β -YF₃ is found as the mineral wairerite-(Y).⁹ Ore forming and enriching processes are generally dominated by simple electrostatics driven by ionic radius and charge.² The ionic radius of 107.5 pm found for

Y(III) is well within the range of middle to late lanthanides of samarium(III)–lutetium(III).²¹ Consequently, these are found in relatively high concentrations within wairerite.⁹ Nevertheless, as Y is 4–74 times more abundant within the upper continental Earth's crust than Sm–Lu, it remains the dominant cation within the lattice.^{22,23} The accumulation of REE within ores in general, as well as the enrichment of other high field strength elements (HFSE) is reasoned to be mainly driven by fluoride, because of the stronger complexes formed than with chloride.^{1,2,4,24–26} This is especially pronounced for the later lanthanides, due to their smaller ionic radii and thus even harder ionic character.²⁷ Ab initio molecular dynamics (AIMD) simulations of Y(III) in aqueous solutions of 1 molal NaCl and 0.0001–0.1 molal NaF have shown a clear preference for fluoride. For concentrations below 0.01 molal NaF, YCl₂⁺ has been found the dominant Y-species.

This is an open access article under the terms of the [Creative Commons Attribution](https://creativecommons.org/licenses/by/4.0/) License, which permits use, distribution and reproduction in any medium, provided the original work is properly cited.

© 2023 The Authors. *Journal of Computational Chemistry* published by Wiley Periodicals LLC.

However, above that threshold, YF_3 has been predicted the most dominant Y-species, despite the still 100 times higher availability of chloride.⁵ The difference in affinity for chloride and fluoride shown by the HFSE can already be qualitatively predicted by electrostatics, only, or the simple concept of hard and soft Lewis acids and bases (HSAB). However, electrostatics alone cannot predict that two cations of equivalent charge to radius ratio show a different affinity for the same anion. However, such fluoro-specific interactions have been found within dissolving measurements of solid $\beta\text{-YF}_3$ and $\beta\text{-HoF}_3$ in aqueous HF (0.001–0.3 molal), which revealed that both equally sized cations form different fluoride-species of YF_2^+ and HoF^{2+} in solution.⁴ This difference in fluoride affinity can only occur if besides simple electrostatics, the different nature of their occupied orbitals plays a role. It is not possible to directly access the energy of electrostatics versus orbital contributions, as well as bonding patterns of hydrogen bonds (H-bonds) by experiments. Consequently, this gap may be ideally filled by computational insights. To illuminate, whether this preference for fluoride over chloride is also present in the solid state, and especially, if this applies to all surface cuts, we invest adsorptions of HF, HCl, or H_2O onto several pristine $\beta\text{-YF}_3$ surfaces. By this simplistic model system, we aim to quantify the difference in affinity between chloride and fluoride in reference to water, explore how large the ratios of electrostatics versus orbital contributions vary, which bonding patterns are inherent to these, and to which degree they depend on the chosen surface.

2 | METHODOLOGY

2.1 | YF_3 structure and surfaces

Below temperatures of 1350 K, YF_3 crystallizes in its orthorhombic β -phase.^{15,28} The $Pnma$ -symmetric unit cell (see Figure 1) is constituted by four formula units of YF_3 fully occupying the Wyckoff positions 4c (Y), 4c (F), and 8d (F).

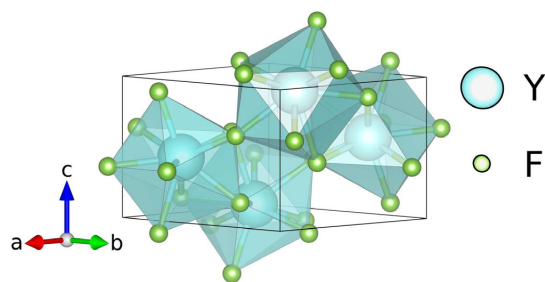


FIGURE 1 Unit cell of $\beta\text{-YF}_3$ with (PBE) relaxed lattice parameters of $a = 6.3215 \text{ \AA}$, $b = 6.8059 \text{ \AA}$, and $c = 4.3300 \text{ \AA}$.²⁹ Each unit cell contains four F bridging two Y and eight F coordinating to three Y. All Y are symmetry-equivalent, each coordinated by nine F forming a distorted tricapped trigonal anti-prism.

Within a previous study, the surface formation energies (E_{surf}) have been calculated from the difference in total energies of the slab supercell (E_n) and the bulk unit cell (E_{bulk}) multiplied by the number of unit cells within the slab (n).²⁹ This difference has been divided by double the surface area (A) as symmetric slabs have been used.

$$E_{\text{surf}} = \frac{E_n - nE_{\text{bulk}}}{2A} \quad (1)$$

For the substoichiometric surface of (101), the F potential (μ_{F}) is added to the numerator for each missing F. μ_{F} itself has been derived from the unit cells of YF_3 and metallic Y. Applying a Wulff analysis on these energies, we found the following abundances for the different low-lying Miller indices surfaces (hkl): 26% (010), 22% (011), 20% (101), 10% (001), 10% (111), 7% (100), and 5% (110).^{29–31} The two most available surfaces, (010) and (011) possess terminations that are stoichiometric, whereas the third most abundant surface (101) prefers a substoichiometric termination missing one surface fluorine atom (F_{surf}) per four surface yttrium atoms (Y_{surf}). Together, these three surfaces constitute 68% of the overall crystalline surface. Additionally, we also include the lesser abundant stoichiometric surface (100) to compare to future studies on HoF_3 surface, as in contrast to YF_3 , it is with 25% the second most available surface in HoF_3 . All four surfaces cover 75% of the YF_3 crystal. Within the bare relaxed surface supercells, (010) only contains eight-fold coordinated Y_{surf} (see Figure 2). (100) and (011) show six- and nine-fold coordinations, in which the six-fold coordination of (100) leaves the Y_{surf} more exposed. The substoichiometric (101) contains Y_{surf} in six-, seven-, and eight-fold coordination. These six-fold coordination polyhedra leave the Y_{surf} much more accessible, than in the other surfaces. Thus, the accessibility of Y_{surf} increases as (010) < (011) < (100) < (101).

2.2 | Approach to model adsorptions

The studied adsorption structures originate from scanning the conformational landscape of HF and H_2O adsorptions onto the three most stable YF_3 surfaces of (010), (011), and (101) done in a preceding study.³² It covered 200 ps of AIMD simulations, as well as over 300 systematically created, differently orientated monolayers of adsorbate molecules. From these, coordinations of single or multiple molecules have been extracted. The lesser stable surface of (100) was not part of this conformational scan. Instead, the (100)-Ads (Ads = H_2O , HF, HCl) structures have been obtained by transferring adsorbate coordinations from other surfaces. Moreover, all single HCl adsorptions of $\text{YF}_3\text{-HCl}$ originate from the respective $\text{YF}_3\text{-HF}$ structures. From all $\text{YF}_3\text{-Ads}$ structures, 38 chemically nonequivalent single adsorbate structural isomers (grouped from 46 relaxed structures) and 8 multiple adsorbate structural isomers are considered within this work. These are visualized in Figures S5–S17. Their adsorption energies are split into their subcomponents yielding insight into their

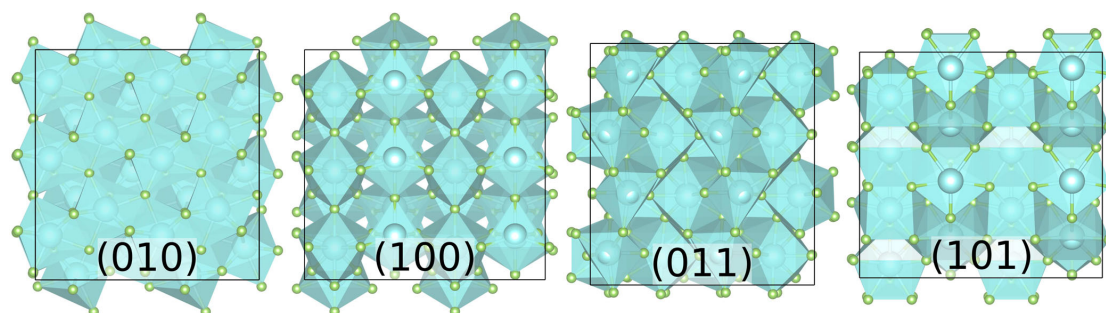
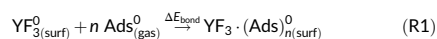


FIGURE 2 Topview onto the bare surface supercells of $(4 \times 3 \times 4)$ YF_3 -layers for (010) and (100) or $(4 \times 4 \times 4)$ YF_3 -layers for (011) and (101), each with the top two layers (PBE+D3(BJ)) relaxed.

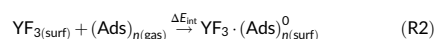
covalent versus ionic character. This also allows to quantify the contributions of H-bond to F_{surf} versus direct coordination to Y_{surf} . This division is done with the pEDA with NOCV extension method as implemented in AMS-BAND and described below. However, for periodic systems, a plane waves basis set as used in VASP is much more efficient than an atom-centered one, especially if these are Slater-type orbitals as in AMS-BAND. Therefore, all atomic coordinates are kept as relaxed inside VASP and only the electronic structure is recalculated inside AMS-BAND. We validated this approach by calculating the bonding energy with relaxed reactants (ΔE_{bond}) for all (010)-(Ads) $_n$ according to Reaction R1. We found an excellent agreement ($R^2 = 0.9999$, $\Delta \Delta E_{\text{bond}} \leq 2 \text{ kJ mol}^{-1}$ per adsorbate molecule) between ΔE_{bond} determined purely within VASP and by recalculating the electronic energies within AMS-BAND (see Figures S3 and S4). For the other stoichiometric surfaces of (100) and (011) showing stronger adsorptions, $\Delta \Delta E_{\text{bond}}$ remains almost identical with $\leq 3 \text{ kJ mol}^{-1}$ (see Table 2). For substoichiometric (101), the difference grows to $\leq 5 \text{ kJ mol}^{-1}$, however, given the much larger absolute values, these are just $\leq 1.6\%$.

2.3 | Quantifying adsorption by pEDA with NOCV extension

Within this paper, we quantified the electronic adsorption energies of different adsorbates (Ads) onto different surfaces of YF_3 . The adsorption energy with relaxed atomic structures (superscript 0) of reactants and product according to Reaction R1 is referred to as bonding energy (ΔE_{bond}). For ΔE_{bond} with multiple molecules adsorbed, a multiple of the isolated molecule was taken.



In contrast, the interaction energy (ΔE_{int}) refers to the adsorption energy obtained from reactants with the same atomic structure as inside the product (see Reaction R2).



Therefore both adsorption energies differ by the relaxation (or preparation) of the reactants (ΔE_{prep}).

$$\Delta E_{\text{bond}} = \Delta E_{\text{prep}} + \Delta E_{\text{int}} \quad (2)$$

Using a PBE+D3 approach,³³ the energy attributed to dispersion interaction (ΔE_{disp}) may be separated from ΔE_{int} leaving an electronic term ($\Delta E_{\text{int}}(\text{elec})$) associated with covalent bonding.

$$\Delta E_{\text{int}} = \Delta E_{\text{disp}} + \Delta E_{\text{int}}(\text{elec}) \quad (3)$$

By periodic energy decomposition analysis (pEDA), $\Delta E_{\text{int}}(\text{elec})$ can be separated further into its subcontributions of semi-classical electrostatics (ΔE_{elstat}), as well as attractive orbital contributions (ΔE_{orb}), and a repulsive term to account for the Pauli principle (ΔE_{Pauli}).³⁴⁻³⁶

$$\Delta E_{\text{int}}(\text{elec}) = \Delta E_{\text{elstat}} + \Delta E_{\text{orb}} + \Delta E_{\text{Pauli}} \quad (4)$$

The first two terms of Equation (4) may be combined to the attractive interaction (ΔE_{attr}).

$$\Delta E_{\text{attr}} = \Delta E_{\text{elstat}} + \Delta E_{\text{orb}} \quad (5)$$

Finally, ΔE_{orb} is split into pairwise orbital interactions of natural orbitals for chemical valence (NOCV) between the surface and the adsorbate.^{37,38} The NOCVs are the eigenvectors of the deformation density matrix, which is the density difference between the intermediate and the final state in the EDA procedure. The corresponding eigenvalues are a qualitative measure of the amount of charge transferred.

2.4 | Computational details

All atomic structures within this study have been partially (adsorbates and top two YF_3 -layers) relaxed. These originate from our preceding

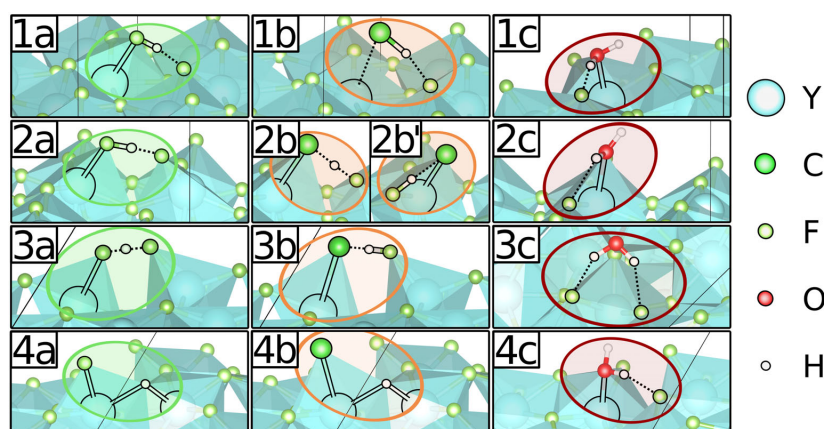


FIGURE 3 Atomic structures of the respective strongest adsorptions of $\text{YF}_3 \cdot \text{HF}$ (1-4a), $\text{YF}_3 \cdot \text{HCl}$ (1-4b), and $\text{YF}_3 \cdot \text{H}_2\text{O}$ (1-4c) onto (010) (1a-c), (100) (2a-c), (011) (3a-c), or (101) (4a-c).

TABLE 1 Comparison of studied surfaces ordered according to their Y_{surf} accessibility listing their surface energies (E_{surf} ; PBE) and ratios ($\%_{\text{surf}}$)²⁹ with the respective strongest bound YF_3 -Ads (see Figure 3; PBE+D3(BJ)) yielding the strongest interaction (ΔE_{int}), as well as bonding energy (ΔE_{bond}); for (100)-HCl, these are obtained by two different structures giving the one with the strongest ΔE_{int} (2b') in parenthesis; the coordination numbers ($\text{CN}_{\text{surf}}^{\text{Y}}$) correspond to the empty adsorption site Y_{surf} of the bare surface.

(hkl)	E_{surf} in $\text{J} \cdot \text{m}^{-2}$	$\%_{\text{surf}}$ in %	$\text{CN}_{\text{surf}}^{\text{Y}}$		$ \Delta E_{\text{int}} $ in kJ mol^{-1}			$ \Delta E_{\text{bond}} $ in kJ mol^{-1}		
			HF/HCl	H_2O	HF	HCl	H_2O	HF	HCl	H_2O
(010)	0.58	26	8	8	106	57	104	75	42	86
(011)	0.61	22	6	6	253	265	135	123	90	114
(100)	1.03	7	6	6	194	227 (376)	102	134	97 (83)	93
(101)	0.76	20	6	8	969	821	130	310	306	111

work on YF_3 surface adsorptions³² done within the Vienna Ab Initio Simulation Package (VASP, version 5.4.4)³⁹ applying the computational setup showing very good agreement with the crystal unit cell.²⁹ Summing up, the Perdew–Burke–Ernzerhof (PBE) functional⁴⁰ with the projector augmented wave (PAW) method^{41,42} with a kinetic cutoff of 772.6 eV using the soft valence Y, as well as the hard H, O, F, and Cl core PAW potentials yielding respective valence electron numbers of 11, 1, 6, 7, and 7. The previously tested effect of normal versus hard core potentials showed a better description using the latter, especially for HF.³² Around the isolated molecules and perpendicular to the surface plane, 25 Å vacuum has been applied as converged in our previous YF_3 study.²⁹ A neglectable adsorbate-adsorbate interaction using the Γ -point only was found at supercell sizes of $(4 \times 3 \times 4)$ YF_3 -layers for (010) and (100) or $(4 \times 4 \times 4)$ YF_3 -layers for (101) and (011) with respective surface areas of 164 Å² (010), 177 Å² (100), 204 Å² (011) or 209 Å² (101).³² These are visualized in Figure 2. The adsorbate molecules and the first two YF_3 -layers of each surface have been relaxed in atomic coordinates with allowed spin polarization, Gaussian smearing with a width of 0.2 eV and Grimme's dispersion correction with Becke–Johnson damping (D3(BJ)).^{33,43} For the bare surfaces, the first two layers consist of 48 atoms for (010) and (100) or 64 atoms

for (101) and (011). The atomic structure relaxations performed inside VASP have been done with an energetic atomic relaxation criterion of 10^{-4} eV between two ionic steps and a self-consistent field (SCF) convergence criterion of 10^{-5} eV. Final electronic structures have been calculated with a SCF criterion of 10^{-6} eV. Onto all VASP calculations, a self-consistent field (SCF) convergence criteria of 10^{-5} eV for atomic structure relaxations and 10^{-6} eV for the final electronic structure have been applied.

VASP-derived energies (E^{VASP}) given are labeled accordingly. All energies without superscript label originate from PBE+D3 (BJ) electronic energies by AMS-BAND version 2021.102.⁴⁴ Frozen core sizes have been chosen to obtain the same number of valence electrons as within VASP. This corresponds to a large frozen core on Cl and small frozen cores on O, F, and Y. Tests of applying the default, large frozen core on Y yielded unsatisfactory results (see Figure S1 and Table S1). The effects of basis set, k -grid and numerical quality were tested (see SI Section 1). These tests yielded TZ2P at the Γ -point only with a very good numerical quality as the best setup. The letter corresponds to a SCF criterion of at least 1.6×10^{-7} eV. Scalar relativistic effects were treated by the zeroth order regular approximation (ZORA).^{45,46} All systems that converged

TABLE 2 Energy contributions (PBE+D3(BJ)) to ΔE_{bond} in kJ mol^{-1} with ΔE_{int} (ΔE_{disp} , ΔE_{elstat} , ΔE_{orb} , ΔE_{Pauli}) and ΔE_{prep} of the adsorbate and surface of the strongest adsorbed YF_3 Ads with percentages among ΔE_{attr} (%) or ΔE_{int} (%) given in parenthesis; for (100)-HCl, both strongest adsorptions are listed in order of strongest by ΔE_{bond} (**2b**) or ΔE_{int} (**2b'**); the VASP-derived $\Delta E_{\text{bond}}^{\text{VASP}}$ as in Reference 32 are given for comparison.

HF	(010)	(100)	(011)	(101)
$\Delta E_{\text{bond}}^{\text{VASP}}$	-75	-135	-125	-315
ΔE_{bond}	-75	-134	-123	-310
ΔE_{int}	-106	-194	-253	-969
ΔE_{disp}	-12 (11% _i)	-9 (5% _i)	-9 (4% _i)	-10 (1% _i)
ΔE_{elstat}	-179 (55% _a)	-251 (51% _a)	-305 (48% _a)	-503 (29% _a)
ΔE_{orb}	-145 (45% _a)	-244 (49% _a)	-333 (52% _a)	-1230 (71% _a)
ΔE_{Pauli}	230	310	394	774
$\Delta E_{\text{prep}}(\text{Ads})$	9	33	60	547
$\Delta E_{\text{prep}}(\text{surface})$	22	27	70	111

HCl	(010)	(100) 2b	(100) 2b'	(011)	(101)
$\Delta E_{\text{bond}}^{\text{VASP}}$	-41	-99	-86	-93	-311
ΔE_{bond}	-42	-97	-83	-90	-306
ΔE_{int}	-57	-227	-376	-265	-821
ΔE_{disp}	-21 (36% _i)	-18 (8% _i)	-18 (5% _i)	-16 (6% _i)	-19 (2% _i)
ΔE_{elstat}	-106 (55% _a)	-313 (42% _a)	-445 (39% _a)	-328 (40% _a)	-466 (32% _a)
ΔE_{orb}	-88 (45% _a)	-436 (58% _a)	-708 (61% _a)	-484 (60% _a)	-1003 (68% _a)
ΔE_{Pauli}	157	540	795	562	667
$\Delta E_{\text{prep}}(\text{Ads})$	2	82	196	89	412
$\Delta E_{\text{prep}}(\text{surface})$	13	48	96	86	102

H ₂ O	(010)	(100)	(011)	(101)
$\Delta E_{\text{bond}}^{\text{VASP}}$	-85	-92	-114	-113
ΔE_{bond}	-86	-93	-114	-111
ΔE_{int}	-104	-102	-135	-130
ΔE_{disp}	-17 (16% _i)	-10 (10% _i)	-19 (14% _i)	-21 (16% _i)
ΔE_{elstat}	-199 (65% _a)	-153 (68% _a)	-219 (67% _a)	-221 (64% _a)
ΔE_{orb}	-108 (35% _a)	-72 (32% _a)	-107 (33% _a)	-123 (36% _a)
ΔE_{Pauli}	220	133	210	235
$\Delta E_{\text{prep}}(\text{Ads})$	1	2	1	1
$\Delta E_{\text{prep}}(\text{surface})$	17	7	20	18

to a closed shell electronic structure inside VASP have been calculated with spatial orbitals inside AMS-BAND neglecting symmetry. Consequently, only the substoichiometric surfaces of (101) have been calculated with spin orbitals. Due to SCF convergence issues and to reduce computational time, these runs are performed utilizing symmetry at the good numerical quality yielding a SCF criterion of 1.6×10^{-6} eV, as well as with an enforced ferromagnetic magnetic arrangement as found by VASP (see SI Section 3). Partial charges originate from the Charge Model 5 (CM5) scheme.^{47,48} The NOCV deformation densities are plotted in AMSview and atomic structure visualizations are done in VESTA.⁴⁹

3 | RESULTS AND DISCUSSION

3.1 | Strongest single adsorptions

The structure of the obtained strongest single adsorptions of each surface and adsorbate molecule are shown in Figure 3. Within each (hkl)-Ads, the strongest adsorption by ΔE_{bond} with relaxed reactants (Reaction R1) or ΔE_{int} with nonrelaxed reactant (Reaction R2) are obtained by the same structural isomer, with the exception of (100)-HCl, for which both structures are given. While the H-bond within the strongest adsorption by ΔE_{bond} (see Figure 3 2b) is formed to the

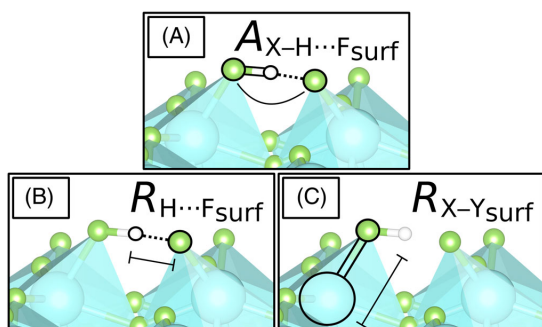


FIGURE 4 Visualization of the analyzed structural adsorption parameters of H-bond angle ($A_{X-H...F_{surf}}$, **A**) and distance ($R_{H...F_{surf}}$, **B**), as well as direct O/F/Cl to Y_{surf} coordination ($R_{X-Y_{surf}}$, **C**) on the example of the strongest bound (100)-HF.

neighboring surface polyhedron, the one with the strongest ΔE_{int} (**2b'**) is formed within the same polyhedron, which goes along with a much stronger H-Cl bond elongation.

In Table 1, their respective adsorption energies are related with the properties of the bare surface as Y_{surf} accessibility, surface energy (E_{surf}), and ratio of that surface within a perfect nanocrystal at 0 K ($\%_{surf}$). It also gives the Y_{surf} coordination numbers ($CN_{Y_{surf}}^Y$) referring to the empty adsorption sites of the bare surfaces.

For (011) and (100), each direct coordination to a Y_{surf} or H-bond to a F_{surf} are formed to six-fold coordination polyhedra. A difference between the adsorbates is only found for the substoichiometric surface (101), for which H_2O coordinates directly to an eight-fold coordinated Y_{surf} (III). On the other side, HF and HCl are bound to six-fold coordinated Y_{surf} at a formal oxidation state of (II). These give the by far strongest ΔE_{int} as they dissociated in a hydride-forming manner discussed below. Comparing the adsorption of HF and HCl between the different surfaces, we find that ΔE_{bond} grows stronger with the Y_{surf} accessibility. For ΔE_{int} the same relation is found for HCl adsorptions, while for HF, (011) and (100) swap positions. For E_{surf} of the bare surfaces, no correlation to the most stable adsorptions is found. While (010) and (011) hardly differ in E_{surf} , the latter binds any adsorbate much stronger. On the contrary, the bare surface of (100) is significantly less stable but regardless of reactant relaxation, HF and HCl adsorb only slightly stronger onto (100) than (011). The opposite is even found for H_2O . Within $YF_3 \cdot H_2O$, the four surfaces seem to form two groups of slightly weaker (010) and (100) versus slightly stronger (011) and (101) interacting surfaces. However, these differences are much less pronounced than those found for $YF_3 \cdot HF/HCl$. A more detailed comparison of the strongest single adsorptions is given in Table 2 listing the different energy contributions to ΔE_{int} and ΔE_{bond} .

ΔE_{disp} remains practically constant, while ΔE_{elstat} and ΔE_{orb} significantly vary and grow by ΔE_{int} . The role of each of this three contributions is discussed in more detail for all adsorptions below. By ΔE_{orb} , naturally also the counter-acting ΔE_{Pauli} grows. The listed ΔE_{prep} is foremost an indicator for the structural change within the reactant

upon adsorption. Accordingly, it is largest by far for the hydride-forming adsorptions by HF and HCl onto substoichiometric (101). Within the nonhydride-forming adsorptions, ΔE_{prep} correlates with the change in adsorbate bond length due to the formed H-bond (see Figure 9 3a). Consequently, it is very low for the weaker adsorptions shown by H_2O , as well as those onto (010). By the [FHF]-like moiety forming HF adsorptions onto (100), ΔE_{prep} is almost half of the total ΔE_{bond} . Finally, by the even stronger change in adsorbate bond length in (011)-HF and the respective HCl adsorptions onto (100) and (011), ΔE_{prep} is found to be larger than ΔE_{bond} itself. The largest ratio of ΔE_{prep} to ΔE_{bond} is found in (100)-HCl **2b'** with more than three times the latter.

3.2 | Structural features

For all adsorptions, the structural parameters for H-bond and direct coordinations are analyzed according to Figure 4. The results for single adsorbates versus ΔE_{int} are plotted in Figure 5. Practically equivalent trends are observed against ΔE_{elstat} or ΔE_{orb} (see Figures S18 and S19). The respective means over all surfaces weighted linearly by ΔE_{int} are also plotted. The Boltzmann weighted and nonweighted means within each or among all surfaces are listed in Table S2.

According to Jeffrey's classification,⁵⁰ H-bonds spanning an angle of $130-170^\circ$ and/or measuring a distance of $150-220$ pm may be considered moderately strong (see gray area in Figure 5A-B). Most $A_{X-H...F_{surf}}$ and distances $R_{H...F_{surf}}$ fall into this range. Strong H-bonds are found for HF and HCl adsorptions of about $|\Delta E_{int}| > 100$ kJ mol⁻¹ (see gray vertical line), while even the strongest bound $YF_3 \cdot H_2O$ only exhibit weak to moderate H-bonds. Taking a look at how these structural H-bonds parameters influence ΔE_{int} , we find that the H-bond angle and more importantly its distance correlate with a stronger interaction for adsorptions of HF and HCl onto any surface (see Figure 5A-B). At comparable H-bond distances, $YF_3 \cdot HF$ and $YF_3 \cdot HCl$, both give comparable ΔE_{int} . However, as HCl is a much better H-donor than HF, the stronger bound $YF_3 \cdot HCl$ form H-bonds of $Cl \cdots H \cdots F_{surf}$ yielding the shortest $R_{H...F_{surf}}$ (see Figure 9 3a). Accordingly, these also come at the strongest ΔE_{int} giving a slightly (15 pm) lower weighted mean for HCl than HF adsorptions. On the contrary, the $YF_3 \cdot H_2O$ adsorptions show little variation and correlation. Only within (010), the dependence of ΔE_{int} onto the H-bond distance is clearly given. This already indicates, that the H-bond contributes less to the adsorption compared to those of HF and HCl.

In contrast to the H-bond distance, a shorter $R_{X-Y_{surf}}$ correlates to a stronger interaction for all three adsorbates (see Figure 5C). At similar distances, similar ΔE_{int} for $YF_3 \cdot HF$ and $YF_3 \cdot H_2O$ are found, while the respective $YF_3 \cdot HCl$ adsorptions show an about 50 pm larger distance due to the equally larger ionic radius.²¹ As the hydride-forming adsorptions onto the electron-rich, substoichiometric (101) possess no H-bond, these are also not given in Figure 5A-B. The formed negatively charged hydride ($q_{CM5}(H) = -0.2$ e) bridges two Y_{surf} atoms with $R_{H-Y_{surf}} = 208-220$ pm. Moreover, by their large ΔE_{int} (see Figure 7D), their direct coordinations ($R_{F-Y_{surf}} = 200$ pm, $R_{Cl-Y_{surf}} = 252$ pm) are

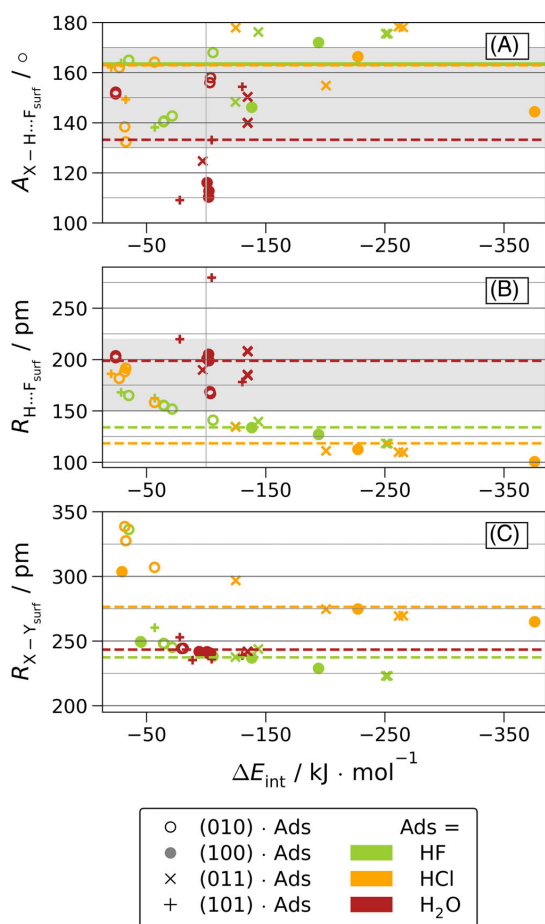


FIGURE 5 Angles ($A_{X-H...F_{surf}}$, **A**) and distances ($R_{H...F_{surf}}$, **B**) of H-bond and direct O/F/Cl to Y_{surf} coordinations ($R_{X-Y_{surf}}$, **C**) versus the interaction energy (ΔE_{int} ; PBE+D3(BJ)) for single nonhydride-forming adsorptions; the averages over all (hkl) weighted linearly by ΔE_{int} are also given (dashed lines).

also outside the zoomed window of Figure 5C. In the following, the hydride-forming adsorptions are labeled (101)- $H_{3\text{\AA}}F/Cl$ according to the relaxed interatomic distance of $R_{H-F/Cl} = 3 \text{ \AA}$ of the dissociated adsorbate.

3.3 | Dispersion energy

The strength of dispersion is linked to the polarizability, which is especially low for fluorine. Therefore, the energy attributed to dispersion interaction is low but increases as $YF_3 \cdot HF < YF_3 \cdot H_2O < YF_3 \cdot HCl$ (see Figure 6A). It only contributes $< 10\%$ to the sum of attractive interactions and ΔE_{disp} (see Equation 5 and Figure 6B). Even for very weak ΔE_{int} and thus also weak electrostatics and orbital interactions,

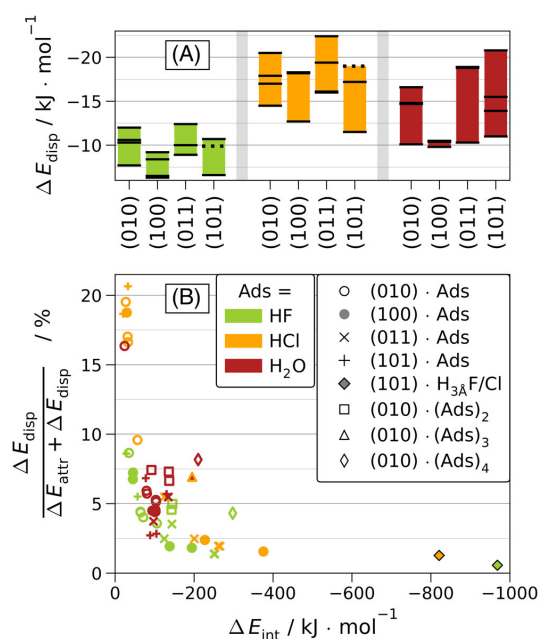


FIGURE 6 Ranges of dispersion energy determined with PBE+D3(BJ) (ΔE_{disp} , **A**) per surface (hkl) for all single adsorptions. The individual values are marked by black bars or dotted bars for the hydride-forming structures of (101)- $H_{3\text{\AA}}F/Cl$. Ratio of ΔE_{disp} within the sum of ΔE_{disp} and attractive energies (ΔE_{attr} , **B**) versus the interaction energy (ΔE_{int}) for all surfaces and adsorbates.

dispersion accounts for only a fifth of the adsorption. The relation of ΔE_{disp} versus ΔE_{int} is plotted in Figure S20.

3.4 | Electrostatic and orbital contributions in single adsorptions

As discussed above, ΔE_{int} is only little effected by dispersion. The significant contributions originate from electrostatics and orbital interactions. Their ranges within each surface are plotted together with the adsorption energies in Figure 7. As this study did not sample the conformational space in its entirety, but focused on the adsorption sites of strongest interactions, the plotted ranges rather visualize the limit of strongest energy contributions. We expect that a more complete scan of the conformational space would include very weak adsorptions with near zero energies for any of these ranges.

Extremely large energy ranges are observed for (101)-HF/HCl due to the very strong hydride-forming adsorptions on one side and very weak adsorptions otherwise. On the contrary, $YF_3 \cdot H_2O$ adsorptions are rather insensitive to the surface and the overall ΔE_{int} or ΔE_{bond} hardly differ between the four surfaces. Within each (hkl)-Ads, the conformation with the strongest ΔE_{int} also shows the strongest ΔE_{elstat} , as well as ΔE_{orb} with the exception of (101)- H_2O . Comparing the strongest (Figure 3 4c) and second strongest interacting

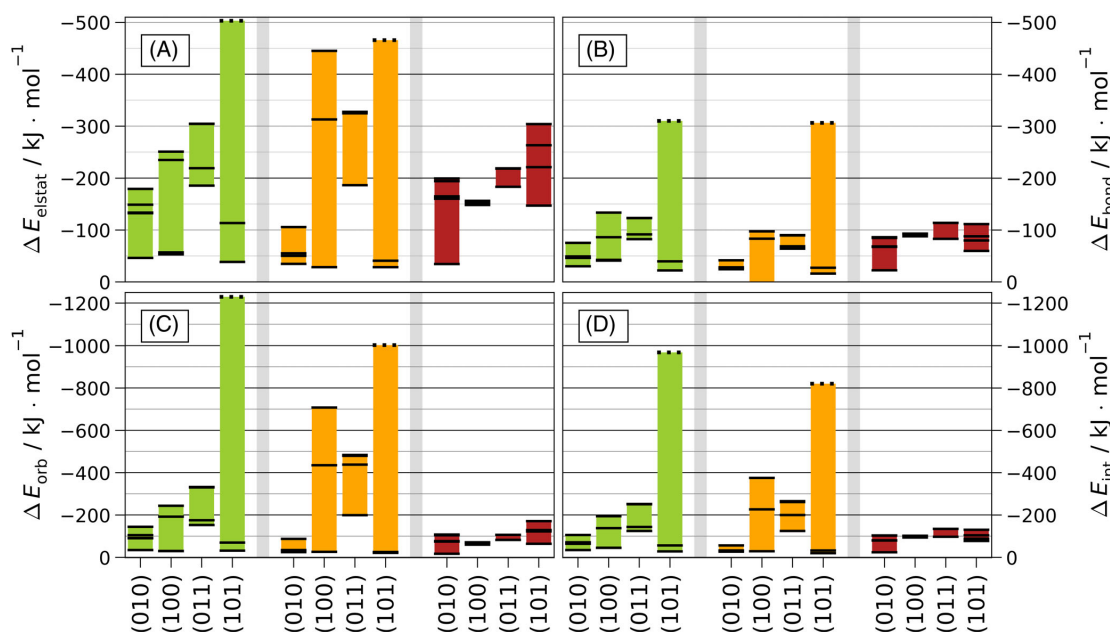


FIGURE 7 Ranges of electrostatic energy (ΔE_{elstat} , A), bonding energy (ΔE_{bond} , B), orbital energy (ΔE_{orb} , C), and interaction energy (ΔE_{int} , D) per surface (hkl) for all single adsorptions of $\text{YF}_3 \cdot \text{HF}$ (green), $\text{YF}_3 \cdot \text{HCl}$ (orange), and $\text{YF}_3 \cdot \text{H}_2\text{O}$ (red). The individual values are marked by black bars or dotted bars for the hydride-forming structures of (101)- $\text{H}_{3\text{A}}\text{F/Cl}$.

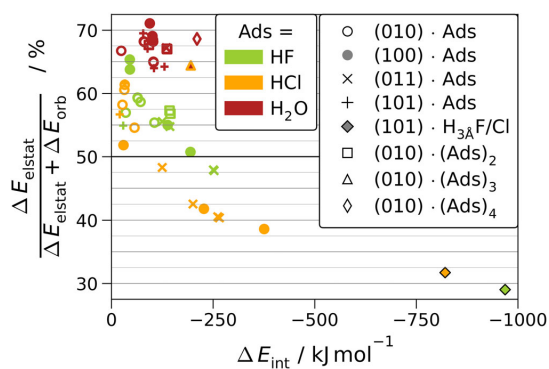


FIGURE 8 Ratio of electrostatic energy (ΔE_{elstat} ; PBE+D3(BJ)) within the attractive energies (ΔE_{attr}) versus the interaction energy (ΔE_{int}) for all adsorptions.

structures, the latter is by about 40 kJ mol^{-1} weaker in ΔE_{int} , but stronger by the same magnitude in each of ΔE_{elstat} and ΔE_{orb} . This goes along with a considerable shift in electron density at Y_{surf} only found in the latter structure ($\Delta q_{\text{Bader}}(\text{Y}) = +0.4 \text{ e}$).³² However, by the significant shift in electronic density, the repulsive ΔE_{Pauli} is also considerably larger and overcompensates the gains in electrostatic and orbital interactions. The ratio of ΔE_{elstat} within ΔE_{attr} , the sum of ΔE_{elstat} and ΔE_{orb} (see Equation 5) is visualized in Figure 8. Depending on which term dominates within this ratio, an adsorption may classify

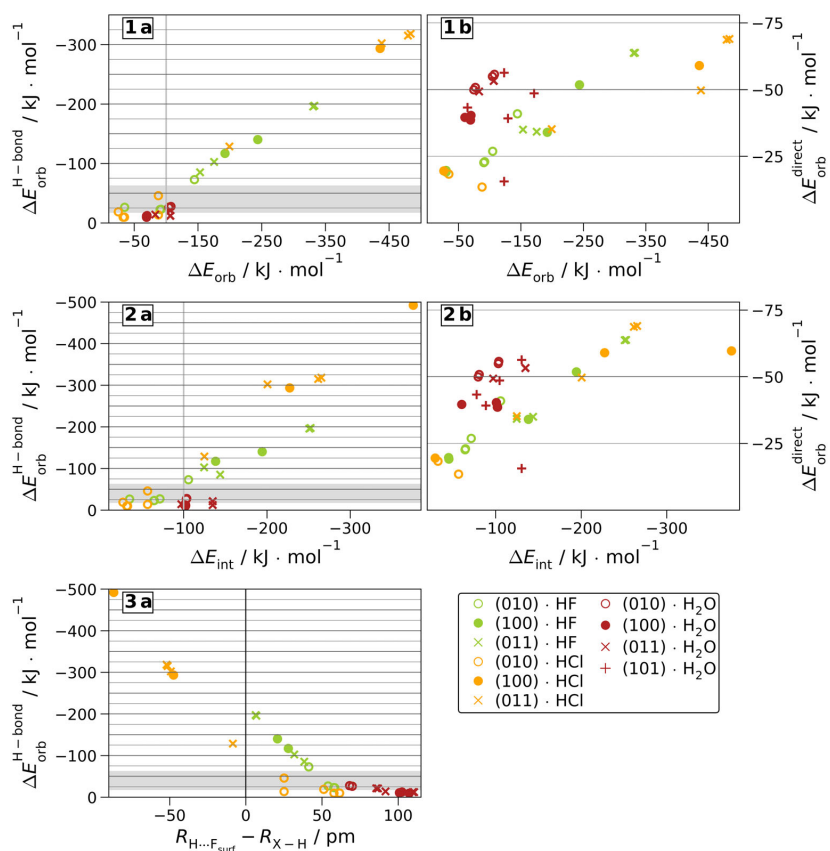
as ionic or covalent. For $\text{YF}_3 \cdot \text{HF}$ and $\text{YF}_3 \cdot \text{HCl}$ adsorptions of at least $|\Delta E_{\text{int}}| \geq 60 \text{ kJ mol}^{-1}$, for which the weak contribution of ΔE_{disp} becomes negligible, ΔE_{int} grows stronger with the degree of covalency. This correlation is not found for $\text{YF}_3 \cdot \text{H}_2\text{O}$, for which electrostatics strongly dominate the interaction regardless of ΔE_{int} . The ionic versus covalent bonding character described for the single molecule adsorption remain the same for the simultaneous adsorption of multiple molecules. ΔE_{int} per adsorbate molecule is also not significantly altered up to the maximum tested number of $\text{YF}_3 \cdot (\text{Ads})_4$.

Within the nonhydride-forming adsorptions, the increase in covalent bonding character correlates with the formation of strong H-bonds to F_{surf} introduced above (see Figure 5). For $\text{YF}_3 \cdot \text{HF}$, it is the formation of rather symmetric [FHF] moieties (see Figure 3 2–3a). For $\text{YF}_3 \cdot \text{HCl}$, it is the partial dissociation of H–Cl to form a H-bond of $\text{Cl} \cdots \text{H} - \text{F}_{\text{surf}}$ (see Figure 3 2b'+3b and Figure 9 3a). Alike, structural features that come with dominating electrostatics are weak or even absent H-bonds. Instead, the adsorption is dominated by a direct coordinated via $\text{X}-\text{Y}_{\text{surf}}$ with $\text{X} = \{\text{O}, \text{F}, \text{Cl}\}$. This supports that the direct coordination to Y_{surf} is electrostatic dominated, while the H-bond to F_{surf} is orbital dominated.

3.5 | Pairwise electron interactions

The orbital energy is further divided into pairwise NOCV interactions between surface and adsorbate. All corresponding deformation densities are considered, which show an electronic charge displacement

FIGURE 9 PBE+D3(BJ) energies of H-bonds to F_{surf} ($\Delta E_{\text{orb}}^{\text{H-bond}}$, **a**) or direct coordinations to Y_{surf} ($\Delta E_{\text{orb}}^{\text{direct}}$, **b**) versus the orbital energy (ΔE_{orb} ; **1a–b**), interaction energy (ΔE_{int} ; **2a–b**) or the difference of H-bond and adsorbate bond length ($R_{\text{H}\cdots F_{\text{surf}}} - R_{\text{X-H}}$, **3a**) with $X = \{\text{O}, \text{F}, \text{Cl}\}$ for all nonhydride-forming single adsorptions.



upon adsorption of $\nu_n \geq 0.1$ e. This relatively low cutoff is chosen as the overall ΔE_{orb} within many YF_3 -Ads, and thus, also their ν_n , are rather small. All ν_n versus their corresponding contribution to the orbital energy (ΔE_{orb}^n) are plotted in Figure S21. The flatter slope of $\Delta \nu_n / \Delta E_{\text{orb}}^n$ shown by the stronger adsorbed HF or HCl onto (100), (011) or (101) also supports that their bonding character is less ionic than within the weaker adsorbed (hkl)-Ads. The NOCV deformation densities are grouped into different interactions of σ -like or π -like interactions of three-centered H-bonds of $\text{X-H}\cdots F_{\text{surf}}$ (or $\text{X}\cdots\text{H}-F_{\text{surf}}$) in contrast to two-centered direct coordinations of $\text{X}-Y_{\text{surf}}$ with $X = \{\text{O}, \text{F}, \text{Cl}\}$ or $\text{H}-F_{\text{surf}}$. However, only the σ -like $\text{X-H}\cdots F_{\text{surf}}$ and σ -like $\text{X}-Y_{\text{surf}}$ are found within most YF_3 -Ads. These two interactions also give the largest ν_n for all nonhydride-forming adsorptions. Their ΔE_{orb}^n are plotted in Figure 9 versus the overall ΔE_{orb} or ΔE_{int} (for the corresponding ν_n see Figure S23). Note that within the former (**1a–b**), the strongest bound (100)-HCl by ΔE_{int} (**2b**) is outside the zoom because of its very large ΔE_{orb} (see Table 2). Its deformation densities are discussed versus the strongest bound (100)-HCl by ΔE_{bond} (**2b**) in the SI (see Figure S24). The same applies to the hydride-forming adsorptions of (101)- $\text{H}_3\text{AF/Cl}$ (see Figure S25). On the opposite, weak end of the ΔE_{int} range, several H-bonds and direct coordinations found by atomic

positions (see Figure 5) are too weak in their pairwise electron interaction to meet the applied threshold. This is most prominently the case within the weak, nonhydride-forming adsorptions onto (101), for which no H-bond, but only the direct coordinations of (101)- H_2O show. For these, the sum of α and β -components are plotted.

Moderate H-bonds are defined to be bound by 17–63 kJ mol^{-1} (see gray area in Figure 9 **1–3a**).⁵⁰ Thus, YF_3 -HF/HCl adsorptions with an interaction energy stronger than -100 kJ mol^{-1} possess H-bonds classifying as strong by their $\Delta E_{\text{orb}}^{\text{H-bond}}$. This energy agrees excellently with the criteria on H-bond distances $R_{\text{X-H}\cdots\text{F}}$ (see gray line in Figure 5A–B). For the H-bond strength, we find a strong dependence on the surface by HF and even more so by HCl, but practically none for H_2O . For the latter, all H-bonds are much weaker than those formed by HF or HCl. Among the adsorbates, the increasing H-bond strength can be ordered as (hkl)- $\text{H}_2\text{O} < (\text{hkl})\text{-HF} < (\text{hkl})\text{-HCl}$ for all (hkl) but (010), for which the strongest bound (010)-HF possess a 27 kJ mol^{-1} stronger $\Delta E_{\text{orb}}^{\text{H-bond}}$ than (010)-HCl. However, the fluorine-rich surface of (010) shows the smallest differences between the adsorbates, as well as the smallest overall $\Delta E_{\text{orb}}^{\text{H-bond}}$. Note that these trends observed for the H-bond strength support the findings on the maximum adsorption strengths and ionic versus covalent adsorption character discussed

above. We therefore conclude that the formation of strong H-bonds sets the interaction of YF_3 towards HF and HCl apart from H_2O . Coming to the electrostatic-driven direct coordinations, we find that the total ranges of $\Delta E_{\text{orb}}^{\text{direct}}$ are much smaller than the corresponding H-bond terms (see Figure 9 2a–b). Accordingly, the direct coordination strength is less decisive for the bonding than the H-bond strength for the moderately and strongly bound $\text{YF}_3 \cdot \text{HF}/\text{HCl}$. On the contrary, it is more decisive than the H-bond strength for $\text{YF}_3 \cdot \text{H}_2\text{O}$. For a detailed look at the bonding patterns, it should be noted that several weakly, but also moderately ($|\Delta E_{\text{int}}| < 95 \text{ kJ mol}^{-1}$) bound adsorbates coordinate via the direct $\text{X}-\text{Y}_{\text{surf}}$ only, whereas a few weakly ($|\Delta E_{\text{int}}| < 35 \text{ kJ mol}^{-1}$) coordinations coordinate by the H-bond only. Furthermore, within some weakly and moderately bound (hkl)-HF/HCl, NOCV deformation densities are found that show a combination of $\text{X}-\text{H} \cdots \text{F}_{\text{surf}}$ and $\text{X}-\text{Y}_{\text{surf}}$. Therefore, the corresponding energy contributions were chosen to be halved to enter each of the categories. From these, only within one (010)-HCl, both ν_n remain above the threshold and are thus also present as two entries at the same overall ΔE_{orb} or ΔE_{int} . The only actual, although weak bifurcated H-bond is found for the strongest adsorbed (011)- H_2O ($\Delta E_{\text{int}} = -135 \text{ kJ mol}^{-1}$) with $\Delta E_{\text{orb}}^{\text{H-bond}} = -\{12, 21\} \text{ kJ mol}^{-1}$ (see Figure 3 3c). The dependency of H-bond energy to the difference in H-bond and adsorbate bond length is shown in Figure 9 3a. Equivalent plots for the eigenvalues and the overall orbital energy are given in Figure S22. For the moderate and strong H-bonds, the H-bond strength increases linearly with a decreasing $R_{\text{H}-\text{F}_{\text{surf}}} - R_{\text{X}-\text{H}}$. The strongest H-bond formed by HF is found for (011)-HF forming a [FHF] moiety (see Figure 10 1a). Before adsorption, the F_{surf} is bridging two six-fold coordinated Y_{surf} . Upon HF adsorption, this bridge is elongated to a [FHF] leaving the Y_{surf} coordination number unchanged. The [FHF] angle is almost linear and the two $R_{\text{H}-\text{F}}$ differ by only 6 pm among each other and are very close to the symmetric H-F lengths of 114 pm within gaseous [FHF].^{51,52} Because the H-F interaction is much stronger than the respective H-Cl one, or in other words, because HF is the worse H-bond donor, the strongest H-bonds within $\text{YF}_3 \cdot \text{HCl}$ are of $\text{Cl} \cdots \text{H} - \text{F}_{\text{surf}}$ type, in which the hydrogen is much closer to F_{surf} (see Figure 10 1b). Within (011)-HCl, the H-bond is about 120 kJ mol^{-1} stronger than within the respective HF structure (see Figure 10 2a–b).

At the same time, the direct coordinations of $\text{Cl}-\text{Y}_{\text{surf}}$ and $\text{F}-\text{Y}_{\text{surf}}$ are very similar in $\Delta E_{\text{orb}}^{\text{direct}}$ (see Figure 10 3a–b). However, the NOCV deformation density predominantly attributed to $\text{F}-\text{Y}_{\text{surf}}$ also accumulates electron density along $\text{H}-\text{F}_{\text{surf}}$. Noteworthy is also the third main contribution of the two adsorptions, which favors $\text{Cl} \cdots \text{H} - \text{F}_{\text{surf}}$ by another 20 kJ mol^{-1} over $\text{F}-\text{H}-\text{F}_{\text{surf}}$ (see Figure 10 4a–b). A very similar energy difference reproduces itself also in ΔE_{elstat} . On the other hand, the H-bond-driven much larger ΔE_{orb} of (011)-HCl is counter-balanced by ΔE_{Pauli} leaving an overall difference of merely about 10 kJ mol^{-1} within ΔE_{int} (see Table 2). Finally, due to the large ΔE_{prep} required for the partial H-Cl dissociation, the (011)-HCl adsorption is even about 30 kJ mol^{-1} weaker judged by ΔE_{bond} .

Among all studied adsorptions, the largest ΔE_{orb} , as well as overall ΔE_{int} is shown by (101)- $\text{H}_3\text{AF}/\text{Cl}$, which spontaneously dissociated in a hydride-forming possess. This is accompanied by a reduction in

magnetic moment from eight to six. At the bare substoichiometric surface, all formal 8 Y(II) centers orientate ferromagnetically. However, within (101)- $\text{H}_3\text{AF}/\text{Cl}$, the Y-centers coordinated by the anions lost their magnetic moment. Something that is not observed for weakly bound (101)-HF/Cl or the (101)- H_2O . The classification as charge transfer is backed up by the change in electron density topography leading to the change in partial Bader charges.³² The Löwdin-based CM5 partial charges are smaller in magnitude but qualitatively agree. These show a reduction from $\pm 0.2 \text{ e}$ in free HF or $\pm 0.1 \text{ e}$ in free HCl to $q_{\text{H}} = -0.2 \text{ e}$, $q_{\text{F}} = -0.5 \text{ e}$ or $q_{\text{Cl}} = -0.4 \text{ e}$ for (101)- $\text{H}_3\text{AF}/\text{Cl}$. The dissociated atoms coordinate to the same polyhedron (see Figure 3 4a–4b). Nonetheless, in contrast to the H-bond partially dissociated adsorbates (see negative distance differences of (100)/(011)-HCl in Figure 9), within in this hydride-forming dissociation, the two anions are almost 1 \AA further apart with $R_{\text{H}-\text{F}} = 2.57 \text{ \AA}$ or $R_{\text{H}-\text{Cl}} = 2.85 \text{ \AA}$ versus for example, $R_{\text{H}-\text{Cl}} = 1.87 \text{ \AA}$ in (100)-HCl. Their spin-asymmetric NOCV deformation densities are visualized in Figure 11 using arabic labels for (101)- H_3AF and roman labels for (101)- $\text{H}_3\text{AF}/\text{Cl}$.

The deformation densities of both adsorptions are equivalent in shape. However, due to the smaller electronegativity of Cl and therefore less ionic character of the (101)- H_3AF adsorption (see Figure 8), the respective $\Delta E_{\text{orb}}^{\text{a}}$ are smaller than those of (101)- H_3AF . This is especially pronounced (23%) for the strongest $\Delta E_{\text{orb}}^{\text{a}}$ (2a, IIa). It corresponds to one transferred α -electron previously rather localized at Y_{surf} towards H and F or Cl spanning a larger volume as typical for anions. By the second strongest interaction (2b, IIb), β -electron

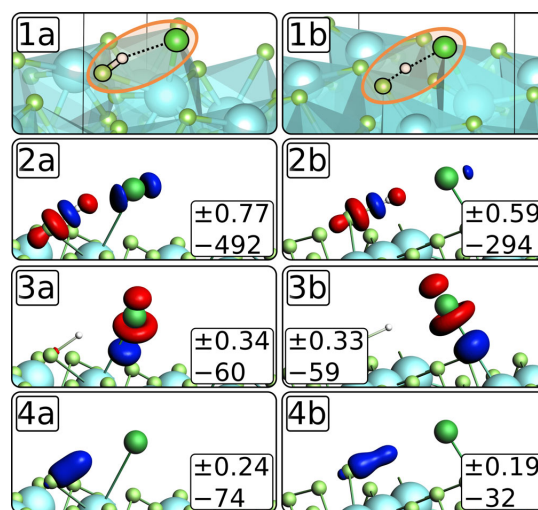


FIGURE 10 Strongest adsorbed structures within (011)-HF (1a) and (011)-HCl (1b), with respective NOCV deformation densities (red = reduction / blue = accumulation of electron density) of $|\Delta E_{\text{orb}}^{\text{a}}| > 20 \text{ kJ mol}^{-1}$ visualized with isosurface values of 0.006 (2a–b), 0.0015 (3a–b), and 0.0003 (4a–b). Within the inserts, the first row gives the eigenvalues (ν_n) in e and the each second row the $\Delta E_{\text{orb}}^{\text{a}}$ in kJ mol^{-1} .

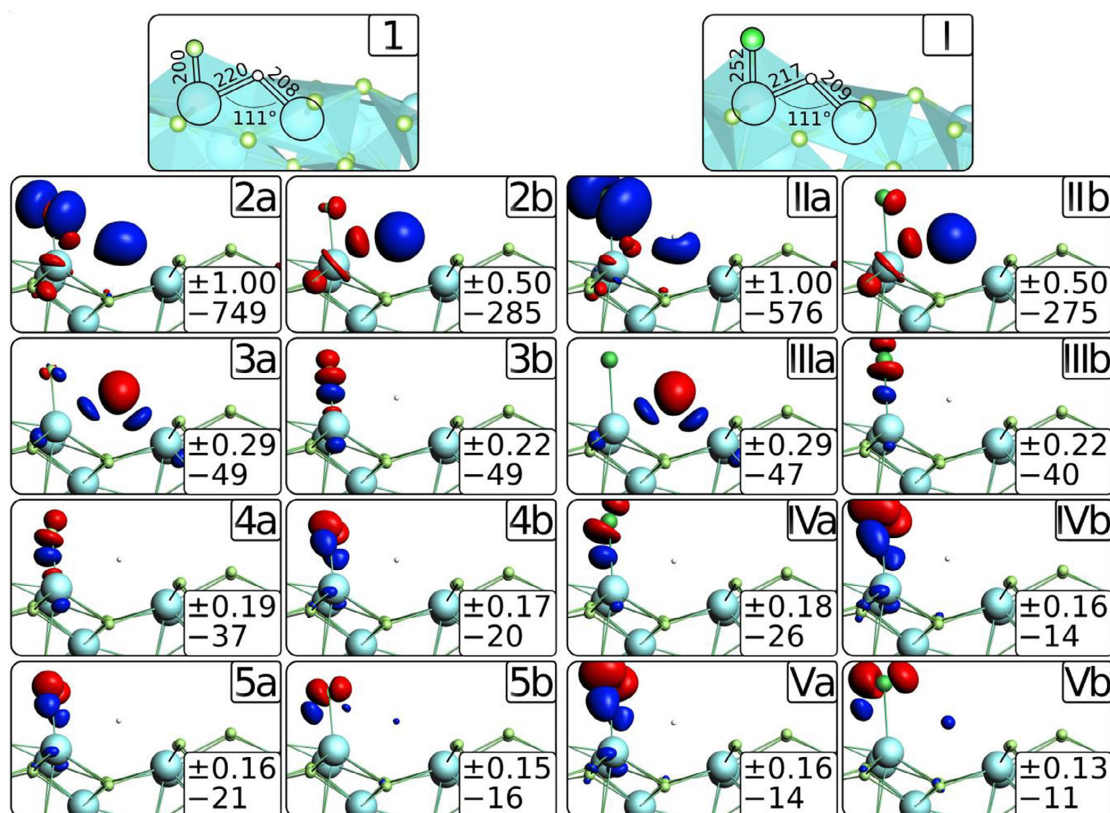


FIGURE 11 Strongest adsorbed structures of (101)-H₃A F (1) and (101)-H₃A Cl (I) with respective NOCV deformation densities (2–5, II–V) for α (a) and β -spin components (b) visualized with isosurface values of 0.0035 (2a, IIa), 0.0030 (2b, IIb), 0.0015 (3b, IIIb), 0.0010 (3–4a, IIIa), 0.0007 (IVa), 0.0004 (4b, 5a–b), and 0.0002 (IVb, Va–b). Within the inserts, the first row gives the eigenvalues (ν_n) in e and the second row the ΔE_{orb}^n in kJ mol⁻¹.

density of 0.5 e further accumulates at H, while along the same directions 0.3 e of α -electron density depletes from H (3a, IIIa). The next weaker interactions show the same σ -like direct coordination of F–Y_{surf} (4a–b) and Cl–Y_{surf} (IVa–b) with a comparable ν_{direct} and $\Delta E_{orb,direct}$ as within the nonhydride-forming YF₃-Ads (see Figure 10 3a–b). The weaker contributions are π -like direct coordinations of F–Y_{surf} (4b, 5a–b) or Cl–Y_{surf} (IVb, Va–b). In accordance to the negative polarization of H, no deformation density indicates an H-bond.

4 | CONCLUSIONS

Four surfaces, (010), (100), (011), and (101) of β -YF₃ have been studied for their binding affinity and chemisorption bonding patterns towards HF, HCl, and H₂O. Applying density functional theory with periodic energy decomposition and natural orbital for chemical valence analysis, the adsorption energies were quantified according to their subcomponents. We found that the H₂O adsorptions are strongly ionic with electrostatics constituting about 65% of all

attractive forces for practically any surface and adsorption energy. As a result, we find a very low sensitivity towards the surface termination. This is accompanied by a bonding pattern dominated by the O–Y_{surf} coordination. On the other hand, the adsorptions of HF and HCl show a varying electrostatic ratio from 30% to 60% between and within the different surfaces. We find a correlation of an increasing H-bond strength with a growing covalent bonding character and growing adsorption strength. These adsorptions are therefore highly sensitive to the surface termination and show a large range within the interaction energy. H-bonds with similar distances give comparable interaction, electrostatic, and orbital interaction energies. For HF, the strongest H-bonds are the most symmetric F–H–F_{surf}. Overall, the strongest H-bonds and thus most covalent adsorptions of Cl–H–F_{surf} are formed by HCl due to its better quality as H-donor. However, including the relaxation of the reactants, each surface favors the adsorption of HF over HCl. These findings reproduce the reported higher affinity of Y(III) solutions towards fluoride over chloride. No change in bonding patterns has been found upon the co-adsorption of up to four adsorbates.

ACKNOWLEDGMENTS

The authors thank the North-German Supercomputing Alliance (Norddeutscher Verbund zur Förderung des Hoch- und Höchstleistungsrechnens HLRN) and the Zentraleinrichtung für Datenverarbeitung (ZEDAT) at the Freie Universität Berlin for computational resources and the German Science Foundation (DFG) for funding (Project-ID 387284271) within the CRC 1349—Fluorine-Specific Interactions. Open Access funding enabled and organized by Projekt DEAL.

DATA AVAILABILITY STATEMENT

All surface structures relaxed within VASP are available within the NOMAD repository (ID: xoipefEvRGOWfNVsX_R1MA). All electronic structures obtained within AMS-BAND are available at ZENODO (<https://doi.org/10.5281/zenodo.7784827>; <https://doi.org/10.5281/zenodo.7788901>; <https://doi.org/10.5281/zenodo.7788977>; <https://doi.org/10.5281/zenodo.7789104>; <https://doi.org/10.5281/zenodo.7789115>). Further data can be requested from the authors.

ORCID

Jennifer Anders  <https://orcid.org/0000-0001-6941-2001>

Florian Kreuter  <https://orcid.org/0000-0001-5938-9071>

Ralf Tonner-Zech  <https://orcid.org/0000-0002-6759-8559>

Beate Paulus  <https://orcid.org/0000-0002-9834-4949>

REFERENCES

- [1] M. Bau, P. Dulski, *Contrib. Mineral. Petrol.* **1995**, *119*, 213.
- [2] M. Bau, *Contrib. Mineral. Petrol.* **1996**, *123*, 323.
- [3] A. A. Migdisov, A. E. Williams-Jones, T. Wagner, *Geochim. Cosmochim. Acta* **2009**, *73*, 7087.
- [4] A. Loges, A. A. Migdisov, T. Wagner, A. E. Williams-Jones, G. Markl, *Geochim. Cosmochim. Acta* **2013**, *123*, 403.
- [5] J. Stefanski, S. Jahn, *Solid Earth* **2020**, *11*, 767, <https://se.copernicus.org/articles/11/767/2020/se-11-767-2020.pdf>
- [6] Q. Guan, Y. Mei, B. Etschmann, D. Testemale, M. Louvel, J. Brugger, *Geochim. Cosmochim. Acta* **2020**, *281*, 168.
- [7] Q. Guan, Y. Mei, B. Etschmann, M. Louvel, D. Testemale, R. Spezia, J. Brugger, *Geochim. Cosmochim. Acta* **2022**, *330*, 27.
- [8] M. R. Payne, A. P. Gysi, N. C. Hurtig, *Chem. Geol.* **2023**, *617*, 121256.
- [9] D. Atencio, A. C. Bastos Neto, V. P. Pereira, J. T. M. M. Ferron, M. Hoshino, T. Moriyama, Y. Watanabe, R. Miyawaki, J. M. V. Coutinho, M. B. Andrade, et al., *Mineral. Mag.* **2015**, *79*, 767.
- [10] A. Zalkin, D. H. Templeton, *J. Am. Chem. Soc.* **1953**, *75*, 2453.
- [11] V. Pankratov, M. Kirm, H. von Seggern, *J. Lumin.* **2005**, *113*, 143, <http://www.sciencedirect.com/science/article/pii/S002231304004351>
- [12] A. Kaminski, *Laser Crystals: Their Physics and Properties*, 2nd ed., Springer, Berlin **1990**. <https://doi.org/10.1007/978-3-540-70749-3>
- [13] Z. Kollia, E. Sarantopoulou, A. C. Cefalas, C. A. Nicolaidis, A. K. Naumov, V. V. Semashko, R. Y. Abdulsabirov, S. L. Korableva, M. A. Dubinskii, *J. Opt. Soc. Am. B* **1995**, *12*, 782, <http://josab.osa.org/abstract.cfm?URI=josab-12-5-782>
- [14] E. Sarantopoulou, Z. Kollia, A. C. Cefalas, *Opt. Mater.* **2001**, *18*, 23, <http://www.sciencedirect.com/science/article/pii/S0925346701001240>
- [15] M. M. Lage, A. Righi, F. M. Matinaga, J.-Y. Gesland, R. L. Moreira, *J. Phys.: Condens. Matter* **2004**, *16*, 3207, <https://iopscience.iop.org/article/10.1088/0953-8984/16/18/021>
- [16] M. O'Keefe, *Science* **1973**, *180*, 1276.
- [17] Y. V. Pogorenko, R. M. Pshenychnyi, V. I. Lutsyk, A. O. Omel'chuk, *IOP Conf. Sci. Eng.* **2017**, *175*, 012039.
- [18] P. P. Fedorov, N. I. Sorokin, *Inorg. Mater.* **2017**, *53*, 1307.
- [19] X. Cui, T. Hu, J. Wang, J. Zhang, X. Zhong, Y. Chen, X. Li, J. Yang, C. Gao, *Nanomaterials* **2018**, *8*, 995.
- [20] X. Dai, Y. Komatsu, R. Shimizu, T. Hitosugi, *Appl. Phys. Express* **2020**, *13*, 85507, <https://doi.org/10.35848/1882-0786/aba22d>
- [21] R. D. Shannon, *Acta Cryst. A* **1976**, *32*, 751.
- [22] K. Hans Wedepohl, *Geochim. Cosmochim. Acta* **1995**, *59*, 1217, <https://www.sciencedirect.com/science/article/pii/S0016703795000382>
- [23] A. A. Yaroshevsky, *Geochemistry Int.* **2006**, *44*, 48.
- [24] A. Loges, A. A. Migdisov, T. Wagner, A. E. Williams-Jones, G. Markl, Proceedings of the 22nd Goldschmidt Conference, Montréal, QC, Canada, 24–29 June 2012, The Mineralogical Society, 2013.
- [25] W. Zhang, T. Yan, *J. Mol. Liq.* **2022**, *347*, 118367, <https://www.sciencedirect.com/science/article/pii/S0167732221030920>
- [26] K. Newcomb, S. P. Tiwari, N. Rai, E. J. Maginn, *Phys. Chem. Chem. Phys.* **2018**, *20*, 15753.
- [27] G. P. Shironosova, I. R. Prokopyev, *Engineering* **2019**, *330*, 7.
- [28] F. H. Spedding, D. C. Henderson, *J. Chem. Phys.* **1971**, *54*, 2476.
- [29] J. Anders, N. Limberg, B. Paulus, *Materials* **2022**, *15*, 6048.
- [30] G. Wulff, *Z. Kristallogr. Cryst. Mater.* **1901**, *34*, 449.
- [31] M. V. Laue, *Z. Kristallogr. Mater.* **1943**, *105*, 124.
- [32] J. Anders, H. Wiedenhaupt, B. Paulus, *Crystals* **2023**, *13*, 555.
- [33] S. Grimme, J. Antony, S. Ehrlich, H. Krieg, *J. Chem. Phys.* **2010**, *132*, 154104.
- [34] K. Kitaura, K. Morokuma, *Int. J. Quantum Chem.* **1976**, *10*, 325.
- [35] T. Ziegler, A. Rauk, *Theor. Chim. Acta* **1977**, *46*, 1.
- [36] M. Raupach, R. Tonner, *J. Chem. Phys.* **2015**, *142*, 194105.
- [37] M. P. Mitoraj, A. Michalak, T. Ziegler, *J. Chem. Theory Comput.* **2009**, *5*, 962.
- [38] L. Pecher, R. Tonner, *Wiley Interdiscip. Rev. Comput. Mol. Sci.* **2019**, *9*, 1759.
- [39] G. Kresse, J. Hafner, *J. Phys.: Condens. Matter* **1994**, *6*, 8245.
- [40] J. P. Perdew, K. Burke, M. Ernzerhof, *Phys. Rev. Lett.* **1996**, *77*, 3865, <https://link.aps.org/doi/10.1103/PhysRevLett.77.3865>
- [41] P. E. Blöchl, *Phys. Rev. B* **1994**, *50*, 17953, <https://link.aps.org/doi/10.1103/PhysRevB.50.17953>
- [42] G. Kresse, D. Joubert, *Phys. Rev. B* **1999**, *59*, 1758, <https://link.aps.org/doi/10.1103/PhysRevB.59.1758>
- [43] S. Grimme, S. Ehrlich, L. Goerigk, *J. Comput. Chem.* **2011**, *32*, 1456.
- [44] BAND, SCM, *Theoretical Chemistry, Vrije Universiteit, Amsterdam, The Netherlands* **2021**, <http://www.scm.com>
- [45] E. Van Lenthe, E. J. Baerends, *J. Comput. Chem.* **2003**, *24*, 1142.
- [46] P. H. T. Philipsen, E. van Lenthe, J. G. Snijders, E. J. Baerends, *Phys. Rev. B* **1997**, *56*, 13556, <https://link.aps.org/doi/10.1103/PhysRevB.56.13556>
- [47] A. V. Marenich, S. V. Jerome, C. J. Cramer, D. G. Truhlar, *J. Chem. Theory Comput.* **2012**, *8*, 527.
- [48] C. A. Peeples, G. Schreckenbach, *J. Chem. Theory Comput.* **2016**, *12*, 4033.
- [49] K. Momma, F. Izumi, *J. Appl. Crystallogr.* **2011**, *44*, 1272.
- [50] G. Jeffrey, *An Introduction to Hydrogen Bonding*, Oxford University Press, New York, Oxford **1997**.
- [51] J. W. Larson, T. B. McMahon, *Inorg. Chem.* **1984**, *23*, 2029.
- [52] S. Gronert, *J. Am. Chem. Soc.* **1993**, *115*, 10258.

SUPPORTING INFORMATION

Additional supporting information can be found online in the Supporting Information section at the end of this article.

How to cite this article: J. Anders, H. Wiedenhaupt, F. Kreuter, R. Tonner-Zech, B. Paulus, *J. Comput. Chem.* **2023**, *1*. <https://doi.org/10.1002/jcc.27168>

Supporting Information on: Chemical Bonding of HF, HCl, and H₂O onto YF₃ Surfaces - Quantification by First Principles

Jennifer Anders¹, Henrik Wiedenhaupt¹, Florian Kreuter²,
Ralf Tonner-Zech², Beate Paulus¹

Contents

1	Computational Method Validation	2
1.1	Basis Set and Frozen Cores	2
1.2	<i>k</i> -Grid	3
1.3	Numerical Quality	3
2	Transferability of VASP to AMS-BAND	4
3	Spin Arrangement in Substoichiometric Surface (101)	5
4	Structural Scope	5
4.1	(010)	6
4.1.1	HF	6
4.1.2	HCl	7
4.1.3	H ₂ O	7
4.1.4	HCl/H ₂ O	8
4.2	(100)	8
4.2.1	HF	8
4.2.2	HCl	8
4.2.3	H ₂ O	9
4.3	(011)	9
4.3.1	HF	9
4.3.2	HCl	9
4.3.3	H ₂ O	10
4.4	(101)	10
4.4.1	HF	10
4.4.2	HCl	10
4.4.3	H ₂ O	11
5	pEDA and NOCV Plots	12
5.1	Structural Data vs. Electrostatic and Orbital Contributions	12
5.2	Averages over Structural Properties	13
5.3	Dispersion Energy	15
5.4	NOCV Eigenvalues and Energies	15
5.5	NOCV Deformation Densities of (100)-HCl	17

¹Institut für Chemie und Biochemie, Freie Universität Berlin, Arnimallee 22, 14195 Berlin, Germany

²Wilhelm-Ostwald-Institut für Physikalische und Theoretische Chemie, Universität Leipzig, Linnéstraße 2, 04103 Leipzig, Germany

1 Computational Method Validation

1.1 Basis Set and Frozen Cores

The AMS-BAND basis set library contains Slater-type orbital basis sets of SZ, DZ, TZP, TZ2P or QZ4P quality, as well as small (11 valence electrons) and large frozen core (3 valence electrons) for Y. The large core is the default setting. We tested the effect of the 9 more valence electrons and the effect of the basis set size itself onto the pEDA terms of the most stable (010)-HF adsorption (structural isomer **d**) shown in Figure S5 **d** (see Figure S1 and Table S1). All other details as in the computational details.

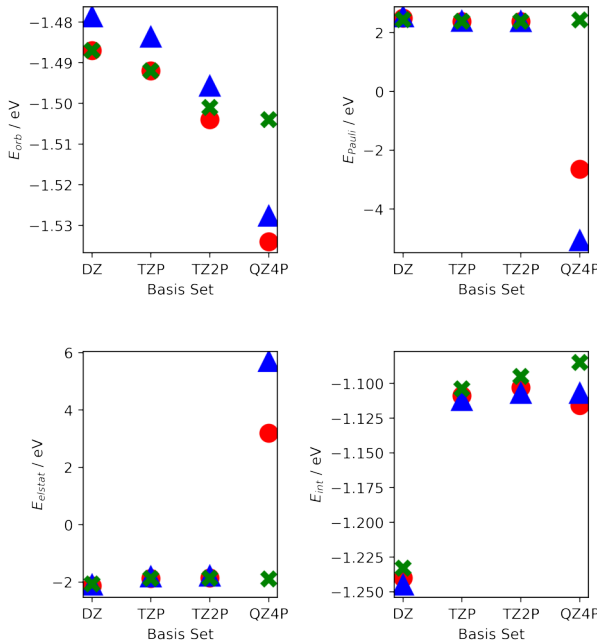


Figure S1: Effect of basis set size from DZ to QZ4P onto the pEDA terms onto (010)-HF **d** Figure S5 at a supercell size of $(4 \times 2 \times 2)$ YF₃-layer with a large core on Y (red cycle) or $(4 \times 3 \times 2)$ YF₃-layer with a large (blue triangle) or small core on Y (green cross). All values given in eV.

The dispersion energy is not given in Figure S1–S2 or Table S1 because it does not depend on the electronic density. Looking at the large core setups of the two different supercell sizes (red cycles and blue triangles), one sees that at the large QZ4P basis set, ΔE_{elstat} turns strongly repulsive while ΔE_{Pauli} becomes strongly attractive. However, the 10 highest occupied molecular orbitals (MOs) do not change in order or exchange with an unoccupied MO comparing TZ2P/large core with QZ4P/large core. This has to be connected to Y³⁺/large core being left without valence electrons but a bare frozen core, while including a very large number of then empty basis function. The respective Mulliken charges suggest even Y^{3.3+}, which should not be possible by its 3 valence electrons. According to the Mulliken charge contributions, Y-5s and Y-4d STOs spill out too much electron density in QZ4P/large core compared to the QZ4P/small core or TZ2P/large core. Consequently, the QZ4P basis set seems unbalanced for Y and should not be applied with a large core. Due to this instability, we chose to use the second largest available basis set TZ2P with the small core (green crosses).

Table S1: Comparison of pEDA terms with TZ2P basis set size but 11 (small core) vs. 3 (large core) valence electron per Y on (010)-HF **d** (see Figure S5) at a supercell size of $(4 \times 3 \times 4)$ YF₃-layers. The bottom row gives the difference of both calculations. All energies in kJ·mol⁻¹:

PBE/TZ2P/ Γ -only	ΔE_{Pauli}	ΔE_{elstat}	ΔE_{orb}	ΔE_{int}
small core on Y	230.0	-179.3	-144.5	-105.8
large core on Y	218.7	-169.7	-144.0	-107.0
$\Delta(\text{small} - \text{large core})$	11.3	-9.6	-0.5	1.2

We found that upon increasing the number of electrons on Y, ΔE_{orb} and ΔE_{int} change by only 1 kJ·mol⁻¹. The former shows that the orbital contribution of this adsorption is hardly affected by the additional basis functions onto the cation. This can be explained by looking at the orbital interactions of the small core calculations (see Figure 9 **1-2a** within the main paper), which are strongly dominated with -73 kJ·mol⁻¹ by the F-H···F_{surf} H-bond involving no Y. The direct coordination of F···Y_{surf} is a considerably weaker contribution with -41 kJ·mol⁻¹. In contrast to these hardly affected terms, ΔE_{Pauli} and ΔE_{elstat} both increase by about 10 kJ·mol⁻¹ in strength between the two cores. Consequently, the ratio of ΔE_{elstat} to ΔE_{orb} increases significantly by the smaller core on Y. This is linked to the better polarizability of Y, because Y³⁺/large core is left without valence electrons and a bare frozen core. Therefore, we consider the results by applying a small core on Y as more reliable.

1.2 *k*-Grid

We tested the effect of regular *k*-grid sizes of Γ -only, 3×3 and 5×5 onto the pEDA terms of (010)·HF **d** (see Figure S5) at a supercell size of $(4 \times 3 \times 2)$ YF₃-layer. All other details as in the computational details. Note that by the atom-centered basis set of AMS-BAND, the dimension perpendicular to the surface is not subject to periodic boundary conditions and thus does not use *k*-points. The two given *k*-point dimensions refer to the dimensions containing the surface. We found that all pEDA terms only change within 0.1 kJ·mol⁻¹ or 1 meV. The energy of formation by AMS-BAND of the YF₃·HF structure was also only reduced by 0.13 kJ·mol⁻¹ or 1.3 meV when increasing the *k*-grid from Γ -only to 5×5 . The energy reduction from 3×3 to 5×5 was found to be only 0.5 meV. Because of the very low effect of just about 0.1 kJ·mol⁻¹, we consider Γ -only as sufficient for the AMS-BAND calculations.

1.3 Numerical Quality

AMS-BAND provides numerical quality settings from so called basic, normal, good, very good to excellent, which set a number of cutoffs for the calculation. We tested their effect onto the pEDA terms of (010)·HF **d** (see Figure S5 **d**) at a supercell size of $(4 \times 3 \times 2)$ YF₃-layers (see Figure S2). All other details as in the computational details. In tradeoff to the exponentially growing CPU time, we chose the very good setting as sufficient.

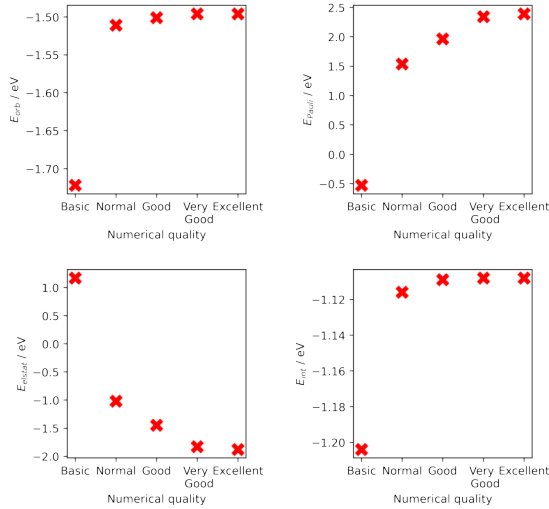


Figure S2: Effect of numerical quality setting onto the pEDA terms onto (010)·HF **d** at a supercell size of $(4 \times 3 \times 2)$ YF₃-layer.

2 Transferability of VASP to AMS-BAND

Within the main paper, all atomic coordinates have been relaxed inside VASP and only the electronic structure has been recalculated using AMS-BAND. We validated this approach by calculating the bonding energy including the reactant relaxation (ΔE_{bond} , see Reaction R1 of the main paper) of the $(010)\cdot(\text{Ads})_n$ ($\text{Ads} = \text{H}_2\text{O}, \text{HF}, \text{HCl}$) by energies determined in VASP ($\Delta E_{\text{bond}}^{\text{VASP}}$), as well as those determined using AMS-BAND ($\Delta E_{\text{bond}}^{\text{AMS}}$). Within the latter, single points in AMS-BAND have been calculated on the VASP relaxed product structure, as well as on the VASP relaxed reactants. Note that within the main paper, all energies are derived from AMS-BAND and thus, ΔE_{bond} without superscript equals $\Delta E_{\text{bond}}^{\text{AMS}}$. The only $\Delta E_{\text{bond}}^{\text{VASP}}$ are given in Table 2 for comparison. Both E_{bond} for $(010)\cdot(\text{Ads})_n$ and their differences are plotted in Figure S3 and S4, respectively.

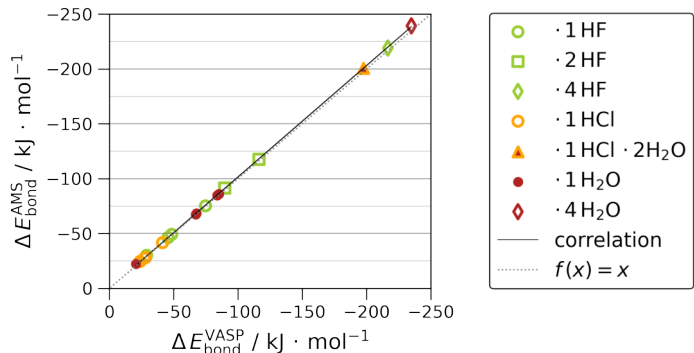


Figure S3: Adsorption bonding energies for $(010)\cdot(\text{Ads})_n$ including reactant relaxation (E_{bond}) determined in AMS-BAND vs. determined in VASP; the correlation between the two is plotted (solid line) and a line of $f(x) = x$ is given to visualize equality (dotted line).

Figure S3 shows the excellent agreement between the ΔE_{bond} values obtained by VASP or AMS-BAND. Both ΔE_{bond} correlate linearly with a slope of 1.015 and R^2 of 0.9999 without allowing an offset. We find that adsorption energies obtained by AMS-BAND are systematically slightly more negative for all $(010)\cdot\text{Ads}$. The bonding energies differ by only $< 2.0 \text{ kJ}\cdot\text{mol}^{-1}$ for a single molecule adsorption between AMS-BAND and VASP or $< 2.5 \text{ kJ}\cdot\text{mol}^{-1}$ for the adsorption of two molecules. Both are within chemical accuracy of $1 \text{ kcal}\cdot\text{mol}^{-1}$. Only the adsorption of four water molecules exceeds this mark with a difference of $4.4 \text{ kJ}\cdot\text{mol}^{-1}$. However, considering the relative difference to $\Delta E_{\text{bond}}^{\text{VASP}}$, this is less than 2%. It should be noted, that both determined ΔE_{bond} systematically slightly overestimate the binding strength, as the zero-point-energy correction is missing.

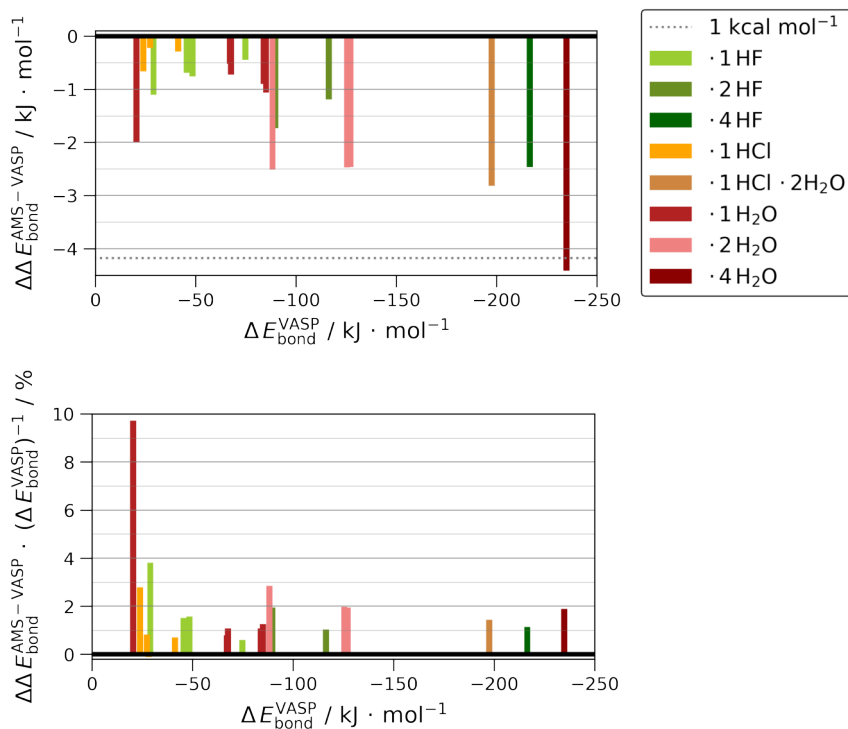


Figure S4: The difference of $\Delta E_{\text{bond}}^{\text{AMS}} - \Delta E_{\text{bond}}^{\text{VASP}}$ vs. $\Delta E_{\text{bond}}^{\text{VASP}}$ (top) for $(010) \cdot (\text{Ads})_n$; the chemical accuracy of $\pm 1 \text{ kcal} \cdot \text{mol}^{-1}$ is visualized (dotted line); the difference of $\Delta E_{\text{bond}}^{\text{AMS}} - \Delta E_{\text{bond}}^{\text{VASP}}$ as ratio to $\Delta E_{\text{bond}}^{\text{VASP}}$ vs. $\Delta E_{\text{bond}}^{\text{VASP}}$ (bottom).

3 Spin Arrangement in Substoichiometric Surface (101)

As given in the computational details, the substoichiometric surface (101) yielded non-singlet spin configurations. As each (101) surface unit cell is missing one F atom, the calculated $(2 \times 2 \times 4)$ bare supercell is missing eight F in total. This leaves Y-centers with an unbound electron as formally Y(II). VASP predicts a ferromagnetic alignment of all eight spins giving a collinear magnet moment of eight for the whole bare surface supercell. For the adsorbed systems of $(101) \cdot \text{Ads}$, several adsorbates of HF and HCl spontaneously dissociated and got reduced in their oxidation state by $-II$ in sum leaving a collinear magnetic moment of six for the whole supercell with adsorbate. More details on these VASP results are given elsewhere.¹

Within AMS-BAND, the same bare (101) surface converged to a ferrimagnetic alignment with a collinear magnetic moment of four. At the top, as well as at the bottom surface, the eight Y(II) centers partially co-aligned. When enforcing a ferromagnetic arrangement of eight, the obtained electronic energy is 23 meV less stable. Thus, the unrestricted calculation with a collinear magnetic moment of four is used to calculate ΔE_{relax} or ΔE_{bond} . Because of SCF convergence issues inside AMS-BAND observed when applying no restrictions onto the spin for the $(101) \cdot \text{Ads}$ structures, the ferromagnetic spin arrangement as found by VASP of eight (or six for the hydride-forming structured) was enforced. The bare surfaces within the final $(101) \cdot \text{Ads}$ structure needed for ΔE_{int} were done in the same spin arrangement of eight (or six).

4 Structural Scope

This subsection visualizes all found 38 single adsorbate structural isomers (grouped from 46 relaxed structures) and the 8 multiple adsorbate structural isomers. All surface structures relaxed within VASP are available within the NOMAD repository (ID: xoipefEvRGOWfNVSx.R1MA). Note that the dataset was also built for our previous study comparing YF_3 and HoF_3 surface adsorptions.¹ It therefore also contains HoF_3 structures. Moreover, some

weakly adsorbing structural isomers, as well as those dissociated by more than 3 Å final adsorbate bond length have been excluded from this work. Accordingly, the enumeration of the structural isomers may differ, please refer to the dataset explanation at the NOMAD repository. All electronic structure data generated within AMS-BAND used for this paper are available at Zenodo: <https://doi.org/10.5281/zenodo.7784827>; <https://doi.org/10.5281/zenodo.7788901>; <https://doi.org/10.5281/zenodo.7788977>; <https://doi.org/10.5281/zenodo.7789104>; <https://doi.org/10.5281/zenodo.7789115>

4.1 (010)

4.1.1 HF

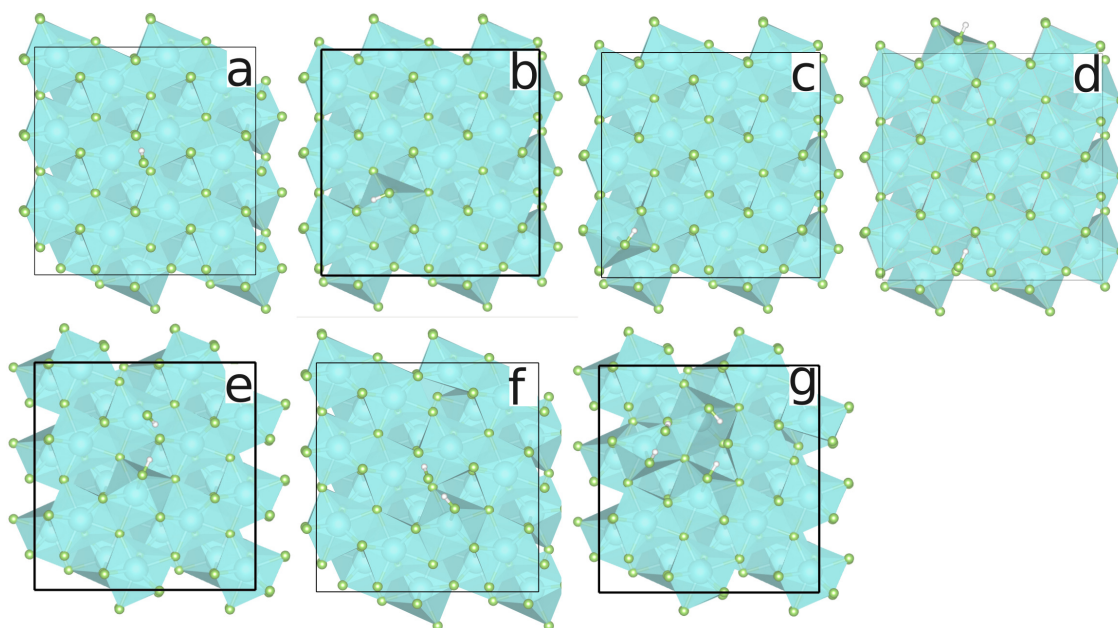


Figure S5: Relaxed adsorption structures of (010)-1HF (**a-d**), (010)-2HF (**e-f**) and (010)-4HF (**g**) in order of increasing $|\Delta E_{\text{bond}}|$ viewing onto the surface unit cell (black frame) made from $(2 \times 3 \times 2)$ bulk unit cells. Structural isomer **d** equals **1a** in Figure 3 of the main paper. For isomer **b**, two nearly equivalent structures were considered within the dataset.

4.1.2 HCl

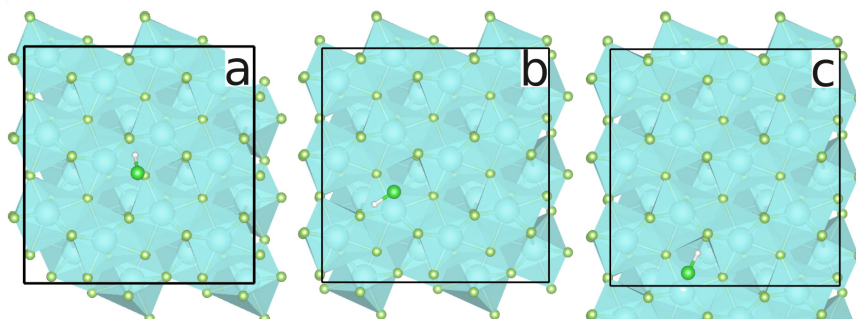


Figure S6: Relaxed adsorption structures of (010)·1HCl in order of increasing $|\Delta E_{\text{bond}}|$ viewing onto the surface unit cell (black frame) made from $(2 \times 3 \times 2)$ bulk unit cells. Structural isomer **c** equals **1b** in Figure 3 of the main paper. For isomer **b**, two nearly equivalent structures were considered within the dataset. This figure is reprinted from [1 (SI Figure S3)].

4.1.3 H₂O

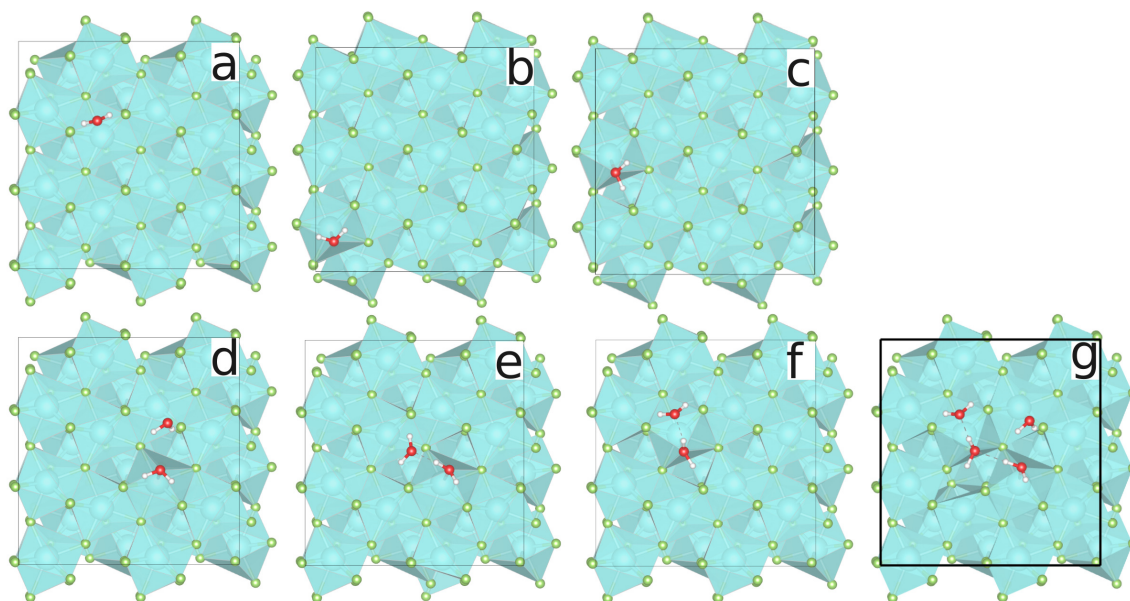


Figure S7: Relaxed adsorption structures of (010)·1H₂O (**a–c**), (010)·2H₂O (**d–f**) and (010)·4H₂O (**g**) in order of increasing $|\Delta E_{\text{bond}}|$ viewing onto the surface unit cell (black frame) made from $(2 \times 3 \times 2)$ bulk unit cells. Structural isomer **c** equals **1c** in Figure 3 of the main paper. For isomers **b** and **c**, two nearly equivalent structures were considered within the dataset.

4.1.4 HCl/H₂O

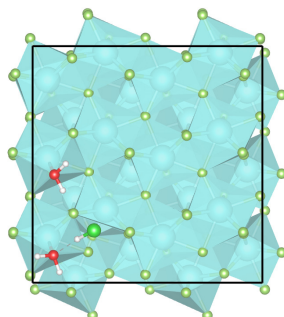


Figure S8: The relaxed adsorption structure of (010)·1HCl·2H₂O viewing onto the surface unit cell (black frame) made from (2 × 3 × 2) bulk unit cells.

4.2 (100)

4.2.1 HF

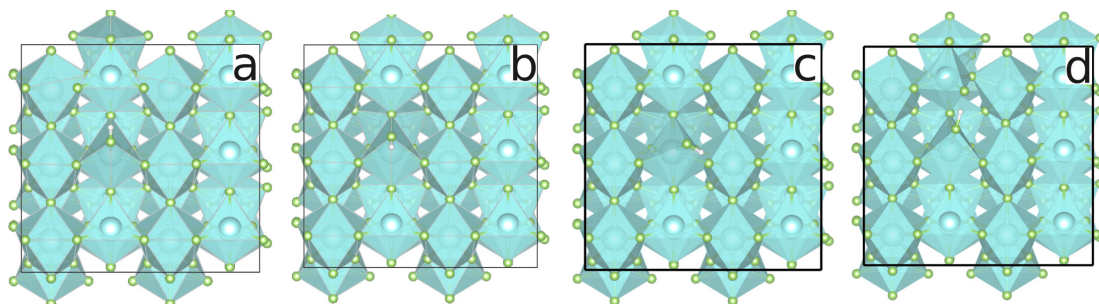


Figure S9: Relaxed adsorption structures of (100)·1HF in order of increasing $|\Delta E_{\text{bond}}|$ viewing onto the surface unit cell (black frame) made from (2 × 3 × 2) bulk unit cells. Structural isomer **d** equals **2a** in Figure 3 of the main paper. This figure is reprinted from [1 (SI Figure S5)].

4.2.2 HCl

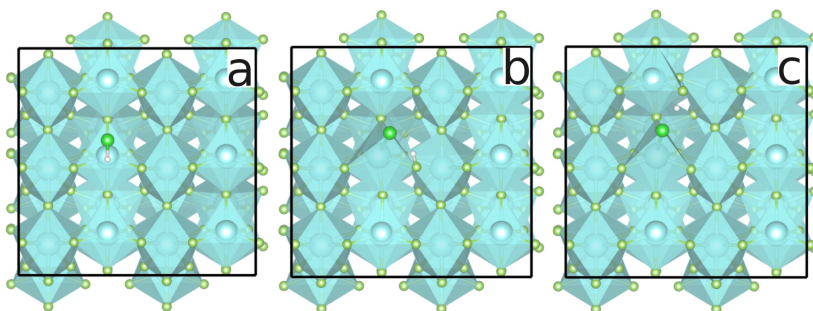


Figure S10: Relaxed adsorption structures of (100)·1HCl in order of increasing $|\Delta E_{\text{bond}}|$ viewing onto the surface unit cell (black frame) made from (2 × 3 × 2) bulk unit cells. Structural isomers **c** and **b** equal **2b** and **2b'** in Figure 3 of the main paper, respectively.

4.2.3 H₂O

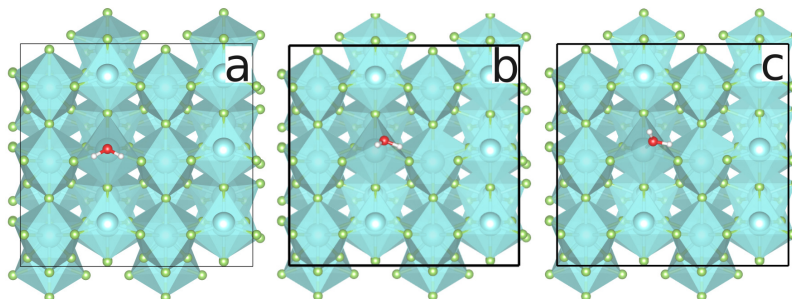


Figure S11: Relaxed adsorption structures of (100)-1H₂O in order of increasing $|\Delta E_{\text{bond}}|$ viewing onto the surface unit cell (black frame) made from $(2 \times 3 \times 2)$ bulk unit cells. Structural isomer **c** equals **2c** in Figure 3 of the main paper. For isomer **a**, two nearly equivalent structures were considered within the dataset. This figure is reprinted from [1 (SI Figure S4)].

4.3 (011)

4.3.1 HF

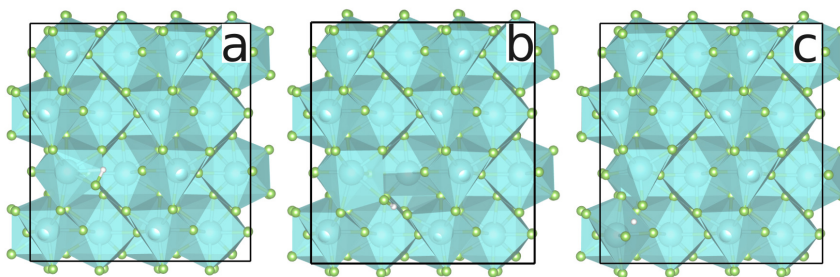


Figure S12: Relaxed adsorption structures of (011)-1HF in order of increasing $|\Delta E_{\text{bond}}|$ viewing onto the surface unit cell (black frame) made from $(2 \times 2 \times 4)$ bulk unit cells. Structural isomer **c** equals **3a** in Figure 3 of the main paper. For isomer **c**, two nearly equivalent structures were considered within the dataset. This figure is reprinted from [1 (SI Figure S8)].

4.3.2 HCl

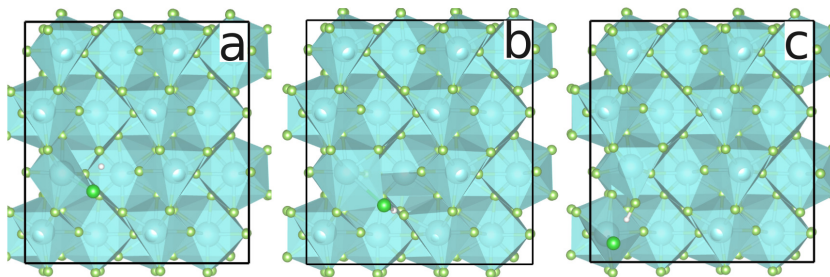


Figure S13: Relaxed adsorption structures of (011)-1HCl in order of increasing $|\Delta E_{\text{bond}}|$ viewing onto the surface unit cell (black frame) made from $(2 \times 2 \times 4)$ bulk unit cells. Structural isomer **c** equals **3b** in Figure 3 of the main paper. For isomer **c**, two nearly equivalent structures were considered within the dataset. This figure is reprinted from [1 (SI Figure S9)].

4.3.3 H₂O

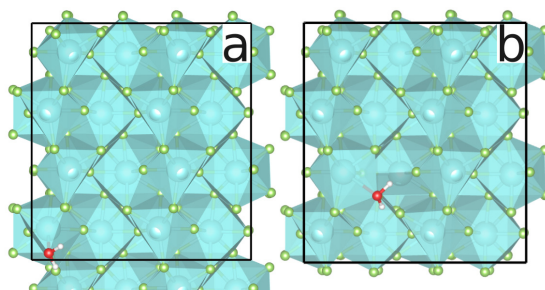


Figure S14: Relaxed adsorption structures of (011)·1H₂O in order of increasing $|\Delta E_{\text{bond}}|$ viewing onto the surface unit cell (black frame) made from $(2 \times 2 \times 4)$ bulk unit cells. Structural isomer **b** equals **3c** in Figure 3 of the main paper. For isomer **b**, two nearly equivalent structures were considered within the dataset. This figure is reprinted from [1 (SI Figure S10)].

4.4 (101)

4.4.1 HF

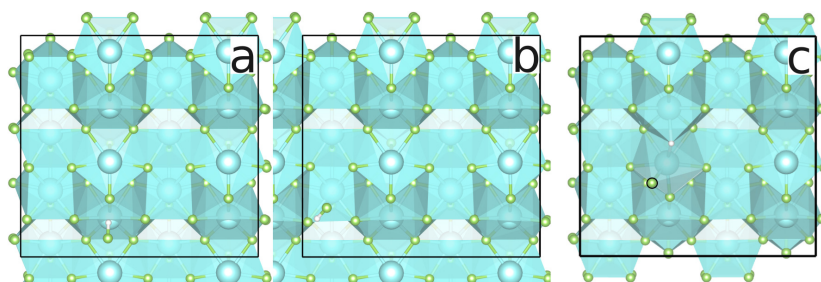


Figure S15: Relaxed adsorption structures of (101)·1HF in order of increasing $|\Delta E_{\text{bond}}|$ viewing onto the surface unit cell (black frame) made from $(2 \times 2 \times 4)$ bulk unit cells. Structural isomer **c** equals **4a** in Figure 3 of the main paper.

4.4.2 HCl

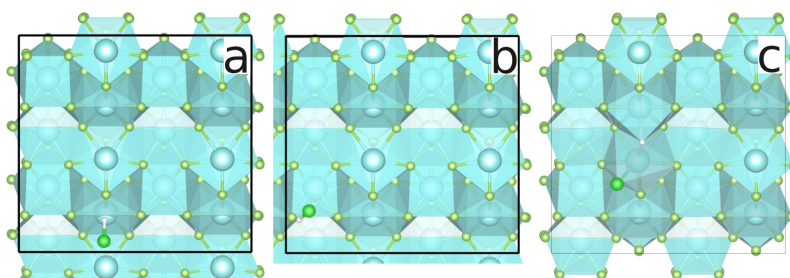


Figure S16: Relaxed adsorption structures of (101)·1HCl in order of increasing $|\Delta E_{\text{bond}}|$ viewing onto the surface unit cell (black frame) made from $(2 \times 2 \times 4)$ bulk unit cells. Structural isomer **c** equals **4b** in Figure 3 of the main paper.

4.4.3 H₂O

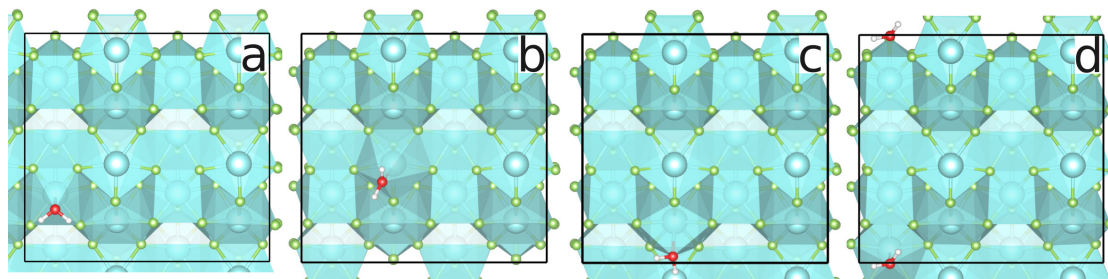


Figure S17: Relaxed adsorption structures of (101)-1H₂O in order of increasing $|\Delta E_{\text{bond}}|$ viewing onto the surface unit cell (black frame) made from $(2 \times 2 \times 4)$ bulk unit cells. Structural isomer **d** equals **4c** in Figure 3 of the main paper. This figure is reprinted from [1 (SI Figure S13)].

5 pEDA and NOCV Plots

Within this subsection further pEDA result plots are given to support the main paper.

5.1 Structural Data vs. Electrostatic and Orbital Contributions

Figure S18 and Figure S19 give the structural parameters vs. ΔE_{elstat} and ΔE_{orb} , respectively. Compared to the analogous Figure 5 of the main paper, they visualize the equivalent trends of these parameters to any of these three energies.

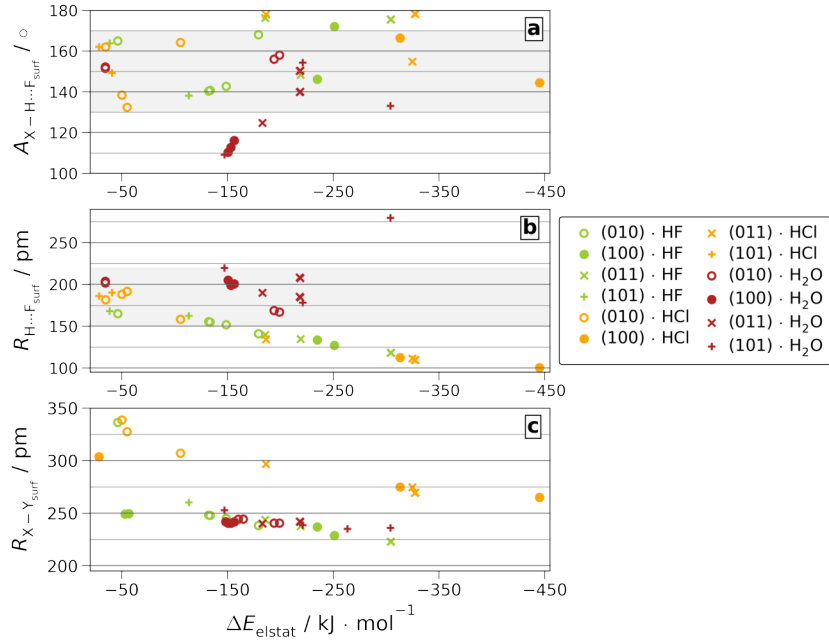


Figure S18: Angles ($A_{X-H \dots F_{\text{surf}}}$, **a**) and distances ($R_{H \dots F_{\text{surf}}}$, **b**) of H-bond and direct ($R_{X-Y_{\text{surf}}}$, **c**) surface coordination for $X = \{\text{O}, \text{F}, \text{Cl}\}$ vs. ΔE_{elstat} for all single adsorptions without charge transfer.

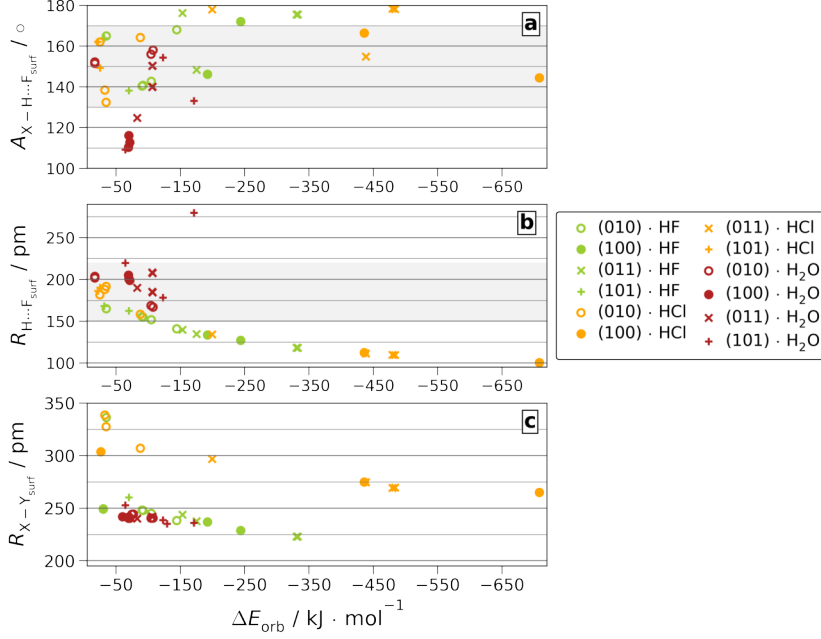


Figure S19: Angles ($A_{X-H\dots F_{\text{surf}}}$, **a**) and distances ($R_{H\dots F_{\text{surf}}}$, **b**) of H-bond and direct ($R_{X-Y_{\text{surf}}}$, **c**) surface coordination for $X = \{O, F, Cl\}$ vs. ΔE_{orb} for all single adsorptions without charge transfer.

5.2 Averages over Structural Properties

The mean (\bar{a}_E) of property a is weighted linearly by ΔE_{int} .

$$\bar{a}_E = \frac{\sum_i (-\Delta E_{\text{int},i} a_i)}{\sum_i (-\Delta E_{\text{int},i})} \quad (\text{S1})$$

The mean (\bar{a}_B) of property a is Boltzmann weighted by ΔE_{int} .

$$\bar{a}_B = \frac{\sum_i \left(\exp \frac{-\Delta E_{\text{int},i}}{k_B T} a_i \right)}{\sum_i \left(\exp \frac{-\Delta E_{\text{int},i}}{k_B T} \right)} \quad (\text{S2})$$

\bar{a}_B was calculated for a variety of temperatures. The values obtained at $T = 200$ K, the temperature used for the majority of AIMD simulations¹ are given in Table S2. However, given the large energy gaps between the structural isomers, no temperature induced population shift is observed. Consequently, the strongest adsorbed structural isomer dominates \bar{a}_B fully. Thus, \bar{a}_B remains unchanged to the digits given with the tiny exception of $A_{O-H\dots F_{\text{surf}}}$ for $YF_3 \cdot H_2O$, which alter by 1° only.

Table S2: Calculated means of H-bond angles ($A_{X-H \dots F_{\text{surf}}}$) and distances ($R_{H \dots F_{\text{surf}}}$), direct O/F/Cl to metal coordinations ($R_{X-Y_{\text{surf}}}$) without weight (\bar{a}) or weighted by ΔE_{int} as given in Equation S1 (\bar{a}_{E}) or S2 (\bar{a}_{B}) for all single adsorptions without the charge transfer; the \bar{a}_{E} over all (hkl) (highlighted bold) are plotted in Figure 5 of the main paper:

(hkl)	$\bar{A}_{X-H \dots F_{\text{surf}}} / ^\circ$			$\bar{R}_{H \dots F_{\text{surf}}} / \text{\AA}$			$\bar{R}_{X-Y_{\text{surf}}} / \text{\AA}$			
	\bar{a}	\bar{a}_{E}	\bar{a}_{B}	\bar{a}	\bar{a}_{E}	\bar{a}_{B}	\bar{a}	\bar{a}_{E}	\bar{a}_{B}	
HF	(010)	151	152	168	1.5	1.5	1.4	2.6	2.5	2.4
	(100)	159	161	172	1.3	1.3	1.3	2.4	2.4	2.3
	(011)	169	171	176	1.3	1.2	1.2	2.3	2.3	2.2
	(101)	151	147	138	1.7	1.6	1.6	2.6	2.6	2.6
	all	158	163	176	1.4	1.3	1.2	2.5	2.4	2.2
HCl	(010)	149	151	164	1.8	1.8	1.6	3.2	3.2	3.1
	(100)	155	153	144	1.1	1.1	1.0	2.8	2.7	2.6
	(011)	172	173	178	1.2	1.1	1.1	2.8	2.7	2.7
	(101)	156	154	149	1.9	1.9	1.9	–	–	–
	all	159	163	144	1.5	1.2	1.0	2.9	2.8	2.6
H2O	(010)	154	156	157	1.9	1.7	1.7	2.7	2.5	2.4
	(100)	113	113	112	2.0	2.0	2.0	2.4	2.4	2.4
	(011)	141	142	145	2.0	2.0	2.0	2.4	2.4	2.4
	(101)	126	130	154	2.2	2.2	1.8	2.4	2.4	2.4
	all	132	132	145	2.0	2.0	2.0	2.5	2.4	2.4

5.3 Dispersion Energy

Figure S20 gives ΔE_{disp} vs. ΔE_{int} . In all (hkl) -Ads, but (011) -HF/HCl, ΔE_{disp} is strongest for the strongest ΔE_{int} . For (011) -HF/HCl ΔE_{disp} grows stronger for longer adsorbate to surface distances and shorter inner-adsorbate distances. It therefore behaves anti-proportional to ΔE_{int} .

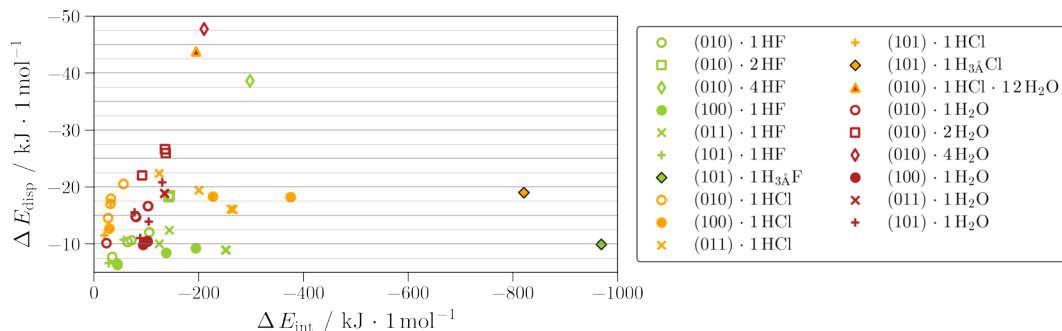


Figure S20: Energy contribution to the adsorption by dispersion (ΔE_{disp}) vs. the overall interaction energy (ΔE_{int}) for all surfaces and adsorbates.

It should be noted that ΔE_{disp} is obtained from the semi-empirical D3(BJ) correction and is thus independent from the actual electron density. Instead it only depends on the atomic positions and its inherent dispersion coefficients. These are fitted for each DFT functional. Therefore another, than the used PBE, functional might obtain slightly different ΔE_{disp} on the same structures.

5.4 NOCV Eigenvalues and Energies

Figure S21 **a** gives the NOCV eigenvalues and energies of any type (n). The slope of $\Delta \nu_n / \Delta \Delta E_{\text{orb}}^n$ is steeper for smaller values. The interactions above $\nu_n > 0.35$ e or $\Delta E_{\text{orb}}^n < -70$ $\text{kJ} \cdot \text{mol}^{-1}$ of (100), (011) and (101) (hkl) -HF/HCl give a flatter slope, in accordance to the lower ratio of ΔE_{elstat} vs. ΔE_{orb} and thus more covalent character of the adsorptions (see main paper Figure 8). Figure S21 **b** is a zoom into the weaker interactions of **a**.

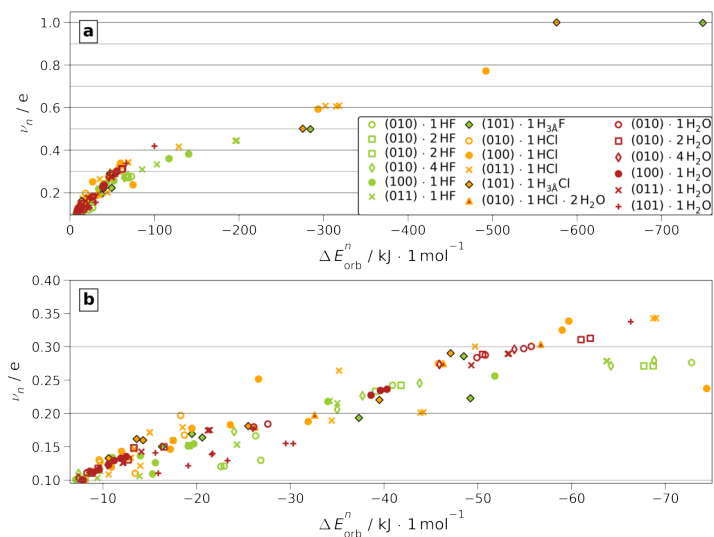


Figure S21: NOCV deformation density eigenvalues in absolutes ($\nu_n \geq 0.1$ e) vs. the corresponding contribution to the orbital energy (ΔE_{orb}^n) for all adsorptions (**a**) and zoomed in to the weaker ΔE_{orb}^n (**b**).

Figure S22 expands Figure 9 **3a** of the main paper to the corresponding $\nu_{\text{H-bond}}$ and the overall ΔE_{orb} . The relation of H-bond eigenvalues and the overall orbital energy, dominated by the H-bond energy show very similar dependencies on $R_{\text{H}\cdots\text{F}_{\text{surf}}} - R_{\text{X-H}}$.

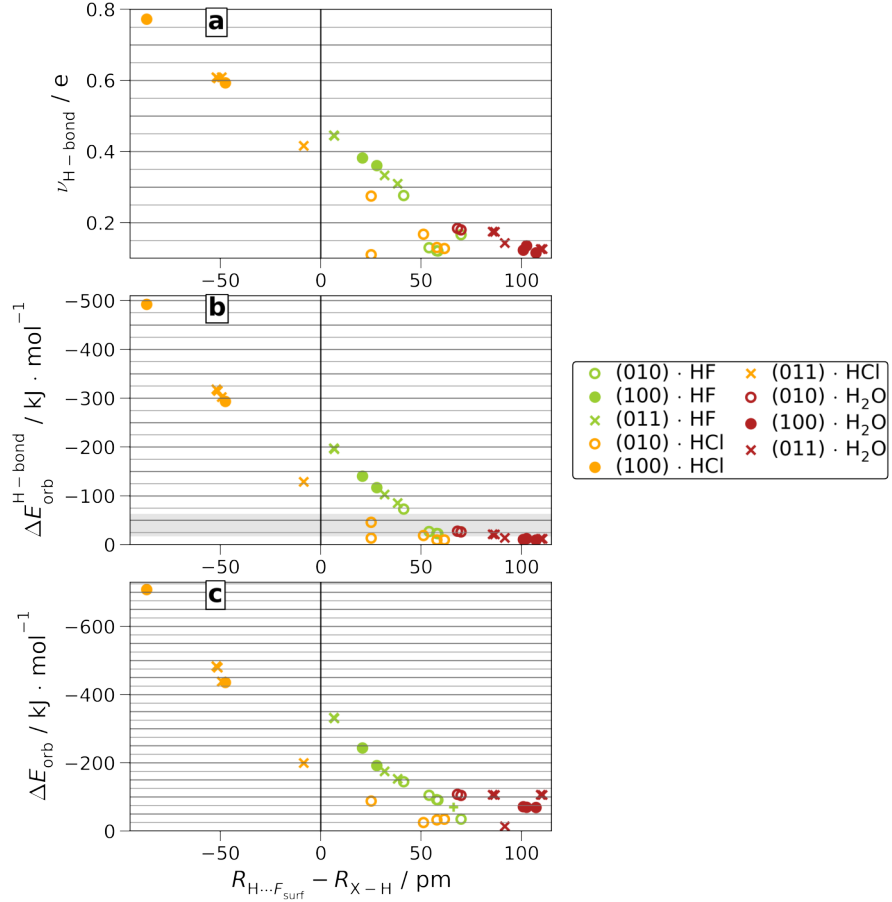


Figure S22: NOCV deformation density eigenvalues in absolutes ($\nu_{\text{H-bond}}$, **a**), contributions to the orbital energy ($\Delta E_{\text{orb}}^{\text{H-bond}}$, **b** with Jeffrey's criteria of medium strong H-bonds highlighted) and the overall orbital energy (ΔE_{orb} , **c**) vs. the difference of H-bond length and adsorbate bond length ($R_{\text{H}\cdots\text{F}_{\text{surf}}} - R_{\text{X-H}}$) with $\text{X} = \{\text{O}, \text{F}, \text{Cl}\}$ for all single non-hydride-forming adsorptions.

Figure S23 gives the eigenvalues of the NOCV deformation densities for the corresponding ΔE_{orb}^n given in Figure 9 of the main paper. Again, the sum of α and β -components grouped into the same category are plotted for the non-hydride-forming adsorptions onto substoichiometric (101). Note that it zooms to the same lower energy regime, which neglects (100)-HCl **2b'** (see Figure S10 **b** and Figure 3 from the main paper) due to its large ΔE_{orb} . These deformation densities are plotted below in Figure S24. The order between the surfaces and adsorbates judged by the strongest ν_n or ΔE_{orb}^n is in general equivalent for the H-bond strength, as well as the direct coordination strength. Exceptions are found within the H-bond strengths of (010)-HCl and the structural isomer of (011)-HCl bound by $\Delta E_{\text{int}} = -125 \text{ kJ}\cdot\text{mol}^{-1}$. Their $\nu_{\text{H-bond}}$ corresponds to a smaller $\Delta E_{\text{orb}}^{\text{H-bond}}$ than within the other (hkl) -Ads. An exception of the opposite case is found within the direct coordinations. Here, (011)-HF has the second strongest $\Delta E_{\text{orb}}^{\text{direct}}$ but only medium-strong ν_{direct} . In other words, these (010)/(011)-HCl possess $\text{Cl-H}\cdots\text{F}_{\text{surf}}$ that are less sensitive to displacement of electron density, while $\text{F}-\text{Y}_{\text{surf}}$ in (011)-HF, a displacement of the same electron density has a larger effect than in the other (hkl) -Ads.

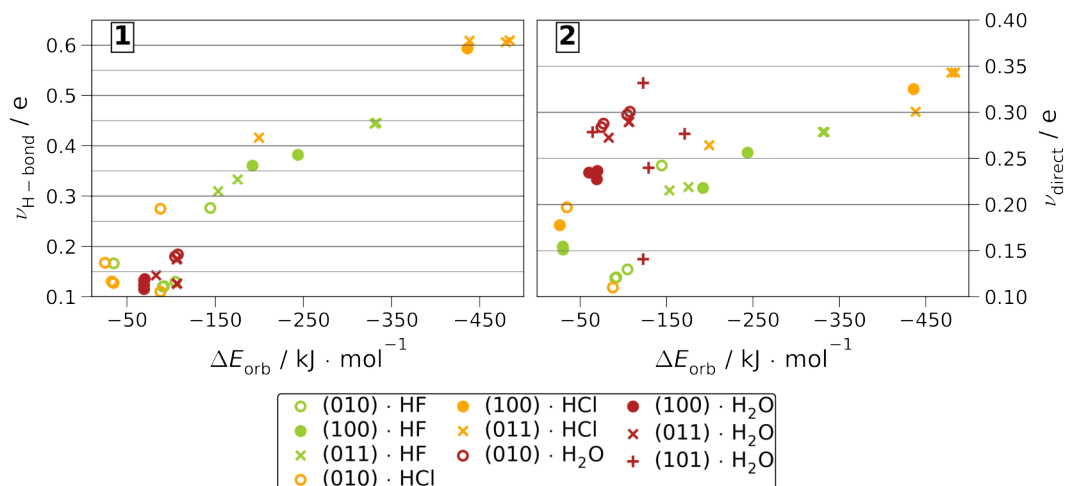


Figure S23: -NOCV deformation density eigenvalues in absolutes ($\nu \geq 0.1$ e for H-bonds (1) or direct O/F/Cl to metal coordinations (2) vs. the overall orbital energy (ΔE_{orb}) for all non-hydride-forming single adsorptions.

5.5 NOCV Deformation Densities of (100)·HCl

The NOCV deformation densities of the strongest bound (100)·HCl by ΔE_{int} (2b') or by ΔE_{bond} (2b) are visualized in Figure S24 2-4a or 2-4b, respectively.

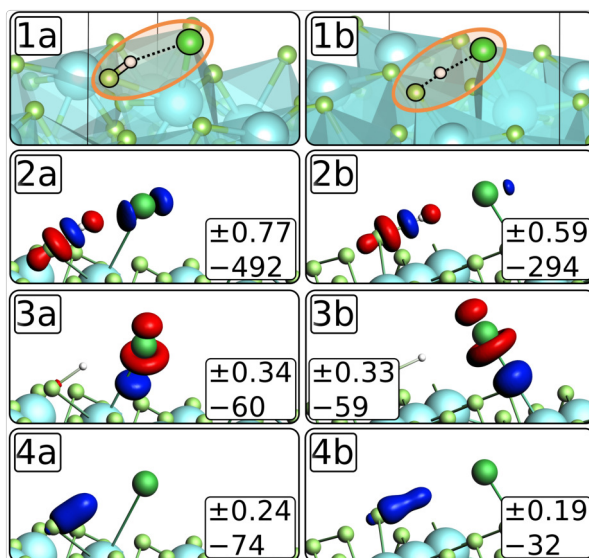


Figure S24: Highlighted adsorption structures of (100)·HCl 2b' (see 1a, Figure S10 b, and Figure 3 from the main paper) and (100)·HCl 2b (see 1b and Figure S10 c), with NOCV deformation densities (red = reduction / blue = accumulation of electron density) of 2b' (2-4a) and 2b (2-4b) for isosurface values of 0.014 (2a-b), 0.0025 (3a-b) and 0.0015 (4a-b). Each first row number gives the eigenvalues (ν_n) ≥ 0.1 e and each second row number the orbital energy (ΔE_{orb}^n) in $\text{kJ}\cdot\text{mol}^{-1}$.

As seen in Figure S24 1a, within (100)·HCl 2b' H and Cl, both coordinate to the same YF_3 polyhedron, whereas in structural isomer 2b (see Figure S24 1b), these are bridging two neighboring polyhedrons. The former has a final bond length of $R_{\text{H-Cl}} = 1.87$ Å vs. $R_{\text{H-F}} = 1.01$ Å and slightly higher Bader (or CM5) charges of $q_{\text{H}} = 0.7$ e (0.2 e) and $q_{\text{Cl}} = -0.7$ e (-0.3 e). Due to the larger H-Cl bond elongation, it shows a very strong ΔE_{orb} but also

a stronger preparation term of the fragments. Therefore, a stronger ΔE_{bond} is observed for (100)·HCl **2b**, in which H is still more shared between F and Cl with $R_{\text{H-Cl}} = 1.60 \text{ \AA}$ and $R_{\text{H-F}} = 1.13 \text{ \AA}$, yielding slightly lower charges of $q_{\text{H}} = 0.6 \text{ e}$ (0.2 e) and $q_{\text{Cl}} = -0.7 \text{ e}$ (-0.2 e).

According to the NOCV, the main orbital interaction is the Cl-H \cdots F_{surf} or Cl \cdots H-F_{surf} H-bond (see Figure S24 **2a-b**). In both structural isomers, it constitutes about 70% of the overall ΔE_{orb} . For the bridging coordination **2b**, it is about 200 kJ·mol⁻¹ weaker, even though its H-bond is 22° more linear. In accordance to the longer H-F_{surf} distance, its two-centered interaction (see Figure S24 **4a-b**) is also considerably weaker in **2b** than **2b'**. However, the direct coordination of Cl-Y_{surf} remains equivalent in both contributions, which means it contributes only 8% in **2b'** but 14% in **2b**. Within the remaining, minor contributions, a π -back donation along the H-bond F_{surf}-H \cdots Cl is found that contributes 27 or 18 kJ·mol⁻¹ for **2b'** or **2b**.

References

- [1] J. Anders, H. Wiedenhaupt, B. Paulus, *Crystals* **2023**, 13, 555.

4. Summary and Discussion

This thesis was devoted to find and investigate subtle differences shown between the geochemical twins of Zr:Hf or Y:Ho as crystalline fluorides. From aq. solutions, it is known, that these high field strength elements (HFSE) differ in their affinity for fluoride.^[18,37–39,41] The respective twin element, which possesses a higher fluoride affinity in solution, namely Y or Hf, is also found at significantly enriched concentrations within fluoride-rich hydrothermal veins.^[3,15,30] It is therefore suggested, that this small gap in fluoride affinities is the main reason behind the extraordinary fractioning among the twin elements.^[3,31–33] However, prior to this work, no theoretical, neither experimental study illuminated, whether this effect also showed within the crystalline compounds, even though, the transport of elements is largely affected by precipitations and re-solutions. Moreover, the crystalline geochemical twin element fluorides, themselves have been practically a blind spot in computational research. Given the widespread application of crystals and glasses based on these fluorides, it was time to reduce this blindness.^[49–53,56–65] Along the varieties, the solid phase offers, the publications within this work took a journey from bulk crystals (**A**), to pristine surfaces (**B.1**) to arrive at the description of adsorbate-surface interactions (**B.2–B.3**).

In the following, the major points of each paper are summarized and discussed in context of literature. Paper **A** illuminated the differences within the geochemical twin pair of Zr:Hf. It aimed to evaluate their affinities for oxide, fluoride, and hydroxide within the solid phase by their respective cohesive energies. The former two, oxide and fluoride were compared as the respective, experimentally known binary crystals. The naturally occurring baddeleyite (α - MO_2) and fluorozirconate or fluorohafnate (β - MF_4) were considered (see Fig. 4.1 a and c).^[45–48] Their affinity for fluoride vs. hydroxide is modeled by mono-hydroxylation of the respective fluorides or hypothetical oxofluorides. Experimentally, two Zr(IV) oxofluoride crystal structures have already been measured about 40 years ago.^[169–171] However, neither possessed an easy integer ZrO_xF_y stoichiometry, nor distinguished positions of F and O. The 1:2 mixed oxofluorides (MOF_2) are only known as molecules within a solid argon matrix, not as crystalline compounds.^[172] Instead, the calculated, hypothetical crystalline model was based on the known crystal structure of Te(IV) OF_2 .^[173] Such a theoretical crystalline form was chosen as a simplification for anion affinity model purposes, just as the theoretical, endothermic anion exchange of a fluoride for a hydroxide. As all studied crystals possess a strongly ionic character with band gaps far in the insulating regime, simple periodic density functional theory (DFT) at the generalized gradient approximation (GGA) level has been applied.

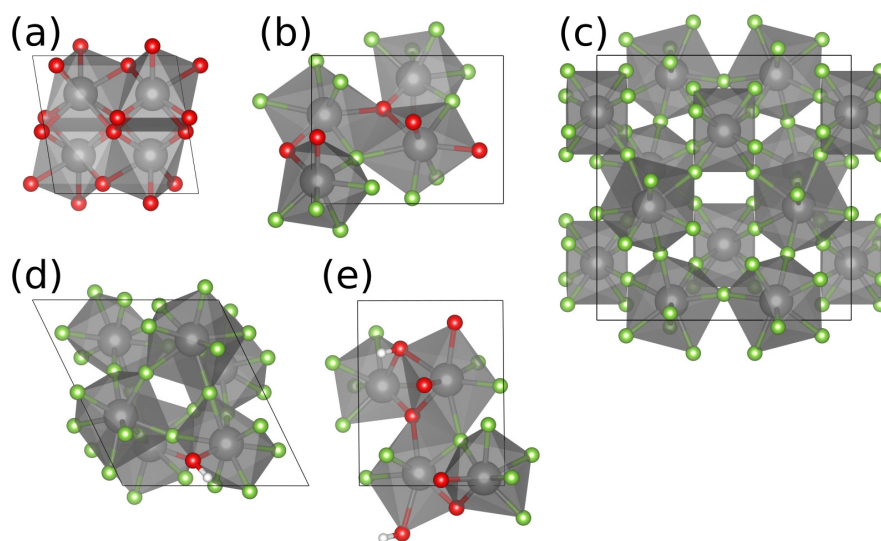


Figure 4.1 paper **A** contrasting the cohesive energies (PBE/773 eV/ $4 \times 4 \times 4$) of the geochemical twins Zr:Hf as monoclinic crystals of **(a)** α - MO_2 ($P2_1/c$), **(b)** MOF_2 ($P2_1$), **(c)** β - MF_4 ($C2/c$), and respective most stable mono-hydroxylation products of the unit cells of β - MF_4 yielding **(d)** $\text{M}_6\text{F}_{23}\text{OH}$, or of MOF_2 yielding **(e)** $\text{M}_4\text{O}_4\text{F}_7\text{OH}$.

Following published method testing results, which revealed ordinary Perdew-Becke-Ernzerhof (PBE) as the best suited functional for Zr(IV) oxide,^[174] we chose the same. Despite the wide application of the binary fluorides, this paper was the first DFT and second computational investigation^[175] overall to be conducted on fluorozirconates or fluorohafnates, just as on crystalline Zr(IV) or Hf(IV) oxofluorides of any stoichiometry. Experiments have shown that solvated Hf/Zr(IV)-species in aq. solution are fluoro hydroxido complexes. Thus, paper **A** also probed the affinity for hydroxide by the cohesive energies of the hypothetical, endothermic mono-hydroxylation of the respective fluorides or oxofluorides. Again, no simple Zr(IV) or Hf(IV) crystals are known that incorporate hydroxides within the lattice. Therefore, only a low degree of hydroxylation was modeled by replacing a single fluorine per unit cell. This equaled a F:OH ratio of 7:1 within the mono-hydroxylated oxofluorides or 23:1 within the mono-hydroxylated fluorides (see Figure 4.1 d–e). It was found that the geochemical twins favor the same position for mono-hydroxylation. For binary and ternary oxo-/fluorides, the relaxed interatomic distances of Hf–O/F were slightly shorter than Zr–O/F, agreeing well with the respective crystal structures. That our PBE-relaxed atomic structures reproduced this, suggested that no explicit relativistic treatments were needed for Hf(IV) within the periodic bulk, at least for the applied plane wave PAW ansatz. Also within the solvated fluoro hydroxido complexes, the average radial distance over Hf–F/OH was measured to be slightly shorter than the respective average distance to Zr.^[176] This is consistent with our found slightly shorter bond distances for Hf–OH than Zr–OH within the mono-hydroxylated products. In agreement with the shorter bond distances, also the cohesive energies have

been found to be more negative for the crystals of Hf(IV) compared to those of Zr(IV). This suggested that Hf(IV) formed stronger bonds to any of these three anions. The fluorination reaction from oxide to fluoride showed that the affinity gap between Zr(IV) and Hf(IV) was slightly larger for the fluorides than the oxides. This agreed with the higher fluoride affinity shown by Hf(IV) than Zr(IV) within diluted aq. HF.^[38,39] Within all respective four most stable mono-hydroxylation products, trifurcated H-bonds were found. However, only for the mono-hydroxylated fluorides, such trifurcated H-bonds were a reoccurring feature regardless of the position of mono-hydroxylation. The strength of their H-bond correlated with the energetic order of the positional isomers. Compared to averages among transition metal compounds,^[177] the main O–H···F interaction of these trifurcated H-bonds were found to be quite strong. For the Zr(IV) and Hf(IV) oxides, a publication has shown,^[178] that the subtle differences between the electronic energies at the PBE level are of equivalent size as those of the free energies at elevated temperature. Consequently, either the differences themselves within zero point energy (ZPE), temperature-dependent enthalpic term, translational entropy, and volume work have been of even smaller magnitude or canceled each other. For the ZPE itself, it has been found that the almost doubled mass of Hf–O compared to Zr–O was counterbalanced by the higher force constant, which results in practically identical ZPE for the bulk unit cell.^[179,180] Due to the absence of literature phonon spectra for ZrF₄ or HfF₄, we investigated the ZPE differences for the molecular counterparts. According to these calculations at the PBE/def2-TZVP level applying zeroth order regular approximation (ZORA), both ZPE have been identical. This agrees well with the known equivalency in ZPE for the respective solid MO₂. Therefore, we considered the approach of comparing purely electronic energies as a sufficient first approximation to evaluate the difference between the respective bulk Zr(IV) and Hf(IV) crystals. The same paper also evaluated the fluorination reaction of crystalline Zr(IV) and Hf(IV) oxides.^[178] In contrast, however, they considered molecular oxo-/fluorides as products within the gas phase. Interestingly, they found the reversed Zr:Hf trend suggesting a higher fluoride affinity shown by Zr(IV). From this follows, that the stability of the molecular products must have been reversed compared to our crystalline fluorides. Mullins et al.^[178] state that the enthalpic and entropic terms for molecular MF₄ were calculated at the PBE/TZ2PP level, presumably applying effective core potentials (ECPs) and presumably also deriving the ZPE from this setup. No explicit relativistic correction was applied onto the basis functions. Within our own, analogous molecular test calculations of PBE/TZ2P, we found that applying the default, large ECP of 60 electrons onto Hf results in overestimated Hf–F bond lengths and underestimated ZPE. Accordingly, these results are in great contrast to the ones obtained from expanding all electrons in basis functions and explicitly treating the scalar relativistic effects. This suggested, that the ZORA/all-electron ansatz was essential for molecular Hf(IV) fluoride. However, as this work focused on the Zr:Hf differences within the solid state, we chose to dive not too deep into the

underlying reasons for the odd, method-depending gas phase behavior. We left this question open for further studies.

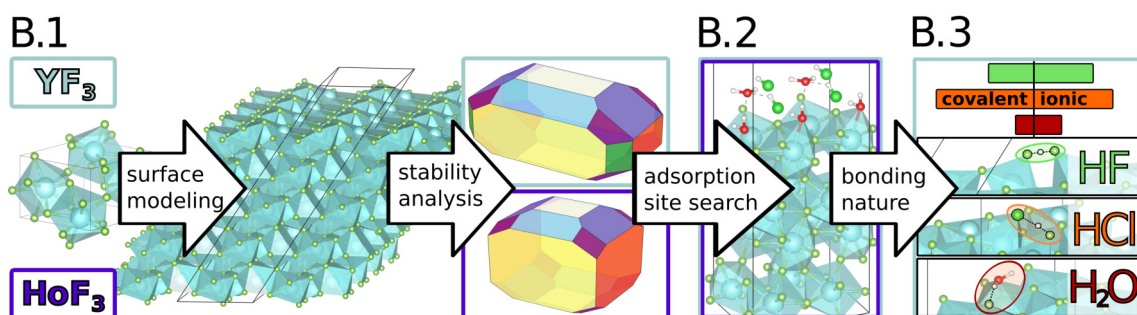


Figure 4.2 geochemical twin surface modeling and fluoride vs. chloride affinities at surfaces: the study of the geochemical twin pair Y(III) (cyan frame) and Ho(III) (violet frame) trifluorides started from modeling the low-lying Miller indices surfaces as slabs within paper **B.1** to analyze their relative stabilities and abundances; onto the few most abundant surfaces of both materials, the configurational landscape of adsorption sites is probed within paper **B.2** by a full coverage of HCl, HF, or H₂O molecules; for YF₃, the bonding nature of these adsorptions is analyzed in paper **B.3** allowing to assign covalent vs. ionic contributions.

So far, the differences within a geochemical twin pair have only been discussed for bulk crystals. In the upcoming part, the discussion is expanded to the situation at pristine surfaces (see Fig. 4.2). While numerous experimental works exist on wairerite-structured β -YF₃-based thin films^[56,67–69] or nanoparticles,^[61–63,66,70–73] prior to our work, no publication evaluated the surfaces without external influences from the particle growth procedure. In paper **B.1**, we performed the first comprehensive surface stability analysis for any wairerite-structured crystal (orthorhombic, *Pnma*). The surface stabilities and abundances were evaluated for the prototype structure of β -YF₃ itself and its geochemical twin compound β -HoF₃. Due to the practically identical ionic radii of both cations, their crystalline unit cells are also very alike.^[181,182] However, at the surfaces, there are non-saturated electrostatic interactions by the missing counter ions, as well as missing orbital interactions by the dangling bonds. While we expected the former to influence the two twin elements equivalently, this was not clear for the missing orbital interactions. Consequently, the surface stability analysis was performed for both, β -YF₃ and β -HoF₃, independently.

Before the surface results are discussed, comments on the electronic structure methods applied on β -HoF₃ should be made. Within this work, Ho has been the only element with unpaired electrons in its most stable oxidation state. The electronic configuration of Ho(III) is [Xe] 4f¹⁰. Conveniently, the 4f-shell of lanthanides has been found to generally not participate in chemical bonding.^[5–11] Especially, as this work aimed for correct atomic structures, not for optical properties, we chose it a valid approach to use a 4f-in-core ansatz for the electronic structure of Ho. Additionally, treating the 4f-electrons explicitly would demand a method beyond ordinary DFT (see section 2.4). The 4f-shell of LnF₃ is known to produce split

bands of an occupied valence band and an unoccupied conduction band.^[101] Applying a plain GGA (e.g., PBE), this cannot be reproduced. Instead, a single, joint 4f-band was formed. Subsequently, the Fermi-level lies within the band yielding a pseudo-metallic character. By using exact Hartree-Fock exchange as in hybrid DFT (e.g., the Heyd-Scuseria-Ernzerhof hybrid functional of HSE06), the 4f-band splitting was reproduced. To avoid the costly hybrid functional, the 4f-splitting can also be achieved by applying a Hubbard-type correction with an empirical U parameter onto the respective DFT Kohn-Sham orbitals (see subsection 2.1.5). Within paper **B.1**, we used PBE to apply the same functional on the MF_3 crystals, as well as on the molecular adsorbates for the further studies already planned. The U parameter for Ho was scanned within a range of 1–10 eV in steps of 1 eV for f-orbitals of Ho (U_f). The experimental unit cell data^[181] and HSE06 band gaps served as references. The d-shells of isolated Ln(III) ions are either fully occupied (3d and 4d) or empty (5d). However, our density of states (DOS) calculation for β - HoF_3 showed, that the 5d-bands of Ho not only constituted the conduction band (CB), to a smaller portion, these also overlapped with the 2p-band of fluorine forming the valence band (VB). Due to their VB contribution, we also tested a Hubbard-type correction onto the d-orbitals of Ho with $U_d = 1$ –10 eV in steps of 1 eV. We found that the relaxation with PBE+ $U_d/4f$ -in-core applying 3 eV reproduced the experimental crystal structure,^[181] as well as the HSE06 band gaps best. All these points suggested, that the explicit treatment of 4f-electrons was not needed for, or even led away from, a reasonable electronic structure. Finally, on the magnetic structure, it should be commented, that β - HoF_3 is anti-ferromagnetic below 0.53 K and paramagnetic above.^[183] This means, that magnetism is only of importance at extremely low temperatures. Given the low magnetic coupling, we expected little influence on the atomic structure. Therefore, paper **B.1** applied PBE+ U_d 3 eV/4f-in-core to obtain and investigate the atomic structure of β - HoF_3 .

The aim of this paper was to find the most stable surface terminations and consequently, surface abundances for the seven low-lying Miller indices surfaces (hkl) of β - YF_3 and β - HoF_3 . From all stoichiometric surface terminations and those, with a small to moderate fluorine-deficit of one or two F per surface unit cell, the most stable ones have been determined (see Fig. 4.3 c). This yielded a scope of 24 terminations. According to their inherent quantum chemical stabilities, both trifluorides were found to prefer the same termination for each Miller indices surface, with the exception of substoichiometric (111), for which different coordination polyhedra are formed at the surface. Linked to their surface geometry, the respective surface abundances were determined by a Wulff plot construction (see Fig. 4.3 a–b). The highest abundances within β - YF_3 and β - HoF_3 were found for (010). However, already the second most abundant surface differed between the two twins. While (100) was found to be the second most abundant surface for β - HoF_3 , it was the second least one for β - YF_3 . The contribution of substoichiometric surfaces of (101) and (111) varied from

one fifth in β -HoF₃ to one third in β -YF₃. Averaged over the overall quantum chemically predicted surface, the thermodynamical barrier for the formation of surfaces from bulk was found to be higher for β -YF₃ than β -HoF₃.

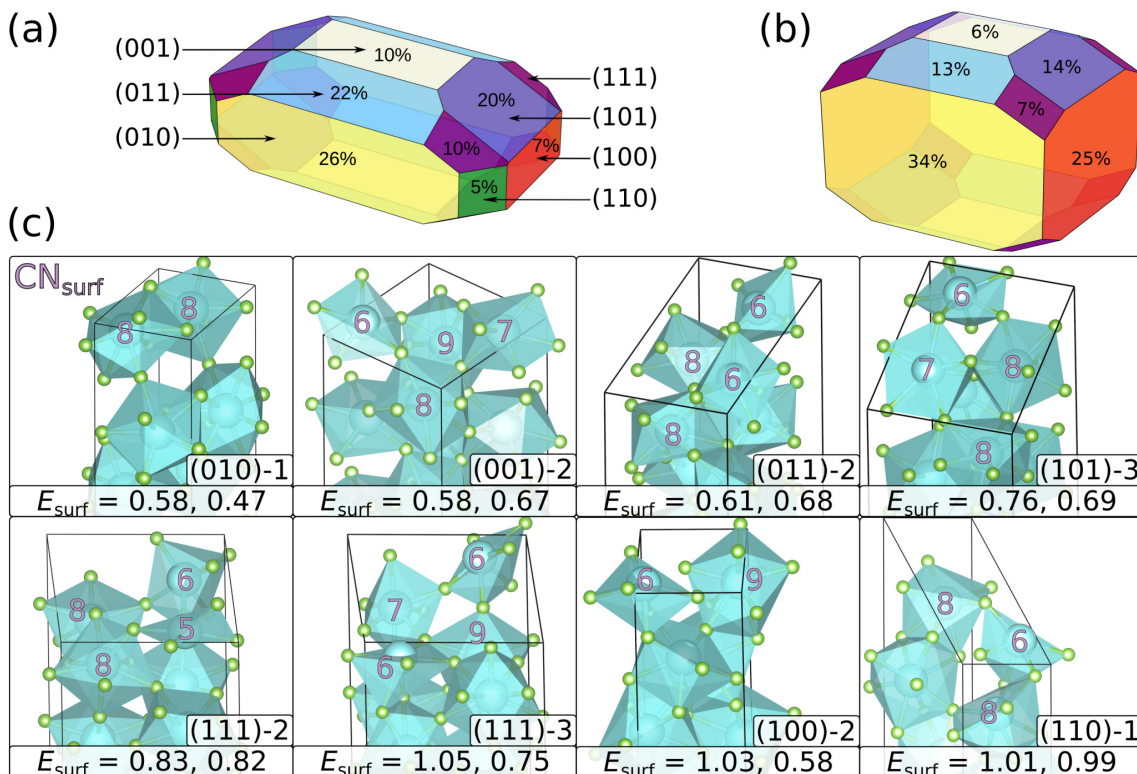


Figure 4.3 paper **B.1** scanning surface stabilities of β -YF₃ (PBE/772.6 eV/ $9 \times 9 \times 9$) and β -HoF₃ (PBE+U_d 3 eV/772.6 eV/ $7 \times 7 \times 7$): Wulff plots of **(a)** β -YF₃ and **(b)** β -HoF₃ with respective surface abundances (%_{surf}); **(c)** most stable surface terminations with surface energies (E_{surf}) in J m⁻² of first β -YF₃, then β -HoF₃; within (111) β -YF₃ prefers (111)-2, while β -HoF₃ prefers (111)-3, which differ in metal coordination numbers (CN_{surf}).

On the atomic surface structures determined in paper **B.1**, the adsorbate-surface interactions with HF, HCl, and H₂O were examined in paper **B.2**. Its aims were to first, scan the vast configurational space of possible adsorptions (see Fig. 4.4 a), second, to determine whether the adsorbate-surface interactions differ between β -YF₃ and β -HoF₃, and third, to reveal if this is dependent on the chosen surface cut. The four most abundant surfaces of stoichiometric (010), (100), and (011), as well as (101) showing a substoichiometric F-content were considered. The fluoride and chloride affinities have been probed using the neutral species of HF and HCl, in accordance to the applied periodicity. The possible adsorption sites were scanned by > 300 generically created adsorbate conformations and 200 ps of ab initio molecular dynamics (AIMD) simulations. Both considering surfaces fully covered by adsorbates. From those, 44 single adsorbate configurations were structurally and energetically compared between β -YF₃ and β -HoF₃. The chosen reference of H₂O adsorptions

showed themselves as weak and insensitive to the surface cut (see Fig. 4.4 b). Onto any surface, H₂O adsorbed slightly stronger onto β -HoF₃ than β -YF₃. For the adsorptions of HF or HCl, we found a strong dependence of bonding energy (ΔE_{bond}) on the chosen surface cut. For HCl, this even showed within its Bader charges. Contrasting HF vs. HCl, we found that both β -MF₃ show considerably higher ΔE_{bond} for HF than for HCl onto any of the three stoichiometric surfaces. This agreed with the preference for fluoride over chloride found for Y(III) in aq. solutions by AIMD simulations.^[54] Consequently, the preference for fluoride shown by Y(III) is not only present in solution. Unfortunately, no such reference publication could be found for the behavior of Ho(III). Between the surface cuts, it varied whether the respective ΔE_{bond} was stronger for Y(III) or Ho(III). The bulk-like surface of (010), with a low metal accessibility, showed a slight preference of both halides for β -HoF₃ over β -YF₃, which were comparable to that of H₂O. Onto the stoichiometric surfaces with a higher metal accessibility of (100) and (011), ΔE_{bond} of HF and HCl were significantly stronger. This correlated with both surfaces also yielding the strongest H-bonds. By the stronger interactions, also the structural changes upon adsorption were higher. Interestingly, these surfaces showed a varying metal preference. HF and HCl, both gave a considerable preference of β -HoF₃ over β -YF₃ onto (100). As described in paper **B.1**, this surface was found to be much more available for β -HoF₃ than β -YF₃. However, onto (011), HF and HCl showed the reversed preference by forming the stronger ΔE_{bond} with β -YF₃. This surface was also more abundant within β -YF₃ than β -HoF₃. Comparing these surface interactions with the literature on aq. solutions, we found that only the adsorptions onto (011) and (101) agreed with the described stronger affinity for fluoride, as well as for chloride shown by Y(III) compared to Ho(III).^[18,37,41,54,55] Thus, the variety for one adsorbate between different surfaces was found to be much larger than the difference between adsorbates onto the same surface. This illustrated that, in contrast to free Y(III) and Ho(III) cations in solution, the local environments at β -YF₃ and β -HoF₃ surfaces have been much more diverse. These produced very surface dependent binding situations for the adsorbates, even though, the two respective ions are as similar as Y(III) and Ho(III). The differences within the local environments affected the two twin elements differently. Consequently, it shifted been the surfaces, which of the two β -MF₃ could bind HF or HCl a little stronger compared to the other metal fluoride.

Coming to the substoichiometric surface of (101), both, HF and HCl adsorbed considerably stronger onto β -YF₃ than β -HoF₃. However, adsorptions onto the (101) surface revealed themselves as special, as the molecular adsorbate dissociated in a hydride-forming manner. Three different final hydride to fluoride distances were obtained. (101)·H₃ÅF/Cl, (101)·H_{3.5}ÅF, and (101)·H₇ÅF/Cl, which according to the charge repulsion, are listed in order of stability. For HCl, the medium hydride to chloride distance of 3.5 Å was not found to be meta-stable. Instead, HCl posed it as more mobile than HF directly yielding the 7 Å sepa-

rated positional isomer. The hydride formation was possible, as (101) contained formal M(II) centers, whose electron density was transferred to the adsorbate. We tested the effect of the applied $U_d = 3$ eV onto Ho-d orbitals onto the electronic and magnetic structure of bare (101). PBE and PBE+ U_d agreed on all considered quantities.

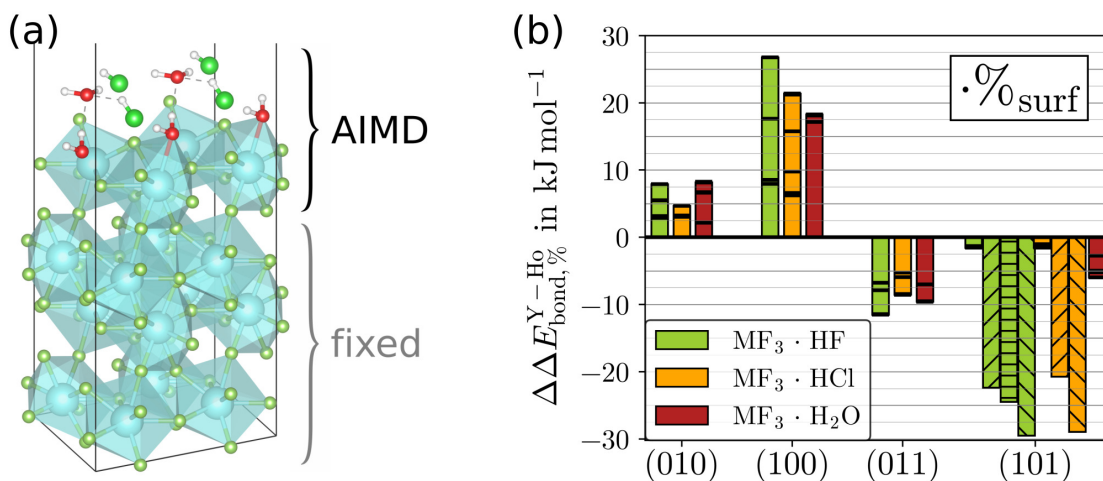


Figure 4.4 paper **B.2** of YF₃ vs. HoF₃ surface-adsorbate interactions to HF, HCl, or H₂O (PBE+D3(BJ)/773 eV/Å) with $U_d = 3$ eV on Ho: **(a)** with exemplary structure of (HCl)₄(H₂O)₄·(010) for the adsorption site scan applying AIMD; **(b)** $\Delta E_{\text{bond},\%}(\text{YF}_3) - \Delta E_{\text{bond},\%}(\text{HoF}_3)$, the difference in bonding energy between isolated adsorptions onto YF₃ or HoF₃ multiplied by the respective surface abundance (%_{surf}); bar plots highlight the respective strongest adsorptions among all values (black lines); the hydride-forming adsorptions are given separately as (101)·H_{3.5}ÅF/Cl (upward stripes), (101)·H_{3.5}ÅF (horizontal stripes), or (101)·H₇ÅF/Cl (downward stripes).

Since by electrostatics alone, Y(III) and Ho(III) should act equally, any difference must originate from unequal orbital interactions and thus covalent contributions. To explore these, periodic energy decomposition analysis (pEDA) was applied to break the overall interaction energy (ΔE_{int}) of adsorbate-surface interactions into its subcomponents (see subsection 2.2.3). Within paper **B.3**, the same atomic structures for β -YF₃ as obtained in paper **B.2** were analyzed further. Its aim was to reveal the electrostatic vs. covalent contributions for the three adsorbates of HF, HCl, or H₂O and to illuminate which effect the chosen surface of (010), (100), (011), or substoichiometric (101) had, before moving on towards the respective β -HoF₃ adsorptions. To apply pEDA, the VASP-determined electronic structures have been recalculated within AMS-BAND. This approach was validated by comparison of the overall ΔE_{bond} with relaxed reactants from the VASP and AMS-BAND-derived electronic structures. No difference within the bonding pattern was observed between the adsorptions of a single molecule or multiple molecules of up to four adsorbates (see Fig. 4.5 (b)). We found all H₂O adsorptions to be very ionic. The attractive contributions were made from 65% electrostatics. This yielded a very low sensitivity for the surface structure. The corresponding

atomic bonding pattern was dominated by a direct $O-Y_{\text{surf}}$ coordination. Quite contrary, the adsorptions of HF and HCl varied in their ionic to covalent character with electrostatic ratios of 30–60%. Accordingly, these have been found to be very sensitive for the surface structure. With a decreasing electrostatic ratio, the adsorption strength increased. The overall ΔE_{int} varied by almost 1000 kJ mol^{-1} . Again, the electrostatic interaction mainly corresponded to a direct $F/Cl-Y_{\text{surf}}$ coordination (see 4.5 (a) 3a–3b). The increased covalency and therefore surface-sensitivity was found to be correlated to a H-bond of $F/Cl-H \cdots F_{\text{surf}}$ (see 4.5 (a) 2a–2b), which was much stronger than the direct coordination. H-bonds of comparable distance also gave similar interaction, electrostatic, and orbital interaction energies. For the adsorption of HF, the formed H-bond has been highly symmetrical forming a [FHF]-like moiety. With $X = Cl$, the surface fluorine abstracted the hydrogen from HCl. The most asymmetrical $Cl \cdots H-F_{\text{surf}}$ were found to yield the strongest H-bonds resulting in the most covalent adsorptions among the stoichiometric surfaces. However, due to the H–Cl dissociation, these also came with the highest preparation energies. Including the relaxation of the reactants, each surface formed the strongest adsorption with HF instead of HCl. The preference for HF has been in line with the higher affinity for Y(III) in solution for fluoride than chloride.^[54] From the hydride-forming dissociated structures, only $(101) \cdot H_3\bar{A}F/Cl$ could be evaluated by pEDA, as the further separated anions gave no suitable fragment. According to the large change in electron density, these possessed the strongest ΔE_{int} and covalency, from which both, was found to be stronger for the dissociated fluoride than the chloride.

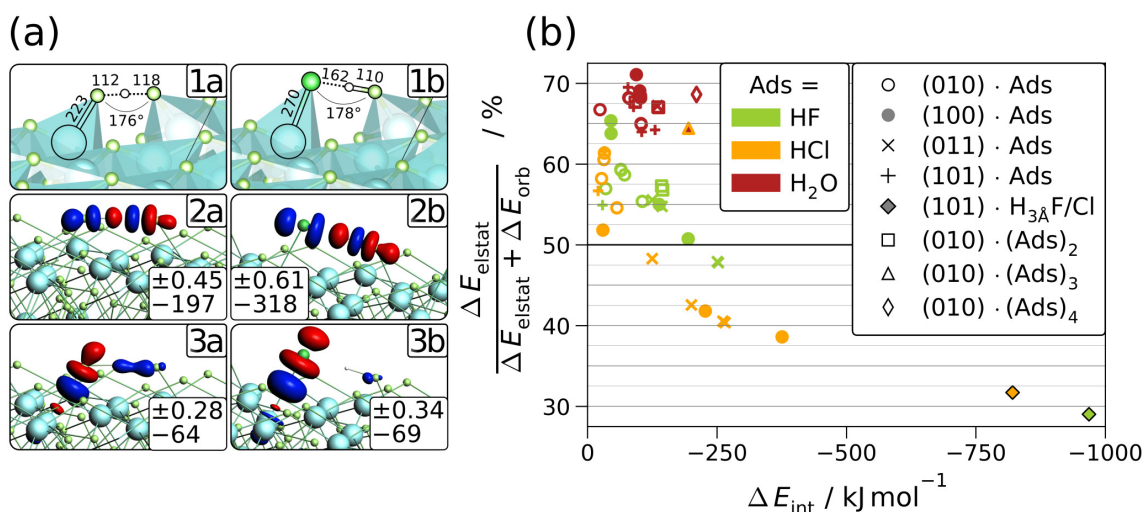


Figure 4.5 paper **B.3** of β -YF₃ surface-adsorbate interactions to HF, HCl, or H₂O applying pEDA (PBE+D3(BJ)/ZORA/TZ2P/ Γ): **(a)** comparison of strongest adsorbed structures within (011)·HF (1a) or (011)·HCl (1b) with the respective two strongest NOCV deformation densities (red = reduction / blue = accumulation of electron density) with isosurface values of 0.006 (2a–b) or 0.0015 e \AA^{-3} (3a–b); the inserts state the respective eigenvalues in e (top) with their contribution to the orbital energy (ΔE_{orb}) in kJ mol⁻¹ (bottom); **(b)** ratio of electrostatic energy (ΔE_{elstat}) among its sum with ΔE_{orb} vs. the overall interaction energy (ΔE_{int}).

As a whole, this work was dedicated to find subtle differences within the atomic and electronic structures between crystalline fluorides of the geochemical twin pairs of Zr:Hf (paper **A**) and Y:Ho (paper **B.1–B.3**). This search presented itself as a journey from the bulk, crystalline properties in paper **A**, went over to detect the atomic structures of the pristine surfaces in paper **B.1**, to finally arrive at molecular adsorptions onto these surfaces within paper **B.2–B.3**. Along the way, a broad area of solid state models and varieties was visited.

5. Outlook

Taking this journey further, the next destination would be to isolate the distinct bonding contributions for adsorptions onto HoF_3 . It would be very interesting to compare the degree and nature of covalent bonding character to those onto YF_3 . For the latter, this work revealed within paper **B.3** that strong orbital contributions have been linked to $\text{X}-\text{H}\cdots\text{F}_{\text{surf}}$ H-bonds, while direct $\text{X}-\text{M}_{\text{surf}}$ coordinations contributed only minor to the covalent character and subsequently total interaction energy. Given the different frontier orbitals of Ho(III) , the orbital contributions should effect the adsorptions onto HoF_3 somewhat differently. To make this analysis possible, however, a preceding method developing task is necessary to expand the scope of the applied pEDA onto DFT+U. Moreover, experiments could provide further insights. Especially, adsorption studies onto surfaces of YF_3 and HoF_3 in ultra high vacuum could experimentally prove the found impact of the surface cut. From a practical point of view, water would be the least problematic adsorbate. However, only HF and HCl showed the interesting surface dependency. Handling HF is without doubt challenging given the health risk and special experimental setup needed. To study the interaction of HCl onto the surfaces, on the other hand, should be manageable.

However, apart from this next step at hand, taking that journey further, also demands to take a detour, away from the crystalline phase, back to aq. solutions. To understand the non-chondritic geochemical twin ratios found within the fluoride-rich, hydrothermal vein ores, further experimental and computational studies are needed for both twin pairs. While incomplete and partially incompatible data exists for the twin pair of Y:Ho, it is very rare for Zr:Hf. Even for the former, however, the roles of certain anions are still under debate. On the one hand, Migdisov et al. proposed in 2016, that REE(III) and Y(III) are mainly transported as complexes with chloride or sulfate, while fluoride leads to precipitation.^[42] On the other hand, Louvel et al. emphasized in 2022, that the transport of these cations is very pH-dependent.^[184] At alkaline conditions, the fluoride-induced precipitation of REE(III) and Y(III) is much weaker, as the stability of the solvated fluorido complexes is improved. On the same account, sulfates and chlorides may only transport REE(III) and Y(III) in acidic solutions. Instead, Louvel et al. suggest that precipitation of fluorocarbonates from alkaline solutions plays an important role.^[184]

New lab measurements scanning a range of pH-values, temperatures, and concentrations should be considered. So far, most experimental setups only varied one of these three parameters, which reduces the comparability to other publications. Furthermore, most of these involved a single anionic species only. For example, no solution experiment has been conducted, yet, which contained fluoride as well as chloride, while also containing both twin elements, Y and Ho simultaneously. Such an experiment, also applied on the twin pair of Zr:Hf could finally elucidate their relative affinities.

Also further computational works on aq. solutions are needed. AIMD simulations at elevated temperatures including several of the available anionic species as phosphate, sulfate, hydroxide, carbonate, or hydrogencarbonate simultaneously, could provide a more realistic understanding. These would also allow the formation of e.g. fluorocarbonates.

With a more complete picture of the geochemical twin compounds present in hydrothermal solutions, it would be very interesting to come back to the solid phase. While this work contrasted the fluoride vs. chloride affinities via adsorptions of HF and HCl onto crystalline geochemical twin fluorides, it would be insightful to compare it to the reserved model. Fluorspar is the most common fluoride source in hydrothermal veins. The adsorption of the geochemical twin complexes as found in solution as e.g., fluorides, or chlorides onto fluorspar surfaces could provide a deeper understanding of the precipitation process. Especially, AIMD would be suited to investigate the dynamics, but also the explicit solvent and temperature effects.

6. References

- [1] F. Albarède, *Geochemistry: An Introduction*, 2nd ed., Cambridge University Press, Cambridge, **2009**.
- [2] M. I. Inamuddin, R. Ahamed, T. A. Boddula, *Geochemistry - Front Matter*, John Wiley & Sons, Ltd, **2021**.
- [3] M. Bau, *Contrib. Mineral. Petrol.* **1996**, *123*, 323–333.
- [4] A. Pack, S. S. Russell, J. M. G. Shelley, M. van Zuilen, *Geochim. Cosmochim. Acta* **2007**, *71*, 4592–4608.
- [5] C. Huang, Z. Bian, *Rare Earth Coordination Chemistry - Introduction*, Ch. 1, John Wiley & Sons, Ltd, Singapore, **2010**.
- [6] Z. Barandiarán, L. Seijo, *Computational Methods in Lanthanide and Actinide Chemistry - 4f, 5d, 6s, and Impurity-Trapped Exciton States of Lanthanides in Solids*, 1st ed., (Ed.: M. Dolg), Ch. 9, John Wiley & Sons, Ltd., Chichester, **2015**.
- [7] H. Sicius, *Seltenerdmetalle: Lanthanoide und dritte Nebengruppe - Physikalische und chemische Eigenschaften*, Ch. 3, Springer Spektrum, Wiesbaden, **2015**.
- [8] M. Dolg, *Computational Methods in Lanthanide and Actinide Chemistry - Shell Structure, Relativistic and Electron Correlation Effects in f Elements and Their Importance for Cerium(III)-based Molecular Kondo Systems*, (Ed.: M. Dolg), Ch. 16, John Wiley & Sons, Ltd., Chichester, **2015**.
- [9] J.-B. Lu, X.-L. Jiang, H.-S. Hu, J. Li, *J. Chem. Theory Comput.* **2023**, *19*, 82–96.
- [10] J. Ciupka, X. Cao-Dolg, J. Wiebke, M. Dolg, *Phys. Chem. Chem. Phys.* **2010**, *12*, 13215–13223.
- [11] J. Kuta, A. E. Clark, *Inorg. Chem.* **2010**, *49*, 7808–7817.
- [12] O. Greis, J. Haschke, *Handbook on the Physics and Chemistry of Rare Earths - Rare earth fluorides*, 5th ed., (Eds.: K. Gschneidner, L. Eyring), Ch. 45, Elsevier, Amsterdam, **1982**.
- [13] S. A. Wood, *Chem. Geol.* **1990**, *82*, 159–186.
- [14] M. Bau, P. Dulski, *Contrib. Mineral. Petrol.* **1995**, *119*, 213–223.
- [15] J. Schönenberger, J. Köhler, G. Markl, *Chem. Geol.* **2008**, *247*, 16–35.
- [16] M. R. Payne, A. P. Gysi, N. C. Hurtig, *Chem. Geol.* **2023**, *617*, 121256.
- [17] D. Atencio, A. C. Bastos Neto, V. P. Pereira, J. T. M. M. Ferron, M. Hoshino, T. Moriyama, Y. Watanabe, R. Miyawaki, J. M. V. Coutinho, M. B. Andrade, K. Domanik, N. V. Chukanov, K. Momma, H. Hirano, M. Tsunematsu, *Mineral. Mag.* **2015**, *79*, 767–780.
- [18] A. Loges, A. A. Migdisov, T. Wagner, A. E. Williams-Jones, G. Markl, *Geochim. Cosmochim. Acta* **2013**, *123*, 403–415.

- [19] K. M. Goodenough, J. Schilling, E. Jonsson, P. Kalvig, N. Charles, J. Tuduri, E. A. Deady, M. Sadeghi, H. Schiellerup, A. Müller, G. Bertrand, N. Arvanitidis, D. G. Eliopoulos, R. A. Shaw, K. Thrane, N. Keulen, *Ore Geol. Rev.* **2016**, *72*, 838–856.
- [20] R. Gill, *Chemische Grundlagen der Geo- und Umweltwissenschaften*, 2nd ed., Springer Spektrum, Berlin, Heidelberg, **2020**.
- [21] V. Salters, *Geochemistry. Encyclopedia of Earth Science - Elements: High field strength*, (Eds.: C. Marshall, R. Fairbridge), Springer Netherlands, Dordrecht, **1998**.
- [22] H. Rollinson, V. Pease, *Using Geochemical Data: To Understand Geological Processes - Using Trace Element Data*, 2nd ed., Ch. 4, Cambridge University Press, Cambridge, **2021**.
- [23] Sandbh, CC BY-SA 4.0 via Wikimedia Commons, https://commons.wikimedia.org/wiki/File:B%26W_PT.jpg, **21.12.2020**.
- [24] R. D. Shannon, *Acta Cryst. A* **1976**, *32*, 751–767.
- [25] R. G. Pearson, *J. Am. Chem. Soc.* **1963**, *85*, 3533–3539.
- [26] S. Gao, T.-C. Luo, B.-R. Zhang, H.-F. Zhang, Y.-W. Han, Z.-D. Zhao, Y.-K. Hu, *Geochim. Cosmochim. Acta* **1998**, *62*, 1959–1975.
- [27] J. R. Haas, E. L. Shock, D. C. Sassani, *Geochim. Cosmochim. Acta* **1995**, *59*, 4329–4350.
- [28] A. C. Strzelecki, A. Migdisov, H. Boukhalfa, K. Sauer, K. G. McIntosh, R. P. Currier, A. E. Williams-Jones, X. Guo, *Nat. Geosci.* **2022**, *15*, 327–333.
- [29] P. Möller, M. Bau, P. Dulski, V. Lüders, *Proc. of the Ninth Quadrennial IAGOD Symposium* **1998**, 575–592.
- [30] E. Anders, N. Grevesse, *Geochim. Cosmochim. Acta* **1989**, *53*, 197–214.
- [31] J. M. C. Neves, J. E. L. Nunes, T. G. Sahama, *Contrib. to Mineral. Petrol.* **1974**, *48*, 73–80.
- [32] R. Yin, R. C. Wang, A.-C. Zhang, H. Hu, J. C. Zhu, C. Rao, H. Zhang, *Am. Mineral.* **2013**, *98*, 1714–1724.
- [33] N. M. Kudryashov, S. G. Skublov, O. L. Galankina, O. V. Udoratina, A. V. Voloshin, *Geochemistry* **2020**, *80*, 125489.
- [34] A. Loges, Freie Universität Berlin, Berlin, Germany, private communication, **2023**.
- [35] A. P. Gysi, A. E. Williams-Jones, *Geochim. Cosmochim. Acta* **2013**, *122*, 324–352.
- [36] G. Schwinn, G. Markl, *Chem. Geol.* **2005**, *216*, 225–248.
- [37] A. A. Migdisov, A. E. Williams-Jones, T. Wagner, *Geochim. Cosmochim. Acta* **2009**, *73*, 7087–7109.
- [38] A. Migdisov, A. E. Williams-Jones, V. van Hinsberg, S. Salvi, *Geochim. Cosmochim. Acta* **2011**, *75*, 7426–7434.
- [39] A. Loges, A. A. Migdisov, T. Wagner, A. E. Williams-Jones, G. Markl, *Mineral. Mag.* **2012**, *76*, 2030.

-
- [40] E. Chao, J. Back, J. Minkin, R. Yinchen, *Appl. Geochem.* **1992**, *7*, 443–458.
- [41] A. Loges, Element mobility in hydrothermal systems, PhD thesis, Universität Tübingen (Germany), **2012**.
- [42] A. Migdisov, A. E. Williams-Jones, J. Brugger, F. A. Caporuscio, *Chem. Geol.* **2016**, *439*, 13–42.
- [43] S. A. Wood, *Volcanic, Geothermal, and Ore-Forming Fluids: Rulers and Witnesses of Processes within the Earth - The Geochemistry of Rare Earth Elements and Yttrium in Geothermal Waters*, (Eds.: S. F. Simmons, I. Graham), Society of Economic Geologists Inc., Littleton, **2005**.
- [44] A. Migdisov, X. Guo, H. Nisbet, H. Xu, A. Williams-Jones, *J. Chem. Thermodyn.* **2019**, *128*, 305–319.
- [45] C. J. Howard, R. J. Hill, B. E. Reichert, *Acta Crystallogr. B* **1988**, *44*, 116–120.
- [46] S. Pathak, P. Das, T. Das, G. Mandal, B. Joseph, M. Sahu, S. D. Kaushik, V. Siruguri, *Acta Crystallogr. C* **2020**, *76*, 1034–1042.
- [47] C. Legein, F. Fayon, C. Martineau, M. Body, J.-Y. Buzaré, D. Massiot, E. Durand, A. Tressaud, A. Demourgues, O. Péron, B. Boulard, *Inorg. Chem.* **2006**, *45*, 10636–10641.
- [48] G. Benner, B. G. Müller, *Z. Anorg. Allg. Chem.* **1990**, *588*, 33–42.
- [49] I. Cozmuta, S. Cozic, M. Poulain, S. Poulain, J. R. L. Martini, *Proc. SPIE* **2020**, 11276, Optical Components and Materials XVII, 112760R.
- [50] Z. He, W. Li, A. Yu, Y. Wu, Z. Cai, *Opt. express* **2022**, *30*, 10414.
- [51] W. C. Hasz, J. H. Whang, C. T. Moynihan, *J. Non Cryst. Solids* **1993**, *161*, 127–132.
- [52] L. Dmitruk, N. Vinogradova, V. Kozlov, V. Machov, E. Devitsin, V. Fyodorov, *J. Non Cryst. Solids* **1997**, *213-214*, 311–314.
- [53] M. Brekhovskikh, V. Sukhoverkhov, V. Fedorov, S. Batygov, L. Dmitruk, N. Vinogradova, E. Devitsin, V. Kozlov, A. Provorova, *J. Non Cryst. Solids* **2000**, *277*, 68–71.
- [54] J. Stefanski, S. Jahn, *Solid Earth* **2020**, *11*, 767–789.
- [55] Q. Guan, Y. Mei, B. Etschmann, D. Testemale, M. Louvel, J. Brugger, *Geochim. Cosmochim. Acta* **2020**, *281*, 168–189.
- [56] D. Bezuidenhout, K. Clarke, R. Pretorius, *Thin Solid Films* **1987**, *155*, 17–30.
- [57] V. Pankratov, M. Kirm, H. von Seggern, *J. Lumin.* **2005**, *113*, 143–150.
- [58] E. Sarantopoulou, Z. Kollia, A. C. Cefalas, *Opt. Mater.* **2001**, *18*, 23–26.
- [59] P. S. Peijzel, R. T. Wegh, A. Meijerink, J. Hölsä, R.-J. Lamminmäki, *Opt. Commun.* **2002**, *204*, 195–202.
- [60] C. Peng, C. Li, G. Li, S. Li, J. Lin, *Dalton Trans.* **2012**, *41*, 8660–8668.
- [61] Y. Tian, B. Chen, X. Li, J. Zhang, B. Tian, J. Sun, L. Cheng, H. Zhong, H. Zhong, R. Hua, *J. Solid State Chem.* **2012**, *196*, 187–196.

- [62] R. X. Yan, Y. D. Li, *Adv. Funct. Mater.* **2005**, *15*, 763–770.
- [63] A. A. Ansari, M. A. Manthrammel, *J. Inorg. Organomet. Polym.* **2017**, *27*, 194–200.
- [64] C. Gong, Q. Li, R. Liu, Y. Hou, J. Wang, X. Dong, B. Liu, X. Yang, Z. Yao, X. Tan, D. Li, J. Liu, Z. Chen, B. Zou, T. Cui, B. Liu, *Phys. Chem. Chem. Phys.* **2013**, *15*, 19925–19931.
- [65] H. D. A. Santos, S. M. V. Novais, C. Jacinto, *J. Lumin.* **2018**, *201*, 156–162.
- [66] X. Cui, T. Hu, J. Wang, J. Zhang, X. Zhong, Y. Chen, X. Li, J. Yang, C. Gao, *Nanomaterials* **2018**, *8*, 995.
- [67] H. Uhlig, R. Thielsch, J. Heber, N. Kaiser, *Proc. SPIE* **2005**, 5963, Advances in Optical Thin Films II, 59630N.
- [68] H. Liu, S. Li, D. Chen, X. Yang, J. He, Y. Jiang, L. Wang, D. Liu, Y. Ji, *Optik* **2020**, *205*, 163548.
- [69] J.-x. Chen, X.-p. Wang, L.-J. Wang, X.-w. Yang, Y. Yang, *J. Lumin.* **2020**, *224*, 117310.
- [70] X. Wang, J. Zhuang, Q. Peng, Y. Li, *Inorg. Chem.* **2006**, *45*, 6661–6665.
- [71] J. Lellouche, A. Friedman, A. Gedanken, E. Banin, *Int. J. Nanomed.* **2012**, *7*, 5611–5624.
- [72] E. Talik, P. Zajdel, A. Guzik, D. Skrzypek, L. Lipińska, M. Michalska, *J. Alloys Compd.* **2014**, *616*, 556–568.
- [73] D. González-Mancebo, A. I. Becerro, T. C. Rojas, M. L. García-Martín, J. M. de la Fuente, M. Ocaña, *Part. Part. Syst. Charact.* **2017**, *34*, 1700116.
- [74] A. Szabo, N. S. Ostlund, *Modern Quantum Chemistry: Introduction to Advanced Electronic Structure Theory*, Dover Publications, Mineola, New York, **2012**.
- [75] W. Koch, M. C. Holthausen, *A chemist's guide to density functional theory*, 2nd ed., WILEY-VCH, Weinheim, **2001**.
- [76] E. Schrödinger, *Ann. Phys.* **1926**, 361–376.
- [77] M. Born, R. Oppenheimer, *Ann. Phys.* **1927**, 457–484.
- [78] W. Pauli, *Z. Physik* **1925**, *31*, 765–783.
- [79] J. C. Slater, *Phys. Rev.* **1929**, *34*, 1293–1322.
- [80] V. Fock, *Z. Physik* **1930**, *61*, 126–148.
- [81] J. C. Slater, *Phys. Rev.* **1951**, *81*, 385–390.
- [82] C. C. J. Roothaan, *Rev. Mod. Phys.* **1951**, *23*, 69–89.
- [83] G. G. Hall, *Proc. R. Soc. Lond. A* **1951**, *205*, 541–552.
- [84] P. Hohenberg, W. Kohn, *Phys. Rev.* **1964**, *136*, B864–B871.
- [85] W. Kohn, L. J. Sham, *Phys. Rev.* **1965**, *140*, A1133–A1138.
- [86] S. F. Sousa, P. A. Fernandes, M. J. Ramos, *J. Phys. Chem. A* **2007**, *111*, 10439–10452.
- [87] J. P. Perdew, K. Schmidt, *AIP Conf. Proc.* **2001**, *577*, 1–20.

- [88] J. P. Perdew, K. Burke, M. Ernzerhof, *Phys. Rev. Lett.* **1996**, *77*, 3865–3868.
- [89] A. Jain, S. P. Ong, G. Hautier, W. Chen, W. D. Richards, S. Dacek, S. Cholia, D. Gunter, D. Skinner, G. Ceder, K. Persson, *APL Mater.* **2013**, *1*, 11002.
- [90] G. I. Csonka, A. Ruzsinszky, J. Tao, J. P. Perdew, *Int. J. Quantum Chem.*, *101*, 506–511.
- [91] C. Adamo, V. Barone, *J. Chem. Phys.* **1999**, *110*, 6158–6170.
- [92] J. Heyd, G. E. Scuseria, *J. Chem. Phys.* **2004**, *121*, 1187–1192.
- [93] A. V. Krukau, O. A. Vydrov, A. F. Izmaylov, G. E. Scuseria, *J. Chem. Phys.* **2006**, *125*, 224106.
- [94] S. Grimme, *J. Comput. Chem.* **2004**, *25*, 1463–1473.
- [95] S. Grimme, *J. Comput. Chem.* **2006**, *27*, 1787–1799.
- [96] S. Grimme, J. Antony, S. Ehrlich, H. Krieg, *J. Chem. Phys.* **2010**, *132*, 154104.
- [97] S. Grimme, S. Ehrlich, L. Goerigk, *J. Comput. Chem.* **2011**, *32*, 1456–1465.
- [98] G. Kresse, J. Hafner, *J. Phys.: Condens. Matter* **1994**, *6*, 8245–8257.
- [99] S. A. Tolba, K. M. Gameel, B. A. Ali, H. A. Almossalami, N. K. Allam, *Density Functional Calculations - The DFT+U: Approaches, Accuracy, and Applications*, (Ed.: G. Yang), Ch. 1, IntechOpen, Rijeka, **2018**.
- [100] N. Mott, *J. Solid State Chem.* **1990**, *88*, 5–7.
- [101] E. Rogers, P. Dorenbos, E. van der Kolk, *New J. Phys.* **2011**, *13*, 093038.
- [102] J.-M. Reiner, F. Wilhelm-Mauch, G. Schön, M. Marthaler, *Quantum Sci. Technol.* **2019**, *4*, 035005.
- [103] S. L. Dudarev, G. A. Botton, S. Y. Savrasov, C. J. Humphreys, A. P. Sutton, *Phys. Rev. B* **1998**, *57*, 1505–1509.
- [104] V. I. Anisimov, J. Zaanen, O. K. Andersen, *Phys. Rev. B* **1991**, *44*, 943–954.
- [105] A. I. Liechtenstein, V. I. Anisimov, J. Zaanen, *Phys. Rev. B* **1995**, *52*, R5467–R5470.
- [106] F. Jensen, *Introduction to Computational Chemistry*, 2nd ed., John Wiley & Sons, Ltd, Chichester, **2007**.
- [107] J. Reinhold, *Quantentheorie der Moleküle: Eine Einführung*, 5th ed., Springer Spektrum, Wiesbaden, **2015**.
- [108] BAND 2021.1, SCM, Theoretical Chemistry, Vrije Universiteit, Amsterdam, The Netherlands, <http://www.scm.com>.
- [109] G. te Velde, E. J. Baerends, *Phys. Rev. B* **1991**, *44*, 7888–7903.
- [110] F. Neese, *WIREs Comput. Mol. Sci.* **2022**, *12*, e1606.
- [111] F. Weigend, R. Ahlrichs, *Phys. Chem. Chem. Phys.* **2005**, *7*, 3297–3305.
- [112] R. Ahlrichs, M. Bär, M. Häser, H. Horn, C. Kölmel, *Chem. Phys. Lett.* **1989**, *162*, 165–169.
- [113] D. Andrae, U. Häußermann, M. Dolg, H. Stoll, H. Preuß, *Theoret. Chim. Acta* **1990**, *77*, 123–141.

- [114] L. De Broglie, *Phil. Mag.* **1924**, 47, 446–458.
- [115] P. E. Blöchl, *Phys. Rev. B* **1994**, 50, 17953–17979.
- [116] A. Jain, J. Montoya, S. Dwaraknath, N. E. R. Zimmermann, J. Dagdelen, M. Horton, P. Huck, D. Winston, S. Cholia, S. P. Ong, K. Persson, *Handbook of Materials Modeling - The Materials Project: Accelerating Materials Design Through Theory-Driven Data and Tools*, (Eds.: W. Andreoni, S. Yip), Ch. 1, Springer International Publishing, Cham, **2018**.
- [117] Materials Project, <https://legacy.materialsproject.org/about>, **11.07.2023**.
- [118] R. Dronskowski, *Computational Chemistry of Solid State Materials - Quantum-chemical Approaches: Section 2.11 - 2.19*, Ch. 2, John Wiley & Sons, Ltd, Weinheim, **2005**.
- [119] G. Kresse, D. Joubert, *Phys. Rev. B* **1999**, 59, 1758–1775.
- [120] P. E. Blöchl, J. Kästner, C. J. Först, *Handbook of Materials Modeling - Electronic Structure Methods: Augmented Waves, Pseudopotentials and The Projector Augmented Wave Method*, (Ed.: S. Yip), Ch. 1.6, Springer Netherlands, Dordrecht, **2005**.
- [121] C. Kittel, *Einführung in die Festkörperphysik*, 12., (Eds.: J. M. Greß, A. Lessard), R. Oldenbourg Verlag, München, Wien, **1999**.
- [122] C. Kittel, *Quantentheorie der Festkörper*, R. Oldenbourg Verlag, München, Wien, **1970**.
- [123] H. J. Monkhorst, J. D. Pack, *Phys. Rev. B* **1976**, 13, 5188–5192.
- [124] P. Strange, A. Svane, W. M. Temmerman, Z. Szotek, H. Winter, *Nature* **1999**, 399, 756–758.
- [125] L. Hasni, M. Ameri, D. Bensaid, I. Ameri, S. Mesbah, Y. Al-Douri, J. Coutinho, *J. Supercond. Nov. Magn.* **2017**, 30, 3471–3479.
- [126] M. K. Butt, M. Yaseen, I. A. Bhatti, J. Iqbal, Misbah, A. Murtaza, M. Iqbal, M. mana AL-Anazy, M. Alhossainy, A. Laref, *J. Mater. Res. Technol.* **2020**, 9, 16488–16496.
- [127] S. T. Baidak, A. V. Lukoyanov, *Int. J. Mol. Sci.* **2023**, 24, 8778.
- [128] N. Wiberg, *Lehrbuch der Anorganischen Chemie*, De Gruyter, Berlin, Boston, **2008**.
- [129] A. Kubas, D. Berger, H. Oberhofer, D. Maganas, K. Reuter, F. Neese, *J. Phys. Chem. Lett.* **2016**, 7, 4207–4212.
- [130] B. X. Shi, V. Kapil, A. Zen, J. Chen, A. Alavi, A. Michaelides, *J. Chem. Phys.* **2022**, 156, 124704.
- [131] J. C. Boettger, *Phys. Rev. B* **1994**, 49, 16798–16800.
- [132] G. Wulff, *Z. Kristallogr. - Cryst. Mater.* **1901**, 34, 449–530.
- [133] M. v. Laue, *Z. Kristallogr. - Cryst. Mater.* **1943**, 105, 124–133.
- [134] K. Morokuma, *J. Chem. Phys.* **1971**, 55, 1236–1244.
- [135] K. Kitaura, K. Morokuma, *Int. J. Quantum Chem.* **1976**, 10, 325–340.
- [136] T. Ziegler, A. Rauk, *Theor. Chim. Acta* **1977**, 46, 1–10.

- [137] T. Ziegler, A. Rauk, *Inorg. Chem.* **1979**, *18*, 1558–1565.
- [138] T. Ziegler, A. Rauk, *Inorg. Chem.* **1979**, *18*, 1755–1759.
- [139] M. P. Mitoraj, A. Michalak, T. Ziegler, *J. Chem. Theory Comput.* **2009**, *5*, 962–975.
- [140] M. Raupach, R. Tonner, *J. Chem. Phys.* **2015**, *142*, 194105.
- [141] L. Pecher, R. Tonner, *Wiley Interdiscip. Rev. Comput. Mol. Sci.* **2019**, *9*, 1759–0876.
- [142] M. Reiher, A. Wolf, *Relativistic Quantum Chemistry - Introduction*, Ch. 1, John Wiley & Sons, Ltd, Weinheim, **2009**.
- [143] A. A. Michelson, E. W. Morley, *Am. J. Sci.* **1887**, *34*, 333–345.
- [144] G. F. Fitzgerald, *Science* **1889**, *13*, 390.
- [145] H. A. Lorentz, *Versl. Kon. Acad. Wetensch.* **1892**, *1*, 74.
- [146] O. D. Jefimenko, *Z. Naturforsch.* **1998**, *53a*, 977–982.
- [147] A. Einstein, *Ann. Phys.* **1905**, *322*, 891–921.
- [148] P. A. M. Dirac, *Proc. R. Soc. Lond. A* **1928**, *117*, 610–624.
- [149] P. A. M. Dirac, *Proc. R. Soc. Lond. A* **1928**, *118*, 351–361.
- [150] M. Reiher, A. Wolf, *Relativistic Quantum Chemistry - Concepts of Special Relativity*, Ch. 3, John Wiley & Sons, Ltd, Weinheim, **2009**.
- [151] J. Autschbach, *J. Chem. Phys.* **2012**, *136*, 150902.
- [152] C. van Wüllen, *Handbook of Relativistic Quantum Chemistry - Part 1: Introduction to Relativistic Quantum Chemistry: Relativistic Self-Consistent Fields*, (Eds.: W. Liu, C. van Wüllen), Springer, Berlin, Heidelberg, **2017**.
- [153] R. P. Feynman, *Phys. Rev.* **1949**, *76*, 749–759.
- [154] E. C. G. Stückelberg, *Helv. Phys. Acta* **1942**, *15*, 23–37.
- [155] M. Reiher, A. Wolf, *Relativistic Quantum Chemistry - Relativistic Theory of the Electron*, Ch. 5, John Wiley & Sons, Ltd, Weinheim, **2009**.
- [156] M. Reiher, A. Wolf, *Relativistic Quantum Chemistry - Decoupling the Negative-Energy States*, Ch. 11, John Wiley & Sons, Ltd, Weinheim, **2009**.
- [157] M. Reiher, A. Wolf, *Relativistic Quantum Chemistry - Elimination Techniques*, Ch. 13, John Wiley & Sons, Ltd, Weinheim, **2009**.
- [158] C. Chang, M. Péliissier, P. Durand, *Phys. Scr.* **1986**, *34*, 394–404.
- [159] J.-L. Heully, I. Lindgren, E. Lindroth, S. Lundqvist, A.-M. Mårtensson-Pendrill, *J. Phys. B: Atom. Mol. Phys.* **1986**, *19*, 2799–2815.
- [160] E. van Lenthe, E. J. Baerends, J. G. Snijders, *J. Chem. Phys.* **1993**, *99*, 4597–4610.
- [161] E. van Lenthe, J. G. Snijders, E. J. Baerends, *J. Chem. Phys.* **1996**, *105*, 6505–6516.
- [162] E. van Lenthe, E. J. Baerends, J. G. Snijders, *J. Chem. Phys.* **1994**, *101*, 9783–9792.
- [163] P. H. T. Philipsen, E. van Lenthe, J. G. Snijders, E. J. Baerends, *Phys. Rev. B* **1997**, *56*, 13556–13562.
- [164] G. H. Dieke, H. M. Crosswhite, *Appl. Opt.* **1963**, *2*, 675–686.
- [165] Y. Shimizu, K. Ueda, *J. Lumin.* **2015**, *168*, 14–19.

- [166] P. Dorenbos, *J. Lumin.* **2004**, *108*, Proceedings of the Fourteenth International Conference on Dynamical Processes in Excited States of Solids, 301–305.
- [167] J.-B. Lu, D. C. Cantu, M.-T. Nguyen, J. Li, V.-A. Glezakou, R. Rousseau, *J. Chem. Theory Comput.* **2019**, *15*, 5987–5997.
- [168] A. Kramida, Yu. Ralchenko, J. Reader, and NIST ASD Team, NIST Atomic Spectra Database (ver. 5.10), [Online]. Available: <https://physics.nist.gov/asd> [2023, May 15]. National Institute of Standards and Technology, Gaithersburg, MD. **2022**.
- [169] P. Joubert, B. Gaudreau, *Rev. Chim. Mine.* **1975**, *12*, 289–302.
- [170] R. Papiernik, B. Frit, *Mater. Res. Bull.* **1984**, *19*, 509–516.
- [171] B. Holmberg, *Acta Crystallogr. B* **1970**, *26*, 830–835.
- [172] Y. Gong, L. Andrews, C. W. Bauschlicher, K. S. Thanthiriwatte, D. A. Dixon, *Dalton Trans.* **2012**, *41*, 11706–11715.
- [173] L. Guillet, A. Ider, J. P. Laval, B. Frit, *J. Fluor. Chem.* **1999**, *93*, 33–38.
- [174] M. Delarmelina, M. G. Quesne, C. R. A. Catlow, *Phys. Chem. Chem. Phys.* **2020**, *22*, 6660–6676.
- [175] J. F. Rivas-Silva, A. Flores-Riveros, J. S. Durand-Niconoff, N. Aquino, *Int. J. Quantum Chem.* **2004**, *97*, 815–825.
- [176] A. Loges, M. Louvel, M. Wilke, S. Jahn, S. Klemme, E. Welter, M. Borchert, S. Qiao, M. Manni, B. Keller, T. John, Preprint: Fluoride complexation of Zr and Hf in hydrothermal aqueous fluids, **2022**.
- [177] L. Brammer, E. A. Bruton, P. Sherwood, *New J. Chem.* **1999**, *23*, 965–968.
- [178] R. Mullins, S. Kondati Natarajan, S. D. Elliott, M. Nolan, *Chem. Mater.* **2020**, *32*, 3414–3426.
- [179] X. Luo, W. Zhou, S. V. Ushakov, A. Navrotsky, A. A. Demkov, *Phys. Rev. B* **2009**, *80*, 134119.
- [180] P. E. Quintard, P. Barbéris, A. P. Mirgorodsky, T. Merle-Méjean, *J. Am. Ceram. Soc.* **2002**, *85*, 1745–1749.
- [181] A. Zalkin, D. H. Templeton, *J. Am. Chem. Soc.* **1953**, *75*, 2453–2458.
- [182] A. K. Cheetham, N. Norman, *Acta Chem. Scand.* **1974**, *28*, 55–60.
- [183] P. J. Brown, J. B. Forsyth, P. C. Hansen, M. J. M. Leask, R. C. C. Ward, M. R. Wells, *J. Phys.: Condens. Matter* **1990**, *2*, 4471–4484.
- [184] M. Louvel, B. Etschmann, Q. Guan, D. Testemale, J. Brugger, *Nat. Commun.* **2022**, *13*, 1456.